UNIVERSIDAD AUTÓNOMA DE MADRID

FACULTAD DE CIENCIAS - DEPARTAMENTO DE FÍSICA APLICADA

DOCTORAL THESIS

presented in fulfillment of the requirements for the Degree of

PhD. in Advanced Materials and Nanotechnology

by

Guillermo Domínguez Cañizares

Nanostructured Nickel Oxide thin films grown by Reactive RF Magnetron Sputtering

Thesis Advisor: Alejandro Gutiérrez Delgado

May 2014

Entregada en el Registro de la Universidad Autónoma de Madrid el 13 de mayo de 2014.
Director de la Tesis Doctoral: **Prof. Dr. Alejandro Gutiérrez Delgado**.

Composición del Tribunal de evaluación:

Presidente: Prof. Dr. Leonardo Soriano de Arpe (UAM)
Secretario: Dr. José Antonio Jiménez (CENIM-CSIC)
Vocal 1: Dr. Maurizio Sacchi (SOLEIL)
Vocal 2: Dr. Germán Rafael Castro (ESRF)
Vocal 3: Dr. Iulian Preda (ALBA)
Suplente 1: Prof. Dr. Carlos Palacio Orcajo (UAM)
Suplente 2: Dr. Juan Trigo Escalera (CIEMAT)

Fecha de defensa de la Tesis Doctoral: 16 de junio de 2014.

Ilustración de portada y contraportada: micrografía FESEM de lámina de NiO crecida sobre una membrana porosa de Alúmina (AAM) bajo condiciones de sputtering 70 %-75W-5h-150ºC (figura 4.12c).

contact@guillermodominguez.net

Grupo de Recubrimientos, Intercaras y Nanostructuras
Departamento de Física Aplicada, Facultad de Ciencias
Universidad Autónoma de Madrid (UAM)

Escrito con LaTeX y JafRef 2.9.2
Maquetado con TeXstudio 2.6.2

Contents

List of Figures

List of Tables

A Sandra, por su paciencia.
A Valeria, por sus sonrisas

Chapter 1

Introduction

> "*You've got to forget the memorizing of formulas, and to try to learn to understand the interrelationships of nature. That's very much more difficult at the beginning, but it's the only successful way.*"
>
> Richard P. Feynman

Transition metal oxides have attained much attention in the last years due to their outstanding properties that make them attractive not only for fundamental studies, but also for a wide range of applications in nanotechnology. Among the transition metal oxides, Nickel Oxide (NiO) is being used nowadays in several technological applications, such as electrochromic display devices, gas and fluid sensors, resistive-switching memories, catalysis, electrochemical capacitors, or electrodes in lithium-ion batteries. In many of these applications, such as in catalysis or gas sensing, the interaction with the surrounding environment plays a very important role. The use of nanostructured materials increases the effective surface, and, consequently, enhances the yield of the surface reactions of interest. The physical properties of any nano-material, and thus the actual feasibility of its application, strongly depend on the stoichiometry, density of defects, and crystallinity, which are very sensitive to growth conditions.

Even though NiO has been profoundly studied during decades and has been pointed as a prototypic solid state system due to its basic structure but unexpected properties, it still has obscure fundamental attributes which make it attractive as an object of study [1, 2].

In particular, the electronic structure of Nickel Oxide together with its magnetic properties are subject of controversy and many studies and interpretations have appeared [3, 4]. Different electrical and optical models proposed do not agree with the experimental data, increasing the interest on this material. Whether the electrical conduction in NiO is driven by free polarons or electron hopping depends on the crystal structure, the environment conditions and the chemical composition. Nickel is said to have only one valence, though several works assign to it more oxidation states mainly due to the flexibility of its orbital bonding.

The aim of this work is to study the properties of Nickel Oxide when deposited in the form of thin films with dimensions in the nano-scale by means of reactive RF magnetron sputtering. Are those properties still unclear in this nanostructured form? Which of them are modified when reducing the thickness, creating pores or increasing the impurities concentration? Answers to these questions will be given following a method of working which starts from understanding the morphology and structure of the deposited films, continues with the electro-optical properties and ends with the understanding of the electronic structure, providing models and correlated results that support the work.

Nickel Oxide properties change dramatically when the system is arranged in nanostructured thin films specially due to the lack of stoichiometry. Dealing with such systems need a com-

prehensive study of its different physical properties. We will show that it is possible to tune some of the properties of the thin films, especially the electrical, by choosing the suitable growth conditions, considering the degrees of freedom of our experimental set-up. The first approach is to explore and control the deposition method, reactive RF magnetron sputtering, a reproducible, scalable and middle-range energy PVD method, as it is shown in chapter 4.

A model for the growth of the porous nanostructured films will be given in chapter 4, and correlated with the internal structure and morphology, obtained by means of scanning electron microscopy (SEM), profilometry, X-ray diffraction (XRD) and X-ray absorption (EXAFS). By controlling the morphology it will be possible to control the effective surface. Upon certain conditions, out-of-equilibrium growth leads to disorder and impurities, which in turn lead to new properties far from the stoichiometric NiO.

The electrical and optical aspects of a coating are not only useful to complete the comprehension of fundamental properties but are also one of the most valuable properties for industrial applications. A perfect stoichiometric Nickel Oxide is very complicated to obtain due to its tendency to have impurities in many forms. In chapter 5 we will show, regarding the structural information obtained previously, the consequences of the disorder and non-stoichiometry on the properties of the thin films. The controlled presence of Ni vacancies in the films will make it possible to tune their resistivity down to the range of some ohm-cm, which, together with their partial transparency, makes these films very interesting for electro-optical applications. Inspired by the native oxidation layer of metals, we propose a model to explain coherently the electrical resistivity evolution of the films, and the definite influence of thermal treatment. As expected, the optical absorption is also modified at will, placing these films at the centre of potential applications arising from these oxides [5].

Finally, in chapter 6 the electronic structure of the NiO oxide films will be correlated with the previous results on the geometric structure and the functional properties. Although many works studied the NiO electronic structure, only some approaches explain the non-local screening effects and surface contribution to the photoemission spectra. However, the possibility of existence Ni^{3+} ions due to unstable non-stoichiometric NiO remains as an open question. We show by means of X-ray absorption (XANES) with cluster model calculations and X-ray photoemission (XPS) measurements an interpretations of Ni vacancies as such ions. This strongly supports the previous results confirming the impurities influence in the conduction band and hence the decrease in resistivity. Thermal treatment is shown to be highly efficient by healing the surface crystal structure, reducing the amount of Ni vacancies.

Chapter 2

Introducción

Los óxidos de metales de transición han recibido mucha atención en los últimos años debido a sus excepcionales propiedades que les hacen atractivos no solo desde el punto de vista fundamental sino también para un amplio abanico de aplicaciones en nanotecnología.

De entre los óxidos de metales de transición, el óxido de níquel (NiO) se usa hoy día en varias aplicaciones tecnológicas tales como pantallas electrocrómicas, sensores de gases y fluidos, memorias de conmutación resistiva, catálisis, condensadores electroquímicos o en electrodos de baterías de ión-litio.

En muchas de estas aplicaciones tales como en catálisis o sensores de gases, la interacción con el ambiente circundante juega un papel muy importante. El uso de materiales nanoestructurados aumenta la superficie efectiva y, consecuentemente, mejora el rendimiento de las reacciones superficiales de interés. Las propiedades físicas de cualquier *nano-material*, y por lo tanto la viabilidad real de su aplicación, dependen en gran medida de la estequiometría, densidad de estados y cristalinidad, que son muy sensibles a las condiciones de crecimiento.

A pesar de que el NiO ha sido profundamente estudiado durante décadas, estableciéndose como un sistema prototípico dentro del estado sólido debido a su estructura básica y propiedades inesperadas, tiene aún aspectos fundamentales que le hacen atractivo como objeto de estudio [1, 2].

En particular, la estructura electrónica del óxido de níquel junto con sus propiedades magnéticas son objeto de controversia surgiendo muchos estudios e interpretaciones [3, 4]. Diferentes modelos eléctricos y ópticos propuestos no reproducen los datos experimentales, aumentando el interés en este material. Si la conducción eléctrica en el NiO se debe a polarones libres o al salto de electrones, ésta dependerá de la estructura cristalina, las condiciones ambientales y la composición química. El níquel es conocido por tener solo una valencia, aunque varios trabajos le asignan más estados de oxidación, principalmente debido a la flexibilidad de su enlace orbital.

El objetivo de este trabajo es estudiar las propiedades del óxido de níquel depositado en forma de láminas delgadas con dimensiones en la nano-escala mediante pulverización catódica reactiva por magnetrón de radiofrecuencia. ¿Siguen siendo estas propiedades inciertas en esta forma nanoestructurada? ¿Cuáles de éstas se modifican al reducir el espesor, crear poros o aumentar la concentración de impurezas? Se darán respuestas a estas preguntas siguiendo un método de trabajo que comienza entendiendo la morfología y estructura de las láminas depositadas, continúa con las propiedades electro-ópticas y finaliza con la comprensión de la estructura electrónica, proporcionando modelos y correlacionando resultados que apoyan el trabajo.

Las propiedades del óxido de níquel cambian dramáticamente cuando el sistema se dispone en láminas delgadas nanoestructuradas, especialmente debido a la falta de estequiometría. Tratar con tales sistemas necesita de un estudio exhaustivo de sus diferentes propiedades físicas. Mostraremos que es posible modificar algunas de las propiedades de las láminas delgadas, especialmente las eléctricas, eligiendo las condiciones de crecimiento adecuadas, dentro de los grados de libertad

disponibles en el montaje experimental. La primera aproximación es la de explorar y controlar el método de deposición, pulverización catódica reactiva por magnetrón de radiofrecuencia, un método físico (PVD) reproducible, escalable y en un rango medio de energía, como se muestra en el capítulo 4.

En el capítulo 4 se muestra un modelo para el crecimiento de láminas porosas nanoestructuradas, correlacionado con la estructura interna y la morfología, obtenido mediante microscopía electrónica de barrido (SEM), perfilometría, difracción de rayos-X (XRD) y absorción de rayos-X (EXAFS). Mediante el control de la morfología será posible controlar a su vez la superficie efectiva. Bajo ciertas condiciones, crecimientos fuera del equilibrio conducen a desorden e impurezas que a su vez llevan a nuevas propiedades lejos del NiO estequiométrico.

Los aspectos elétricos y ópticos del recubrimiento no sólo son útiles para completar la comprensión de las propiedades fundamentales sino también uno de las propiedades más valoradas en aplicaciones industriales. Un óxido de níquel perfecto y estequiométrico es muy complicado de obtener debido a su tendencia a tener impurezas de muchas formas. En el capítulo 5 mostraremos, en relación con la información estructural obtenida previamente, las consecuencias del desorden y la no-estequiometría en las propiedades de las láminas delgadas. La presencia controlada de vacantes de Ni en las láminas harán posible llevar la resistividad al rango de unos pocos ohm-cm, lo que, junto con su parcial transparencia, hacen estas láminas muy interesantes para aplicaciones electro-ópticas. Inspirados en la capa nativa de óxido sobre los metales, proponemos un modelo para explicar coherentemente la evolución de la resistividad eléctrica de las láminas y la influencia real del tratamiento térmico. Como era de esperar, la absorción óptica se modifica también a voluntad, situando estas láminas en el centro de potenciales aplicaciones que surgen de estos óxidos de transición [5].

Finalmente, en el capítulo 6 la estructura electrónica de las láminas óxido de níquel será correlacionada con los resultados previos de estructura y propiedades funcionales. Aunque muchos trabajos han estudiado la estructura electrónica del NiO, sólo algunos enfoques explican los efectos de apantallamiento no locales y la contribución superficial en el espectro de fotoemisión. Sin embargo, la posibilidad de la existencia de iones Ni^{3+} debido al NiO inestable no estequiométrico permanece como una cuestión abierta. Mostraremos una interpretación de las vacantes de Ni como iones mediante absorción de rayos-X (XANES) con cálculos de clusters y mediante medidas de fotoemisión de rayos-X (XPS). Esto apoya en gran medida los resultados previos confirmando la influencia de las impurezas en la banda de conducción y por lo tanto una disminución en la resistividad. El tratamiento térmico ha mostrado ser muy eficiente curando la estructura cristalina superficial, reduciendo la cantidad de vacantes de Ni.

Chapter 3

Experimental Techniques

> "*How often have I said to you that when you have eliminated the impossible, whatever remains, however improbable, must be the truth?*"
>
> Sherlock Holmes, The sign of the four.
> *Arthur Conan Doyle*

This chapter deals with the experimental set-up developed for this research work and a brief description of the different characterization techniques and the corresponding equipments used. Among all accessible characterization techniques we used those which complement each other and explore different aspects of the deposited thin films.

The main set-up for thin films growth consisted of a high vacuum chamber equipped with a RF magnetron sputtering system and a rotary and heated sample holder. We will show different aspects of the magnetron sputtering system as well as the targets materials employed.

3.1. Experimental set-up for thin films deposition

The NiO thin films were grown using a vacuum chamber (see figure 3.1), colloquially named *Chambao*, developed mainly by *Dr. Iulian Preda* at the Coatings, Interfaces and Nanostructures Group (UAM) and subsequently improved and maintained during this research work. The experimental set-up is composed of a high vacuum chamber, with a base pressure $< 5 \cdot 10^{-7}$ mbar and a radio frequency magnetron system. The vacuum is achieved by means of a Turbo Molecular pump assisted by a Dry Scroll pump and monitored by a double range vacuum Gauge (*Bayard Alpert* hot ionization cathode for low pressure and *Pirani* for high pressure). Although the molecular regime (pressure in the range $10^{-8} - 10^{-4}$ mbar) is adequate for preserving the chamber in clean conditions before any sputter gas mixture, reactive magnetron sputtering technique requires working pressures in the viscosity range ($P > 5 \cdot 10^{-3}$ mbar). In order to achieve this viscosity range a right angle valve which dramatically reduces the conductance is installed. This limitation in the pump helps to maintain the working pressure with high stability.

The chamber has a gas mixture inlet system which provides the needed sputtering gas for the reactive plasma. Argon and oxygen are introduced through a variable leak valve by using two independent flow-meters. The flow-meter accuracy (*Bronkhorst High-Tech*) lies between 1% and 4% of his maximum conductance: 200 ml_N/min (millilitres at normal conditions). By varying the percentage of gas with the flow meter a mixture of argon and oxygen can be obtained. The partial pressure of oxygen content in the reactive plasma ranges from 0% to 100% according to the relation:

$$\text{Partial Oxygen pressure} = \frac{P_{O_2}}{P_{O_2} + P_{Ar}}$$

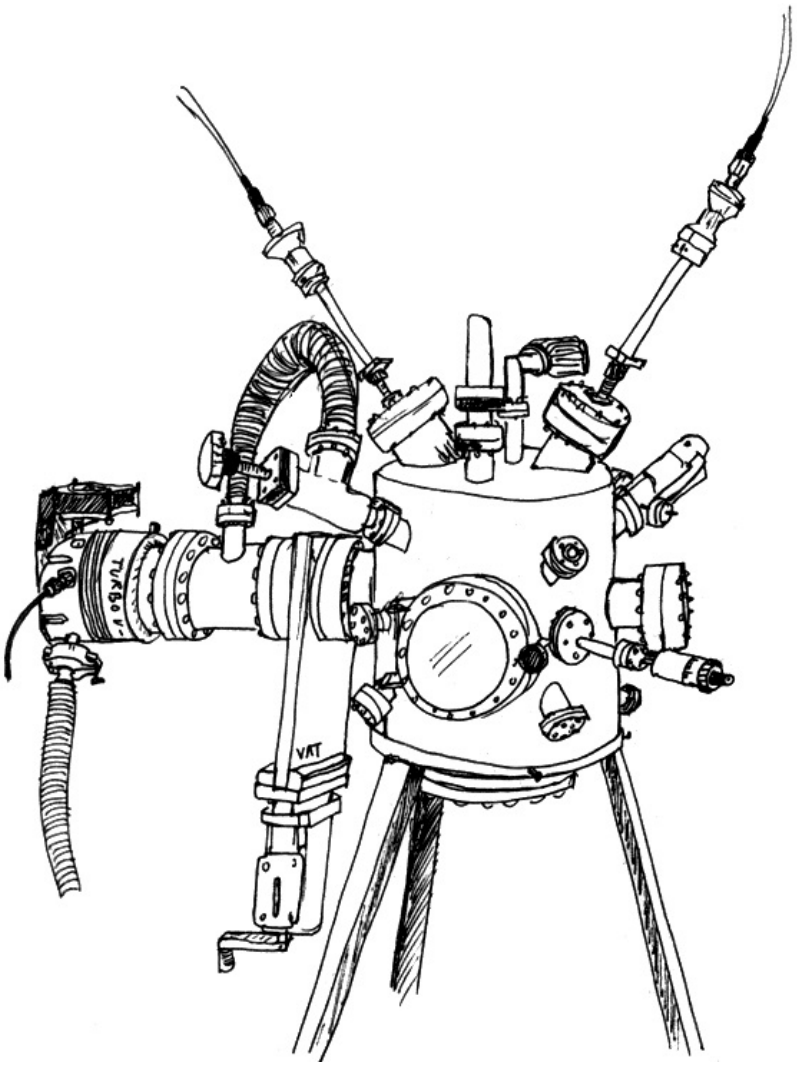

Figure 3.1: Drawing of the High Vacuum synthesis chamber *Chambao* with two off-axis magnetrons (up). The vacuum system is composed of a Turbo Molecular and Dry Scroll pumps and a double-range pressure Gauge, with two valves to reduce the pumping during the deposition. The base pressure is below $5 \cdot 10^{-7}$ mbar.

3.1.1. Sample holder temperature calibration

The rotary sample holder is made of a stainless steel axis connected to a copper plate which rotates at a slow speed (about 10 rpm). On the plate, the substrates are attached with screws to secure their stability during the growth. Below the substrates plate, and with no rotation, there are three halogen lamps (50 W power each one) which provide the heating of the substrates through the plate, made of copper to uniform the temperature. In figure 3.2 a picture of the lateral view of the vacuum chamber is shown. A quick access door with a view port and a Viton seal is used to access the chamber and manipulate the sample holder. Trough the view port the magnetron head, the copper sample holder and the lamps can be seen. The magnetron head is off-axis (23°) with respect to the normal to the sample holder. An argon plasma is ignited with a pale violet colour. In the photograph the three halogen lamps are glowing under the copper sample holder, which is supported and rotated by the steel axis. This axis rotates through bearings located at steel disks which are supported by three long steel rods and give stability to the sample holder. The axis rotation is transmitted from an external motor with a rotary feed through.

It is possible to heat the sample from room temperature (RT) to 320°C. The substrate

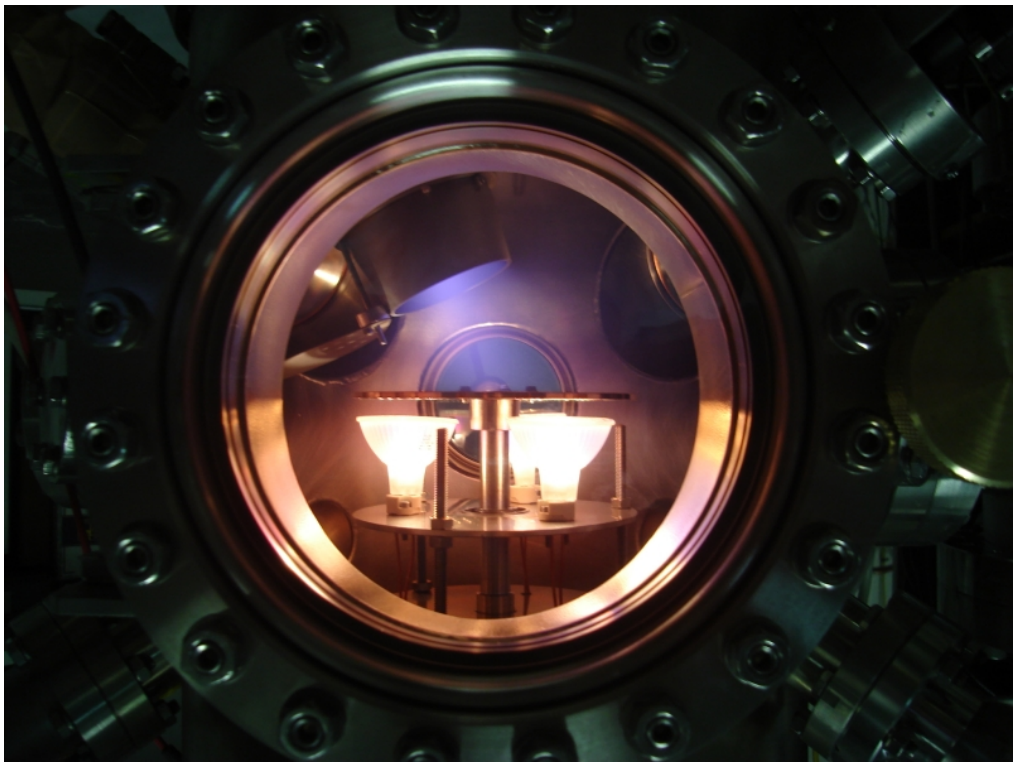

Figure 3.2: Front view of the High Vacuum chamber. The off-axis magnetron is working, the magnetron head with the shutter open and an argon plasma can be seen. The copper sample holder can be seen on top of the halogen lamps, which are glowing underneath.

temperature during growth was measured using an infra-red (IR) pyrometer, with a range between 100℃ and 700℃. Due to the thermal inertia and the required time to homogenize the whole copper sample holder several calibrations were performed using several thermocouples, in order to obtain the right emissivity values from the copper plate. During these calibrations the rotation of the substrate holder was not applied (so that thermocouples could be attached to different points in the copper surface), but this does not alter the calibration. Actually, the values obtained for stabilization time are upper limits due to the fact that rotation reduced this time to achieve homogenization.

We show in figure 3.3 only an example of this calibration: the halogen lamps, powered by a voltage-current source, were switched on in vacuum at different power outputs during enough time to reach the plateau of stabilized temperature. After several hours at a given power the heating is increased and reaches a stable value. Independent calibrations were performed for each substrate temperature: 200℃ and 300℃. As shown in figure 3.3a four power steps were chosen on halogen lamps: 14, 40, 80 and 140 W. The pyrometer values, above 100℃ are shifted 25℃ to higher temperatures. This difference was corrected in subsequent measurements carried out during growth. Figure 3.3b shows the temperature of the sample holder, after three hours of stabilization time at 140 W and after the RF magnetron was activated at 100 W using only argon in the plasma. The temperature increases about 20℃ with respect to the base value before switching on the magnetron. This increase is caused mainly by the IR emission from the plasma, and also from the energetic transport of sputtered atoms.

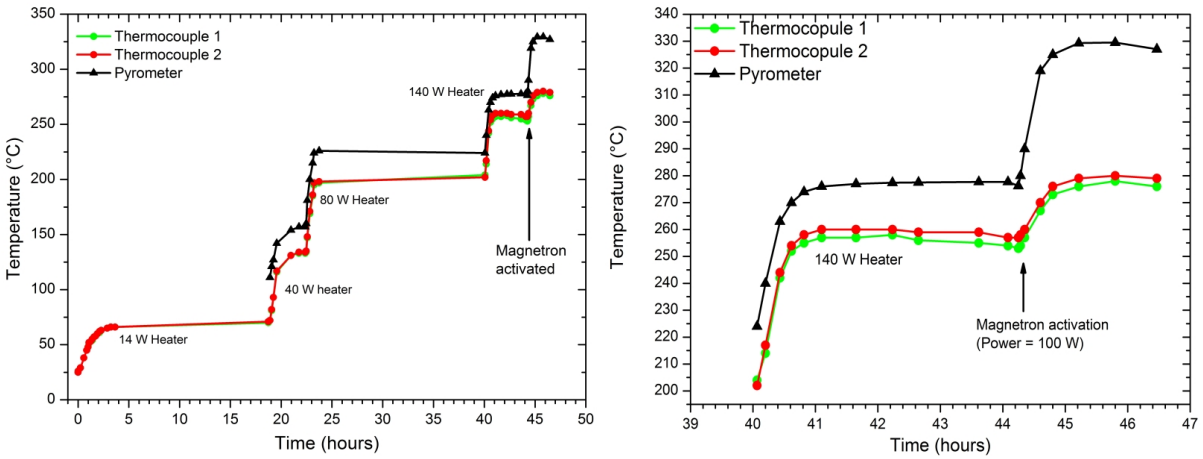

(a) Temperature calibration

(b) Detail of calibration

Figure 3.3: Temperature calibration of the copper sample holder at different heating power output values. The temperature has been measured with two thermocouples and a IR pyrometer (whose range is 100-700ºC). Due to the change in the copper emissivity between polished and partially oxidized material the pyrometer measurements are shifted to higher values. (a) At each power value it is necessary to wait until a plateau of stabilized temperature is achieved. (b) A detail is shown at a heating power output of 140 W showing the effect of switching on the RF magnetron (at 100 W with Ar plasma): the heating of the sputtered atoms towards the sample holder increase the temperature and the IR emission of the plasma is detected in the pyrometer as an additional value.

3.2. Substrate Preparation

Different substrates were used to study the effects of the substrate surface morphology on the final properties of the deposited films. Both planar (Si wafer and glass microscope slides) and nanostructured (Anodic Aluminium oxide Membranes, AAM) substrates were used for this purpose.

The Si wafer conductivity was $\rho = (7.0 - 17.0)\Omega\cdot$cm with a thickness of 0.14-0.16 cm, being p-type doped with Boron.

For a given set of sputtering growing parameters, NiO was deposited simultaneously on all substrates, which guarantees that all samples were grown under identical conditions on all substrates.

Except for the AAM, all substrates were ultrasonically cleaned by immersing them subsequently in acetone and methanol.

3.3. Synthesis method: RF Magnetron Sputtering

Magnetron sputtering has been a powerful technique for industrial applications in the last decades. Much effort has been done to improve this technique from the very basic Direct Current (DC) diode to the last pulsing discharge magnetrons [6] and Highly Ionized Power Impulse Magnetron Sputtering (HIPIMS) [7].

The sputtering process is the physical vaporization of atoms from a surface (called target) through a transference of momentum from impinging particles (ionized atoms) with high kinetic energy. These impinging ions are bombarded towards the surface target material due to a high electric field generated by the potential difference between the cathode and anode of the magnetron. The ejected or sputtered atoms from the target surface have higher kinetic energy (around 10 eV) than those thermally evaporated (as in a Knudsen evaporation cell, between 3

and 5 eV) [8], less than in HIPIMS, which reach the 50 eV [7] and much less than in cathodic arc (20-200 eV) and Pulsed Laser Deposition (PLD) which are extremely energetic (from 10 to 10^4 eV). The sputtered atoms are neutral in charge and deposit on the substrate located at a certain distance from the target surface forming the coating.

The bombarding atoms form a plasma of low density (dependent on the geometry of the magnetron) and because this is a purely transfer momentum process, the higher the mass and kinetic energy of the impinging atoms, the higher the sputter yield. The sputtering yield is the rate of material physically vaporized from the target surface related to the amount of arrival ions.

$$\text{Sputtering Yield} = \frac{\text{Ejected atoms}}{\text{Incoming ions}}$$

Many models have been proposed to calculate the sputtering yield. The theoretical approaches to calculate this rate part from a hard sphere model to a linear cascade collisions model. The complexity of these models and its theoretical nature make this parameter out of the scope of this work.

For each material there is an energy threshold below which it is not possible to sputter any atom from the target. If the target is made of several elements, the different values of these threshold energies between the different atoms at the surface originate a preferential sputtering, a process in which some species are sputtered at a higher rate than others. This process can create differences in the stoichiometry of the deposited coating with respect to the stoichiometry of the target.

The sputtering is driven by a plasma generated by the voltage difference between two electrodes in the presence of a low-pressure gas. In general, a plasma can be classified by its density: from the low density space and stelar plasmas of about 10^7 ions per cm^3 to the high density plasmas in laboratories (up to 10^{20} cm^{-3}). In the middle of this density-range the glow discharges and arcs are the plasmas used in sputtering, of densities between $\sim 10^8 - 10^{14}$ cm^{-3}. A high enough DC voltage between two electrodes in a low-pressure gas can initiate a discharge by ionizing the gas atoms forming a plasma. The relation between voltage, gas density (or pressure) and electrodes distance is governed by the Paschen's Law. At certain voltage range, between $10^2 - 10^3$ volts, the discharge is self-sustaining [9]. Within the plasma there are neutral and charged species (positive and negative) and their populations define the degree of ionization. The self-sustaining occurs when the population of ions is sufficiently high to continuously ionize the neutral species (the plasma as a whole is neutral).

When working with low-conductivity sputtering targets a DC magnetron is useless: in order to obtain a current density of $j = 1mA/cm^2$ on the target surface the needed voltage across the target would be $V = \rho j d$, for the case of our NiO targets of thickness d=0.3 cm and resistivity $\rho \sim 10^9$ Ω·cm this would raise a voltage value of $V = 3 \cdot 10^5$ volts. Such high value is complicated to achieve in a vacuum chamber without arcing and the DC sputtering would not work. This problem is solved with the use of radio frequency magnetrons (RF). Dielectric filled capacitors have low impedance for high frequencies ω, given by $Z = (R^2 + 1/\omega^2 C^2)^{1/2}$. Above 1 MHz electrons in the plasma achieve high kinetic energy sufficient to ionize other atoms by collisions while ions have lower energy. If the voltage is coupled with electrons by an external impedance then the transmitted power is very efficient [9]. This voltage coupling is driven by an external matching device which adjust a series variable coil and variable capacitor within certain limits given by its Schmidt chart. The aim of this auxiliary electronics is to couple the forward RF power with the oscillatory electron movement within the plasma, reducing the power loss by reflected power.

In order to direct the positive ions to the target, this must be negative biased, which is achieved due to the fact that electrons are much mobile than ions, following rapidly the changing electric field. As a consequence it exists an asymmetry of the discharge current-voltage curve: the positive electrode draws more current through electrons than negative isolated electrodes draw

through ions. When AC is applied to the cathode (target material) a large amount of current is drawn during the positive cycle due to electrons while in the negative cycle a small amount of charge flows. The average net current is non-zero but since the target is insulator no charge can be transferred, therefore the target is biased with a negative voltage, where no current flows [9].

When estimating the time interval Δt that a cathode under an AC power is positively charged during a period τ the result is $\Delta t/\tau \simeq 10^{-3}$ thus only 0.1% of the period time the target is positively charged, due to the high electron mobility [9].

As an example, the electric field strength ε_0 to ionize argon (with ionization energy $I_{\mathrm{Ar}} = 15.7$ eV) for a harmonic motion of electrons within the plasma when RF is used is given by $\varepsilon_0 = (2m_e I_{\mathrm{Ar}}\omega^2)^{1/2}/q_e = 11.5$ V/cm for the common radio frequency 13.56 MHz. This value is easily obtained in a laboratory, resembling the more suitable use of RF than DC magnetrons.

Plasma synthesis techniques are complex processes whose study requires simulations, variations in the geometric configurations and several devices to check the plasma properties. This work relies in a well known configuration with a commercial RF magnetron hence its complete characterization was not performed. A complete knowledge of the generated plasma would require the use of a quartz micro balance to check the growth rate and to measure the energy distribution function through a Langmuir probe or optical emission spectroscopy (a RF generated plasma does not follow exactly a Maxwellian energy distribution function [10]) but due to the nature of the radio frequency generated and excited plasma this task is a very difficult one.

The equivalent circuit of an RF sputtering system can be thought as two series capacitors, one at the target sheath region (layer of positive ion density) and other at the grounded region (in our case the vacuum chamber inner surface), with the applied RF power between them. Since the capacitance is proportional to the electrode area (A_G for grounded area and A_{RF} for cathode area, the target surface)) the voltages values at the cathode and area are related in this way: $V_{RF}/V_G = (A_G/A_{RF})^4$ [9], therefore the larger A_G value is more effective in raising the cathode potential and minimizing the sputtering of the grounded region.

Our magnetron operates up to 300 W of maximum Power, 1000 V of maximum Voltage with cylindrical targets of 5 cm diameter (2 to 5 mm thick) resulting in a *Power Density* of 15 W/cm^2 when working at maximum output power. Therefore the upper energetic limit for the impinging ions is 1 keV is this apparatus.

The sputtering gas is formed commonly by noble gases such as argon due to its large mass (but heavier noble gases could be used), chemically inert behaviour, low cost and low ionization energy. Another gases can be used for sputtering: oxygen, nitrogen, methane, or hydrogen sulfide are usually selected in order to deposit oxides, nitrides or carbides. In these cases the process is named *reactive sputtering*. The chemical reactions could occur both at the target and substrate surface.

However, sputtering is an inefficient process: more than 90% of the transferred energy of the bombarding atoms is released in form of heat [8], thus the refrigeration of the magnetron head where the target is located is essential, especially when the target is a ceramic oxide with a high thermal expansion coefficient and low thermal conductivity. In the case of a laboratory magnetron sputtering with water cooling, the target temperature remains below 300°C[11].

The cluster generation in the sputtering process is a common issue profoundly studied in the field of Molecular Simulations. It is established that the cluster abundance distribution follows a power decay [12]:

$$\text{cluster distribution} \propto n^{-\alpha}$$

where n is the number of atoms in a cluster and the exponent α decreases with the sputtering yield. For our work (sputtering of NiO by 1keV Ar ions as the highest energy) α varies from 3 to 4.5 [12]. The low substrate temperatures, the rotation of the sample holder and the off-axis magnetron geometry avoid the formation of clusters during deposition. In the work of S. Pratontep *et al* [13] a complex set-up is necessary to create big clusters, meaning that the initial population of clusters in a RF magnetron sputtering is low.

An improvement of the magnetron device is the unbalance of the magnetron head. This is performed by using permanent magnets below the target material. When locating a ring of magnets around a magnet with inverse polarity the magnetic field lines create therefore a region of higher plasma density.

The secondary electrons produced in the sputtering process are trapped in these field lines by lengthening their path and increasing the probability of ionize the gas used in the sputtering. The secondary electrons and those from the sputter gas atoms do not produce sputtering process. This geometry and the strength of the magnets are such that the field lines are open instead of completely closed and then the electrons path are longer, thus the name *unbalanced*. The plasma density is one order of magnitude higher than in a DC magnetron and this region extends over 6 cm above the target [6]. However, this configuration creates an erosion ring which can be very deep and shorten the target life. Figure 3.4 shows the plasma created by the unbalanced magnetron: the ring shape of higher ion density can be clearly appreciated. The pale violet colour is typical of the argon plasma at this energy. The main emission lines of the plasma were observed with a basic spectroscope confirming the oxygen and argon lines in every case.

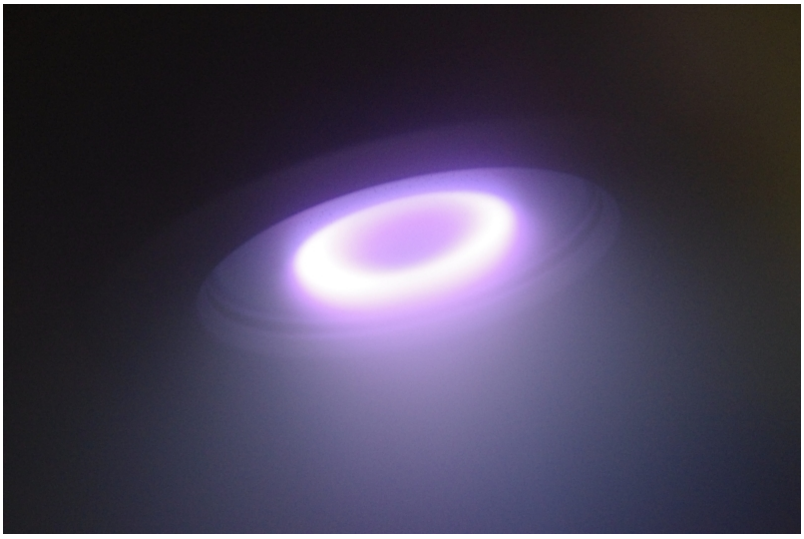

Figure 3.4: Photograph of the argon plasma created by the unbalanced magnetron over the target: the ring shape of higher ion density can be clearly appreciated. The permanent magnets arrangement concentrate the plasma near the target avoiding sputtering of the substrates or growing film.

The use of insulating materials with a DC magnetron is not possible due to the charging effects: as the ions impact the target surface an amount of charge is transferred and if this process continue until the surface is saturated of charge, then no more sputtering processes can be carried out. The use of a radio frequency signal avoids this charging problem. The reserved frequency for magnetron devices is 13.56 MHz.

The self-sputtering process did not occur in our apparatus for the deposit parameters selected. Self sputtering occurs when the sputtered atoms (in our case nickel and oxygen) are ionized and participate in the sputtering process. If the plasma is then composed of Ni ions the sputtering would be much more efficient. Though the ionization energy of the nickel is almost the half of that of the oxygen and the power densities are close to 10 W/cm^2 for samples grown at 200 W, the process still does not occur. In fact A. Anders [14] proposed a tough condition for this process to occur: $\alpha\beta\gamma > 1$, where α is the probability Ni is ionized, β is the probability Ni^+ ion diffuses back through the plasma to the target surface and γ is the sputtering yield. Self sputtering has been observed only for Ag and Cu targets and under higher energies and plasma densities than those used in this work.

3.3.1. Sputtering targets

The properties of the sputtering targets have a great influence in the final coating properties. Although many providers assure the purity of the composition of sputtering materials, there is no definitive method to create a ceramic oxide target with a perfect stoichiometry. In the case of the NiO targets much effort was done (and much work lost) until the properties of the original material were well known and adequate for this research.

Oxides and ceramic sputtering targets are produced by sintering of powders. In this process the powder in a mold is heated in a furnace below its melting point to enhance atomic diffusion. At high temperature, bulk diffusion occurs creating big grains, reducing the grain boundaries to lower energy surfaces and achieving high purity materials. For the case of ceramic targets such as Nickel Oxide the powder is hot pressed in a reducing environment (using graphite molds) to avoid oxygen excess. Achieving a good stoichiometry and correct shape is a difficult task that requires a good knowledge of the technique and material properties such as phase diagram, expansion-temperature curves, etc.

An easy and fast method to check if the NiO target is correctly sintered is to measure the resistance by using the terminal probes of a voltmeter. Many of commercial NiO sputtering targets have too low resistance, i.e., they are conducting materials instead of the strong insulators they are expected to be. This is a clear signal that they are not stoichiometric, and probably they are rich in oxygen. In the case of NiO targets, for perfectly stoichiometry, the resistivity should be of the order of 10^{13} $(\Omega \cdot cm)$ [15], i.e., a high-κ insulator. Several characterization techniques were used to check if the sputtering target was suitable: X-Ray Diffraction (XRD) for the structure and phase determination and Energy Dispersive X-Ray (EDX), Rutherford Backscattering Spectroscopy (RBS) and Differential Thermogravimetric Analysis (DTA) for chemical composition. Some of these techniques were performed until good quality targets were found and subsequently used.

Many targets needed a cleaning of the surface before starting the sputtering in order to obtain homogeneity in composition of the deposit. In vacuum this is achieved by doing a sputtering with argon (higher mass, therefore higher sputtering yield) in order to evaporate any species which do not belong to the target composition, this is called *pre-sputtering*. During this cleaning sputtering (usually between 5 and 20 minutes) a shutter must be used to protect the substrates from the evaporated material. In our chamber this was realized for every set of samples before deposition.

The sintered ceramic oxide targets used in RF magnetron sputtering have very high thermal expansion coefficient and are brittle materials. These targets need a good refrigeration during its use due to the high temperatures generated in the sputtering process. Also the higher the power of the magnetron the higher the rate of impinging ions to the target surface and the more energy released in the sputtering process in heat form. Therefore it is of the utmost importance to assure a good refrigeration of the target. Cooling is commonly done by sticking a copper disk of the same size of the target by using a silver epoxy of high thermal conductivity. This copper disk is attached at the water-refrigerated magnetron side. Even with the use of a refrigeration system some targets crack after many hours of work due to the thermal shocks.

Due to the problems derived from the poor quality of commercial targets, we finally end up with the decision of sinter our proper NiO targets with the help of *Instituto de Cerámica y Vidrio* (ICV-CSIC) laboratories. By using a high purity NiO powder (Sigma-Aldrich, purity of 99%) the NiO targets were sintered at a high temperature furnace ($T > 1500$℃) in graphite molds to create a reducing environment. In such conditions the stoichiometry of the targets was achieved as confirmed by the mentioned characterization techniques. In order to enhance the reducing environment in one case it was necessary to add 2% Polyethylene glycol (PEG). In our work the targets required determined shape and dimensions to fit into the magnetron head, therefore the hot pressing conditions and mold had to be carefully chosen taking into account the shrinkage of the material.

3.3.2. Structure Zone Models

In physical vapour deposition (PVD) methods, Structure Zone Models are main guidelines to sort experimental results and reasonable approaches when process parameters have to be chosen. In the literature several models have been proposed which take into account the final morphology and structure of the deposited films under certains parameters. The first known model was presented in 1969 by B. A. Mochvan and A. V. Demchishin [16] in which the structure of the growing films was classified by the homologous temperature: $T_h = T/T_m$. T_m refers to melting temperature of the grown material and T is the temperature at which the film is deposited. The idea of using the homologous temperature for classification is the separation of activation barriers for different materials. Other models for evaporated films appeared in the following years and different strategies to quantitative analyse were presented [17, 18, 19, 20]. Later, J. Thortorn presented his model for sputtered films [21], this model takes into account not only the substrate temperature, an ever-present parameter, but also the pressure of the sputtering gas.

Figure 3.5 shows the well known Thorton model describing the main structural aspects of films grown by sputtering. This model have been used and revisited in the last years but its simplicity and clarity make it a very useful guide to the growth of thin films at intermediate energies reached by the sputtering technique.

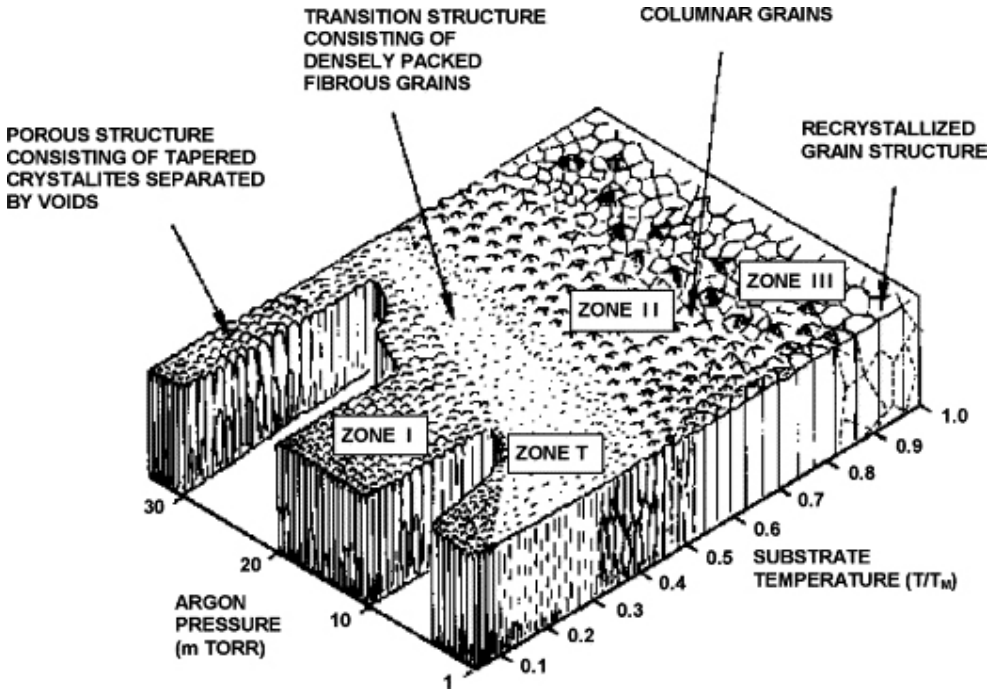

Figure 3.5: Thorton's microstructure zone model, image taken from [21]. The grains shape and film structure are classified in zones depending on T_h and pressure.

These models base the frontiers between the zones primarily on the homologous temperature: the Zone I correspond to low temperatures: for $T < 0 < T_1$, being $T_1 \simeq 0.24T_m$ for oxides [22]. In this Zone I the microstructure of the deposited film is porous (as is in the ballistic regime) and the effects of the surface diffusion are negligible.

According to this zone model the deposited coatings of our study will fall in the so called *Zone I* because the pressure is fixed at $1.5 \cdot 10^{-2}$ mbar (11.2 mtorr) and the temperature will vary between RT and 300℃, this means 0.01-0.15 T/T_m in the diagram. T_m refers to the melting temperature of the grown material, which for NiO is T_m(NiO)=1984 ℃ (2257 K). At these low temperatures the thermally activated surface diffusion processes have no great influence and the growth is dominated by surface shadowing, allowing the coatings to be porous, formed by columns with voids between them [21]. S. Nandy *et al* [23] and T.Y. Kuo *et al* [24] proved the

improvement of the NiO thin films crystallinity by decreasing the pressure to $1.5 \cdot 10^{-3}$ mbar, as expected due to the higher contribution of the surface diffusion and the lower contribution of energy losses through scattering between the sputtered atoms.

3.3.3. Growth parameters

Because the reactive RF magnetron sputtering is an out-of-equilibrium technique, the different parameters used during growth do not affect the process linearly and equally. The amount of sputtered material is determined by four correlated parameters: magnetron power, deposition time, target-to-substrate distance and pressure in the sputtering gas. The pressure and the target-to-substrate distance were not varied in this work. The off-axis angle of the sputtering permitted to grow more porous films without cluster formation and was neither varied in this work. The substrate temperature during growth is an interesting parameter, but it is difficult to control due to the low values that can be achieved with our experimental set-up (from RT to 320℃). Among the many possibilities, we have focused on those growth parameters that permit a columnar growth of the coating and, especially, a porous film on the nanostructured Anodic Alumina oxide Membranes (AAM or AAO).

In magnetron sputtering, the working pressure can be classified into three different ranges according to the mechanism of transport of the sputtered atoms. At low pressures the transport is *ballistic* so that the sputtered atoms have almost no collisions with residual gas atoms. At intermediate pressures (those used in this work) the lighter sputtered atoms (oxygen) undergo momentum variations by collisions more easily than the heavier atoms (nickel). In the third regime at high pressure the transport is a purely diffusive mechanism where all the sputtered species suffer collisions and lose their high kinetic energy leaving less energy for surface diffusion [25]. These three regimes are established following an approximation that uses the kinetic theory of gases and relates it with the target-to-substrate distance: if the pressure is increased so that the mean free path for elastic collisions between the sputtered atoms and sputtering gas is below the target-to-substrate distance, then the oblique component of the flux increases due to the gas scattering leading to a more open structure. On the other hand lowering the pressure the oblique component disappears and the ballistic arrival of the atoms create a more dense coating. For the conditions used in this work the mean free path length is one order of magnitude lower than the target-to-substrate distance when working at higher temperatures (for 300℃ is about $\sim 1cm$) and two orders of magnitude when working at room temperature ($\sim 1mm$).

The angle of the sputtering cathode with respect to the normal to the substrates surface was 23° (the so-called off-axis geometry). This angle helps to produce nanostructured coatings with high porosity [26] due to the arriving of sputtered species with higher horizontal component. The distance between target and substrate was 8 cm and was maintained throughout all this work. The sputtering deposition rate decays as $1/r^2$ as expected for a solid angle particle distribution coming from the target surface. Atoms sputtered from the target surface distribute primarily along the directions crystalline structure, which allows to obtain more uniform deposits [8].

The off-axis geometry also reduces the irradiation of the substrate by high-energy particles sputtered from the target surface decreasing the stresses in the films originated from impinging ions [11].

The sample-holder is rotating in order to produce isotropic coatings with no dependence of any planar direction due to the off-axis flux of material. If this rotational sample holder were not used then the coating would have a preferred growth direction and the tangent rule will describe the vertical growth of the films. Measurements carried out on obliquely evaporated films reveal that the columns are oriented toward the vapour source. The angle between the column axis and the substrate normal (β) is universally observed to be smaller than the angle between source and substrate normal (α). These angles are connected approximately by the relation $\tan(\alpha) = 2\tan(\beta)$, commonly known as the *tangent rule* [9].

Therefore the pressure was maintained in the intermediate regime favouring the columnar

growth of the films, the off-axis angle was optimal for our objective of porous films and was maintained as well. Taking into account the Zone Model of deposited films with magnetron sputtering from Thornton [21] as a guideline, the substrate temperature was varied in the allowed range of our apparatus (from RT to 300ºC) and the deposition time and magnetron power, which define the amount of material sputtered, were selected in order to maintain the porosity.

From now on we will refer to the growing conditions used in the sputtering plasma in the compact notation Oxygen(%)-Power(Watts)-Time(hours)-Temperature(ºC) such as 20%-100W-1h-200ºC.

3.4. Characterization Techniques

Different characterization techniques were used in this work in order to study the basic aspects of the grown thin films. Among all the accessible techniques, we have chosen those that helped us to understand the different aspects of the NiO coatings: crystal and electronic structure, morphology and electrical and optical properties.

Because nowadays the accessibility to any of these techniques is high and the literature is rich and plentiful we will only describe roughly each technique used and will give some details about the apparatus and experimental set-up, the advantages and drawbacks of its use and the suitability of the technique.

Of all the techniques used only SEM can be considered as destructive.

3.4.1. Field-emission Scanning Electron Microscopy (FESEM)

Scanning Electron Microscopy is a powerful technique to study in a direct way the morphology of a surface. In this work FESEM has been used to analyse the morphology, grain size, porosity, growth stages and estimate the thickness of the deposited NiO coatings on several substrates.

Electron microscopy is based on the lower De Broglie wavelength of the electrons in comparison with visible light, allowing to resolve smaller features below 400 nm, which is not possible with optical microscopy. A beam of electrons is accelerated towards the sample surface, obtaining information on the morphology and topography. Backscattered and secondary electrons emitted from the surface atoms of the sample are collected in a detector and subsequently counted and processed to form an image, a process which is quickly performed. The electron beam is collimated and focused through a column of electric lenses, producing a scanning of the surface sample using magnetic coils or electrostatic plates [27]. The depth contrast is achieved due to the fact that the electrons emitting from the surface greatly depend on the angle, therefore the electron detector is able to generate images with depth resolution. Faceted, stepped and pointed features on the surface sample emit more electrons, therefore are better detected and brighter than smooth and planar surfaces, the so-called edge effect. At smaller areas the electric potential is higher and the secondary electrons emission is larger. The resolution of SEM is between 1 nm and 20 nm, depending greatly on the collimated beam and focusing devices.

This technique has variants due to the different particles emitted by the surface: secondary electrons image (SEI), backscattered electrons image (BEI), Energy-dispersive X-ray spectroscopy (EDX) and visible light (cathodoluminiscence), being possible to analyse the chemical composition of the scanned surface. The sample surface needs to be electrically grounded to pump charge. For this reason, the quality of the images when insulating samples are measured is low. In some cases a thin film of a highly conducting metal has to be deposited on the surface sample (generally a plasma enhanced sputtered Au or Ag film).

More information about the origin, development and complete descriptions of the technique can be found in material science manuals and booklets such as those from the company JEOL [28, 27].

In this work the high resolution electron microscopes used were Field Emission SEM. The

Field Emission is an improvement of the source electron gun that increases greatly the flux of particles and the image resolution. The emission of electrons is driven by an electrostatic field instead of thermoionic emission, which is more compatible with high vacuum, does not need to achieve high temperatures, increases the flux of emitted particles and reduces the dimensions of the emission source (a sharp tip). The lifetime and brightness are also better [28]. In Field Emission microscopes the acceleration voltage needed is lower than in conventional microscopes, and thus the charge generated on the sample is not as high, which improves the quality of the image.

The electron microscopes used in this work are listed in the table 3.1. Each equipment belongs to a different institution and all of them have similar capabilities.

Model	Institution	Acc. Voltage	Magnification	Spatial resolution
Philips XL30 S-FEG	SIdI-UAM	0.2-30 kV	10x to 400,000x	1.5 nm
JEOL JSM 6500F	CENIM-CSIC	0.5-30 kV	10x to 500,000x	3 nm
Hitachi S-4700	ICV-CSIC	0.5-30 kV	30x to 500,000x	1.5 nm

Table 3.1: Scanning electron microscopes used in this research work. All of them are of similar capabilities and well suited to resolve the structures of the deposited thin films.

Throughout this text the images presented have been treated in brightness and contrast to obtain a better quality when printed. The information about acquiring parameters of each micrograph has been unified in the Appendix 1.

Porosity estimation

In order to quantify some of the aspects derived from the images obtained by FESEM the free software Image J was used [29]. With this software the approximative estimation of the porosity was done as well as the basic distance measurements when the quality of the image allowed it. The procedure to measure the porosity is as following: first the threshold of contrast is moved until the pores area is completely darked, afterwards the image is converted to 8 bits in order to make calculations on it. The background is set to its maximum in order to have a monochrome image. The tool *particle and area count* of the program Image J allows to calculate the area of the particles (pores in our case) above certain size and with approximately circular shape, discarding isolated points or lines which have not origin in a pore. Finally the pore area percentage can be calculated with respect to the whole image area. This was performed on each SEM micrograph on porous samples at different scales in order to have reliable statistics. In figure 3.6a we show a porous NiO coating grown on an AAM substrate at 100W-1h-RT conditions with 80% oxygen content in the plasma. After image treatment the pores have been isolated and the image transformed (see figure 3.6b) to a 8 bit map where the calculations can be performed. The porosity of this image is 8.4%.

3.4.2. Profilometry

To measure the thickness of the coatings, contact profilometry was used. This technique relies on a stylus in physical contact with the sample surface, and a normal force in the range 1-15 mg (10-150 mN). The stylus can be scanned along the surface sample. Any step higher than the vertical resolution of the profilometer (*Sensibility*, *S=15* nm) can be detected and monitored in the scanning program.

In this work the thickness of the thin films is a key parameter: firstly because it defines the dimension of the samples in the nanoscale and secondly because several other techniques need the thickness as a complementary information. For instance, in optical measurements the thickness

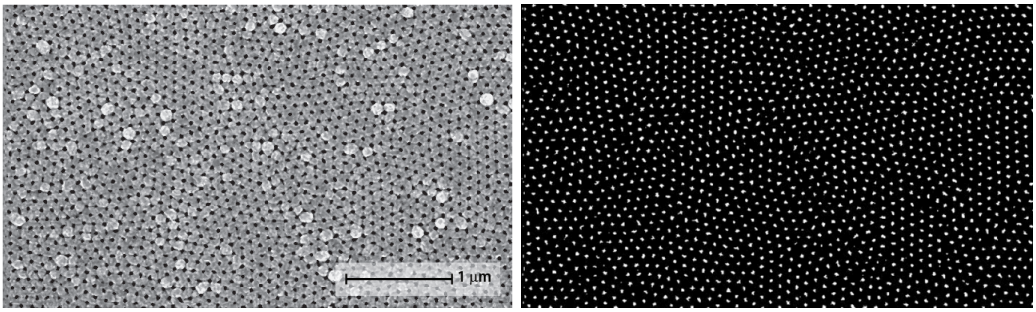

(a) As deposited porous film (b) After image treatment

Figure 3.6: Porosity calculation using Image J program [29]. (a) FESEM image of a porous film grown on an AAM substrate at 100W-1h-RT with 80% oxygen in the sputtering plasma. The pores area with respect to the total area is the porosity percentage. (b) After image treatment the pores have been isolated and the image transformed to an 8 bit map where the calculations can be performed. The porosity is in this case 8.4%

is necessary as initial parameter of the fitting; in spectroscopies such as RBS, XPS and XAS the thickness of the films is important to understand and interpret the results obtained. When studying the FESEM images, the thickness helps and supports the micrograph interpretation of the growth dynamics.

In order to use this technique, planar substrates were prepared prior to the deposition with masks that create a well defined step during the coating growth. Because of the high roughness of the films grown on the AAM substrates, profilometry measurements could only be performed on planar substrates, namely glass and Si wafers.

The next items summarize the different stages needed to measure the thickness of the films:

- A planar mask with sharp edges must be located on the substrates before deposition. Care has to be taken to avoid material growth beneath the mask.
- The step must be visible after deposition by visual inspection.
- Several scans have to be done at different places at the mask position in order to have a statistical representative value.

In this work a Dektak 150 Profilometer (Veeco manufacturer) with 3-5 mg force of the stylus has been used. This apparatus has a high vertical sensibility (below 10 Å according to the manufacturer) with a stylus mechanically coupled to the core of a Linear Variable Differential Transformer. The stylus tip has a radius of 12.5 μm. The density of points used was high and the mechanical stability of the apparatus allows to take measurements of the surface roughness. In figure 3.7 we show two profiles (red and black lines) performed on sample 100%-200W-1h-200ºC on Si wafer substrate across the step. The high narrow peaks correspond to vibrations detected on the apparatus support and amplified by the surface roughness. The dashed blue lines indicate the substrate and coating surfaces. When the scan is far extended from the step, about 1 mm at each side, and the step is well resolved, the vertical displacement of the blue lines mark the step height, marked with vertical dashed green lines. By measuring the length of these vertical green lines at the midpoint of the step the thickness of the film can be estimated. We have performed several profiles across the step for each growth on Si and glass substrates to obtain an averaged value of the thickness. These values are confirmed by the FESEM estimations as well.

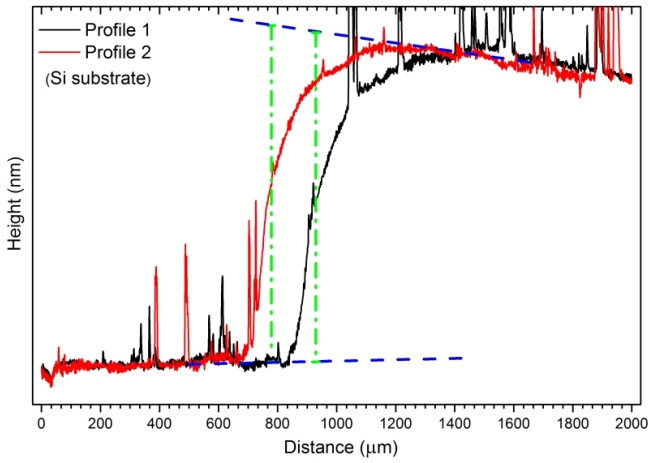

Figure 3.7: Example of two profilometry measurements performed on sample 100%-200W-1h-200℃ on a Si wafer substrate. The high narrow peaks correspond to vibrations detected on the apparatus support and amplified by the surface roughness. The dashed blue lines indicate the substrate and coating surfaces, vertically separated by the film thickness, which is indicated by the vertical lines. Several scans are performed across the step, their averaged value is the estimated thickness.

3.4.3. Synchrotron Radiation

During this work we had access to synchrotron radiation facilities to perform unusual but powerful techniques. With the particular characteristics of the synchrotron radiation, diffraction (GIXRD) and spectroscopic (XAS) techniques were used to study complementary information about the coatings.

We will present here a brief summary of the main properties of the synchrotron radiation used at two facilities: the European Synchrotron Radiation Facility (ESRF) in Grenoble and the Berliner Elektronenspeicherring für Synchrotronstrahlung (BESSY II) in Berlin.

Synchrotron radiation extraordinary properties make it an extremely useful tool for science. Both introductory and profound descriptions of this radiation can be found elsewhere [30, 31, 32, 33, 34]. Light charge particles circulating at relativistic velocities in curved trajectories emit highly collimated radiation, called *synchrotron radiation*. The main properties of this radiation are:

- High flux of photons with low emittance (low widespread).
- High Brilliance, which is the figure of merit of the beam, defined as the number of photons of similar wavelength (bandwidth, BW) that can be concentrated per unit time per unit area, the units are $photons/(s \cdot mm^2 \cdot mrad^2 \cdot 0.1\%BW)$. This radiation is highly collimated (widespread emission cone close to $1/\gamma$). In bending magnets and wigglers the brilliance is at least four orders of magnitude higher than in X-ray tubes, when using undulators the difference can be eight orders of magnitude [32].
- Tunable energy: depending on the facility characteristics the energies can be selected from IR to hard X-rays, this broad spectrum is extremely useful in spectroscopy.
- Linear polarization in the plane of the storage ring and circular polarization above and below that plane (positive and negative, respectively).
- Depending on the storage ring mode: single and multi-bunch, low-alpha and continuous injection, the pulsed radiation delivered by the electron bunches separated in space and time can be tuned, which is extremely useful for calibration and pulse-dependent experiments.

In our research work we measured GIXRD and XAS (soft and hard X-rays) at BESSY II and ESRF, both third generation facilities that work at top-up mode (continuous refilling of electrons in the storage ring without closing the front end beamshutter of the beamlines for injection). The main facts of these two facilities are summarized in table 3.2.

Synchrotron Facility	Storage ring Energy (GeV)	Storage current (mA)	Circumf. (m)	Emittance (nm×pm rad)	Brilliance ph/($smm^2mrad^2 0.1\%BW$)
ESRF	6.04	200	844	4×4	$8 \cdot 10^{20}$
BESSY II	1.7	280	240	6×100	$5 \cdot 10^{18}$

Table 3.2: Synchrotron Radiation Facilities (ESRF, BESSY II) facts. Storage current is indicated at both facilities working in top-up mode.

At ESRF measurements were carried out at the double beamline BM25-SpLine (bending magnet), which has an X-Ray Diffraction and HAXPES dedicated branch and a second one dedicated to XAS, where the EXAFS experiments were performed (high energy X-rays). At BESSY II the XANES measurements with soft X-rays were carried out at beamlines OpticsBeamline (bending magnet) and UE52-PGM (Undulator). In the sections of XRD and XAS we will describe more details about these beamlines, the experimental set-up and the acquiring calibrations.

3.4.4. X-ray Diffraction (XRD)

X-Ray Diffraction is an old but strong technique to delve into the solid structure of matter. It is based on the diffraction of X-rays when the distances of the diffracted object (atoms within a solid) are of comparable size. The electronic clouds of a periodic crystal lattice produce scattering of the incident X-rays photons, creating patterns corresponding to a determined crystal symmetry according to Bragg's law. These patterns contain information about the crystallographic phase, crystallites size, disorder and strain within the solid, lattice parameter of the unit cell, etc. This information is fundamental when studying nanostructures. When the X-rays beam arrives at low incidence angles to the surface sample the technique is called Grazing Incidence XRD, which is more sensitive to the surface structure. This configuration is the most suitable to study thin films, since the effects of the substrate or support can be highly reduced or even avoided.

XRD is a non destructive technique with a penetration depth of about 30 microns. This is the distance at which selfabsorption of the emitted photos is extinguished, but this is an average and estimations should be performed depending on the source used and the material probed. This technique can detect every kind of atoms provided that they are located in crystallographic planes, therefore amorphous materials cannot be detected. The signal measured greatly depends on the sample crystal quality (and quantity). Although the lower limit detection is a thin film of 20 Å, this could only be achieved with GIXRD. Samples do not require especial preparation and this is a technique routinely used due to its widespread use, although its interpretation and quantification is a more complicated task. Because here we only want to give details of the experimental set-up and main facts, we refer the reader to handbooks dedicated to XRD [35, 36, 37].

According to Bragg's law the relation between the position of the diffraction peaks in the diffraction pattern θ_B, the wavelength of the source λ and the n^{th} inter-planar distance d is:

$$n\lambda = 2d\sin(\theta_B) \tag{3.1}$$

The interplanar distance, as determined by the position of the Bragg peaks, is a discontinuous function of the Miller indices (h k l), which identify the crystallographic planes. This distance is related to the unit cell dimensions. For the case of a cubic crystal system, with cubic side a, the lattice parameter, the relation between these factors is simple:

$$\frac{1}{d^2} = \frac{h^2 + k^2 + l^2}{a^2} \tag{3.2}$$

For a fcc lattice the Miller indices (h k l) must be either all even or all odd. Using this relation the theoretical position of the diffraction peaks in a NiO diffraction pattern have been calculated in table 4.2.

In this work XRD and GIXRD have been used to study the structure of the deposited thin films. This information is fundamental and complementary with the other characterization techniques and has served to determine the influence of the growth parameters on the structure of the films.

X-ray Diffraction measurements have been carried out at two institutions: SIdI-UAM and CENIM-CSIC. At SIdI-UAM the X-rays source was a copper tube with a K_α emission line of $\lambda = 1.5406$ Å and at CENIM-CSIC it was a cobalt tube with K_α of $\lambda = 1.7889$ Å. The differences in wavelength create a shift in the peak positions in the diffraction pattern, which is explained in section 4.3. Another difference between Co and Cu sources is the higher photon flux of the Cu source due to its higher thermal conductivity (by a factor of 4), which allows to use higher values for the voltage of the anode, where electrons are being accelerated. On the other side, the higher energy of the copper source can excite Fe atoms, which will emit fluorescence radiation, changing the expected diffraction profile in samples with some Fe content. This does not happen to Ni-containing samples, so it was possible to measure our NiO samples with both X-ray sources.

In CENIM-CSIC, XRD measurements were carried out with a Bruker AXS D8 diffractometer in grazing incidence condition. In the setup used, a X-ray Co tube is equipped with a Goebel mirror optics to obtain a parallel and monochromatic X-ray beam. A current of 30 mA and a voltage of 40 kV were employed as tube setting. XRD data were collected with a beam incidence angle of 1° and 2θ scan between 20 and 100° with a step size of 0.03° and a counting time of 5 s/step.

In SIdI-UAM the diffractometer used was a Siemens D-5000 model, with Soller slits, and Si-Li detector SOL-X (Bruker). The data were collected at grazing incidence of 1° and 2θ scan between 20 and 70° with a step size of 0.03° and a counting time between 3 and 5 s/step, depending on the data density required.

In both diffractometers the Bragg-Brentano geometry was used, also called $\theta - 2\theta$. In this kind of XRD measurements we work with the assumption of constant irradiated volume: the area of the spot beam times the penetration depth for each incidence angle is constant throughout the acquisition. A diffractometer in Bragg-Brentano geometry only detects the dimensions of crystallites along the vertical section of the coating (through-thickness), therefore information about crystallite shape distribution would not be complete without exploring other tilt angles.

XRD quantification

The quantification performed in the diffraction profiles was performed using both Rietveld and Pawley methods, which give similar information for our purposes. The Scherrer estimation of the crystallites size could be performed with a standard scientific software by fitting pseudo-Voigt functions to the Bragg peaks and studying the peak parameters conveniently.

The Rietveld refinement is the most complete algorithm to fit diffraction data of polycrystalline powder samples (obtained by using both neutrons or X-rays). This method is based on the fitting of the complete diffraction pattern using a non-linear least squares method, having as input the approximate values of the lattice parameters and the atomic positions in the crystal lattice [38]. Instead of fitting each individual peak in the pattern, the Rietveld method uses the information of the complete crystallographic phase of a compound, fitting all peaks simultaneously and avoiding a possible mistake caused by mixing several phases (which would produce peak overlapping) by using their relative positions and intensities. The output of this method are the lattice parameter

of the crystallographic phase, the microstrain contribution to the width of the peaks and the texture grade (variations in the relative intensities) [35].

Rietveld method is strongly based on the theoretical atomic positions of the crystallographic phase and requires prior knowledge of some of the free variables, among them the weight of the relative peak intensities through the structure factor. On the other hand, Pawley method does not rely on the structure factor, but on the decomposition of the profile in terms of independent peaks, not being necessary a previous knowledge of the crystal structure [39]. This method of full pattern decomposition is better for not quite complex diffraction profiles, as is our case, in comparison to Rietveld, more appropriate for fitting a diffraction patterns with a high number of peaks [35].

The application of the Rietveld or Pawley methods to grazing incidence X-ray diffraction patterns requires consideration of all the peculiarities of this technique which may cause significant deviations from the intensities recorded in Bragg-Brentano geometry. In order to take in account such particularities in the refinements, instrument functions were empirically parameterised from the profile shape analysis of an α-Alumina (Corundum) sample measured under grazing incidence at the same conditions. Once this Corundum reference pattern has been measured and analysed a template with the contribution form the measurement equipment can be generated and used with all the samples studied.

In this study, we have used version 4.0 of Rietveld analysis program TOPAS (Bruker AXS) for the XRD data refinement. Refinement analyses were carried out using space group and crystallographic information of NiO obtained from Pearsons Crystal Structure database. The refinement protocol included also the background, zero displacement, the scale factors, the peak width, the unit cell parameter and the texture parameters. The quality and reliability of the Rietveld or Pawley analysis was quantified by the corresponding figures of merit: the weighted summation of residual of the least squares fit, R_{wp}, the statistically expected least squares fit, R_{exp}, the profile residual, R_p, and the goodness of fit (sometimes refered as chi-squared), GoF. Since GoF = R_{wp}/R_{exp}, a GoF = 1.0 means a perfect fitting.

GIXRD at ESRF-SpLine

Grazing incidence X-Ray Diffraction (GIXRD) was measured at the beamline BM25-SpLine branch B experimental station of the ESRF.

The front end of the SpLine bemaline is 9 mrad wide with an energy range between 5 and 45 keV. The branch B, where the GIXRD was carried out, has 2 mrad width and the spot size is $300 \times 100 \mu m^2$ (Horizontal×Vertical). The power load of the beamline is 150 W, therefore a cooling system is needed. The first mirror (Rh strip) after the front end collimates vertically, rejecting high order harmonics, and produces a non dispersive optical setting, reducing as well the heat load. In this first mirror the glancing angle is ~ 2.5 mrad, which corresponds to a cut-off energy of 26.8 keV. The monochromator is a pseudo channel-cut type formed by two Si(111) crystals which rotate on a single table. The second mirror cuts additional harmonics by angular detuning and focuses vertically the beam at different positions in the experimental hutch. These cylinder mirrors are 1.2 m length coated with Si and Rh. The whole optical devices are in Ultra High Vacuum in order to avoid loses, valves and end windows are made of Be. The final photon flux on the sample is $6.5^{11} ph/s$ and the energy resolution is $\Delta E/E = 1.5 \times 10^{-4}$

In our experiment the energy used was E=14.5028 keV, with a wavelength λ=0.8549 Å. In order to perform a GIXRD experiment first the incidence angle of the X-rays beam must be selected, this is taking into account the attenuation length of the X-rays beam on the sample.

The attenuation length of an electromagnetic wave, such as X-Rays in a bulk material, is defined as the average length at which the intensity is reduced by a factor of $1/e \simeq 0.37$. This length, calculated for a stoichiometric bulk of NiO ($\rho = 6.67 gr/cm^3$ at E=14.5 keV) was necessary to estimate the probing depth of our GIXRD measurements. In figure 3.8 this attenuation length is shown (see X-Rays database of Berkeley Lab [40]) as a function of incidence angle of the

incoming X-Rays. At incidence angles below 0.2° the reduction in intensity is greatly increased by one order of magnitude. As the total reflection angle is reached, the intensity loses increase until there is no reflection and the rays come out parallel to the surface. The use of synchrotron radiation in GIXRD helped us in this work to understand better the crystal structure of the thin films when exploring more surface sensitive angles. The information given by GIXRD was complementary with morphology results and standard XRD.

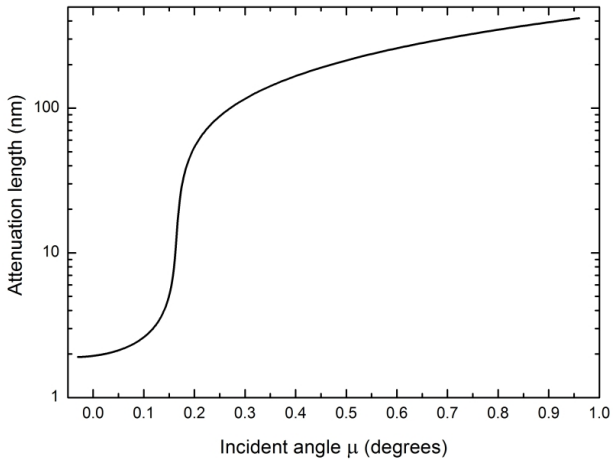

Figure 3.8: Attenuation length of 14.5 keV X-Rays in stoichiometric NiO bulk. GIXRD measurements have to take into account this incidence angle μ in order to probe the topmost layers of the surface sample.

3.4.5. Electric measurements

Electrical properties are very important in materials characterization. The resistivity, defined as $\rho = R \cdot A/l$ (the inverse of the conductivity σ), is the property of any material to obstruct the electrical current flow. In nanostructured materials the electrical properties are strongly related to the crystal order and the electronic structure.

The DC electrical conductivity of the NiO ceramic targets was determined by measuring directly the sheet resistance, measured in ($\Omega/\square$) or Ohms per square as used in films, with a four-probe set-up, without depositing contacts on the target surface. The resistance was measured directly using a voltmeter probe (Keithley).

In order to improve the measurements of the films with respect to the NiO ceramic targets, we measured the NiO films resistivity in a Van der Pauw four-probe set-up. Van der Pauw method measures the voltage drop across four small contacts located at the periphery of an arbitrary shape flat film. By measuring the voltage drop between each pair of the four contacts flowing current through the other two the shape dependence can be neglected [41]. This method applies for a well located contacts (at the periphery, the most symmetrically located as possible) of a small area with respect to the total film area and with ohmic behaviour. Normally the conductivity is studied with temperature variations, as will be explained in chapter 5, in order to obtain an Arrhenius plot, but in this work all measurements were carried out at room temperature.

Our four-probe equipment is a Hall effect station which incorporates two permanent magnets of 0.58 T magnetic field in order to measure carrier concentration, mobility, magnetoresistance and Hall effect. Unfortunately the carrier density of the NiO films was so low that this value was not reliable and therefore the mobility, magnetoresistance and Hall effect parameters, which depend on this concentration, could not be quantified. The equipment used was a HMS-300 model from Ecopia, with resistivity range between $10^{-4} - 10^{7}(\Omega \cdot cm)$ and a current-source (compliance voltage of 12 V) with current range $1nA - 20mA$.

The resistivity of the coatings was measured immediately after the samples were exposed

at open air. After each deposition at the working pressure of $P = 1.5 \cdot 10^{-2}$ mbar the vacuum was restored to almost its initial base pressure $P < 5 \times 10^{-7}$ mbar. This last was performed in order to avoid any possible incorporation of residual Ar and O atoms into the samples through surface and bulk diffusion. Once the sample holder and the samples on it were cooled down to RT, the vacuum chamber was vented. The samples were immediately mounted on the Van der Pauw set-up and the electrical resistance was measured.

Obtaining ohmic contacts is an important problem when measuring the resistivity. These contacts should accomplish certain characteristics: small area over the film, mechanical stability and uniform ohmic behaviour. An ohmic contact should have a behaviour that follows Ohm's rule when voltage is applied between its electrodes. In order to do so some heat treatment may be needed so that the contact atoms diffuse into the film. The work function between the contact and the film should also be similar [42]. In this work Sn, SnIn and Au contacts were tested on different substrates. Finally the material used was an SnIn alloy of composition 95% Sn and 5% In without solder resin. These contacts were soldered on square-planar glass substrates. However, the films grown on the AAM substrates presented more difficulties to be measured due to their morphology. Several try-outs were carried out in order to deposit a good ohmic contact on top of the NiO grown on these AAM substrates. Due to the fragile structure of the Al_2O_3 and its low thickness (about half micron) the possibility of using the SnIn contacts before deposition was discarded. Sputtered gold contacts were deposited but the measurements were not successful either. Finally using the Hall-effect station point probes without any contact on the sample the resistivity could be measured as shown in figure 5.1a. However, this method reduced dramatically the plateau zone of current values for a constant resistivity.

The way of checking a reasonable ohmic behaviour is by performing a V-I curve at each point probe as is shown in figure 3.9 (left). Each colour line represents a voltage measurement in each contact of the sample. The linear relation of voltage versus current indicates that Ohm's law is applicable at certain range. Due to the complexity in making ohmic contacts on semiconductors like NiO, which has a wide-gap, the usual strategy is to increase the doping concentration or to lower the barrier height in order to decrease the contact resistance [42]. In our work the linear relation represents therefore the current values at which a good measurement can be carried out. Figure 3.9 (right) shows a logarithmic graph of resistivity versus current. There are two regions: the plateau of constant resistivity and the negative linear trend. This plateau is directly related with the ohmic behaviour shown in the upper panel, and corresponds to the region in which the compliance voltage of the source can flow current through the sample. The more the insulating behaviour of the sample the shortest the plateau region (the less ohmic contact). The linear points are repeatedly observed with high reproducibility, which indicates that as a reversible process is taking place. The negative linear dependence of resistivity with current suggests an effect caused by joule heating because of the decrease of resistivity with high currents. However, this was observed for low temperatures as well. Some works propose complex models in which the grain boundaries, which conduce the charge, are melted at high current values, reducing the resistivity [43]. However, this effect would not be reversible as it is in our resistivity Van der Pauw measurements. Another hypothesis is the injection of carrier by means of high electric fields, but again this is an irreversible effect. Finally it turned out to be an artefact of our Hall effect station (Ecopia): the compliance voltage of this apparatus is 12 V, therefore in accordance to Ohm's law, in order to maintain that constant voltage at higher current values it is necessary to reduce the resistivity measured. When measuring a highly resistive sample, as is our case for NiO films, the voltage drop of 12 V is not enough to drive high current values (above $25\mu m$ in figure 3.9). Tests of measuring the films resistivity with a different current source of higher compliance voltage have been performed, obtaining constant resistivity values where our equipment gave lower values. This proves that the effect of lower resistivity with the increase of current is an artefact generated by the Hall station we used.

As shown in figure 3.9, when applied a current sweep in a range where the contact behaves

following Ohm's law (left), a plateau of similar values for the resistivity is obtained (right). The DC resistivity is expected to be constant and independent of the current flowing through the material, therefore the reliable ρ values are those of the plateau for current values $10^{-5} - 10^{-8}$, labelled as Ohmic region in the figure. In order to increase the accuracy of the measurements and reduce the data dispersion, all the values in the linear ohmic range were considered and an average of them was taken as the resistivity value. This was done for every measurement of the resistivity on each coating. Measurements were also taken with time, in a scale of several days, in order to study the ageing effect.

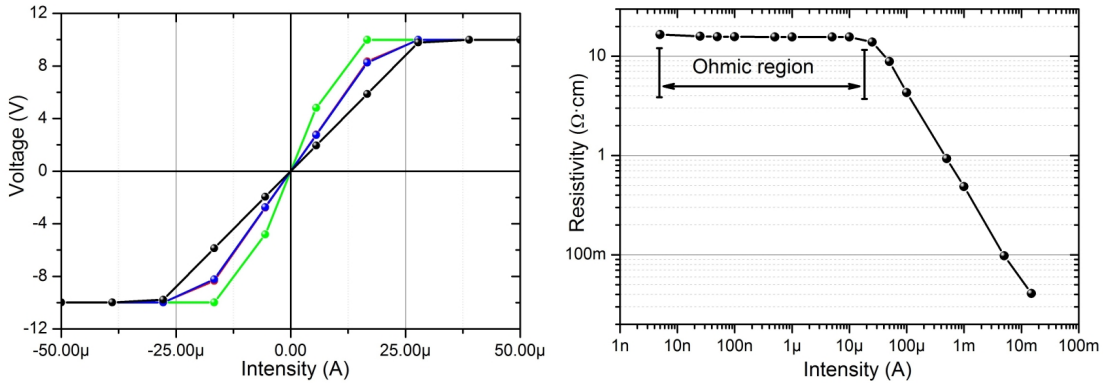

(a) I-V curve for ohmic region

(b) Resistivity vs. current

Figure 3.9: Ohmic contact: in the linear ohmic region of the contact Metal-NiO (left) a good measurement gives a resistivity value independently of the input current (right) for the same range of current.

3.4.6. Optical measurements

UV-Vis spectrophotometry is an absorption spectroscopy that studies the interaction of a material with near infrared (NIR), visible and near ultraviolet (NUV) radiation (from 1.4 to 4 eV). Based on the Beer-Lambert law for absorption, when a beam of known wavelength passes through a material, it is partially (or totally) absorbed and the signal is compared with the original beam. The ratio of the two signals indicates the spectral region of absorption. When absorbing visible or ultraviolet radiation an electron promotes from the valence band to a more energetic state (in our case for NiO from the top of the valence band to d states). Such electronic transitions within this low energy range are not easy to quantify and complex to understand from a theoretical point of view.

The combination of theoretical models with the absorption or transmittance experimental results allows to estimate the optical band gap. Furthermore, if diffuse reflectance is measured, fitting methods can be used to calculate the complex refraction index and the extinction coefficient, $\tilde{n} = n + i\kappa$. In this work absorption measurements have been carried out routinely and the optical gap has been estimated.

The spectrophotometer used in this work was a Varian Cary 100 Bio UV-Visible equipped with a Czerny-Turner monochromator and diffraction grating of 1200 lines/mm. The spectral range varies between 190-900 nm with limiting resolution $\leq 0.24nm$ and wavelength accuracy of $\pm 0.2nm$. This apparatus has a double-beam configuration with double choppers (30 Hz): during the measurement the incident beam was measured simultaneously with the transmitted beam and the output signal is the ratio between the intensity of the beam through the sample and the reference beam.

Additional reflectivity measurements (carried out for one set of samples) were performed on a Perkin-Elmer Lambda 9 Spectrophotometer with integrating sphere detector and double beam configuration.

The spectral transmittance T of a medium (in our case the NiO thin film on the glass substrate) is defined as the ratio of the transmitted and the incident flux. Similarly, the spectral absorbance (or spectral absorptance), A, is the ratio of the spectral power absorbed to the incident spectral power. Both the transmittance and the absorbance, due to their definition, are unitless. It is usual to define the transmittance of a medium in terms of the absorption coefficient, $\alpha(cm^{-1})$ and the pathlength t *(cm)* in this way:

$$T = 10^{-\alpha t} \tag{3.3}$$

obtained from the Beer-Lambert law. The spectral absorbance is usually defined by a logarithmic ratio:

$$A(\lambda) = -\log\left(\frac{I_t}{I_{inc}}\right) \tag{3.4}$$

where I_t is the transmitted intensity and I_{inc} is the incident radiation on the medium. The reflectance R, following the previous definitions, is the ratio of the radiant flux reflected to the incident radiant flux. The reflection can be specular, diffuse or a combination of both. In our case the reflectance was not measured because the spectrophotometer did not have an integration sphere, a special detector which is able to measure the diffuse reflectance.

3.4.7. X-ray Photoelectron Spectroscopy (XPS)

This technique was developed by Kai Siegbahn in 1956, when the first XPS spectrometer was developed, claiming to have precision in the range 1:10^5 [44]. K. Siegbahn received the Nobel prize in 1981. X-ray Photoelectron Spectroscopy (XPS) or Electron spectroscopy for chemical analysis (ESCA) is an electronic characterization technique based on the photoelectric effect. Incident X-rays excite electrons (named photoelectrons) from occupied states to states above the vacuum level within the solid. The excited electrons, diffuse along the solid and eventually escape out of it. Photoelectrons that cross the surface sample are focussed with electrostatic lenses, filtered in their kinetic energy and counted in a detector. XPS process is usually described approximately by the three-step model (stated by T. Koopman): (1) absorption of the photon and excitation of the electron from the initial state (2) transport through the crystal lattice to the surface and (3) escape from the solid through the surface. The total energy conservation equation of this model is written in the following equation (which considers that the photon absorption does not change the binding energy):

$$h\nu = KE + BE + \Phi \tag{3.5}$$

Where $h\nu$ is the incident photon energy, KE is the kinetic energy measured by the electron analyser, BE is the binding energy of the photoelectron bounded to its atom and Φ is the work function of the specimen measured and the analyser together, the energy needed to put an electron from the Fermi energy to the vacuum level. The fact that the BE is different for each atomic state makes this technique element-selective. The inelastic mean free path of photoelectrons within the solid is very low, and depends on their kinetic energy [45]. This fact makes XPS a very surface sensitive technique. Non-spherical states (p, d or f states) are splitted due to spin-orbit interactions, and this gives double peaks with a certain energy separation and a relative intensity proportional to their occupation.

In a XPS spectrum several structures can arise from different physical processes such as Auger emission, shake-ups and shake-down and plasmon resonances but in this work we will not study such effects. However, more information about these structures and the information that can be obtained from them are found elsewhere [46]. Structures of the XPS spectrum which are classified as *satellites* are due to artefacts of the experimental set-up. For the case of our X-ray source: the twin anode of Mg and Al, a *tube* X-rays source, is not actually a

monochromatic source but instead each anode has different emission lines. Each anode has the main line, called $K_{\alpha_{1,2}}$ which is an unresolved doublet, and secondary lines K_{α_3} and K_{α_4} which form a resolved doublet, and lower peaks K_β, etc. Each secondary emission line is well characterized: its separation and intensity relative to the main line is known. The main satellites of our standard X-rays source are shown in the Table 3.3. Other lines that can appear in the XPS spectrum and do not belong to photoemission or Auger processes are the called *ghosts* lines. These lines appear due to a contamination of the target anode (an oxide, generally) or the copper of the cathode or the aluminium from the source head window. These different elements can interfere by emitting X-rays of different intensities creating the ghosts lines. These secondary spurious emission lines appear at higher (or lower kinetic energies) binding energies therefore care must be taken in order not to identify incorrectly with a close photoemission peak. The difference in electronegativity between two elements produces energetic displacements of the bounded electrons sharing the chemical bond and core levels. In XPS this displacement is observed in a shift of the binding energy, called chemical shift, which gives information about the chemical state of the element detected. The chemical shift displacement ranges from 0.1 to 5 eV [46]. An increasing background with binding energy is observed in every photoemission spectrum. This is due to the secondary electrons: those produced upon inelastic scattering of the primary photoelectrons in their path out of the solid. When performing quantitative analysis the background must be subtracted through different functions (linear, Shirley, Tougaard). The cross-section of an atom at certain energy is necessary to estimate the interaction of radiation with matter. The photoionization cross section, i.e., the probability that a photon excites an electron, is given by the atomic sensitivity factors, tabulated from empirically values for each bound state of an element (singlet or doublet, because their cross-section varies) and normally related to F 1s [46]. Only when the different atomic peaks are measured in the same experimental conditions can be used this approximation. Therefore when estimating the atomic composition of a surface one must calculate the ratio of the peak intensity of each element taking into account its atomic sensitivity factor. However, in this work we did not used this estimation since we did not calculate the surface atomic composition but the relative intensities of contribution lines which form the Ni 2p and O 1s independently. The atomic sensitivity factors change depend on the energy of the excitation source, as well as on the incident angle. For studying valence band states, low energy sources, in the range of ultra-violet, are better suited than X-ray sources, since the photoionization cross-sections are higher and better resolution can be obtained [47]. Charging effects are typical in XPS when measuring insulating samples: a net charge can be formed in the sample and photoelectrons coming out of the solid leave its surface with a reduced kinetic energy, which increases virtually their binding energy. In order to avoid this effect (which can shift an spectrum up to 15 eV) a reference peak whose position is well known should be used to shift the spectrum to the correct position. Normally the C 1s (285.5 eV) is used for this purpose, though slight corrections should be carried out at different spectrum energies. In some cases an electron gun can be used to recover the charge neutrality of the sample while measuring.

X-ray line	Mg	Al
K_{α_3}	8.4(9.2%)	9.6(7.8%)
K_{α_4}	10.0(5.1%)	11.5(3.3%)

Table 3.3: Satellites emission lines of Mg and Al anodes of the X-rays twin source. The separation is in eV and the relative intensity is expressed in percentage relative to the main emission line $K_\alpha(100\%)$, [46].

A photoemission peak from a core-level without taking into account electronic correlation has the shape of a Lorentzian curve, with Gaussian broadening owing to instrumental factors, resulting in a convolution of both curves. Usually the curve of a photoemission peak is asymmetric due to plasmons or inelastic scattering of electrons within the lattice. In metals, where the

photoelectrons can interact with the conduction band (Shake-up and Shake-off effects and movements to screen the hole produced) the curve which best describes a peak is a Doniac-Sunjic due to their asymmetry.

The probing depth of the XPS technique can be estimated by the relation:

$$d = 3\lambda(KE)\cos(\theta) \tag{3.6}$$

where $\lambda(KE)$ is the inelastic mean free path (IMFP) for a given Kinetic Energy (KE) and θ is the take-off angle of the photoelectrons coming out from the solid, with respect to the normal to the surface. In our experimental set-up this angle was chosen to be 0°. The IMFP length for NiO was calculated from the empiric universal curve TPP-2M [45] using the software QUASES-IMFP by S. Tougaard [48]. In our study the Mg anode of the X-ray source was used (with a photon energy of 1253.6 eV) therefore the Kinetic Energy of the photoelectrons coming out from the Ni 2p states was about 395 eV, this gives a IMFP of about 9.7 Å for stoichiometric Nickel Oxide, however minor differences in this path length are obtained under low variations of the density. Therefore the probing depth of the XPS measurements for our Nickel Oxide is estimated to be about 20 Å or 2 nm, a short distance compared with the thickness of the NiO films investigated in this work, which allows us to explore the different samples independently of the substrate used. According to S. Tougaard the absolute error in the IMFP estimation is about 20% which still lies, however, in a short range enough for our aim of study the surface of our samples. Due to the short IMFP of the electrons within the solid, the XPS technique needs UHV conditions in order to correctly measure the photoelectron flux and not damage the detectors.

As the equation 3.6 indicates, by changing this take-off angle θ (rotating the sample-holder inside the UHV chamber) it is possible to detect only photoelectrons closer to the substrate (decreasing d) due to their larger IMFP inside the crystal lattice.

More information and details about this widespread technique can be found elsewhere [46].

XPS was measured at our laboratory in the *Coatings, Interfaces and Nanostructures Group* at UAM. Our XPS set-up consists of an Ultra High Vacuum (UHV) chamber with a concentric hemispherical analyser CLAM-4 (VG technologies). The analyser has 9 channeltron that collect the photoelectrons after their kinetic energy has been selected with high resolution, and then integrate the counts. The X-rays source is a twin anode (Mg and Al) located at the magic angle ($\approx 54.7°$). The pass energy (CAE), was set to 20 eV for every sample and region measured, in steps of 0.1 eV, obtaining a resolution of 0.67 eV. This resolution was calibrated by measuring the Au 4f doublet fitting the peaks with an asymmetric Doniac-Sunjic curve. Au 4f is a very chemical stable reference suitable for resolution estimation: the $4f_{7/2}$ peak is very narrow, therefore the analyser able to resolve its FWHM can weight the Gaussian contribution, which corresponds to the instrumental contribution. The analysis area of our set-up is about 1 mm^2. The UHV analysis chamber is connected to a HV chamber and this one to a fast-introduction chamber in order to maintain near UHV conditions when introducing and extracting samples from the analysis chamber.

3.4.8. X-ray Absorption Spectroscopy (XAS)

X-ray Absorption Spectroscopy (XAS) is an electronic element-selective spectroscopy that measures transitions from occupied initial states to bound and continuum final states. The development of XAS has come together with the use of synchrotron radiation: collimated X-rays of high flux and tunable energy are the essential probe for this spectroscopy. Depending on the atoms to be explored and their absorption edges (K, L, M, N in Barkla notation) the energy range must be selected (soft or hard X-rays). Because XAS is a quantum phenomenon the Fermi golden rule, which determines the transition probability between initial and final states, is the basis of the process. When an incident X-ray photon is absorbed by an atom in the sample a photoelectron is liberated from an orbital (from the K, L, M, N shells) having a probability of

reaching a bound orbital of higher energy (or the unbound continuum). Depending on the lifetime of this excited state the electron will sooner or later come back to its initial state, emitting a photon or Auger electrons in the process. Secondary electrons are emitted as well in this process due to inelastic scattering of the primary electrons or photons. The amount of electrons lost in the process or the photons emitted can be measured (Electron or Fluorescence Yield, respectively) and its signal gives information on the unoccupied density of states within the solid, the chemical state and the electronic structure around the absorber atoms. This is called X-ray Absorption Near Edge Spectroscopy (XANES).

One can also understand this process in a wave-like manner. When the wave of a photoelectron scatters from the atoms near the absorber, it creates interferences between the outgoing and scattered waves. These quantum interferences cause a variation in the X-ray absorption probability, which depends on the energy of the incident photon and is proportional to the measured quantity: the absorption coefficient. These oscillations can be treated and analysed providing information about the local structure around the absorber atoms: coordination number, disorder, thermal motion of neighbours and local distances within the unit cell. This is called Extended X-ray Absorption Fine Structure (EXAFS).

XAS technique comprehends both XANES and EXAFS, which depending on the energy range studied give different information. Properly the frontier between XANES (also called NEXAFS) and EXAFS is just the energy range studied. However, the different regions of the spectrum provide quite different information about the sample. XANES ranges from several eV below the absorption edge and about 50 eV above. In turn, EXAFS is usually performed at the K-edge, using high energetic or hard X-rays between several tents of eV below the absorption edge to about 1 keV above, in order to detect all the oscillations of the absorption coefficient. In this section we will only describe the basics of the technique and the experimental conditions employed. More details of these techniques can be found elsewhere [49, 32, 50, 51, 52].

In this research work we have performed XANES at BESSY II, studying the K-edge of the oxygen and the L-edge of nickel atoms while at ESRF facility we have explored EXAFS at the nickel K-edge.

The compatibility of X-rays with air or vacuum will depend on their mass absorption coefficient, which depends on the photon energy. Quite different experimental apparatus can be used when measuring XAS. The data presented in figure 3.10 are obtained from [53]. Regarding this phenomenon it can be understood that the XAS experiments at low photon energy such as that needed in O K-edge measurements will need a high vacuum environment during the whole beam path in order not to loose intensity from the source (Bending Magnet or Undulator at the storage ring, about 35 meters) to the sample. On the other hand experiments carried out with hard X-rays such as EXAFS at the Ni K-edge do not need such a complex set-up because the air absorption is more than four orders of magnitude lower and therefore the intensity loses are insignificant. These data have been calculated for dry air at sea level of air density ρ=1.205·10^{-3} (g/cm^3) with a composition of 0.01% C, 75.5%N, 23.1%O and 1.3%Ar.

Extended X-ray Absorption Fine Structure (EXAFS)

EXAFS was measured above the Ni K-edge (E=8.333 keV) at the ESRF SpLine BM25 experimental station in branch A. Measurements were carried out at room temperature in fluorescence mode at a beam incidence of 45° using a multi-element solid-state multichannel detector of thirteen elements.

In this beamline the optical elements (in vacuum with Be valves between the cooled components) accept 2 mrad horizontal aperture in the spectral range of 5-35 keV. The beam is vertically collimated by a cylindrically bent mirror coated with Si and Rh. Its angle of incidence is set at 2.5 mrad, reducing therefore the higher harmonics and the heat load in the rest of optical components. The monochromator, located at 28.5 meters from the source, is composed by two fixed Si(111) crystals that move together by a goniometer circle. The horizontal focusing

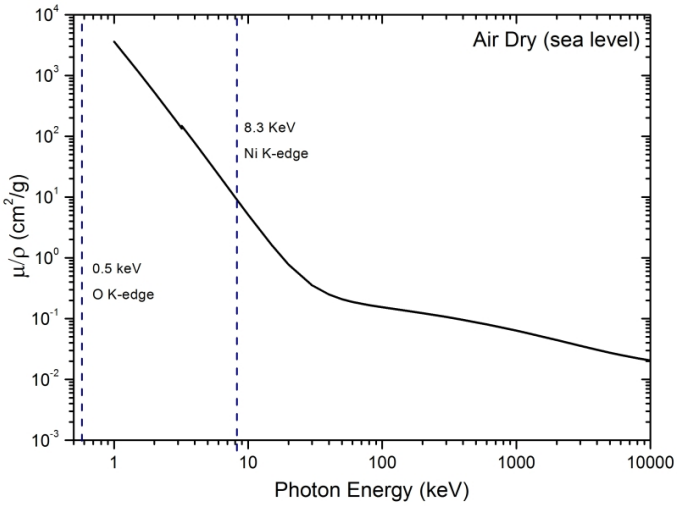

Figure 3.10: Mass absorption coefficient for X-rays in dry air. When working at soft X-rays the experimental set-up need the use of high vacuum environment while high energy X-rays can be used at open air. Data obtained from [53].

is achieved by the second monochromator crystal. This second crystal can be moved with a piezoelectric driver to change very slightly the Bragg angle (pitch adjustment) in order to reduce the harmonic content of the beam and to keep the transmission of the monochromator constant during long time intervals, giving high stability to the beamline experiments. Finally the second mirror focuses the beam into the experimental hutch at two positions 40 and 45 meters from the source (the front end of the banding magnet). The vacuum optical components are separated from the open air hutch with a Be 0.5 mm thickness window, which represents a cut-off energy of 4 keV.

The final flux on the sample is 10^{12} photons/s with a beam spot of $0.1{\times}0.1\ mm^2$. The position and size of the spot is maintained constant thanks to the optical arrangement during 1 keV scan, which is the standard EXAFS scan measurement.

The absorption coefficient μ as a function of energy is the magnitude measured, proportional to the transition probability of the photoelectric event (promoting of an electron from the K shell). This coefficient is affected by the surrounding atoms, which scatter the photoelectron wave creating constructive and destructive oscillations that are observed. The absorption coefficient is related to the incident signal I_0 by the relation $\mu(E) \propto I/I_0$.

Normally the total absorption coefficient $\mu(E)$ is expressed in terms of the absorption coefficient from an isolated atom $\mu_0(E)$ with a correction factor: $\chi(E) = (\mu - \mu_0)/\mu_0$. Its interpretation is the fractional change in the absorption coefficient due to the neighbour atoms. For the K-edge inner atomic orbitals, every atom located at R_i contributes to the EXAFS signal, summing up the EXAFS equation for small variations in distance:

$$\chi(k) = -S_0^2 \sum_i \frac{N_i}{kR_i^2} |f_i(k)| e^{-2R_i/\lambda_e} e^{-2k^2\sigma_i^2} \sin\left(2kR_i + 2\delta_1(k) + \arg\left(f_i(k)\right)\right) \tag{3.7}$$

The damped modulated sinusoidal oscillations of the EXAFS signal are described by this equation by the dependence $1/R_i^2$ which accounts for a propagating spherical wave. The energy is transformed to k-space by $k = (2m(E - E_0)/\hbar^2)^{1/2}$, being E_0 the energy of the absorption edge of an isolated atom. N_i is the number of atoms in the coordination shell. $f_i(k)$ is the complex scattering amplitude of each electron, for which the amplitude and phase is used in the EXAFS contribution signal. δ_1 is the partial wave phase shift due to the central absorbing atom, S_0^2 is a many-body factor, and λ_e is the photoelectron mean free path. These two last factors take into account the coherence losses due to multielectron excitations [50]. The effects of the

lattice disorder are contained in the Debye-Waller (DW) like factor σ_i^2: a mean square variation of the atoms around their equilibrium position, in analogy with a similar factor in diffraction techniques.

This equation 3.7 is based on several theoretical assumptions: first a Gaussian atomic distribution around the absorber atom at R_i distances, second, plane-wave approximation is considered, third, only a single-electron is directly excited, and fourth, the solid where the photoelectron propagates through is approximated by spherically symmetric atoms with a flat region between them (the so-called *muffin-tin approximation*). The equation 3.7 is a local approximation, resembling the high sensitivity of this technique to local structure, and it works for small disorder, which should accomplish the relation $k_{\max}\sigma << 1$ [50]. In our experiment we have $10.3 \times 0.014 < 1$ therefore the EXAFS approximation is valid although our system is highly intrinsic disordered.

The self-absorption of the NiO coating is the phenomenon by which the emitted fluorescence signal is partially absorbed by the NiO layers within the film with high dependence on the incidence angles. In our case this selfsorption length has been estimated in order to consider any corrections (analysis EXAFS software like Viper [54] or Athena-Artemis [55] account for this corrections, if necessary) The cross-sections for Ni and O has been estimated for a photon energy of 8.33 KeV from NIST database [56]:

$$\mu \approx \sum_{i=1}^{n} \rho_i \sigma_i = \rho_{NiO} \left[\left(\frac{m_{Ni}}{Mm} \right) \sigma_{Ni}(E) + \left(\frac{m_O}{Mm} \right) \sigma_O(E) \right] \simeq 5.7 \mu m \tag{3.8}$$

where $\sigma_{Ni}(E)$ and $\sigma_O(E)$ are the cross sections of Ni and O for a given energy, in our case we considered E=8.33 keV. Considering the thickness of our thin films (between 50 and 500 nm) and that the estimated absorption length given by equation 3.8 is far above this value, the self-absorption effects are expected to be low.

The disorder parameters, the Debye-Waller like factors, σ^2 in equation 3.7 (not to be confused with cross-section of equation 3.8), are an estimation of the averaged displacement of the atoms around their equilibrium positions. These factors have two main contributions: the thermal and the static disorder displacements, and are quantified as $\sigma^2 = \sigma^2_{\text{th}} + \sigma^2_{\text{st}}$, respectively [57, 58]. In order to avoid the thermal disorder contribution all the samples were measured at the same room temperature, therefore the static disorder contribution could be isolated. Although disordered systems produce EXAFS data which are rather difficult to interpret, we could study the effects of the deposition parameters by means of this DW like factor.

According to equation 3.7 each shell around the absorber atom has the following characteristic parameters to fit: coordination number (N), DW factor (σ^2), neighbour distance (R) and energy distance to the absorption edge (E_0), which is usually fixed during the fit.

The EXAFS spectra have been processed according to standard procedures: first, the background was removed using a cubic spline polynomial fitting, a pre-edge linear background was also removed, and the magnitude of the oscillations was normalized to the edge jump of the absorption function χ. The treatment detailed above, as well as the subsequent quantification, have been performed using the software Viper [54]. After removing the background and normalizing the signal, the data, expressed in terms of k (Å^{-1}) are weighted by a factor of k^2 in order to avoid loss of information at high k-values, compensating in this way the amplitude reduction.

The processed data are Fourier transformed (FT) and filtered by a Hanning window (a raised cosine with continuous derivatives), which selects k-values within a range where the simple EXAFS theory is valid and minimizes the noise effects produced by high k-values. In our case this window function was in the range $2.3 \leq k \leq 10.3$ Å^{-1}.

Once transformed to r-space, data are fitted with the Viper program for each shell. At this point, there are two strategies for fitting the EXAFS data: one is to use the phase and amplitude transferability method [59]. The backscattering amplitude, phase, and photoelectron mean free path factor are obtained from the experimental EXAFS spectra of the appropriate reference

compound, in our case the sample grown with 0% oxygen in the plasma or a stoichiometric NiO powder. The other method, finally used in this work, is to simulate a cluster and generate the phase and amplitude functions for different possible paths. Proceeding this way, using the Atoms software [60], a stoichiometric NiO cluster (fcc symmetry) of 6 Å size and 93 atoms was calculated. The backscattering amplitude, phase, and photoelectron mean free path factors simulated for this NiO cluster were obtained using the software FEFF5 [61] for a maximum of 4 legs (path segments between atoms). Least squares fitting of the simulated signals was performed using Viper software [54]. Although FEFF5 calculates every possible scattering path, only the most relevant were included in the fitting (too many parameters would be impossible to fit). Finally, only the first two shells were considered: the first six oxygen neighbours (Ni-O) and the twelve second neighbours (Ni-Ni). After fitting in r-space, the simulated signal is back Fourier transformed (BFT) to k-space and compared to the original EXAFS signal.

Each atomic shell around the absorber atom contributes differently to the EXAFS signal, mainly due to its composition. The phase and amplitude signals as a function of k for nickel and oxygen atoms are significantly different due to their dependence on the atomic number Z. For the case of Ni and O atoms their maximum values of the theoretical backscattering amplitude functions are separated by about 4 $Å^{-1}$. Therefore, Ni atoms contribute to middle k-values of the EXAFS selected range while O atoms contribute primary at lower k-values [51, 58].

The central atom contributes as well with a shift in the phase and amplitude, usually by a value of ~ 0.5 Å. Only when this correction is applied we can name the FT EXAFS signal the Radial Distribution Function, which indicates the position of the neighbours and the coordination of the shells (correlated with DW factors) by the position and intensity of the peaks of this function, respectively.

The simulated paths within the NiO cluster account for single and multiple-scattering paths, involving only the absorber and one scatter atoms or more than one scatter atoms, respectively. Although the probability of occurrence is calculated by FEFF5 program we only considered here the first two single-scattering paths corresponding to the first two shells. Considering more shells would have implied larger k-values range in order to have enough experimental data to achieve more degrees of freedom, but unfortunately due to the highly disordered system this was not possible.

The paths given by FEFF5 program for the Atoms generated cluster are 97, however contributions to the EXAFS signal below 2.5% are neglected, remaining 70 paths. Among them we considered the single-scattering more important paths within the first two shells, as indicated in table 3.4. For each path FEFF calculates its phase and amplitude scattering functions with their correspondence degeneracy (number of equal paths, may imply more than one shell) and the effective distance of the total path, R_{eff}, which is the distance of the one-way path until the last scatter atoms (for the case of multi-scattering paths). Although other paths have higher contribution (see table 3.4) the multi-scattering calculations are complicated and considering them would have implied considering as well other inner paths, which is not possible with the experimental data acquired.

The experimental data and their corresponding information that can be obtained from them is estimated by the Nyquist criterion, [62]: the number of relevant independent points that can be fit is proportional to the width of the selected windows in k- and r-space grids [62]: $N_{ind} = (2\delta k \delta R/\pi) + 2$. The fit implies four parameters per shell (4n in total) therefore the degrees of freedom are $\nu = N_{ind} - 4n$.

However, because of the disordered system here studied, the DW factors are strongly correlated with the coordination number, affecting the FT magnitude. A successful fitting should accomplish the convergence criteria in r-space both for the amplitude of the FT signal and its imaginary and real parts. When parameters are highly correlated it is necessary fo minimize simultaneously the FT EXAFS signal weighted by k^2 and by k^3, obtaining a set of possible values for the parameters, and among them the best fit is found when the chosen parameters accomplish a good fit in both

Shells	Complete path	Degeneracy	R_{eff} (Å)	Contribution (%)
First	$[Ni]_{abs}$+$[O]^1$+$[Ni]_{abs}$	6	2.0842	100
Second	$[Ni]_{abs}$+$[Ni]^2$+$[Ni]_{abs}$	12	2.9475	87.9
Third	$[Ni]_{abs}$+$[O]^3$+$[Ni]_{abs}$	24	4.6604	52.3
Second	$[Ni]_{abs}$+$[Ni]^2$+$[O]^1$+ $[Ni]_{abs}$	12	4.1684	47.5
...	...	...	...	...
Second	$[Ni]_{abs}$+$[Ni]^1$+$[O]^1$+$[Ni]_{abs}$	48	3.5580	19.8
Second	$[Ni]_{abs}$+$[O]^1$+$[O]^1$+$[Ni]_{abs}$	24	3.5580	14.1

Table 3.4: Paths calculated by FEFF for a NiO cluster. $[Ni]_{abs}$ refers to the absorber atom that emits the photoelectron; exponents refer to neighbour number (of the two inter-penetrated fcc lattices). Only the First and Second shells were selected for the fit. Multiple-scatterings paths have lower contribution to the EXAFS signal.

weightings [63, 64].

However, EXAFS has intrinsic limitations: its high sensibility to atomic disorder makes quite difficult a calculation for several shells, and this is correlated with the fact that the results need large k-range of data. It must be remarked that increasing the density of points do not improve the results or decrease the experimental error, and only extending the values in k-space helps to improve the minimization (see Viper manual, [54]). The theoretical accuracy of EXAFS for the atomic distances is ± 0.01 Å while for the DW it is ± 20-25% due to the high correlation with the coordination number. When analysing samples of unknown composition the scatter atoms can be detected with an uncertainty of Z ± 1 for light atoms (until Ar) and Z ± 3 for heavy atoms. The coordination number are normally estimated about N ± 10%.

X-ray Absorption Near Edge Spectroscopy (XANES)

In XANES after a photon is absorbed three simplified processes occur that contribute to the yield spectrum: a direct excitation of an electron into the conduction band, the emission of X-rays or Auger electrons and the de-excitation of the core hole. The total yield is the ratio of emitted electrons over incident photons and is proportional to the absorption coefficient [65].

The core hole created by an absorbed X-ray has two decay modes: fluorescence and Auger (non radiative decay). The fluorescence decay at the K-edge is very low for $Z \leq 30$ in comparison to Auger decay for 2p elements, and for the case of 3p and 3d elements the L-edge is lower than 2% [49] therefore the Auger electron yield is the best choice for soft X-rays. In addition to Auger electrons, also photoelectrons are produced in XANES from the core and valence levels provided that the incident photon has energy above the binding energies of the electrons in the sample studied with respect to the vacuum level. Total electron yield mode of measurement (TEY) takes into account both the Auger and photoelectrons and secondary electrons that come out of the sample. Secondary electrons are majority in the TEY signal because they have higher mean free path therefore contribute with higher background [66, 49]. Partial electron yield (PEY) is named when a retarding voltage is placed next to the detector or biasing the sample in order to collect a fraction of the electrons, typically between 50 and 100 V. Measuring only the Auger electrons (AEY) from a given transition is possible by selecting only a specified transition energy. Auger electrons have a very short mean free path so that it is a more surface sensitive technique.

Fluorescence yield measurements (TFY), although not as effective as TEY in the energy range used in this work, was performed by means of a semiconductor photodiode detector, which collects the fluorescence emission in an energy range from a solid angle from the sample converting it to a quantifiable voltage. Also partial fluorescence yield (PFY) can be performed when the fluorescence detector allows the selection of an energy range. In this case more complex detectors should be used instead of a photodiode [33, 50]

XANES experiments were performed at the beamlines *Optics Beamline* (bending magnet) using the SurICat endstation and *UE52-PGM* (undulator) at BESSY II Facility. At both beamlines soft X-rays were used in order to excite the oxygen K-edge located at 530 eV and the Ni L-edge at 852 eV. The spectra were obtained in total electron yield (TEY) mode by measuring the neutralization current with an electrometer (current values in the picoampere). The X-rays incidence was normal to the sample surface. In the undulator beamline the total fluorescent yield (TFY) measurement mode could be performed with the aid of a photodiode. These beamlines were also equipped with hemispherical photoelectron analysers.

The Optics Beamline (bending magnet source) has a Au coated toroidal mirror as premonochromator which deflects the X-ray beam at 176°. This mirror collimates vertically the beam and focuses it horizontally on to the monochromator. The monochromator consists of an Au coated plane mirror and a set of three plane gratings (PGM) of 150, 260 and 1280 lines/mm. Afterwards, the beam is again deflected at 176.8° horizontally and vertically focused onto the exit slit. Before the beam reaches the sample a Au coated refocusing toroidal mirror is located which deflects the beam at 178° focussing vertically and horizontally onto the experimental station SurICat. The Beamline acceptance is $1.6 \times 0.5\text{mrad}^2$ and the spot size at the experimental station is 300 (hor.)$\times$ 90 (ver.) μm The beamline UE52-PGM has an Undulator as a source, the first optical component is an Au coated cylindrical mirror which deflects the beam horizontally at 176°and the monochromator consist of a Au coated plane mirror which deflects vertically the beam at 172° - 178.5° on two Petersen diffraction gratings of 260 and 1200 lines/mm. Afterwards an Au coated cylindrical mirror deflects horizontally the beam at 176° and focuses it vertically. Before enters the experimental station the beam is focused horizontally by means of a Au coated spherical mirror at horizontal deflection of 176°. The spot size on the sample is 300 (hor.)$\times$ 400 (ver.)μm.

Charging do not affects XANES in the same way as in XPS: in XANES the charging only will decrease the intensity of the signal collected in TEY mode [67].

The resolution $E/\Delta E$ is a function of the incident photon energy and the slits width used to collimate the beam. However, within the regions measured the variation was very small, being between 50 and 60 meV with the slits width in the range of 50-100 μm. In order to correctly align the experimental spectra the photon energy must be known within a certain value. By using the first and second orders of the focused beam reflected in the Si mirror it was possible to measure the photoemission peaks of the Au 4f doublet of a clean reference. The core Au 4f core-level is well known to be used as a reference peak for its stability. The kinetic energy of the photoelectrons coming out from the gold reference foil are excited using the first- and second-order X-rays, without moving the monochromator (using the photoemission relation 3.5). The difference between the two Au 4f positions gives the photon energy of the incoming beam at that monochromator position and therefore the peak energies can be calibrated.

In figure 3.11 two photoemission spectra of the Au 4f doublet obtained with first order (right curve) and second order (left curve) are shown. After a scan the monochromator was not moved and at the final position the Au 4f signal was collected. The second order has less intensity therefore the signal-to-noise ratio is lower, as seen in figure 3.11. The more intense peak ($4f_{7/2}$) was fitted with a Voigt profile (red line) obtaining the peak position as labelled in the graph. With first and second order the position of the Au $4f_{7/2}$ peak difference was: $1053.35 - 484.72 = 568.63$ eV, giving the final photon energy.

This method was performed at both the O and Ni edges after each measurement, obtaining slight corrections of about 50-100 meV between each scan improving the accuracy. The spatial resolution of XANES is low, being in the range of mm for a conventional beamline [67].

3.4.9. Rutherford Backscattering Spectrometry (RBS)

Rutherford Backscattering Spectrometry (RBS) is a characterization technique based on the measurement of elastically backscattered beam of ions, which interact with the nuclei within the specimen losing energy in the path going through the sample and coming back to the detector.

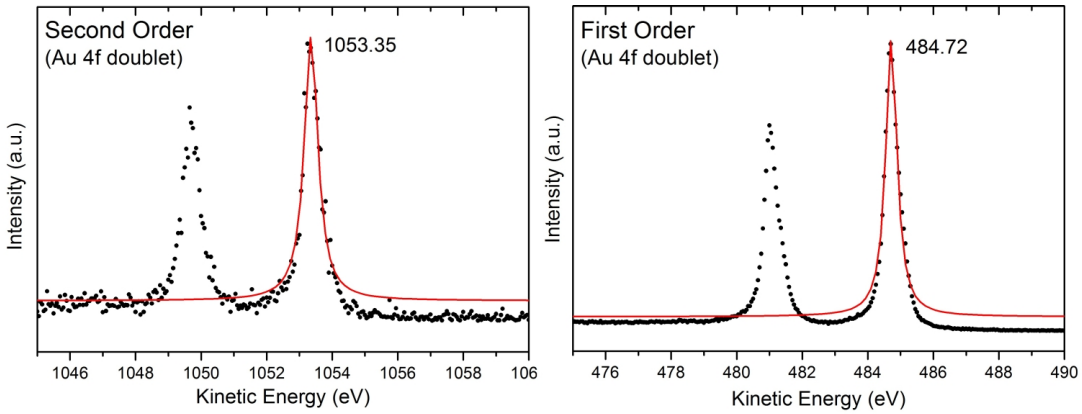

Figure 3.11: Au 4f photoemission spectra using first and second order of the X-ray beam. The difference between the Au $4f_{7/2}$ positions gives the actual photon energy for each monochromator position after each XANES scan. This method helped to align correctly the scans with an accuracy of 50-100 meV.

The energy difference in the spectrum is used to identify scattering depths, obtaining a relative depth profile and chemical analysis of the specimen simultaneously. This is an element selective technique useful to determine surface composition and thickness or film density (provided that the film thickness is known) as well as areal concentrations (atoms/cm^{-2}). Its depth resolution ranges from nm to 1 μm. Measure RBS requires the sample be ground connected as well as measure it in high vacuum in order not to loose beam flux due to scattering. RBS is more sensitive to heavier elements (a coating as thin as a monolayer is able to be measured) than to lighter elements.

In this work, RBS was performed at the Centre for Micro Analysis of Materials (CMAM) at the multipurpose Standard Beamline. The ion accelerator is a Cockcroft-Walton based Tandetron with a terminal voltage of 5 MV [68] manufactured by *High Voltage Engineering Europa B.V.*. In this work we studied NiO thin films using alpha particles $^4_2\mathrm{He}^{2+}$ with 3.045 MeV kinetic energy at carbon resonance (where non-classical Rutherford cross-section applies). The Standard Beamline has two Au-Si detectors (one fixed and one movable) for charged particles detection by means of generating electron-hole pairs. The movable detector was located at 165° with respect to the beam, being the incident beam perpendicular to the surface sample. The energy resolution was 27 keV with 2.61 keV per channel. The intensity of the beam was of the order of nanoamperes therefore the arriving alpha particles was at enough low rate to avoid pile-up effects in the detector. The beam flux was 3.782×10^{11} *(ions/srad)*.

The calculations of RBS experimental data were performed with the software SIMNRA 6.0 [69] simulating a two-layer system for the deposited samples: a thickness and composition variable NiO layer on top of an infinitely-thick Si substrate; and one infinitely-thick NiO layer for the sputtering targets with variable stoichiometry.

Chapter 4

Experimental Results: Morphology and Structure

> "*Las empresas científicas exigen, más que vigor intelectual, disciplina severa de la voluntad y perenne subordinación de todas las fuerzas mentales a un objeto de estudio.*"
>
> Santiago Ramón y Cajal

In this chapter the morphology and structure of nickel oxide films grown by magnetron sputtering, both as porous and continuous films, will be shown. The porosity of the films is obtained only under certain conditions, which are chosen among those allowed in our experimental set-up. The objective of this chapter is to understand the relationship between the morphology and the structure of the films and the growing parameters used to produce them. Additionally, this will lead to an understanding of the macroscopic and electronic properties of the films in terms of their internal structure. The focus will be put on the influence of the growing parameters on the porosity of the films and the crystal structure

The chapter will initially describe the characterization of the sputtering targets used to deposit the coatings, which will be our reference in order to compare the thin films grown. Afterwards, the morphology of the grown films under certain parameters will be studied and related to their structural properties as the growing parameters are varied. These parameters include the sputtering power, the substrate temperature, and the oxygen content of the plasma. The latter will reveal essential for determining the final properties of the films.

In order to assure a correct systematic procedure both clean substrates and bulk NiO references were measured in most of the characterization techniques to correctly check the variations due to the synthesis technique.

The morphology has been studied by FESEM and the structure by XRD and EXAFS analysis. For a more suitable presentation of the results the SEM parameters of the micrographs are shown in a separated table in Appendix 1.

The study of the structure was carried out with two techniques in two different scales: grazing incidence XRD gives information on the long range order of the samples, including the crystal structure and lattice parameter. Additionally, with a proper analysis, either using the Scherrer relationship or Pawley refinement, it is possible to obtain the average crystallite size. On the other hand, EXAFS gives information on the short range structural parameters, such as first and second neighbours distances and coordination numbers. These two scales affect differently the properties of the films. The nanometer range has more impact on the morphology of the films: the surface to volume ratio is a consequence of the nanostructured nature of the columnar films and the porosity of the films is as well related to the crystal size. On the other hand the

atomic scale has a more important impact on the final properties of the films: the electronic structure is highly dependent on the amount of vacancies (in which a slight variation can be of great influence), which can be estimated by EXAFS. The presence of these vacancies would enhance the conductivity and might be related to the optical properties of the films.

The final part of the chapter will relate the structural and morphological properties with the local structural information and the presence of Ni vacancies in the crystal structure, which may enhance the conductivity.

4.1. Substrates and sputtering targets

4.1.1. Substrates characterization

NiO thin films have been grown on different substrates in order to both characterize the deposited coatings by several techniques and to explore the effects of the substrate structure and morphology on the final properties of these films.

Glass microscope cover slides and boron doped single-crystal silicon wafers with (1 0 0) orientation and resistivity values in the range $7 - 17$ (Ω·cm) were used as planar substrates. Commercial (*Synkera Technologies*) Anodic Alumina oxide Membranes grown on aluminium were used as nanostructured substrates.

The self-ordering process of growth of aluminium oxide under certain conditions was discovered by Masuda and Fukuda in 1995 [70] and since then it has been used to synthesize several functional nanostructures. An aluminium film exposed to open air has a native oxide layer of about 2-5 nm. The oxidation of Aluminium can be enhanced trough electrochemical methods and, under certain conditions, the oxidation developes in the form of self ordered nanoporous films, known as anodic alumina membranes (AAM). These films, composed of pure Al_2O_3, are chemically inert, electrically insulating. Their extraordinary characteristics such as the high-ordered porous area, the hexagonally self-assembled pattern and their reproducibility have promoted this material to an important position in the production of nanostructures and nano-devices.

The electrochemical growth of AAM is carried out in a two-step anodization process from Al metal [70]. The first step consists of an anodization within an electrolytic bath with a specific applied voltage, depending on the desired pore diameter and interpore distance. The geometrical properties strongly depend on the electrolyte, the temperature and the bias voltage applied during the anodization process as well as the anodization time [70]. After the first anodization an ordered distribution of pore centres on top of the Aluminium is formed. These pores are, however, not symmetrically distributed. To obtain an almost perfect hexagonal arrangement of pores, it is necessary to remove the Al_2O_3 and perform a second anodization. This second anodization takes place at the well organized pore centres on the aluminium and, under the proper growth parameters, the pores grow parallel and vertically with no inter crossing and with high aspect ratio (the diameter is very small compared with the length). A post anodization wet-etching treatment in diluted phosphoric acid at 30-35℃ can be performed to open the pores until the desired diameter. An schematic view of the cross section of an AAM is shown in figure 4.1, where the hexagonally array of cylindrical pores can be seen. The pores are closed at the bottom (though open pores structures can be obtained) and do not connect with the metallic aluminium foil which supports this structure.

The AAMs used in this work have an average pore diameter of ∼45 nm, and an average distance between pores of ∼100 nm, as given by the supplier. An estimation of the porosity assuming an ideal hexagonal arrangement of the pores gives:

$$p = \frac{\pi}{2\sqrt{3}} \left(\frac{r}{\lambda_{CC}} \right)^2$$

where r is the pore radius and λ_{CC} is the pore-centre to pore-centre distance. This estimation

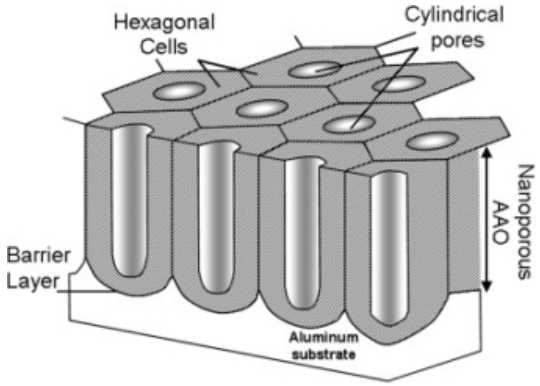

Figure 4.1: Schematic view of the porous AAM. The hexagonally array of pores is presented. The pores are closed at the bottom and not connected with the metallic Aluminium foil which supports the insulator AAM (or AAO) structure. Figure from [71].

gives a porosity of approximately 18% for the membranes used in this work. However, the analysis of the SEM micrographs of an AAM gives a porosity of approximately 13%, which is in agreement with the supplier (*Synkera Technologies*). This disagreement with the calculated value can be due to deviations from the ideal hexagonal arrangement of the pores, or to a distribution of the pore radii and distance between pores different to the supplied values.

The thickness of the AAM used was about 500 nm. Consequently, the AAMs used in this work consist of a 500 nm of AAM supported by an aluminium foil of several microns. The metallic support is electrically insulated from any deposited coating by the ceramic AAM. However during the growth and especially because of the rotation of the sample holder NiO can be deposited of the lateral sides of these substrates (commonly square shaped). This issue is useful when performing SEM micrography, XPS and XAS (in electron total yield mode) because of the ground connection.

As a previous step to the study of the NiO coatings, in this section I will show a characterization of the substrates. Figure 4.2 shows a FESEM view (top view and cross-view) of the AAM used as substrate in this work with no deposit grown on it. Due to its insulating behaviour the resolution of the image could not be improved. In the top-view the hexagonal pattern of pore distribution is clearly observed. An analysis of the image gives a pore diameter of about 40 nm (45 nm according to the supplier). The pores have a conical opening with a small rim after which the pores become wider with uniform diameter along the vertical height. The average size of the domains free of defects is, approximately, 1-1.5 microns large. It is in the borders of these domains where the defects appear in the form of dislocation-like boundaries. These defects consist of a breaking in the hexagonal periodicity in which pentagons of columns appear or a hole is missing. The very low presence of defects makes it possible to correctly study the porosity of the NiO films, as will be shown in subsequent sections. The cross-view in figure 4.2b shows the columnar structure of the AAM. It is a honeycomb structure in which the columns grow vertically and parallel without crossing each other. These columns are ceramic cylinders of Al_2O_3 with a high aspect ratio (45 nm of diameter and 500 nm of height). In this cross-sectional view the columnar growth can be appreciated. This kind of cross-view micrographs will confirm lately in this work that the NiO deposits grow following this vertical direction. The surface around the pores is not planar and the natural amorphous roughness of the Al_2O_3 will form the substrate onto which the sputtered nickel and oxygen atoms will be finally located. The hole's bottom is closed and separated from the Aluminium support by a continuous alumina layer.

The crystal structure of the NiO deposits might be influenced by the crystal structure and orientation of the substrate. Furthermore the study by X-ray diffraction (XRD) of the NiO coatings will require to identify not only the peak positions arising from the grown thin film, but

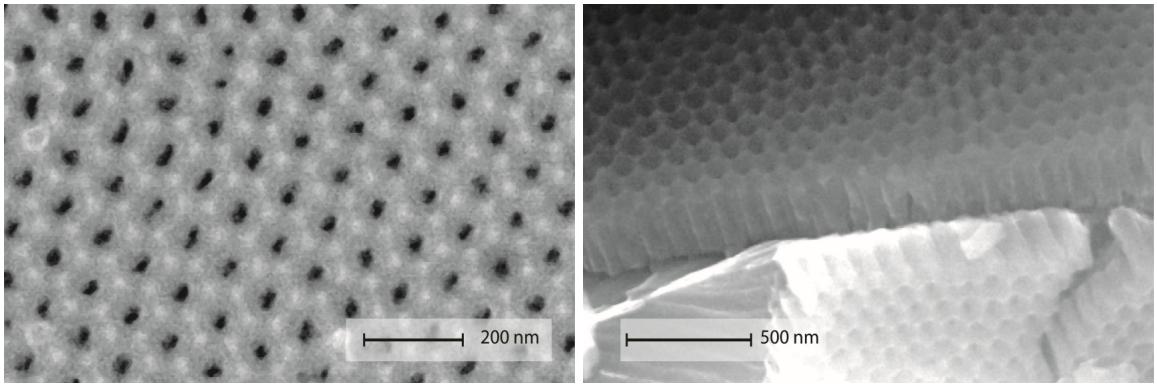

(a) zenith-view (b) cross-view

Figure 4.2: FESEM images of an AAM substrate with no deposit grown on it. (a) the top-view shows the hexagonal array of pores while (b) shows a cross-view where the tight grown columns of about 500 nm can be seen. Due to the insulating behaviour of the AAMs, the FESEM image has not the best quality.

also those from the substrate, due to the fact that X-rays penetrate about 1.5 microns in grazing incidence for Cu K_α. This penetration depth is larger than the thickness of any coating of this work, therefore unless a very small angle of grazing incidence is used the peaks of the support will always be observed in the diffractograms of the NiO deposits on AAM substrates. Therefore, X-ray diffraction measurements were carried out on the substrates before deposition.

In figure 4.3 an XRD diffraction pattern of the two main substrates used in this work is shown. Glass substrates (microscope slides) were also used to perform optical measurements but their amorphous structure does not give any peak in the diffraction patterns. The left curve (figure 4.3a) shows a diffractogram of the AAM supported on Al. The Bragg diffraction peaks show several orientations which correspond to metallic Al (fcc) according to the ICSD card of pure Aluminium [72]. No peaks are present from any alumina phase, which indicates that the Aluminium support predominates in the pattern. Taking into account that the AAM thickness is about 500 nm the absence of peaks coming from the alumina suggest that the AAM layer is amorphous. Indeed, only diffraction peaks from the Al metal have been detected, whose orientations are labelled in the figure. This observation is in agreement with the bibliography, in which the amorphous structure of the AAM as deposited is reported. Only after annealing at temperatures higher than 600℃ do the AAM experiment a transformation to the crystalline γ-Al_2O_3 phase [73, 74].

The use of Al supported AAM as substrates for NiO deposition has the disadvantage that the position of the Al Bragg peaks overlap in some cases with to the NiO peak positions, which makes it difficult to study by XRD these coatings on AAM substrates. This does not occur for NiO films grown on planar Si wafers substrates covered by a native silicon oxide layer. The curve on the right (figure 4.3b) shows a grazing incidence measurement of the Si (1 0 0) wafer substrate. There is a broad peak centered at about 55° and another narrow peak at about 54°. A simulation of the Si diffraction pattern for this wavelength and crystal orientation is included in the figure in red colour, with its three peaks in that region labelled. There is no correlation between the observed peaks at 54° and 55° and the peaks shown in the red curve for Si(100), so we conclude that the observed peaks to arise from an artefact of the measurement XRD set-up. This artefact structure will be observed again later in this chapter for some of the NiO films studied. The lack of Bragg peaks assigned to crystalline Si indicates that, under this grazing angle, all information comes from the native oxide layer, with an amorphous character. Diffraction patterns of Si covered with a SiO_2 layer have been reported in the literature for the same X-ray source [75], and the absence of the peaks observed in figure 4.3 supports our conclusion that this is an artefact.

Therefore the substrates used for the structural characterization by XRD (Si wafers and glass substrates) are amorphous and do not interfere in the diffraction pattern. However, for NiO deposited on AAM diffraction peaks from the metallic Al base are expected to interfere with the NiO diffraction peaks.

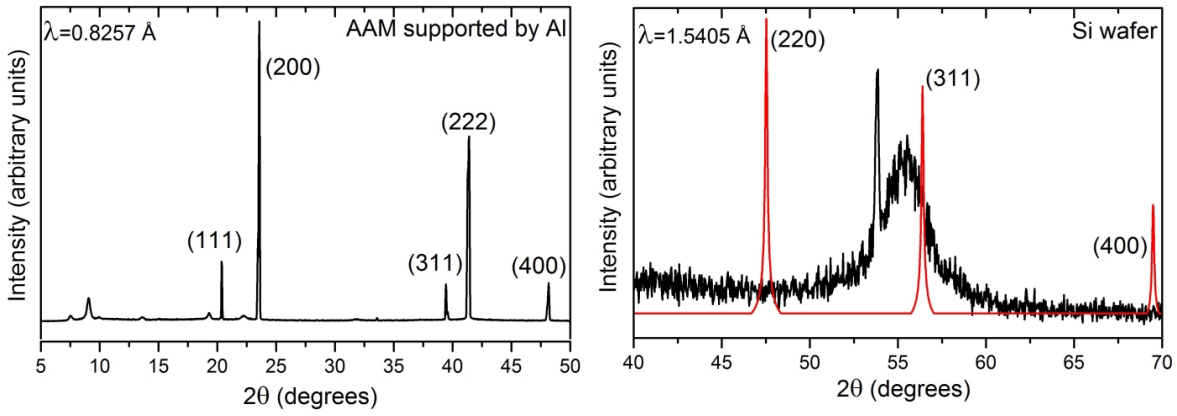

(a) XRD of porous AAM

(b) XRD of Si wafer

Figure 4.3: XRD diffraction patterns of substrates: (left) amorphous AAM substrate on the Al support, the labelled Bragg peaks coincide with metallic Al (fcc) phase. No polycrystalline AAM is found. (right) Si substrate gives a diffractogram with only one broad peak at about 55°, with a narrow peak at 54° which are actually an artefact from the experimental set-up. Si Bragg peaks from a simulated powder pattern are represented in red.

4.1.2. Sputtering targets characterization

The quality of the Nickel Oxide targets is extremely important in the sputtering technique: the stoichiometry of the targets must be maintained during the sputtering process. Therefore the higher the quality of the starting material and the lower the amount of impurities the better controlled the conditions of the growth. For these reasons we have checked the commercial and sintered targets from the chemical and structural points of view. The results obtained from the good quality NiO targets served as well as a bulk reference for the deposited films.

NiO targets, both commercial (*AJA International, Goodfellow*) and sintered at ICV-CSIC from *Sigma Aldrich* powder, as mentioned in chapter 3, were characterized by RBS and XRD. When sintered at high temperatures in a reducing atmosphere the equilibrium is difficult to achieve but necessary to eliminate traces from other chemical compounds or polymers. Too high temperature or a too reducing environment would produce a further reduction of the NiO into metallic Ni.

Rutherford backscattering spectroscopy was used to analyse the chemical composition of the NiO target in depth profile, as shown in figure 4.4. As an example of the RBS spectrum we show the NiO target of the *Goodfellow* supplier in figure 4.4a. The red line corresponds to the fitting of only one layer, whose stoichiometry is shown in figure 4.4b. The experiment was performed at CMAM using impinging α-particles with 3045 keV of kinetic energy, in resonance with the Oxygen cross-section. The energy per channel was 2.6067 keV/ch. Ni atoms appear at channel 845 (corresponding to 2300 keV), as an abrupt increase in intensity, and due to the large thickness of the target studied, this intensity associated to Ni atoms stays for lower channels. At channel 380 (about 1100 keV) the peak of the oxygen resonance can be observed. For lower energies (below channel 300 or 900 keV) the counts increase considerably due to the energy loss of the backscattered ions within the crystal lattice, and in this region the simulation does not correctly reproduce the spectrum. A better fit of this experimental spectrum would

have needed a larger amount of thinner layers close to the surface of the target with varying Ni content. However, using the magnetron sputtering technique the first nanometers layers of the target material are not quite important due to the fact that at the beginning of each deposition a pre-sputtering to clean the surface is performed. Consequently, we were more interested in the bulk stoichiometry of the targets.

The quantitative information given by RBS includes the atomic composition with a high degree of precision. Figure 4.4b shows the chemical composition of the different NiO sputtering targets, as determined by RBS. As can be observed the correct stoichiometry is not achieved in all of the targets, although some of them approach reasonably. This lack of stoichiometry can affect the final properties of the deposited NiO films, since non-stoichiometric NiO has different properties than stoichiometric NiO. For instance, stoichiometric NiO is a high-k insulator, but non-stoichiometric NiO is a semiconductor, with conductivity values that can be relatively high. In order to obtain reliable results and a systematic procedure in this work, we had to choose the most stoichiometric target among the different suppliers: *Goodfellow* (the first of the two targets in our set-up), *AJA Int.* and the ICV-CSIC, made up from NiO powder from *Sigma Aldrich*. The atomic concentration of the *Testbourne* supplier was achieved only after a thermal treatment in vacuum, performed at the ICMM-CSIC institute, however the dimensions of the target changed, and it finally broke after several growths. The suppliers *AJA Int.* and *Goodfellow* only provided us with good quality targets after repeated feedback and discussion with them.

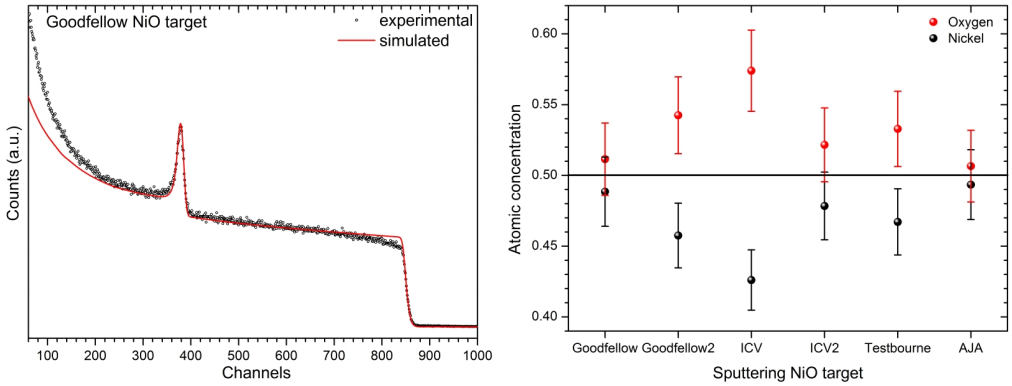

(a) RBS spectrum of *Goodfellow* target (b) Atomic concentration of NiO targets

Figure 4.4: RBS spectrum and results of the atomic concentration of Nickel Oxide sputtering targets. (a) RBS spectrum of a *Goodfellow* target fitted with one layer in red line. The probe was ^{4}He with 3045 keV kinetic energy. (b) Targets from different suppliers show variations in the composition between them. The three targets which finally were used is this work were from *Goodfellow* (the first of the two shown), *AJA int.* and the ICV-CSIC, made up from NiO powder from *Sigma Aldrich*. The line at 0.5 represents the right stoichiometry.

The second parameter of interest to determine the quality of the targets is the crystalline orientation. In order to avoid a preferential direction in the NiO deposits, the starting material should be polycrystalline. We present in figure 4.5 the diffraction patterns of all targets. Note that three different wavelengths: $\lambda = 0.8262$ Å, $\lambda = 0.8508$ Å and $\lambda = 1.5406$ Å have been used, depending on the available set-up at the moment of the measurements. The top curve corresponds to the NiO powder from *Sigma Aldrich*, used to sinter the target at the ICV-CSIC institute. At the bottom of each figure in green the vertical lines mark the Bragg reflections of the stoichiometric NiO (*Bunsenite*) corresponding to the Powder Diffraction File (PDF) card [76]: a face-centred cubic system, with the space group centrosymmetric $Fm\bar{3}m$ (225). The lattice parameter for the *Bunsenite* bulk is $a = 4.1771(8)$ Å with α=90°. These values will be considered our bulk reference from now on in this work. Note that metallic Ni has an fcc lattice with a lattice parameter $a = 3.52$ Å [37]. The Miller indices of each crystal plane have been

labelled next to each peak.

All targets have a polycrystalline structure with the cubic orientations well defined. Although the peak positions for every target coincide with the values expected from the Bunsenite card, the relative intensities differ from the standard values. These differences rely on the preferred orientations of polycrystalline sintered materials: the relative intensities of the *Bunsenite* give to the (2 0 0) orientation the maximum intensity. Although the three targets used in this work have differences between them in this aspect, this issue should not be a problem when working with magnetron sputtering deposition technique, because these targets are polycrystalline and the sputtering yield is not much affected by the texture of the starting material.

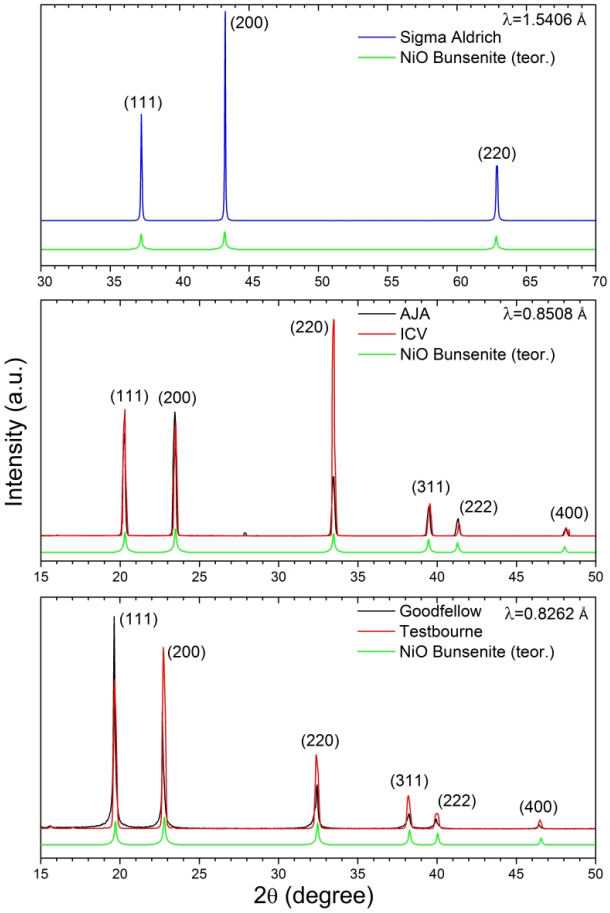

Figure 4.5: XRD diffraction patterns of the NiO sputtering targets used for different wavelengths. Green diffractograms indicate *Bunsenite* NiO reference. The patterns from the different targets coincide with the *Bunsenite* phase with only variations in the relative intensities. All targets are polycrystalline. (Top) Diffraction pattern of NiO powder from *Sigma Aldrich* (Medium) NiO targets from *AJA Int.* and target sintered using the powder of *Sigma Aldrich* at the ICV-CSIC. (Bottom) NiO targets from *Goodfellow* and *Testbourne*, the latter after thermal treatment in vacuum in order to improve the stoichiometry.

4.2. Morphology

As it will be shown in this section, the NiO films produced with magnetron sputtering in this work follow a columnar growth. The study of the dynamics of crystal growth is itself a complete sub-field in the materials science. Many studies, models and simulations have been proposed especially for polycrystalline metallic films (among them, fcc metals) but there is still a low number of works dealing with the growth dynamics of sputtered oxide films. Compounds

and alloys have higher complexity than pure metals when dealing with purity and reproducibility, which may explain this fact. For a complete understanding of the crystal growth of thin films, some in-situ techniques, such as EELS, combined with molecular dynamics or Monte Carlo simulations, can shed some light on this problem. Though the analysis and study of the growth dynamics of thin films is far beyond the scope of this work we will draw some basic aspects of the dynamics of our NiO sputtered films.

Zone models, such as Thorton's [21], are constructed attending to atomic processes, which, in turn, depend greatly on the temperature (such as sublimation or surface and bulk diffusion energy needed to activate the process), and on the pressure of the sputtering gas. This model has been used as a guideline for years and confirmed in a great variety of magnetron grown films (mainly metals). As it was explained in chapter 3, in the *Zone I* of this model, due to the low substrate temperature, the structure is columnar with voids between the dense columns. The adatom mobility may play an important role due to the fact that the kinetic energy of the sputtered atoms is high.

As will be shown in this section, the deposited coatings studied in this work present vertical growth in the form of columns in a temperature range between Room Temperature and 300℃, for magnetron powers ranging between 70 W to 300 W and a deposition time between one and three hours. Although the maximum substrate temperature in this work reaches 300℃ it is still considered as low temperature in the zone model diagram,

For any set of parameters (substrate temperature, magnetron power and deposition time) the oxygen content in the plasma has been varied from 0% to 70% or 100% in order to study the effect of adding Oxygen to the plasma. Figure 4.6 shows FESEM micrographs of NiO films grown on different substrates under different conditions. In all cases a columnar growth can be observed.

Figures 4.6a and 4.6b show NiO coatings grown on AAM substrates for two conditions that preserve the hexagonal pattern of pores distribution: 10%-70W-2h-125℃ and 20%-100W-1h-200℃. In both cases it can be observed that NiO deposits on the pore walls, and the lack of lateral growth keeps the columnar growth in the vertical direction, preserving the pores. On the other hand, figures 4.6c and 4.6d show NiO films grown on Si substrates under conditions 70%-100W-3h-RT and 0%-200W-2h-300℃, respectively. As it can be observed in both cross-sectional figures, the coating is formed by dense columns with scarce voids between them even for quite different growing conditions, similarly to what occur on AAM substrates.

The cross sections shown in figures 4.6c and 4.6d on Si substrates reveal that each grain covers most of the film thickness. The columnar grains are grown continuously along the direction normal to the substrate during the whole growth. The density of the columns resemble more the transition structure consisted of densely packed fibrous grains in Thornton zone model than the pure porous structure corresponding to Zone I. The size and density of intercolumnar spaces depend on the atomic shadowing during deposition, and this shadowing is which is enhanced by the oblique scattering [21].

The sputtered NiO grows vertically in an array of parallel columns on every substrate and preserves the porosity of the AAM substrates. Columnar growth of NiO coatings has been reported previously in several works [77, 78, 79, 80]. Using RF magnetron sputtering, several research groups report similar columnar structures with other materials as well: Park *et al.* obtain columns of ZnAlO doped with group-II elements from oxide ceramic targets [81]; Feldmeier's group finds columnar vertical growth of CdS by RF magnetron in comparison with rounded grains grown by close space sublimation technique [82]; Lead Selenide columns have also been grown on silicon dioxide [83]. All cases are good examples of vertical growth similar to that observed in our coatings.

The structure zone models rely not only on the substrate temperature but also on the physical processes that can occur simultaneously: shadowing processes during growth, surface and bulk diffusion and competition of grains and texture during growth [84, 17].

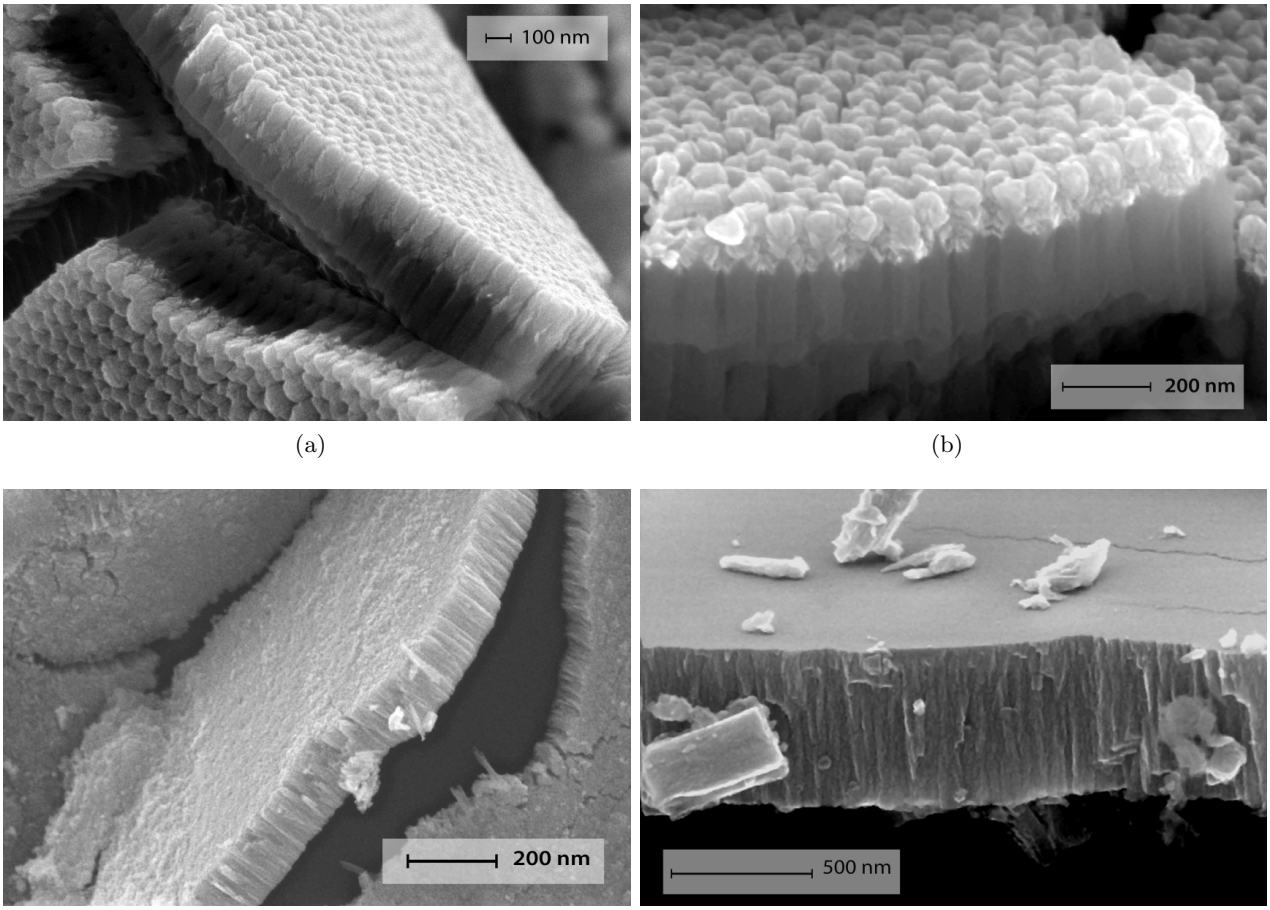

(a) (b)

(c) (d)

Figure 4.6: FESEM of different columnar NiO thin films grown on AAM and Si substrates. For different deposition conditions the growth is columnar on both substrates, a fact repeatedly observed throughout this work: (a) 10%-70W-2h-125℃ on AAM substrate (b) 20%-100W-1h-200℃ on AAM substrate (c) 70%-100W-3h-RT on Si substrate (d) 0%-200W-2h-300℃ on Si substrate

The latter effects might lead to a predominance of one crystallographic direction over the others, producing textured coatings. This is indeed the case, as it is shown in figure 4.7, where peaks indicating NiO orientations appear for samples grown with different oxygen concentrations. These diffraction patterns were acquired with Cu K_α radiation on samples grown with 0% and 70% oxygen content in the plasma, respectively. A variation from the (1 1 1) orientation to the (2 0 0) when oxygen is added can be clearly observed. According to this figure, the NiO thin films are polycrystalline, although with different textures. The labelled peaks correspond to the three first Bragg reflections of a fcc lattice. The narrow peak at 54° and the broad peak at 55° correspond to artefacts from the XRD set-up, as explained in subsection 4.1.1 (see figure 4.3). The change in preferred orientation or texture is independent of the columnar growth of the samples.

Growth Dynamics

The vertical or columnar growth described above obtained by magnetron sputtering with a wide range of materials is a common phenomenon. However, the growth dynamics remains at discussion: the influence of substrate temperature on the surface and bulk diffusion during growth, as well as the plasma pressure, have been remarked by several authors [25, 21, 17, 85, 22].

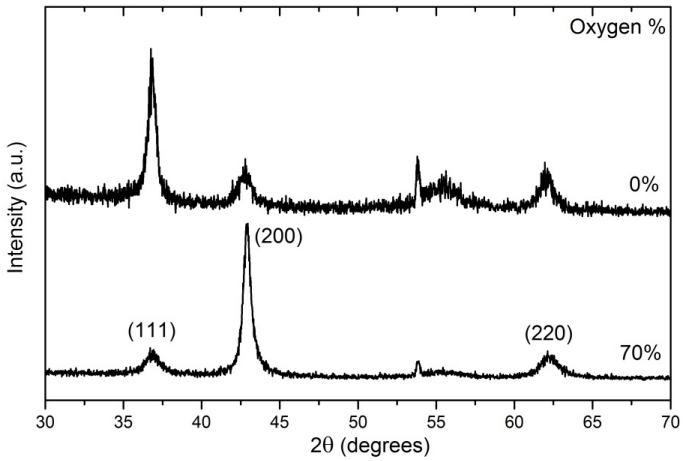

Figure 4.7: Diffraction patterns of NiO films grown on Si substrates at 100W-1h-RT with different oxygen content in the plasma, 0% and 70%. The coatings are polycrystalline with a change in the preferred orientation from (1 1 1) to (2 0 0) when adding oxygen to the sputtering plasma. The measurements were carried out with Cu K_α radiation.

The off-axis incoming of sputtered particles is also determinant for coatings with low density and voids between the grains. In general the evolution of columnar structures of thin films can be interpreted in terms of structure zone models, which do not take into account the chemical composition of the coating, pretending to be of universal application.

The process of thin films growing in terms of nucleation, cluster formation and grain growth is considered in atomistic models. The nucleation of sputtered atoms arrived at the substrate surface is the beginning of the crystal growth. Once the first islands have appeared on the surface they may grow to form clusters until coalescence, forming a uniform layer composed by polycrystalline grains [86]. The process of coalescence of islands is driven by an elastic distortion of the islands surface which eliminate their contact boundary lowering the surface energy. Coalescence generally creates tensile stress during the formation of the films [85, 21]. As more atoms arrive, the crystallites grow, and a competition between grains occur, allowing the formation of columns in the growing film structure with, eventually, re-nucleation on top of the forming film to develop new grains. This occurs with pure materials, but the real structure in the different regions of the zone models is quite more complex. Some authors have included the impurities as a new parameter in the structure zone models [87], understanding impurities as co-deposition, dopant atoms and mixed atmosphere.

In 1967 A. Van der Drift [17] proposed a growth mechanism which has been widely accepted. His model is based on the grain competition: some grains grow faster than others because the growth is favoured in some crystal faces that reduce the surface energy. Therefore, grains with their favoured faces oriented perpendicular to the substrate surface grow faster (vertically) while others grow in other directions which intersect the column walls of bigger grains. The result of this competition is the occlusion of many small grains at the beginning of the thickening, close to the substrate surface, and the surviving of a minor quantity of grains in the form of columns of favoured crystal orientations. Crystal orientations which are more prominent to grow are those that minimize the grain surface energy. The thermodynamic argument here is that arriving atoms that are able to diffuse along the growing surface find primarily their final lattice positions in low-energy surfaces, which minimize the grain surface energy [85]. The columns formed may have V-shape forms [87, 84]. The competition finishes when only grains with the same type of crystal faces reach the film surface. From that moment on, the film grows vertically with parallel columns developing a fibrous coating. This kind of competition occurs more often at low temperatures (those used in this work), where the grain boundaries do not move due to the low

or non-existent bulk diffusion. As a consequence of this competitive growth the grain morphology and texture change during the thickening. A first approach to quantify this competition growth was proposed in 1988 by A. Mazor *et al.* [22] where the surface diffusion plays an important role at low temperatures (bulk diffusion is not expected). In this model a simulation of the occlusion of small grains is presented. This simulation confirms the model of Van der Drift. A scheme of this competitive growth model is shown in figure 4.8 where it can be observed the columnar structure when small grains growth is terminated by grains with favoured orientations. During the grain competition there exists a bimodal distribution of grain sizes while at the end of the competition the average grain size is established and we speak of monomodal distribution [22]. In our work the estimation of the grain size has always been determined when this grain competition is over, however a study of the average grain size for each growing stage remains to be completely developed.

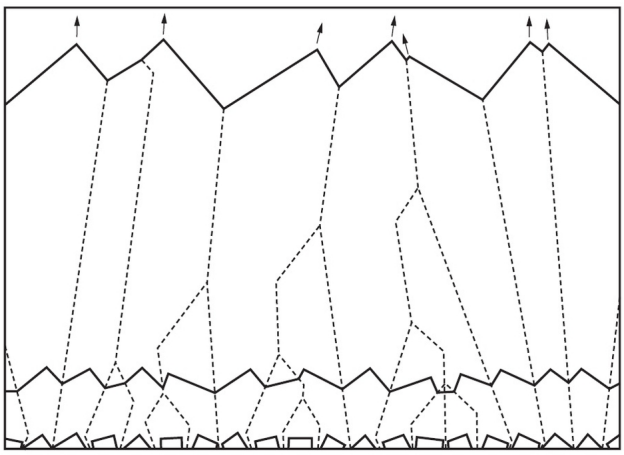

Figure 4.8: Scheme of competitive Van der Drift model [17]. Close to the substrate, islands which give rise to grains with faces with the favoured orientation growing vertically are able to occlude smaller grains. This competition occurs due to the adatom surface mobility, which can condense on lower surface energy grain faces. Figure from [85].

When comparing our NiO films with image 4.8 we can interpret the growth dynamics in our sputtering system in terms of surface mobility and explain the columnar structure. A good example of this competitive mechanism of thickening is shown in the cross section of figure 4.10b for a NiO deposited on Si substrate: it can be observed that close to the substrate the number of small grains is higher while as the film thickens only some survive and grow in a columnar way.

A consequence of this grain competition is the predominance of some crystal orientations within the deposited film, the so-called texture competition [85]. Whether (1 1 1) orientations minimize the surface energy more than (1 0 0) out of plane orientations depends greatly on the deposited material and the amount of energy adatoms that diffuse on the surface.

On amorphous substrates, the forming nuclei are stochastically oriented and, therefore, the textures are evolutionary due to selection mechanisms. The relation of the coatings texture with the morphology is not yet well established and there is still a lack of confirmation of the theoretical simulations by experimental results [86].

According to Thornton's zone model the growth in the *Zone I* is dominated by the angle of arrival of the sputtered atoms and no influence of surface diffusion is relevant at these low temperatures, although we obtain results which can be explained by the Van der Drift model, in which the adatom surface diffusion has an important role.

The columnar growth is the dominant fact of the morphology of these nanostructured coatings, as we have already seen. However the shape of the columns are greatly influenced by the substrate, as expected. Planar substrates favour the growth of fibrous grains as seen in figure 4.10a, whose

structural development is driven by the horizontal competition at the first stages. Grains of inverted narrow cones gain height widening as they grow up toward the surface, while some clusters are occluded and remain smaller close to the substrate (see figure 4.10b).

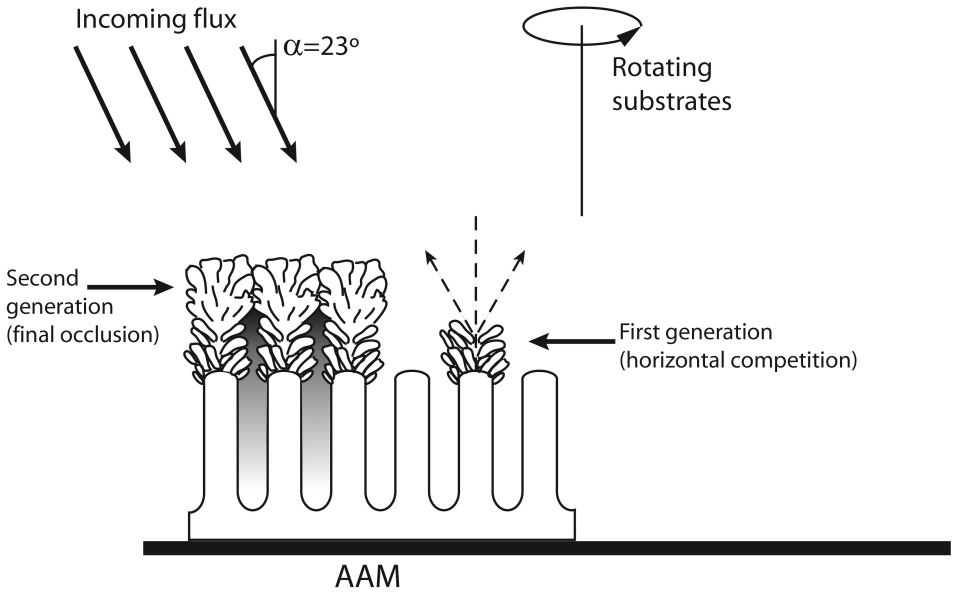

Figure 4.9: Schematic picture of the grain growth evolution on AAM. The first nuclei deposit on the top of the columns at the rim of the pores. The first generation of grains grow symmetrically respect to the axis of the column opening in V-shape. The second generation of grains, which develop with columnar structure and are survivors of the competitive horizontal grain growth, thickens the film vertically until finally occlusion of the pores.

On the basis of our FESEM images we can interpret the growth of the sputtered nickel and oxygen atoms on the AAM substrate following the van der Drift competitive model adapted to the roughness of the porous substrate. The first nucleation generation on top of the amorphous Al_2O_3 between the pores occurs within grain competition. During this first stage the formed grains have a small size and no columnar shape but arrow shape. The grains cover the top of the column between each six pores and evolve with cylindrical symmetry: the axis of the Al_2O_3 column is covered with grains from the centre to outside, as if they were arrow heads, producing a cauliflower like shape. A schematic view of this growing phase can be seen on the right part of the figure 4.9. When several layers of NiO cover the top of the column and the horizontal grain competition seems to be completed, the surviving grains have their faster grow faces oriented perpendicular to the surface substrate, which has high roughness, then they start to grow vertically. These grains of the second generation still have V-shaped form or inverted cones form but with higher aspect ratio (longer length compared with their width) and thicken the film considerably. Finally when the growth of the V-shaped grains has achieved a threshold height the total width of each independent column is high enough to occlude the pores, which were opened since the beginning of the growth. It can also be expected that small amounts of material are deposited through the pores on the internal lateral surface of the cylinder columns, close to the pore rims. The pore diameter is gradually blocked during the whole thickening until finally they are close, as it is shown in the left part of the figure 4.9. We consider this model for the case of rotating substrates and off-axis incoming sputtered atoms (23° respect to the normal of the substrate), as indicated in figure 4.9.

The nature of this growth is based on several factors, highly correlated between them: deposition rate, obliqueness of the incoming flux of atoms, shadowing effect caused by the amorphous substrate and surface diffusivity of the adatoms, which increase with temperature in

the form $\sim e^{(-1/T)}$. Also important is the kinetic energy obtained from the sputtering process (between 10-40 eV). Therefore for some growth we will observe the occlusion of the pores for different thickness regarding the deposition conditions.

As follows from the model proposed in figure 4.9, the growth on AAM substrates resembles cauliflower-like shapes and the initial grains, as seen in figure 4.10c, accommodate themselves to the roughness surface of the AAM. The next grains grow on top more vertically in a similar fashion to the growth on the Si substrates. This second generation of grains that have survived the horizontal competition described above, can grow more vertically in the form of columns. Figure 4.10d shows a cross-view of these columns grown on AAM substrate subsequently separated from the nanoporous membrane. In this micrograph we are able to observe the small grains at the bottom of the coating and how they evolve vertically until they reach a height of about 400 nm. The V-shaped form of the columns can as well be noticed. We can compare how on both substrates (Si and AAM, as seen in figure 4.10) the growth is columnar and how the grain competition derive in such columns. From the set of figures 4.10 and also 4.6 the diameter of the column can be estimated to be about 90 nm on the AAM substrate, which is the space between pores. However on the Si substrate, where the columns seem to be more tightly arranged, the diameter seems to vary from 20 to 150 nm depending on the deposition conditions.

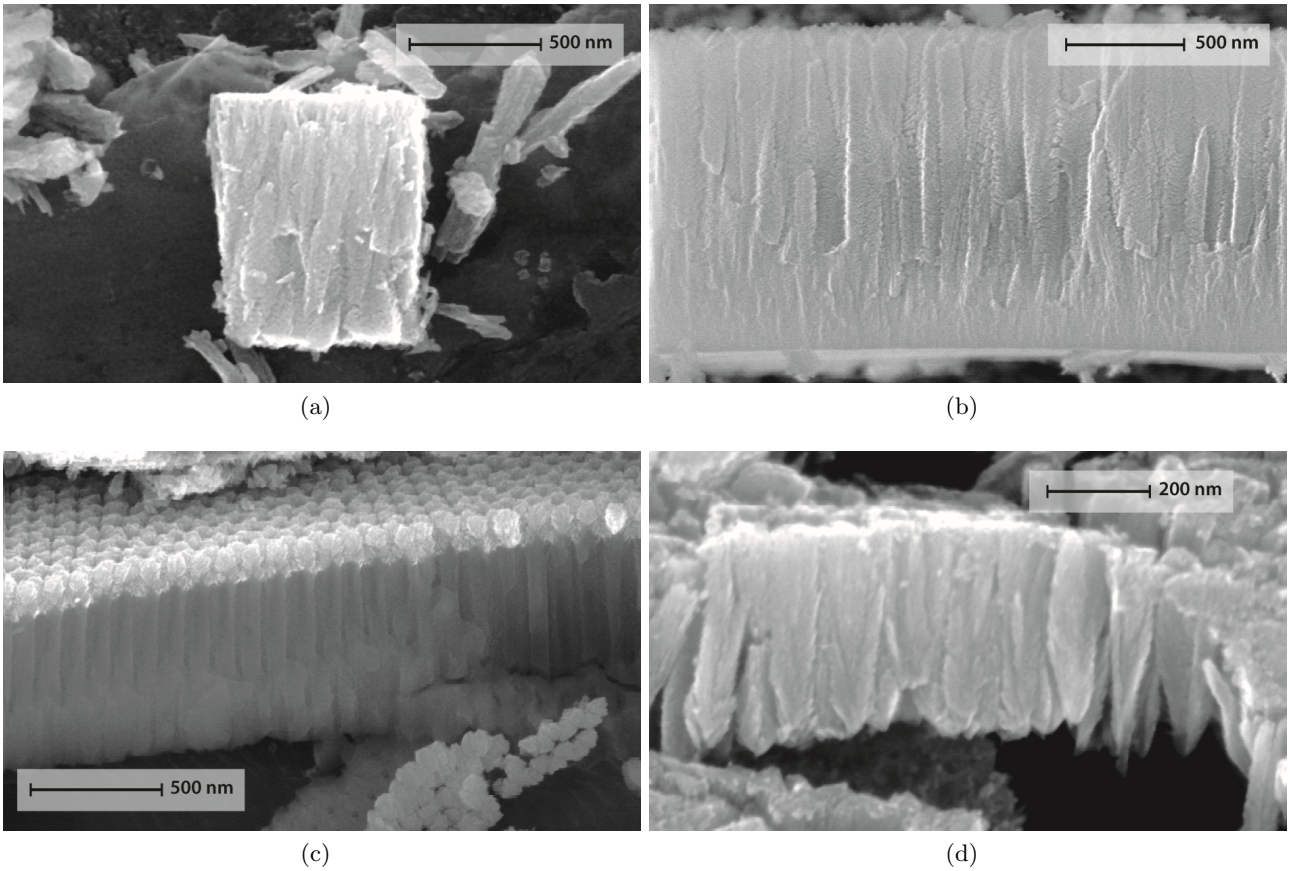

(a) (b)

(c) (d)

Figure 4.10: Cross sections of NiO films on AAM and Si substrates, showing the columnar growth. The horizontal grain competition derive in columns with V-shaped form. (a) Dense columns on a separated piece of film grown on Si, the top of the columns is sharp and cone like (b) Detail of fibrous columns on Si; close to the substrate small occluded grains are observed. (c) Initial cauliflower like grains on top of the interpore columns, which keep the porosity (d) Columns grown on AAM and separated from the AAM substrate, the V-shaped form is observed

Shadowing effect

The shadowing effect occurs often in PVD processes when non smooth substrates are used. When sputtered atoms arrive at an elevated region of the substrate and nucleate there, they receive more flux than other atoms in more depressed regions, which receive less flux. During growth this flux inhomogeneity over the whole substrate area generate more irregularities and increase the roughness, which results in structures that grow oriented toward the incoming flux. Rough substrates and impurities enhance the shadowing effect, and when the flux of arriving atoms is not perpendicular to the substrate surface but has an oblique component, this effect is even more pronounced. Shadowing effect produces more porous films with voids between the grains [88, 9].

Because of the continuous rotation of the substrates during the growth the coatings are more uniform, reducing the high impact of the shadowing effect. Although the voids and open boundaries can be avoided on smooth and planar substrates such as Si and glass, the AAM substrates present a high roughness and a columnar and porous pattern which raises the threshold at which the uniformity of the coating is achieved.

When the amount of sputtered material is large enough, the horizontal growth of the films closes the pores of the NiO coatings. Figure 4.11 illustrates a detail of a NiO film grown on AAM. A macroparticle accidentally and randomly located on the AAM surface before the deposition and removed after it leaved this interesting image: the macroparticle blocked the growth around it due to the shadow it projected onto the flux of sputtered atoms. An increasing thickness film is seen from the lower left part of the image to the upper right part until the pores are totally closed. This didactic detail confirms that the growth is columnar and that there is a limit in the vertical growth at which the porosity can not be maintained, due to the horizontal growth competition. This threshold value will be important throughout this work because it will define the main difference between the properties of coatings deposited on planar and AAM substrates.

If the rotational sample holder were not used then the coating would have a preferred microscopical growth direction which would not be vertical but with an angle easily observed through (FE)SEM. Works on obliquely evaporated films reveal that the columns are oriented toward the sputtering or vapour source. The angle between the column axis and the substrate normal (β) is universally observed to be smaller than the angle between source and substrate normal (α), which in our off-axis magnetron geometry is α=23°. These angles are connected by the empirical relation $\tan(\alpha) = 2\tan(\beta)$, commonly known as the *tangent rule* [9]. Without rotation of the substrates we would observe inclined columns with an angle of approximately 12°, at least, on smooth substrates. Angle impingement of sputtered Au films with inclined columnar structure have been presented recently in the literature [26]. On amorphous and rough substrates, such as the AAM, the columns would not grow so paralell as they appear in figures 4.6a, 4.6b, 4.10c and 4.10d because the lateral growth, which would be enhanced by the inhomogeneous flux, could close the pores at the beginning of the growth.

If instead of an off-axis geometry of the magnetron we had performed these depositions with an axial geometry, then the flux would have arrived homogeneously even without rotation of the substrates, enhancing even more the vertical growth with columnar structure. A homogeneous flux would reduce the lateral growth in favour of vertical growth, raising the threshold height at which the pores would be closed.

4.2.1. Effect of oxygen addition

Some differences in the morphology of the deposited films can be observed between samples grown with and without oxygen in the plasma. Figure 4.12 shows FESEM images of NiO films grown on AAM with different oxygen content in the plasma. Figure 4.12a corresponds to a sample grown without oxygen, and reveals irregular patterns around the pores, with sharp edges and well defined angles, suggesting a polycrystalline growth with crystals of different orientations growing

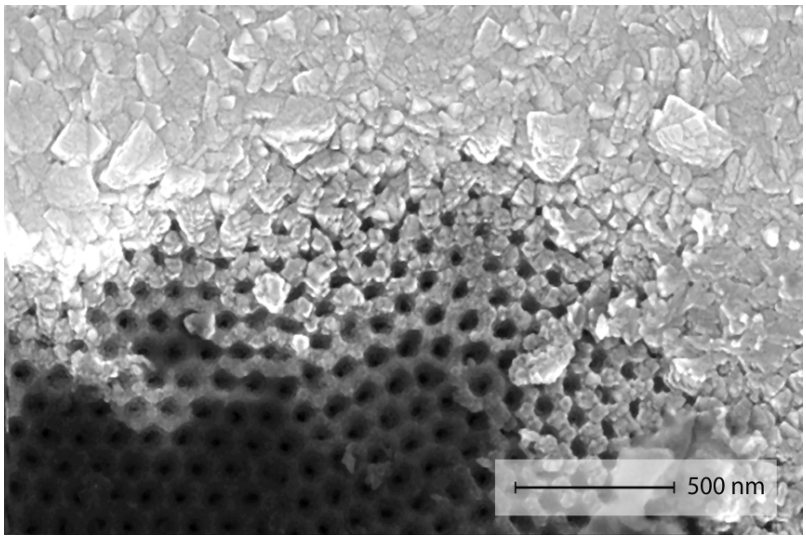

Figure 4.11: FESEM detail of the shadowing effect in a NiO film grown on AAM: due to the rotation of the substrates and the oblique flux, a macroparticle randomly located on the AAM before the deposition shadowed the arriving of atoms onto the surface. The consequence is an increase of the film thickness: from bottom-left where the AAM substrate is seen to upper-right where the lateral growth finally close the pores.

independently of each other, showing up different facets. On the other hand, coatings grown with oxygen in the plasma show a morphology with more softened and smooth edges, resembling amorphous growth, or, at least, a considerable refinement of the crystal size (see 4.12b). This effect can also be observed in the NiO thin films grown on flat Si substrates (see figures 4.20a and 4.20b). The sample grown without oxygen in the plasma shows a fine structure, with very irregular patterns, and grain size large enough to be resolved with the current microscope set-up. In subsection 4.3.1 we will discuss the reduction of the grain size observed by FESEM and confirmed by the XRD results.

However, this sharpening effect of the grains is higher for samples where the grain size has initially less competition to grow, namely the AAM substrates due to their high roughness. The sample shown in figure 4.12c has a thickness of 80 nm while that shown in 4.12d is 300 nm thick. The thicker film, where the pores are closed, presents bigger and sharper grains as compared with the thinner sample. This allows us to conclude that the amount of sputtered material, directly related to the thickness as we saw in the previous section, also produces sharp edges of the grains. This effect is enhanced for certain growing conditions, which could be related to the growth velocity and the surface energy needed to favour the lateral growth. If the film growth occurs during a long time at low deposition rates with high oxygen content, such as that shown in image 4.12c, then the crystallites seems to be smaller. In turn, films grown in less time and with higher deposition rates and with almost pure argon atmosphere, as that shown in figure 4.12d, also have faceted and sharp faces but, in this case, more disordered and with larger crystallite size. These are examples of how highly correlated are the growing parameters and the complexity of their morphology in this out-of-equilibrium synthesis technique. Z. Zhang et al. [78] have similar morphology by depositing long NiO rods by thermal heating on Si (0 0 1) substrates: they obtained cone-shaped vertically aligned columns of NiO which have similar sharp tips to the coatings of this work.

4.2.2. Porosity

The amount of arriving material onto the AAM substrate is a key parameter for keeping the film porosity. The larger the quantity deposited the smaller the pores diameter until they

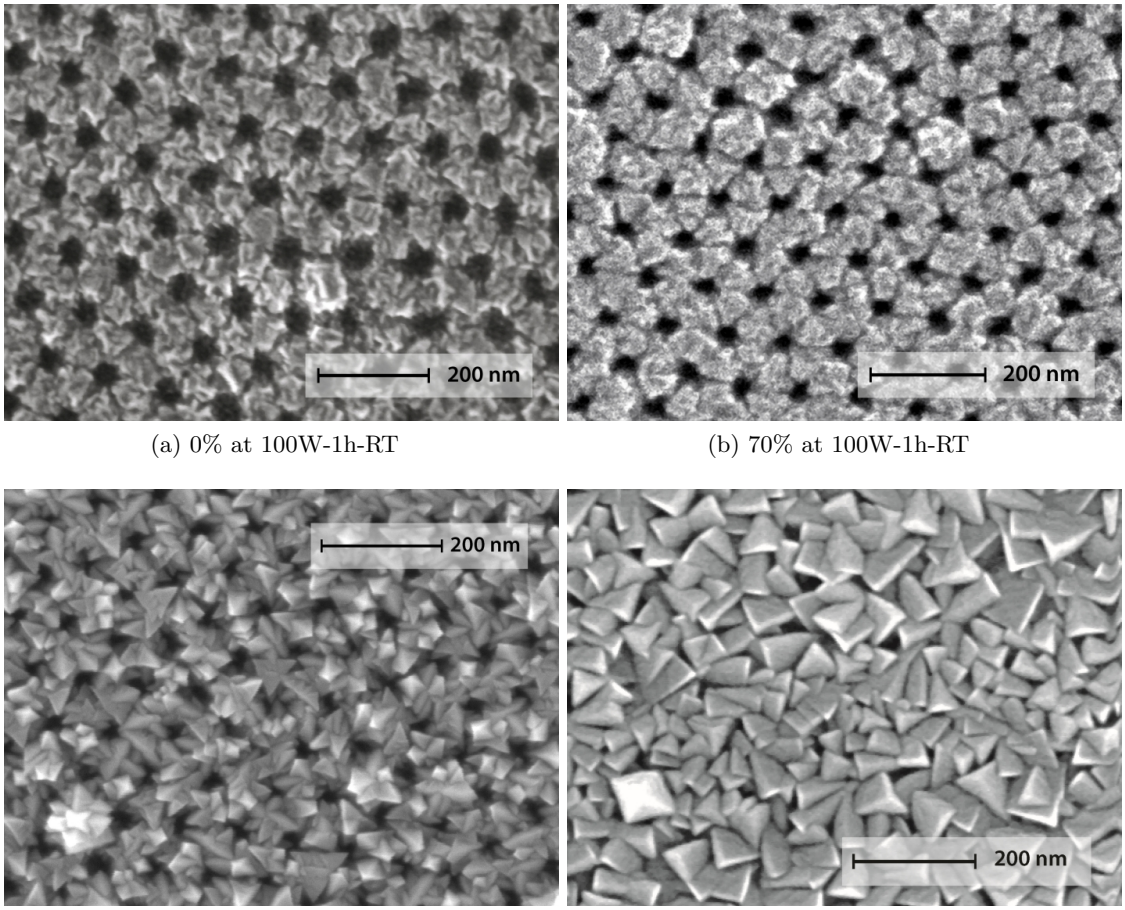

(a) 0% at 100W-1h-RT

(b) 70% at 100W-1h-RT

(c) 70% at 75W-5h-125℃

(d) 5% at 200W-1h-200℃

Figure 4.12: FESEM images of the sharp grain aspect in coatings under different process conditions. The amount of deposited material influences directly to the porosity but for certain growing conditions grains present more faceted and sharp faces. This effect could be related to the growth velocity and the surface energy needed to favour the lateral growth.

definitely close.

Figure 4.13 shows a complete set of coatings grown on AAM substrates at 100W-1h-RT, where the oxygen content increased from 0% to 80%, from a) to f). The amount of material deposited here is low in comparison with other samples but it can be observed that for the sample with 0% oxygen the porosity almost disappears while for higher oxygen concentrations the hexagonal array of pores is kept. In the sample grown with pure Ar the flux of material is higher due to the higher sputtering yield when pure Ar is used as sputtering gas, as compared to O_2-Ar mixtures. The porosity has been estimated using image processing methods with the software *ImageJ* [29] and is shown in table 4.1. The porosity of the AAM substrate was also estimated by the same method and gives a value of 13%. As indicated in table 4.1, the addition of a small quantity of oxygen to the sputtering plasma represents a step in the porosity. This kind of behaviour has been observed in our samples using other characterization techniques, where the pure argon growth is generally different to the rest of the coatings with oxygen. Therefore even the growth with the lowest amount of sputtered material reduces, as expected, the pore diameter of the AAM substrate (from 13% to 8.4%). A dependence of the porosity with the amount of material can be established from the results shown in table 4.1. It can be concluded that the thickness is a key parameter for the porosity of the film.

At the initial stages of growth NiO is deposited onto the top surface of the AAM in the

interpore area including the conical surface of the opening pores. However it can be expected that small amounts of material are deposited through the pores on the internal lateral surface of the cylinder columns, close to the pore rims. Although this was not observed in the cross-section images, it may be due to the low FESEM resolution and insulating behaviour of both the deposit and the AAM.

Pure O_2 gas produces the lowest material flux onto the AAM substrate, and therefore the thickness reaches its minimum value and the porosity its maximum. This phenomenon is observed for each set of samples where the porosity is maintained, whose deposition parameters lie below the flux threshold limit. The preservation of porosity is the most important feature of the morphology, which implies a high surface to volume ratio. This ratio is a key feature in industrial applications in which the nanostructured coatings interact with the environment. Micrographs similar to those shown in figure 4.13 have been obtained with similar morphology and similar trend in the porosity.

Until now we have shown a wide range of sputtering parameters: we have varied the magnetron power from 70 W to 200 W, the substrate temperature from RT up to 300℃ and the deposition time from one to five hours. We finally have chosen a set of parameters within the accessible range of our experimental set-up, attending morphology, structure and deposition criteria. By varying systematically the magnetron power, the substrate temperature and deposition time we will explore the properties of the films with the porosity as an important parameter. On this basis the parameters finally used for the rest of this work were: 100W-1h-RT, 100W-1h-200℃, 200W-1h-RT, 200W-1h-200℃and 200W-2h-300℃.

% Oxygen	Porosity ±0.5%	Thickness ±15(nm)
0	0.7	238
10	5.9	140
20	4.9	96
40	4.2	133
60	4.6	95
80	8.4	86

Table 4.1: Porosity for the coatings grown at 100W-1h-RT

4.2.3. Thickness

When growing thin films the thickness is a key parameter, especially in the field of nanotechnology. We speak of NiO nanostructures attending the geometrical dimensions of the coatings, which fall in the range of some tens nanometres. The thickness of our coatings range from 50 nm to 500 nm with grain size in the range of a few tens nanometres and for the case of porous films grown on AAM, the porosity falls as well in this nanometre range. Unfortunately our deposits presented often a non-uniform thickness with changing colours at different places of the sample (2×2 cm the biggest case) due to interferometric phenomena within the sample, which had a thickness gradient. However we have measured the thickness of the films using planar masks on the substrates during the deposition, which generated a well-defined step easy to be measured. For each sample several thickness profiles were measured in order to have high statistics and therefore more reliable data.

Profilometry results performed on thin films grown both on Si and glass substrates are shown in figure 4.14. It was not possible to perform profilometry on every substrate and thus some points are missed in the graphs. For each set of parameters it can be observed that the oxygen addition decreases the thickness as expected (oxygen ions decrease the sputtering yield in comparison to argon ions). The amount of sputtered material clearly increases the thickness of the coating. Figures 4.14a and 4.14c present coatings with similar thickness due to a low

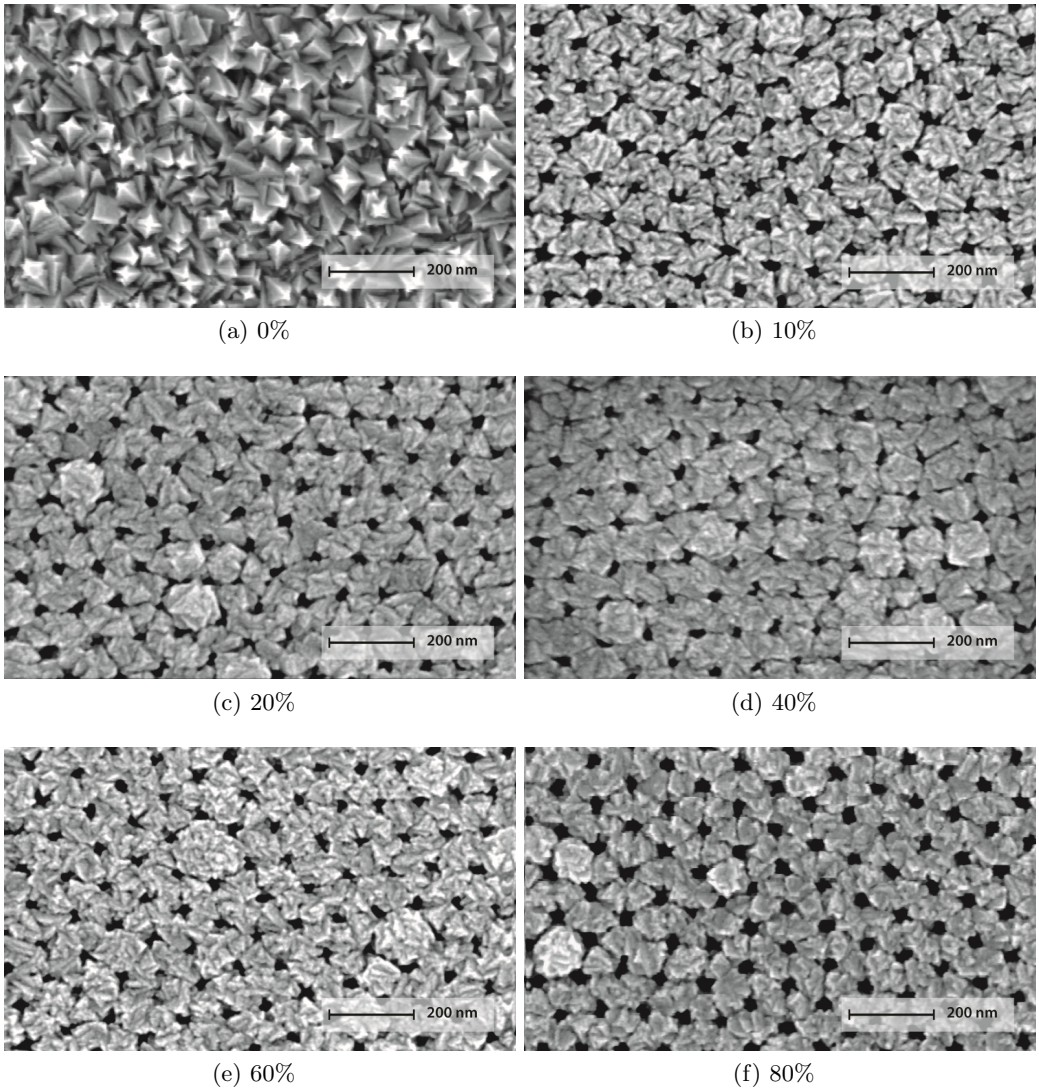

(a) 0% (b) 10%

(c) 20% (d) 40%

(e) 60% (f) 80%

Figure 4.13: FESEM images of a complete set of thin films grown on AAM at 100W-1h-RT. The oxygen content increased from 0% to 80%. The addition of oxygen to the plasma reduced the deposition rate and therefore decreased the thickness, which is directly related to the porosity.

deposition rate in which it can be observed that the addition of oxygen reduces the efficiency of the sputtering process: just a 10% oxygen in the plasma implies a reduction of the thickness down to one half of the value obtained with pure Ar plasma. At these low deposition rates, 100 W, the substrate temperature does not seem to be an important parameter for the increase of thickness. When the deposition rate is increased by applying twice the magnetron power, i.e., 200 W (sets of samples shown in figures 4.14b and 4.14d) we would expect to have twice the thickness but this is observed only for 200℃, and not for RT.

Several facts must be remarked at this point: the sputtering process, as introduced in the previous chapter, is a low efficient process in which a big amount of energy is lost in heat form. Actually, at the end of every deposit performed at 100 W of magnetron power, the non-heated substrate holder was warmed up to 80℃, and coatings grown at 200 W warmed up the substrates to 80℃, independently of the extra heating provided by the halogen lamps used to heat the sample holder. This means that when the deposition rate and the substrate temperature are high then the vertical growth is greatly enhanced, as seen in the results of figures 4.14d and 4.14e. In the case of 2 hours of growth with the maximum magnetron power the thickness is

the highest, as expected due to the total amount of deposited material and high temperature in comparison to the others deposits, as shows figure 4.14e.

Although it is possible to grow films of the desired thickness, in this work we will centre our attention in thin films in which the effects of the porosity are still distinguished. This critical thickness vary between 140 and 240 nm depending on the deposit. Thickness measurements on coatings deposited on AAM could not be achieved due to a very low signal-to-noise ratio. However, FESEM cross-section images of some coatings (see section 4.2) confirm the results obtained by profilometry.

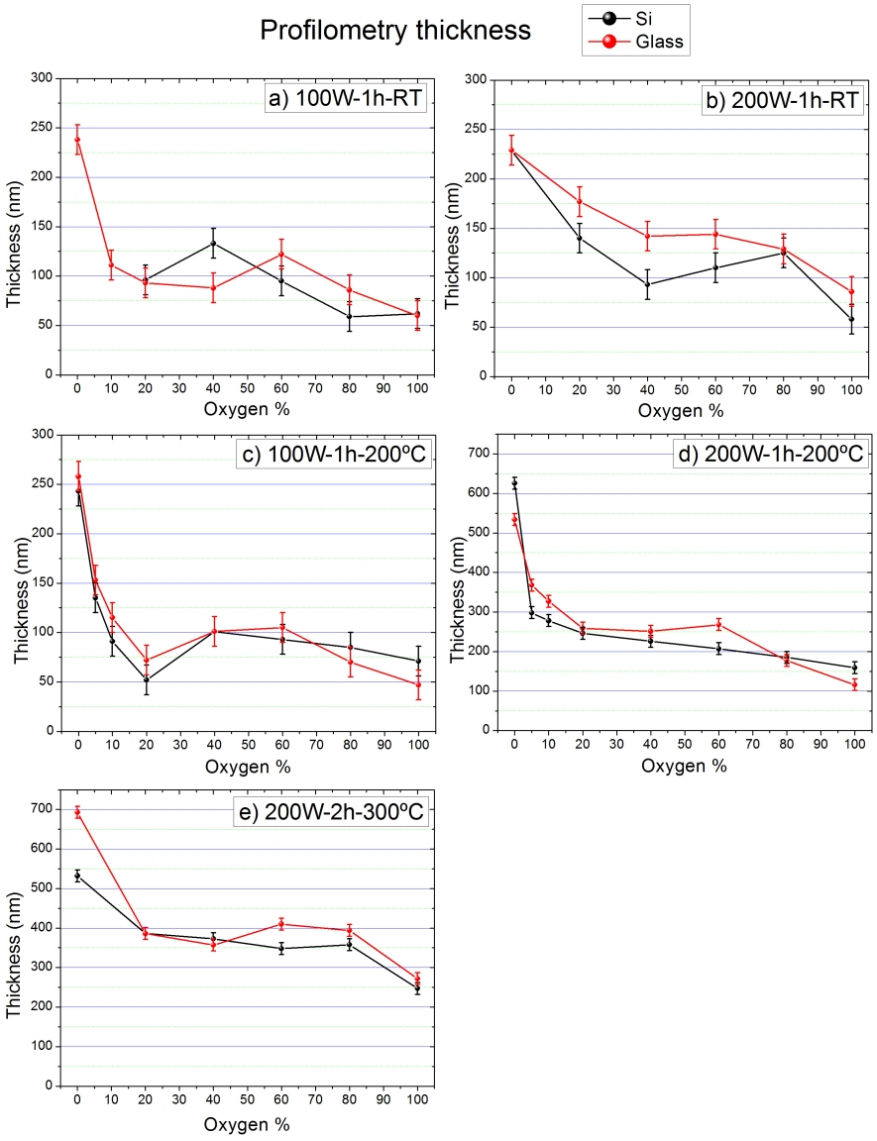

Figure 4.14: Profilometry results for the thickness of NiO thin films grown on Si and glass substrates. The different growth parameters are represented with respect to the oxygen content: a)100W-1h-RT b)200W-1h-RT c)100W-1h-200ºC d)200W-1h-200ºC e)200W-2h-300ºC. The tendency and absolute values are similar for both substrates. The oxygen content reduces the thickness of the coatings for each sputtering parameters. Magnetron power and substrate temperature affect the thickness of the coatings.

Another indirect method to estimate the films thickness is by means of Rutherford Backscattering Spectrometry (RBS). At CMAM-UAM NiO films grown at 100W-1h-RT were measured using alpha particles with 3.045 MeV kinetic energy. Figure 4.15 shows two RBS spectra for 0% and 70% oxygen content films. On top of an infinite-thick layer of Si substrate it was simulated a

layer of NiO (red line). The energy of the probe-particles was tuned at resonance with the oxygen cross-section, hence the high peak at 1.050 MeV. Heavier atoms appear at higher channels (or backscattered ion energy) thus the separation between Ni and Si is due to their difference in atomic mass number (14 amu). The estimated thickness layer is proportional to the width of the structure arising from backscattered ions due to Ni atoms within the specimen. Using the estimated cross-sections for Ni and O atoms and the density of Nickel Oxide the thickness can be known, though with a high uncertainty.

RBS measurements showed that the addition of oxygen to the plasma reduces the film thickness, as indicated by vertical dashed lines. These results confirm the profilometry measurements and the higher sputtering yield obtained with heavier argon than lighter oxygen atoms, which deposit less amount of material.

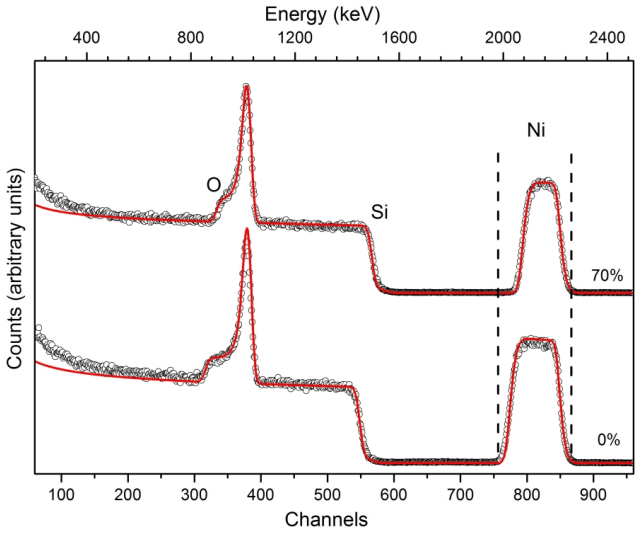

Figure 4.15: RBS spectra of samples grown with 0% and 70% oxygen content in the plasma at 100W-1h-RT conditions. The vertical dashed lines indicate the layer where the nickel is present, higher oxygen content sample has lower thickness layer. The non-Rutherford resonance with oxygen produces a very intense peak at 1050 keV.

4.3. Crystal structure

Determining the crystal structure of the thin films is essential to understand the microscopic aspects, evolution and macroscopical properties. X-ray Diffraction was used systematically on our deposited samples and served to correlate the microscopic properties with the macroscopic ones and will be a connection with the results shown in the following chapters.

The substrates used to measure with this technique were mainly Si wafers. Samples grown on AAM substrates were also measured in some cases, but the overlap of NiO peaks with the signal coming from the aluminium support prevented a satisfactory analysis. The roughness of the AAM was also a problem to measure XRD.

According to the ICSD card [76] stoichiometric NiO has a simple diffraction pattern shown in figure 4.5, where the patterns from the different sputtering targets used in this work was shown. Some deviations are usually observed in experimental diffraction patterns as compared with the theoretical ones. The most common is the increase of the width, which can be due to natural broadening, the experimental set-up (X-ray source, temperature, etc.), crystal lattice disorder, temperature effects, etc. Figure 4.16 shows two diffractograms of a NiO thin film and a high purity sputtering target. The diffraction pattern of the sputtering target gives well defined narrow peaks, indicating large grain size and ordered atoms along these orientations in

comparison to the diffractogram from the thin film, where the peaks are broader. As explained in subsection 4.1.1, an artefact from the XRD set-up generates the broad structure at 55 and the narrow peak at 54°.

Sputtering target peaks have relative intensities in accordance with the ICSD card while the thin film may not preserve that relation. This is an important fact called texture factor, which will be decisive when choosing the fitting method. The signal-to-noise ratio is a factor that determines the quality of the measurement. One of the factors that can increase the intensity is the amount of irradiated sample volume. In figure 4.16 the intensity has been normalized to compare the relative height and shape of both diffraction pattern, but in fact the signal from the target was much higher, as observed by the signal-to-noise ratio. The final shape of the peaks is due to both experimental and sample contributions. Therefore, the relative measurements between samples and a good set-up calibration will separate the different contributions from the coatings and from possible experimental artefacts.

Peak positions may change with respect to the Bunsenite reference card, which corresponds to high purity stoichiometric NiO in powder form or as a sintered target. Therefore nanostructured NiO thin film may have a different lattice parameter. After checking that the phase and peaks correspond to NiO, the lattice parameter can be calculated and the obtained variations between thin films and bulk NiO can be associated with the different sputtering conditions studied in this work. However the out-of-equilibrium technique and the highly correlated deposition parameters will increase the complexity of the diffractograms analysis.

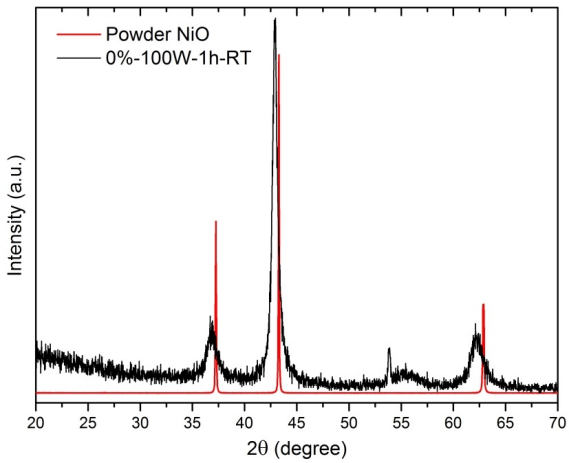

Figure 4.16: Diffractograms of a NiO thin film and a high purity NiO sputtering target. The texture factor changes the relative intensities of the peaks. The fact that the peak position do not coincide exactly is due to a variation of the lattice parameter of the fcc lattice. An artefact from the XRD set-up generates the wide structure at 55° and the narrow peak at 54°.

Before discussing the XRD results obtained we will remark here the positions of the Bragg peaks for the NiO fcc lattice. Because we measured XRD with different sources, we needed to re-calculate these positions for each wavelength: in table 4.2 theoretical reflections are calculated using Bragg's law for a face cubic lattice.

As observed in figure, 4.16 the main differences between the high purity NiO target and the NiO coating are the peak widths and the peak positions, which are caused by the crystallite grain size and the lattice parameter, respectively. We will study our nanostructured coatings by X-ray diffraction regarding these main characteristics and the relation with other properties. In this work the pressure was not varied during the growing process but T.Y.Kuo et al [24] obtained what is expected from section 3.3: a reduction of the pressure implies a higher quality in the crystalline structure.

Miller Indices (h k l)	$2\theta_B$		
	λ_{ESRF}=0.8549 Å	Cu K$_\alpha\lambda$ = 1.5406 Å	Co K$_\alpha\lambda$ = 1.7889 Å
(1 1 1)	20.40	37.23	43.51
(2 0 0)	23.60	43.25	50.68
(2 2 0)	33.62	62.83	74.49
(3 1 1)	39.65	75.35	90.43
(2 2 2)	41.49	79.34	95.68
(4 0 0)	48.29	94.97	117.73
(3 3 1)	52.94	106.89	137.74
(4 2 0)	54.43	111.00	146.27

Table 4.2: Theoretical Bragg peak positions for a fcc lattice with different wavelengths.

4.3.1. Grain size reduction

The effect of grain reduction has been previously observed by FESEM, as mentioned in subsection 4.2.1. In this section we will study this effect with X-ray diffraction for coatings grown at room temperature when oxygen has been added to the sputtering plasma. The increase of the peak width will be quantified and an estimation of the micro-crystallites size that form the grain coatings can be performed using the Scherrer relation. This technique will as well provide information about the preferred orientations, if any.

As mentioned above, X-ray diffraction data will be presented only on: Si wafer substrates. The oxygen content of the plasma is shown at the right of each curve. Figure 4.17 shows diffractograms of samples grown on Si at 100W-1h-RT, measured with Cu K source. Note that sets measured with the Cu source have a 2θ range varied between 30° and 70° while those measured with the Co source have range, between 35°and 105°, due to the fact that Co K$_\alpha$ has a longer wavelength than that of Copper, causing the Bragg peaks to be more separated and located at higher 2θ values.

The bottom curve in figure 4.17 corresponds to the sample grown with pure argon plasma, and it shows the typical features of cubic NiO, with the (1 1 1) peak at 36.8° the (2 0 0) peak at 42.9°, and the (2 2 0) peak at 62.3°. Compared with the intensity of the standard 2θ peaks reported on the ICSD card for bunsenite [76], the (2 0 0) peak has a higher relative intensity than expected, which indicates that the film growth follows preferentially this orientation. Similar behaviour has already been reported for other nanostructured NiO films [89]. The features observed in the range between 53° and 57° come from an artefact of the XRD set-up of the Cu source, as explained previously. The addition of oxygen to the sputtering plasma has remarkable effects on the structure of the grown films. First, a broadening of the peaks and a decrease of their intensity is clearly observed, the latter evidenced by a decrease in the signal to noise ratio. These changes can be associated to more disorder, smaller crystallite size, and even lattice microstrains. A second effect of the oxygen addition on the films growth is the change of preferential orientation. Already for 10% O_2, the prevalence of the (2 0 0) peak disappears, with an intensity ratio closer to standard polycrystalline NiO [76]. By increasing the oxygen content of the plasma, the (1 1 1) and (2 2 0) peaks gradually increase, while the (2 0 0) relative peak intensity decreases. The final situation, for 70% oxygen, shows a clear preferential orientation along the (1 1 1) direction. Although there are some works in the literature reporting the evolution of the crystallographic texture with the oxygen content, there is not a clear uniformity in the trends [80, 90, 91, 89, 24, 92]. In any case, it is clear that, while the columnar growth shown in figure 4.6 is kept for all samples, the crystal orientation of the columns seems to depend somewhat on the oxygen content of the plasma. The prevalence of the (1 1 1) peak for a higher oxygen ratio in the plasma is probably related to free energy considerations of the NiO growth in

an oxygen-rich atmosphere, as has been proposed in a previous work [79].

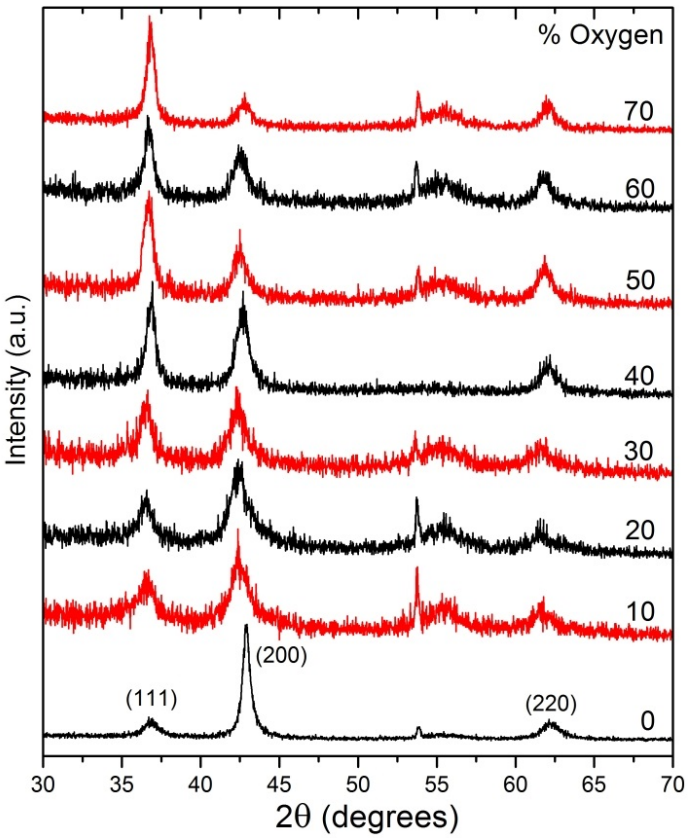

Figure 4.17: Diffractograms of the samples grown at 100W-1h-RT, measured with Cu K_α source. The addition of oxygen increases the width of the peaks (related to the disorder), the preferred orientation: from (1 1 1) to (2 0 0) and decreases the signal-to-noise ratio.

Figure 4.18 shows a detail of peak (2 0 0) for the extremes of the set grown at 100W-1h-RT. The upper curve represents the pure argon growth and the lower curve the growth with 70% oxygen content in the sputtering plasma. The solid line through the data points is the result of a standard least squares fit using a pseudo-Voigt curve. Table 4.3 shows the contribution of the gaussian width to the pseudo-Voigt curves used to fit the (2 0 0) peaks. The increase of the gaussian contribution to the total width indicates that the addition of oxygen to the sputtering plasma reduces the crystal quality. The width of a Bragg peak is affected by the natural broadening, the experimental set-up, the crystal size and the disorder of the crystal structure. The systematic study of a set of samples in the same diffractometer set-up under the same measurement conditions makes easier to quantify the crystallite size and extract conclusions of the crystal order.

The width of the diffraction peaks can be associated to the mean crystal size in nanocrystalline materials: the larger the width, the smaller the crystal size. The larger width observed for the 70% sample as compared with the sample grown with pure Ar indicates that the mean size of NiO grains in the former case is smaller than in the latter one.

The intensity of the diffraction peak for the 70% sample shown in figure 4.17 is about eight times lower than that of the 0% sample, although an arbitrary scale has been used to plot both peaks with a similar aspect, in order to emphasize their differences in width and position. This difference in intensity is evidenced, however, by the different signal-to-noise ratio of both curves. The lower intensity of the diffraction peaks for the sample grown with oxygen points out towards a lower crystal quality resembling more disordered structure.

According to the Scherrer equation [36], there is a relationship between the broadening of a

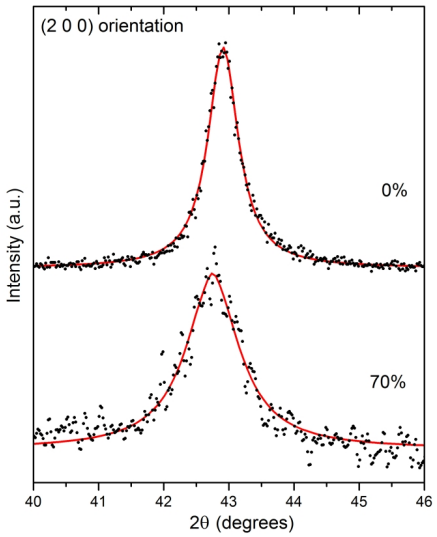

Figure 4.18: Detail of peak (2 0 0) for coatings grown at 100W-1h-RT, with pure argon and 70% oxygen. Pseudo-Voigt curve fit for (2 0 0) peak: width peak increases with the addition of oxygen and Bragg peak position shifts to lower value.

Oxygen content (%)	Width (°)
0	0.45
10	0.60
20	0.66
30	0.68
40	0.76
50	0.82
60	0.86
70	0.88

Table 4.3: Width of the gaussian contribution to the pseudo-Voigt curves used in the fittings of the XRD peak (2 0 0) in samples grown at 100W-1h-RT.

peak in a diffraction pattern and the average size of sub-micrometric crystallites, τ:

$$\tau = \frac{K\lambda}{B\cos(\theta)}$$

where λ is the wavelength of the source, K is the Scherrer constant and 2θ is the position of the diffracted peak and B is the width of the peak in radians measured at FWHM. This relation gives a number related to the distribution of length of columns composing the sample. However, this equation is a rough estimation valid only for crystallites smaller than half micron of diameter and is supported by the assumptions of a perfect crystal lattice and an incident beam composed of parallel and monochromatic radiation. This average estimation is a low boundary and it should not be confused with grain size: a particle or a grain can be made up of one or more crystallites, therefore we can no speak of grain size estimated by Scherrer but we can confirm the correlation between these two concepts. The Scherrer constant K is usually taken to be 0.9, but its value depends greatly on the crystallite shape [93]. In our study the Scherrer relation will be an estimation of the crystallite size and because we do not know the shape of individual crystallites we take the approximate value of $K = 0.94$ for spherical crystals with cubic symmetry [93]. However, it is possible to have an idea of the crystallite shape: anisotropic peak shapes can be identified by anisotropic peak broadening, if a single peak orientation broadens more than

other peaks then crystallites have that dimension reduced.

We have made use of Scherrer equation to obtain the mean crystal size of all samples grown between 0 and 70% oxygen. The results are shown in figure 4.19. In all cases, the original data were fitted using a pseudo-Voigt curve. The gaussian contribution to this curve increases with the oxygen content, which suggests that there is more disorder as the oxygen content of the plasma increases (see table 4.3). The mean crystal size for the sample grown without oxygen is about 20 nm, which is in agreement with the microstructure shown in figures 4.12a and 4.20a. As some oxygen is added to the plasma, there is a sudden drop in the crystallite size, down to 6 nm for the 10% sample. This crystal size is approximately kept constant when increasing the oxygen content in the plasma. According to these results, samples prepared in the presence of oxygen in the plasma present a considerable grain refinement. However, this trend has to be taken cautiously, since the variation is lower than the height of the error bars.

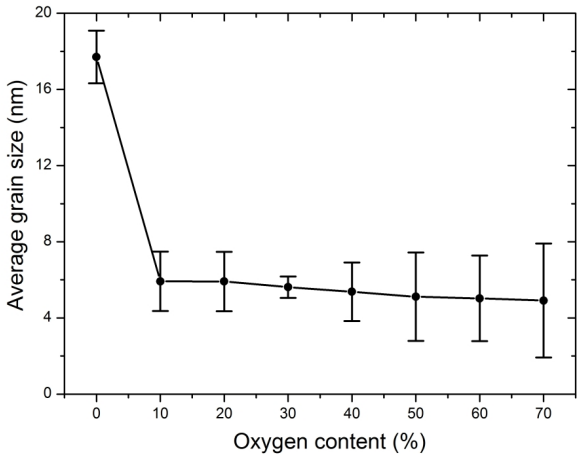

Figure 4.19: Crystallite size estimation using Scherrer relation for the NiO films grown. The size of the sample grown with pure Ar is the largest compared to other samples with any oxygen composition.

In order to know whether this grain size reduction effect is particular of samples grown at 100W-1h-RT or is a general effect we have measured other sets of samples, both by FESEM and by X-ray diffraction. conditions. In figure 4.20 FESEM micrographs of samples grown under three different deposit conditions are shown: 100W-1h-RT, 100W-1h-200℃ and 200W-1h-200℃ for different O_2 concentrations: a), c) and e) have low oxygen contents in the sputtering plasma. The low O_2 content produces larger grains than those observed in films grown with higher oxygen concentrations b), d) and f)). We can conclude that the oxygen addition not only smooths the sharp edges of the grains as seen before, but also generates smaller grains. This phenomenon is observed in every set of samples under different conditions and has been as well obtained previously by other research groups [79, 94].

Both the decrease in intensity and the increase in width of the diffraction peaks of samples grown with oxygen in the plasma suggest partial amorphization and grain refinement, which correlates with that observed by FESEM in figure 4.20.

We will now proceed to show XRD results for NiO coatings when the magnetron power is doubled: from 100 W to 200 W. Although the deposition rate increases the surface energy of sputtered atoms the surface diffusion is affected mainly by the temperature, which is maintained at room temperature. The increase in kinetic energy of the sputtered atoms seems not to change considerably the properties of the films. At 200W-1h-RT the main aspects are kept, as shows figure 4.21: in comparison to what was obtained for samples grown at 100W-1h-RT, the change in preferred orientation from (2 0 0) to (1 1 1) is more evident when oxygen is added. The intensity of the peak (2 0 0) drops dramatically when there is a small quantity of oxygen in the sputtering plasma. There is, therefore, a less gradual trend with the oxygen content. The signal-to-noise

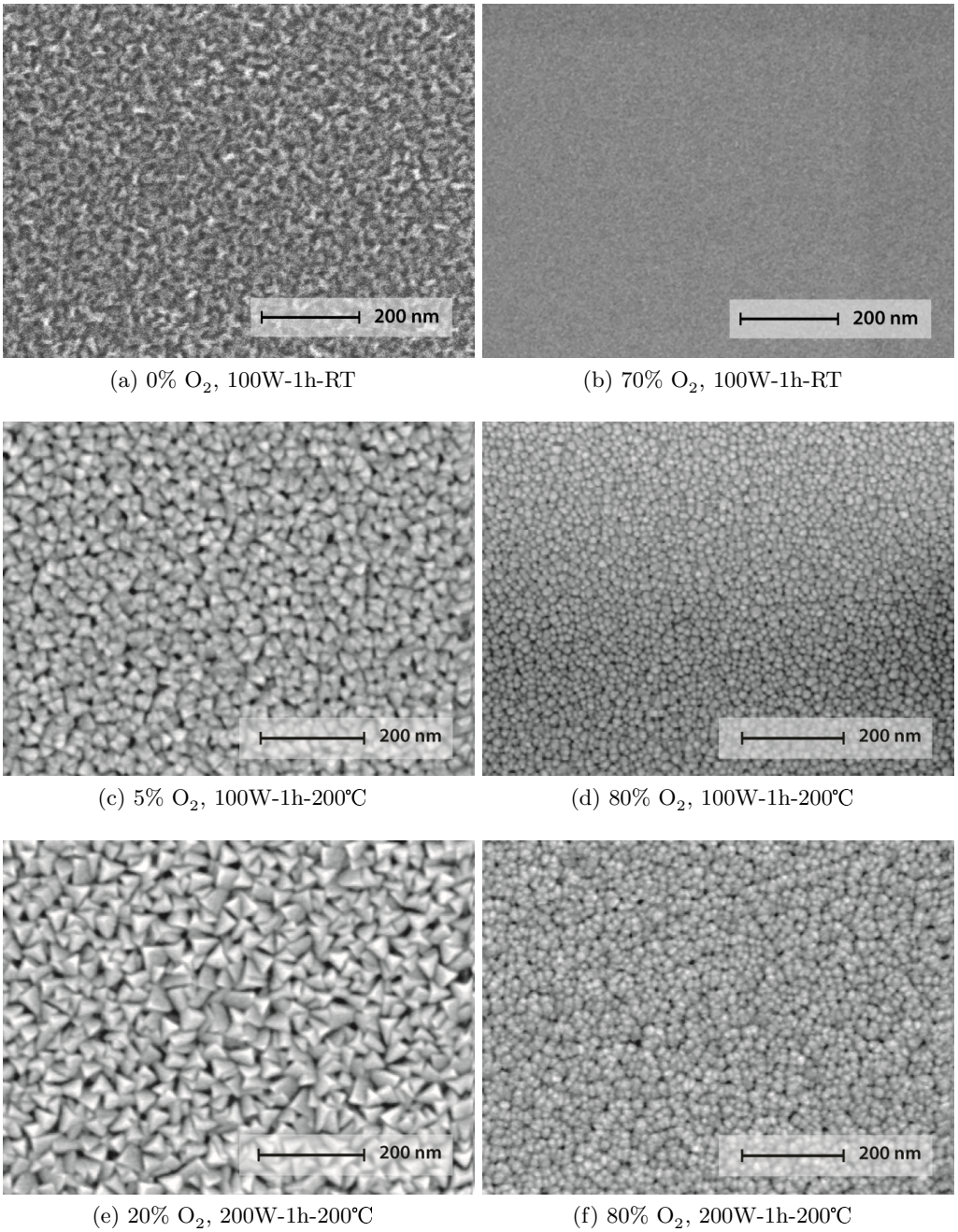

(a) 0% O_2, 100W-1h-RT

(b) 70% O_2, 100W-1h-RT

(c) 5% O_2, 100W-1h-200℃

(d) 80% O_2, 100W-1h-200℃

(e) 20% O_2, 200W-1h-200℃

(f) 80% O_2, 200W-1h-200℃

Figure 4.20: FESEM of several films grown on Si: the grain size is reduced with the addition of oxygen.

ratio is best for the initial curve grown with pure Ar plasma. This ratio is decreasing as the oxygen is added to the gas mixture, but in general the intensity of this series is higher than that observed in the diffractograms of the 100W-1h-RT series. On the other hand, the relative intensities between the different peaks in this series have the same behaviour than in the previous series. For the sample grown with pure Ar plasma the (2 0 0) peak is more intense than expected, but the addition of oxygen changes the texture from the (2 0 0) orientation to the (1 1 1) until its intensity is five times larger than the (2 0 0), while the (2 2 0) peak remains at the same level as in as the NiO reference.

Similarly to the procedure followed for the first series, we have studied in detail the peak (2 0 0) to compare the width between sample grown with pure argon and that grown with the highest

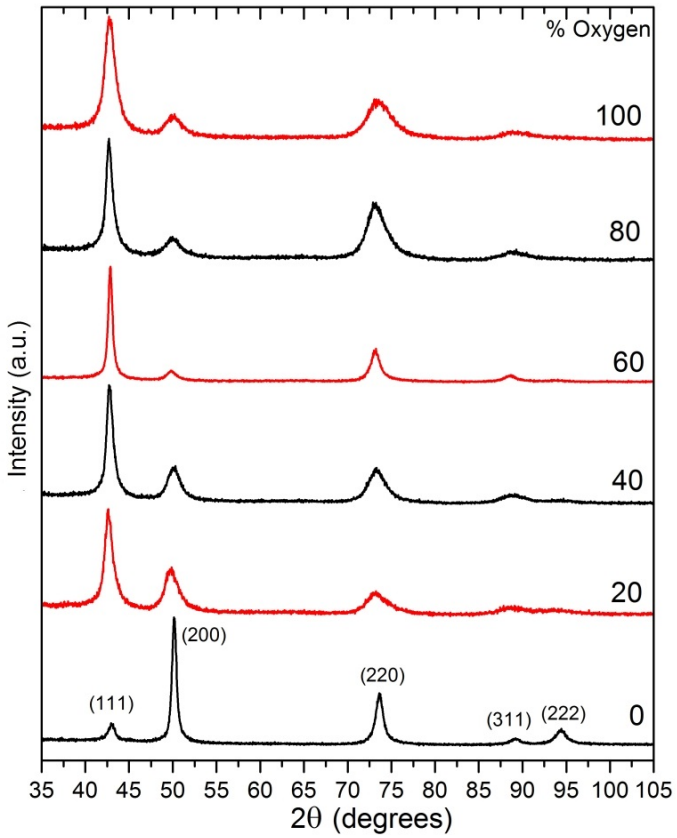

Figure 4.21: Diffractograms of samples grown at 200W-1h-RT, measured with a Co K_α source. The addition of oxygen increases both the peak width, and the preferred orientation: from (1 1 1) to (2 0 0), and also decreases the signal-to-noise ratio.

oxygen content (see figure 4.22). As expected, the peak width increases with the oxygen addition, as shown in the figure 4.22a. The signal-to-noise ratio is also reduced and the width is greatly increased. Additionally, a shift to lower values in peak position is observed as well. The red line represents the pseudo-Voigt curve obtained from the data fitting, from which an estimation of the crystallite size can be performed, through the Scherrer relation. The corresponding average crystal size for all oxygen contents is shown in figure 4.22b and, similarly to previous results for the 100W-1h-RT series, the pure argon growth is quite different to samples grown with any oxygen content in the plasma. For these coatings grown at 200W-1h-RT the tendency is the same: the larger crystallites are those of the sample grown with pure Argon, but in this case their average value is 50 nm, three times larger than that obtained for the sample grown with pure Argon and with 100W of magnetron power. When exploring the grain size with FESEM it can be observed that the oxygen addition confirms this grain size reduction, as shown in figure 4.23.

4.3.2. Lattice parameter

Additionally to the mentioned changes in the diffraction patterns, a slight shift of the peaks towards lower angles for higher oxygen content in the plasma can also be observed, which suggests an increase of the lattice parameter. This can be observed in the position of the (2 0 0) peak for samples grown with high O_2 content in figures 4.18 and 4.22a, which differ from the position of the same peak for samples grown with pure Ar. This effect has been reported in previous works [58, 95] and can be associated to a distortion of the lattice induced by an excess oxygen.

A quantification of the X-ray diffractograms can be performed using refinement methods. Through this calculations the lattice parameter of the Nickel Oxide Rocksalt structure can be obtained and correlated with the growth parameters.

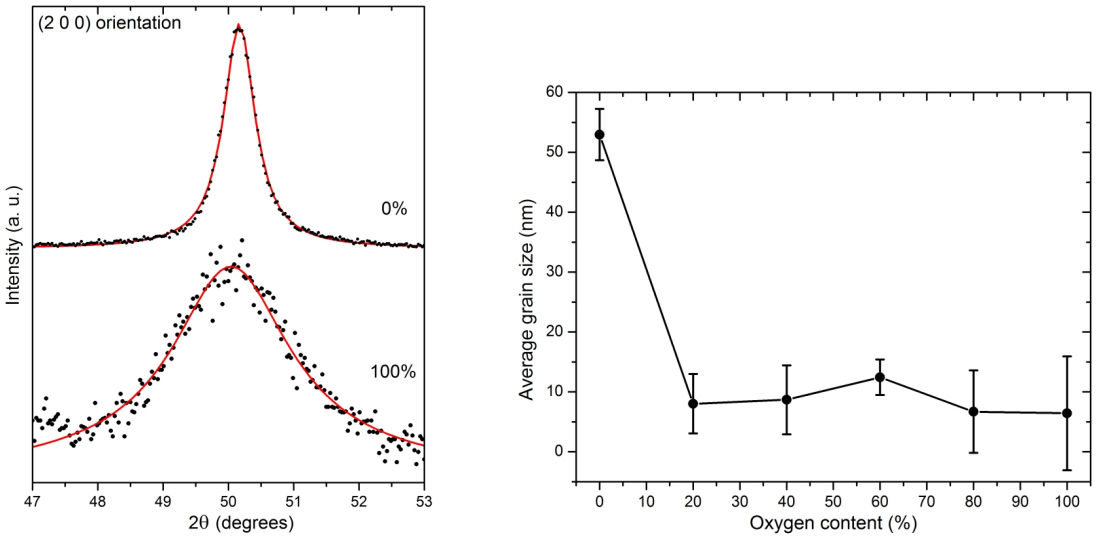

(a) (b)

Figure 4.22: (a) Detail of the (2 0 0) diffraction peak for samples grown with pure Ar and with the highest oxygen O_2 concentration in the plasma. The signal-to-noise ratio decreases with the addition of oxygen and the peak width clearly increases, the pseudo-Voigt fit is represented in red line. (b) Larger crystallite size estimation using Scherrer relation. At these growth conditions the average size is larger than for 100 W.

In order to refine the observations of X-ray diffraction, a profile fitting method was performed by using the software *Diffrac. Suite TopAs* [96]. Among the different strategies to analyse diffraction data Pawley, Le Bail and Rietveld methods are the most known, but its use depends on the information about the sample and the quality of the data [35].

By performing a Pawley refinement (see section 3.4.4) we have obtained the lattice parameter for films grown on Si at room temperature (100W-1h-RT and 200W-1h-RT), as shown in figure 4.24, where the lattice parameter of standard polycrystalline NiO (a = 4.177 Å [76]) is also shown for comparison. In the 100W-1h-RT series the value obtained for the sample grown under pure Ar atmosphere is slightly larger than that of the NiO reference, suggesting a small lattice expansion for this sample. The expansion increases with the oxygen content of the plasma, although this increase slows down at higher oxygen contents. A similar increase of the lattice parameter with the oxygen content of the plasma has already been observed in previous works [97, 89, 95]. This lattice expansion, together with the lattice disorder coming from the increase in peak width, as explained in the previous subsection, might be originated by an excess oxygen in the NiO lattice, which, in turn, affects the grain evolution from the first growth stages. This lattice expansion takes a maximum value of about 2%. When increasing the magnetron power to 200W the lattice parameter has a higher value for the sample grown with pure Argon but still the oxygen addition produces a further increase of the lattice parameter. These films grown at 200W appear to have a saturated value of the lattice parameter with only 20% of oxygen content in the plasma while samples grown at 100W need 40% oxygen to reach those values. Although the fitting error is low, as it is shown in figure 4.24 with the corresponding error bars, this is a mathematical error estimation provided by the fitting software. The highly correlated parameters of the magnetron sputtering technique do not allow us to conclude a direct relation between the magnetron power used and the variation of the lattice parameter. When depositing with 200W of magnetron power the heat caused by the plasma, raise the substrate temperate to about 80°C. Therefore it is not straightforward to estimate the error in the lattice parameter calculation. We will discuss later the convenience of this fitting approach when discussing other results.

The different contributions to each peak in a diffraction pattern come from different crystallites,

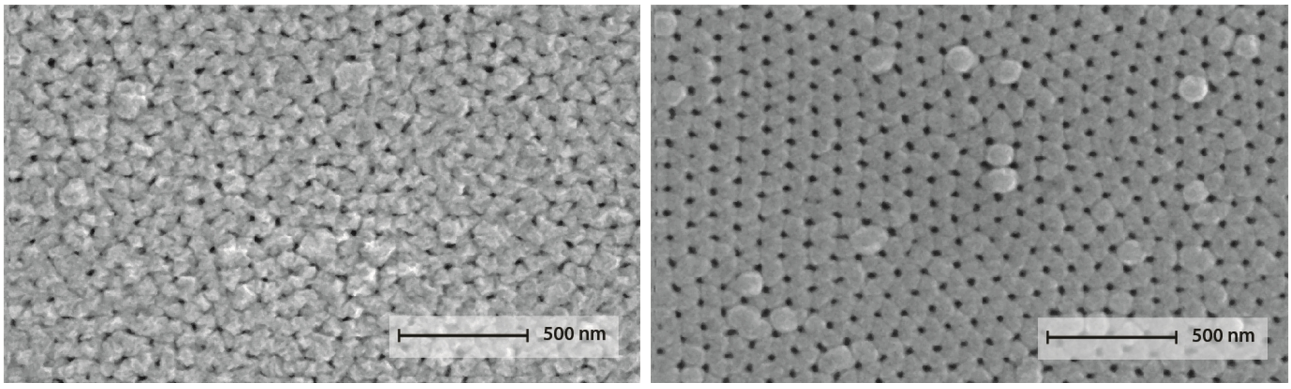

(a) Pure Argon growth (b) Pure Oxygen growth

Figure 4.23: FESEM images of samples grown under 200W-1h-RT conditions on AAM substrate for pure Ar and pure O_2 plasma. The grain size is reduced when oxygen is used in the sputtering plasma: the amorphization is higher and the facets are smoother.

whose crystal planes are parallel to the surface. Hence, the addition of Oxygen, which decreases the grain size and, subsequently, the number of planes, produces broader peaks in the diffractogram. Microstrain can affect only to one crystallographic direction and, therefore, affects only to one peak. The disorder created due to vacancies in the lattice affects to the diffraction profile at determined Bragg peaks: only those planes with higher amount of vacancies. A vacancy will also contribute to the lattice strains.

When comparing the calculated peaks with the experimental profile it can be observed that the theoretical peaks are narrower, as is evidenced by the difference curves (painted in blue) of figure 4.25a. These difference curves result from the subtraction of the calculated profile from the experimental one. The red line in figures 4.25 and 4.26 correspond to the result of the fitting, including the simulated lattice and the background. The simulated lattice is represented in green in figure 4.25, corresponding to an fcc lattice (4.25a) and to a rhombohedral lattice (4.25b). In figure 4.26, three different fcc lattices were included in the simulation. In general, diffraction peaks are slightly asymmetric, indicating that each peak has at least two contributions. Consequently, only one fcc lattice is not enough to correctly fit the experimental values, as evidenced by the difference curve. Therefore the observed structural broadening cannot be associated only to grain size effects or microstrain of the cubic crystal lattice.

The experimental peak broadening and the observed asymmetry can be simulated by including two or more ovelapping lines associated to the crystal lattice in the fitting. Additionally to the cubic phases, there is a non-cubic phase that is commonly found in NiO: a rhombohedral phase [98], $R\overline{3}m$ (166) with lattice constants: $a = 2.95\,\text{Å}$ and $b = 7.23\,\text{Å}$. This phase is a slight distortion of the cubic phase, has the diffraction planes at a very close position to those of the fcc lattice and, hence, its determination is quite difficult, but plausible to fit our experimental diffractograms. I. Hotovy *et al.* [99] claim to have found such phase after unsuccesfully trying to fit their data with a fcc NiO phase. In any case, probably due to the high similarity between the diffraction pattern of both phases, the literature about this Rhombohedral in binary Nickel Oxide is a minority. In our case, the goodness of fit using one fcc phase of this fit is 1.72, with a lattice parameter of $a = 4.1946(2)$ Å while using a rhombohedral phase gave a goodnes of fit of 1.48 (the fit improved) and the lattice parameters of the primitive cell were: $a = 2.969(1)$ Å and $c = 7.258(4)$ Å, which is a difference of 0.5% with respect to the ICDD card for NiO [98]. In table 4.4 the positions and relative intensities of the face-centred cubic and rhombohedral primitive cells and the relative intensities are shown, calculated for a Cu K_α source. It can be seen that the rhombohedral phase, which is only a slight distortion from the cubic cell, can

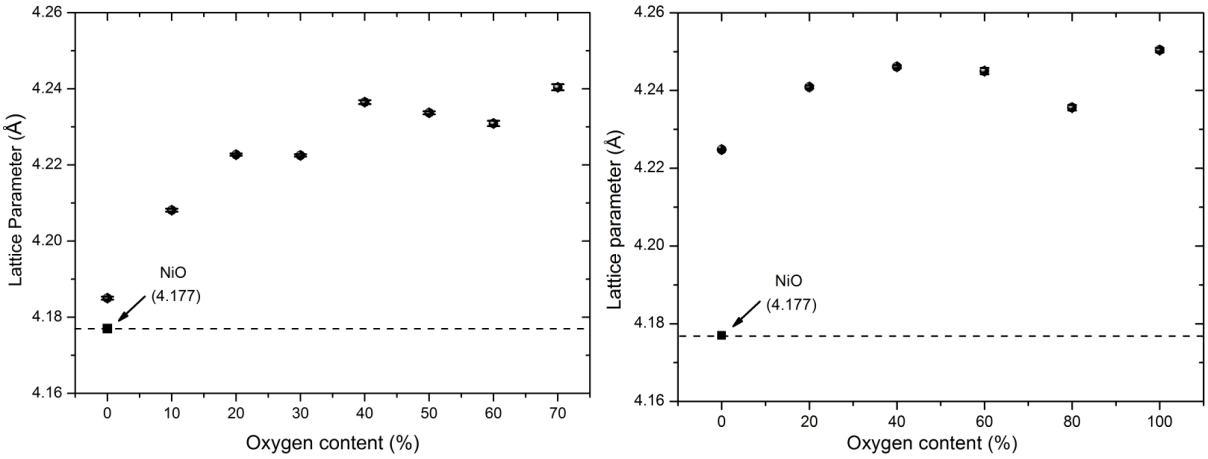

(a) 100W-1h-RT (b) 200W-1h-RT

Figure 4.24: Lattice parameter calculated by the Pawley method for coatings grown at 100W-1h-RT and 200W-1h-RT on Si substrate. The line indicates the lattice parameter of stoichiometric NiO [76]. The addition of O_2 implies a gradual increase of the lattice parameter.

easily be mixed up when performing a fitting, especially using the Pawley method, in which the structure factor is not used. Anyway, the differences between both the positions and the intensities of both cubic and rhombohedral phases are very small, so the reasons to decide to use both phases in the fit must be based on a previous knowledge of the sample and other experimental results that indicate another plausible explanation. The Néel temperature (T_N) for Nickel Oxide is 573 K. Above this value the antiferromagnetic NiO becomes paramagnetic. Below T_N the magnetic ordering consists of ferromagnetics sheets of spins in (1 1 1) planes which are antiferromagnetically stacked along the [111] directions [100]. This magnetic ordering creates a rhomdohedral distortion, which contracts the cubic cell along [111] direction resulting at room temperature a variation of cell angle from 90° to 90° 4', as measured by M.T.Hutchings *et al.* in 1972 by inelastic neutron diffraction [100], and confirming previous results from W.L. Roth *et al.* in 1958 [101]. Few authors claimed to have found a rhombohedral phase, and those who found it always used neutron diffraction [102].

Cubic cell			Rhombohedral cell		
(h k l)	$2\theta_B(°)$	I/I_0	(h k l)	$2\theta_B(°)$	I/I_0
(1 1 1)	37.2476	61	(1 0 1)	37.2481	60
(2 0 0)	43.2748	100	(0 1 2)	43.2859	100
(2 2 0)	62.8776	35	(1 1 0)	62.8524	30
(3 1 1)	75.4141	13	(1 0 4)	62.9122	25
(2 2 2)	79.4066	8	(1 1 3)	75.4036	14
(4 0 0)	95.0554	4	(2 0 2)	79.3719	9
(3 3 1)	106.9887	3	(0 0 6)	79.5015	4
(4 2 0)	111.1184	7	(0 2 4)	95.0518	6

Table 4.4: Positions, indices and relatives intensities of the cubic and rhombohedral Nickel Oxide, according to the ICDD cards [76, 98]. Bragg positions are calculated for Cu K_α (λ=1.5406 Å).

As clearly shown by the difference curve in figure 4.25, the rhombohedral phase fit is an improvement. However, some evidences from FESEM and XRD results suggest that there may be

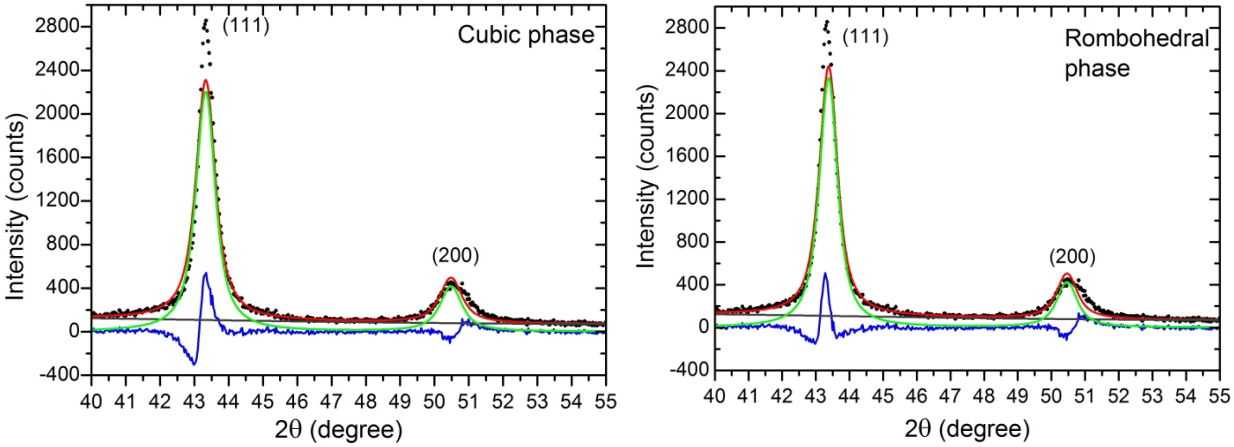

(a) Cubic phase fit

(b) Rhombohedral phase fit

Figure 4.25: Pawley fittings performed on 0%-100W-1h-RT for one cubic (a) and one rhombohedral lattice (b). Only one fcc phase is not enough to fit the asymmetric peaks (see difference curve in blue). The rhombohedral phase improves the fit, although based on literature references is less plausible.

more than one fcc phase for the crystallites close to the substrate, which represent an important contribution to the diffraction profile when the thickness is low. When the films have higher thickness it seems that the larger grains, as explained in section 4.2, accommodate themselves reducing the microstrain and therefore the lattice parameter converges to its standard value. These arguments lead us to propose an alternative explanation for the profile broadening: A mixture of two or more fcc phases with different lattice parameter. This would be the case for NiO phases of different atomic compositions, out of the stoichiometry. To clarify this hypothesis a Pawley fitting was performed with two or even three fcc phases. This is shown in figure 4.26 for the same coating as previous fittings (see figure 4.25). Now the difference curve is reduced, achieving a goodness of fit of 1.08 with three cubic lattice parameters in incremental values: $a_1 = 4.185(2)$Å, $a_2 = 4.1938(9)$Å and $a_3 = 4.205(3)$Å. Mathematically, the more phases included in the calculation make the fit better, reducing virtually to zero the difference curve. However, the resolution of a well aligned diffractometer allows to resolve two overlapped Bragg peaks of similar intensity provided that their position is separated about one fourth or one half their FWHM. Here a physical interpretation must be taken into account: if a variation of the grain size with the thickness is expected, being the grains closer to the substrate those with higher strain and more distorted, then the lattice parameter will be different. The solution is to consider two or more phases in a compromise method to enclose all the lattice parameter possibilities within certain boundaries. The use of only one fcc phase, as shown in figure 4.24, serves as an approximative idea of the average lattice parameter of a coating due to the fact that the error estimation will be higher than using several fcc phases.

Following this strategy we performed Pawley fittings to the x-ray diffraction results of the measured samples under certain growing parameters with a variation of the oxygen content from 0% to high values (70% or 100%) in order to compare the average lattice parameter calculated with one or more fcc phases.

The lattice parameter is a key parameter of this Pawley calculations, therefore we will centre our attention on its evolution within each sputtering condition and the relevance of the oxygen addition to the sputtering plasma. It must be remarked here that the lattice parameter of standard polycrystalline NiO is $a = 4.177$ Å [76].

To check whether the structure of the NiO coatings depends on the distance to the substrate, we need XRD measurements measurement sensitive to the different structures along the thickness.

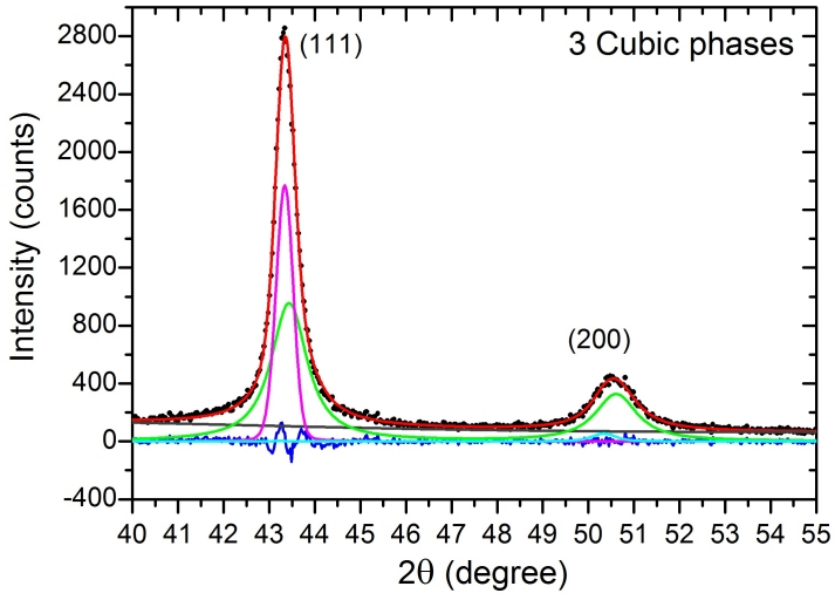

Figure 4.26: Pawley fittings performed on 0%-100W-1h-RT sample with three fcc lattices. The difference curve is now reduced in comparison with fitting with only one fcc phase or one rhombohedral phase. Based on the growth dynamics model we can explain the presence of three NiO fcc phases with increasing lattice parameter. This behaviour is enhanced for samples with low thickness, while for thicker samples the microstrains relax, which makes the lattice parameter converge to higher values.

Grazing Incidence X-ray diffraction measurements (GIXRD), with variable probing depth, can give this information. GIXRD measurements were carried out at ESRF with $\lambda = 0.8257$ Å for coatings grown at 100W-1h-RT. The incidence angle, μ, was explored within the range 0.1° to 2°. As was explained in chapter 3, the probing depth of X-rays on stoichiometric NiO is only of about 3 nm for the lowest μ value of 0.1°, while for 2° the probe depth is more than 400 nm, that is, for this angle the whole thickness is explored. In figure 4.27 we show a detail of the diffractograms obtained for two NiO coatings with low and high oxygen content 20% and 70%, respectively. Only the peak (1 1 1) is shown to appreciate the slight shift of the peak position to lower values of 2θ as the probing depth increases. There are two factors that contribute to the shift of the peak location: the already mentioned shift due to the increasing oxygen content in the plasma and the one observed when different incident angles are explored. The vertical axis indicates the counts collected for each curve, in which it can be seen that the higher oxygen content has lower intensity, that is a lower signal-to-noise, as observed previously. For more surface sensitive values the peaks are located at higher Bragg positions, 19.67° for 20% and 19.5° for 70% while more penetrating incidence angles shift the position to lower values: 19.47° for 20% and 19.2° for 70%. In both cases the decrease in Bragg angle is between 0.2° and 0.3°. According to Bragg's law the lower 2θ indicates higher lattice parameter. The variation of 0.3° observed in figure 4.27, for the wavelength of the experiment and the cubic phase of the Rocksalt structure corresponds to a variation of 0.006 Å in the lattice parameter.

These GIXRD results confirm our hypothesis of higher lattice parameter for the lowest layers of the NiO coating. The crystallites closer to the substrate, due to the horizontal competition and strain accommodation, have higher lattice parameter. This means that more than a monomodal distribution of crystallite size exists in the thin films: more than an average crystallite size coexist in the NiO coating, having a gradient of the lattice parameter with the thickness of the film. This supports the hypothesis of more than a face centred cubic for NiO as discussed previously. Considering more than one fcc phase for the coatings we will perform fittings in order to obtain the average lattice parameters resulting from Pawley method.

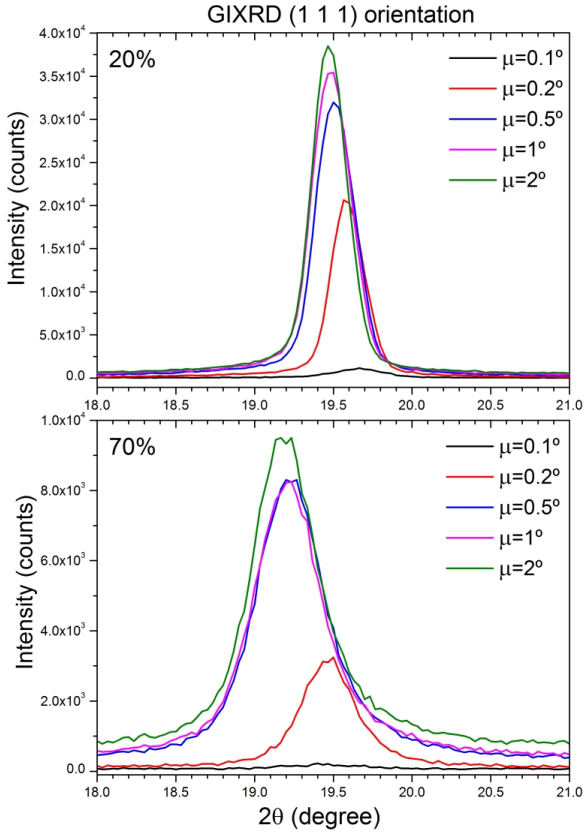

Figure 4.27: GIXRD for 20% and 70%-100W-1h-RT samples grown on Si substrates for different incidence angles μ. Only the orientation (1 1 1) is shown. The lowest incidence angle is more surface sensitive (about 5 nm probe depth), while μ =2° values explore more than 400 nm. For each curve the higher incidence angle gives a peak position which shifts to lower values, which indicates a larger lattice parameter for regions closer to the substrate than near the surface. For both curves the total shift is about 0.3°. The oxygen content contributes to shift to lower values of peak location, as discussed earlier.

Taking into account the possibility of having more than one Rocksalt phase for NiO within the coatings structure we can calculate the lattice parameter of the thin films using the Pawley method. As explained before, Pawley method suits better for our purpose regarding the quality of the experimental data, the low number of peaks to fit (only those arising from the Nickel Oxide) the changes in the texture factor and the fact that the crystal lattice can be distorted, which generates asymmetries in the peaks.

Using two fcc NiO phases calculated with Pawley method for samples grown at room temperature (100W-1h-RT and 200W-1h-RT) we can calculate the difference between these two phases. Figure 4.28 shows this difference in the lattice parameter obtained for samples grown at room temperature. The variation of the lattice parameter with the film thickness represents a gradient of the distortion and lattice disorder. According to our growth model proposed in subsection 4.2 the average crystallite size has a higher statistical deviation for initial grain stages, close to the substrate (see figure 4.27). The crystallites which build up the grains have higher strain at the beginning of growth but a new parameter is introduced: the oxygen composition of the plasma. We have shown previously that the oxygen addition reduces the grain size and increase the strain and disorder (as observed through the widening of the peaks). This increasing oxygen composition of the plasma will therefore increase as well the lattice parameter of the crystallites enhancing the bimodal distribution of average sizes and estimated inter-atomic distances. Although the error bars are high in both calculations of figure 4.28 the

general tendency is an increase of this difference between phases when the oxygen is increased in the plasma.

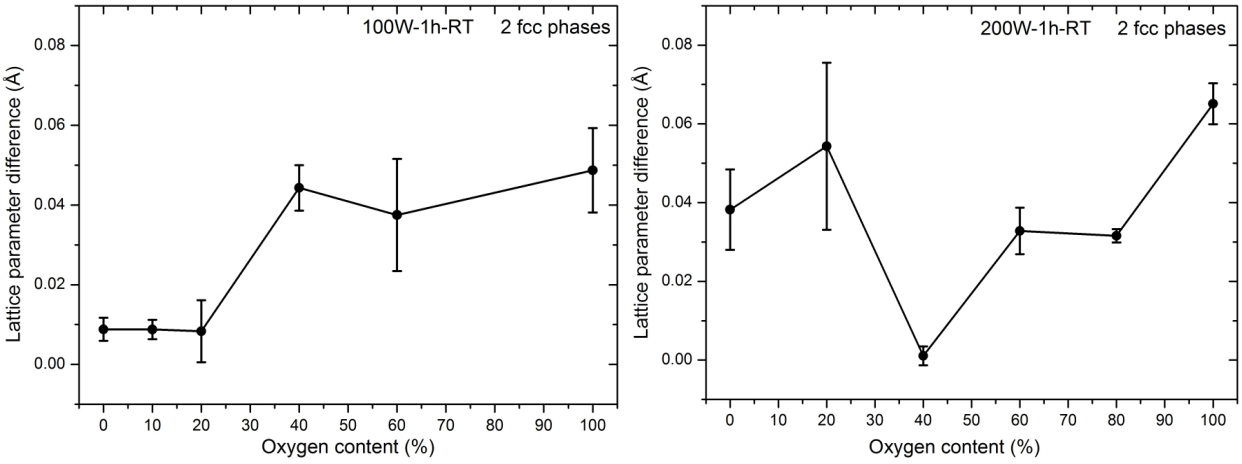

(a) 100W-1h-RT (b) 200W-1h-RT

Figure 4.28: Difference of lattice parameter between the two Pawley calculated fcc phases in coatings grown at RT on Si substrates. The O_2 content enhances the disorder and strain and this could be correlated with a difference in lattice parameter between the two calculated distributions.

This lattice expansion, together with the increase of the disorder is an important effect of the oxygen addition to the plasma which will be confirmed by other characterization techniques and will have macroscopical consequences, as will be explained in next chapter.

4.3.3. Effect of substrate temperature

Temperature is an important parameter for understanding the growth process. Several coatings were grown under process conditions where the substrate temperature was 200℃. We expect some variations with respect to the growth at room temperature, although this temperature is still low for activating processes such as bulk diffusion or for enhancing surface diffusion.

At room temperature, a change in texture from the (2 0 0) to the (1 1 1) directions was observed when the oxygen content in the plasma was increased. We did the same experiment for samples grown at 200℃. The results are shown in figure 4.29, where the diffractograms of all films measured on Si substrates can be seen. Note that (a) represents 100W-1h-200℃ samples, which were measured using a Co source, while (b) represents 200W-1h-200℃ samples, measured with a Cu source. The bottom curve for each set belongs to the sample grown with pure Ar and the oxygen content is increased in the curves from bottom to top. In both sets of samples the trend of the preferred orientation is different to that observed at room temperature. For the coatings grown at 100W-1h-200℃: the (2 2 0) intensity dominates for pure Ar, while the addition of oxygen promotes a change in orientation towards the (1 1 1) direction at low oxygen contents. When more oxygen is added, the polycrystalline thin films do not have a clear preferred orientation, being the three main peaks (1 1 1), (2 0 0) and (2 2 0) of similar intensity.

When the magnetron power is doubled to 200 W at this substrate temperature, the tendency is different. The sample grown with pure Ar has a texture along the (1 1 1) direction, but the oxygen addition at intermediate levels changes this preference to a coexistence of the three main peaks, with more intensity for the (1 1 1) and (2 0 0) directions. However this crystalline behaviour recovers the predominance of the (1 1 1) texture for sample grown with pure oxygen. Despite this similarity in texture between both samples grown with pure argon and pure oxygen, the latter one shows a lower signal-to-noise ratio and broader peaks.

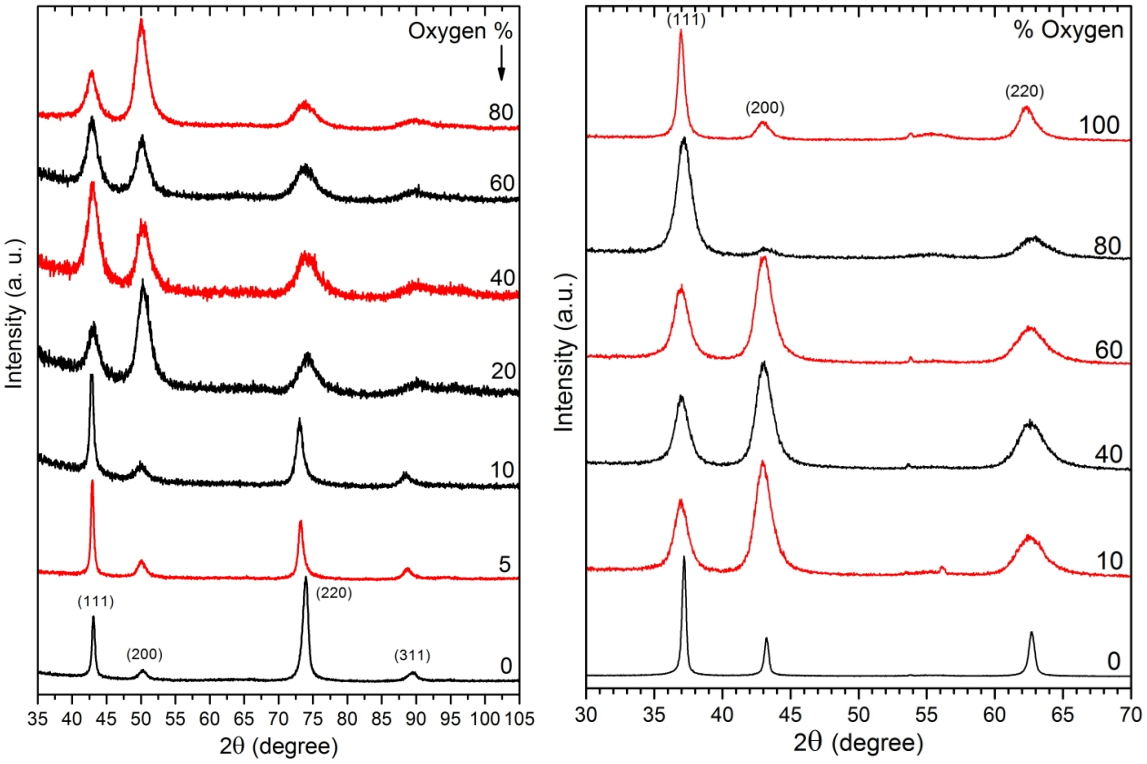

(a) 100W-1h-200℃ with Co source

(b) 200W-1h-200℃ with Cu source

Figure 4.29: Diffractograms of films grown at 200℃ of substrate temperature on Si substrates: (a) samples grown at 100W-1h-200℃, measured with Co source, (b) samples grown at 200W-1h-200℃, measured with a Cu source. The change in texture is not gradual and the influence of oxygen is different for each condition. Any oxygen addition changes rapidly the texture and a coexistance of two preferred orientations can occur.

This broadening of the peaks and decrease in the signal-to-noise ratio when increasing the oxygen content can be observed in both series, and was also observed for samples grown at room temperature. As mentioned previously, both properties indicate a higher disorder and a lower crystallite average size. The broadening of the peaks is shown in detail in figure 4.30 for the (1 1 1) peak for both series of samples grown at 200℃ substrate temperature. As observed in the two peaks of samples grown with pure Ar, the intensity is higher, and the FWHM lower than peaks of samples grown with high oxygen content. This is in agreement with the grain size reduction shown in figure 4.20 for samples grown at room temperature, where the oxygen addition clearly affects these parameters.

4.3.4. Surface Energy

P. W. Tasker [103] proposed in 1979 a classification of the ionic crystal planes regarding its electrostatic distribution: if an electric dipole exists perpendicular to the surface the Madelung cohesive energy summations diverge and theoretically such distribution of ions in a plane should not exist. Tasker mentioned the case of the ionic crystal Nickel Oxide for which the planes (1 0 0) and (1 1 0) are classified as type-1: neutral planes with zero net charge. Planes (1 1 1) are classified as type-3: formed of a stacking sequence of negative and positive planes which produces a non-vanishing electrostatic field due to the presence of a dipole moment in the repeat unit, remaining a polar plane. These type-3 surfaces can occur in a crystallite through external reconstruction or adsorption of extra charge. These out-of-equilibrium conditions are met in the magnetron sputtering technique. However A. Barbier et al [104] confirmed the possibility of

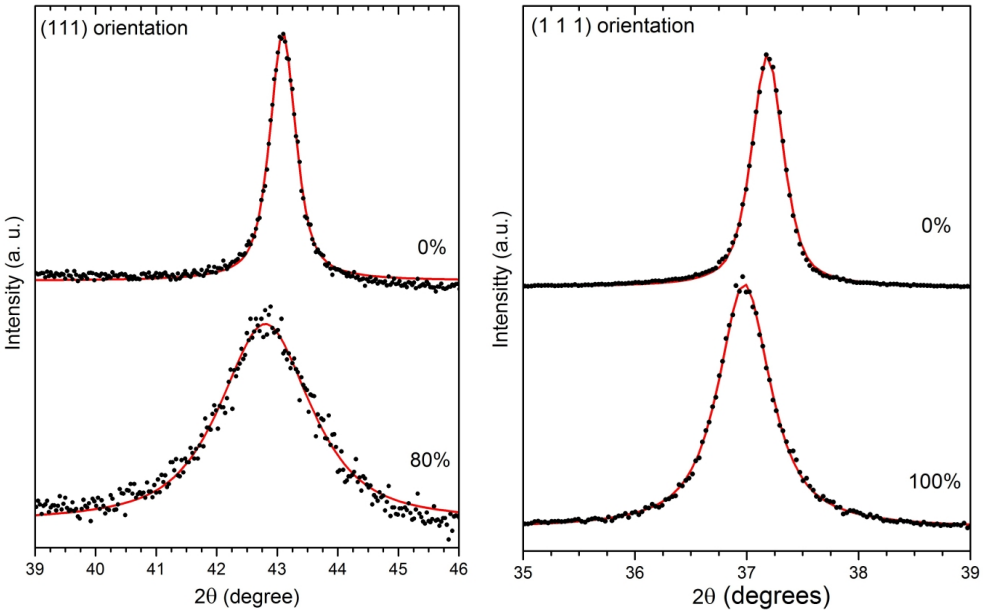

(a) 100W-1h-200℃ (b) 200W-1h-200℃

Figure 4.30: Peak (1 1 1) of low and high oxygen growth at 200℃ substrate temperature on Si. Again, the addition of oxygen reduces the intensity of the signal (a change of texture occurs together with a lower signal-to-noise), broadens the peak shape and shifts their position to lower Bragg angles.

self-reconstruction of type-3 surfaces with O-terminated octopoles as a manner of self stabilize the polar surfaces. The technological importance of these charge sheets along the (1 1 1) direction is high due to their applications in catalysis and exchange coupling.

Using the software Jmol [105] three cubic orientations are illustrated in figure 4.31 where the red balls represent the oxygen anions and the green balls represent the nickel cations. The relative size is similar to their relative ionic radii: 0.140 nm for O^{2-}, and 0.069 nm for Ni^{2+} [106], twice in size.

The surface energy is the energy required to cleave the crystal into two free surfaces. In a growing film, crystal planes with lower surface free energy have lower growth rates, remaining parallel to the surface. In a fcc lattice the (1 1 1) plane minimizes the surface free energy although its formation requires an increase of the oxygen species arrival on the forming surface. If the thermodynamic conditions are favourable the planes (1 1 1) will be chosen in order to reduce the total surface energy of the crystallites. When the system is not able to arrange the atoms in those planes then the stoichiometric planes (2 0 0) and (2 2 0) will be favoured.

It can be proved that the most densely packed planes in a fcc lattice is the family {1 1 1} and among the stoichiometric planes, the {1 0 0} is the most densely packed. The energetic arguments to explain the crystallographic orientations of NiO thin films are based on Fujii's work in 1996 [80] in which the oxidizing ambient (a high oxygen partial pressure) leads to form NiO molecules before the independent sputtered species land on the forming surface. Because the arrival of molecules is done at 1:1 ratio of Nickel and Oxygen the preferred orientation is the stoichiometric along the (1 0 0) direction. On the other hand, when the activated species of Ni^{2+} and O^{2-} land on the surface separately in a less oxidizing ambient (pure Ar growing or lower partial oxygen pressure) the non-stoichiometric planes (1 1 1) can be primarily formed, reducing the surface energy in this plane, because it is the most densely packed orientation in a fcc lattice.

The highly correlated deposition conditions and the out-of-equilibrium nature of magnetron sputtering makes it difficult to apply these thermodynamics arguments to our results. In our case the (1 1 1) orientation is favoured for pure Ar growth at room temperature, while for

samples grown on substrates heated up to 200°C the tendency is not clear. The atomistic growth model does not take into account the nature of the sputtered atoms and only an *in situ* measurement during the growth or extremely thin films (a few monolayers) could shed light into this problem. Works using Molecular-Dynamic simulations explore the growth of NiO films alogn the crystallographic directions, where the effect of high temperatures (above 500°C) is determining [107].

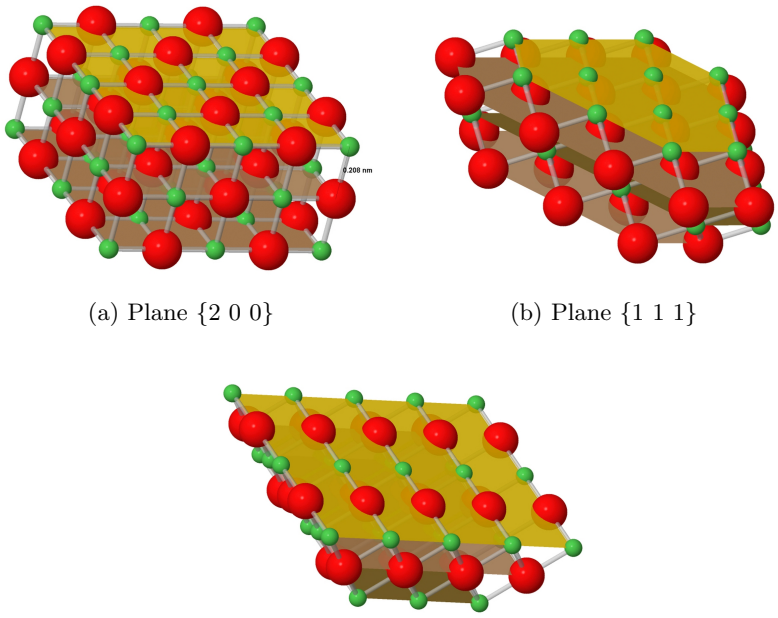

(a) Plane {2 0 0}

(b) Plane {1 1 1}

(c) Plane {2 2 0}

Figure 4.31: Schematic view of atomic planes in a fcc lattice. Planes {2 0 0} and {2 2 0} are neutral with the same number of positive and negative ions, while planes {1 1 1} are charged planes: each layer has entirely the same charge ions. Planes {1 1 1} have higher surface energy, therefore they minimize the total surface energy.

The general tendency observed in this study is an enlargement of the width of the diffraction peaks, which indicates that the crystallite size decreases while the disorder increases with the addition of oxygen, ending up with poor crystalline coatings. If the disorder increases this can be detected by using a high sensitive technique to local order in the crystal lattice, as we will see in next section.

4.4. Local order

In previous sections we showed that the addition of oxygen to the sputtering gas creates smaller grains, as observed in the scanning electron microscope images. X-rays diffraction data confirm that this reduction not only changes the texture of the sample but also enlarge the width of the peaks, confirming the decrease of crystallite size and suggesting more disordered crystal structure.

In this section EXAFS data will be presented in order to establish a relationship with the structural and morphological results obtained before. EXAFS is a powerful technique to obtain information about the local structure around an element inside a material. Although the position of an absorption edge and its line-shape near this edge give information about the chemical environment, that aspect will be treated in chapter 6. Here we will centre our analysis into the structural information that can be extracted from the extended absorption region in the XAS

data. Only one set of samples was studied using this experimental technique, the 100W-1h-RT series, due to the difficulty to obtain beamtime in synchrotron facilities, and the time-consuming character of this technique, especially in the case of thin films. In any case, the series chosen is probably the most representative of this work. As will be shown, some conclusions can be extracted from the data analysis that confirm previous results.

The lattice expansion, together with the peak broadening and the increase of noise with the addition of O_2 observed by XRD, seem to be originated by excess oxygen in the NiO lattice. The presence of oxygen ions in the plasma and their interaction with the NiO target can produce oxygen-enriched NiO particles that would be projected against the substrates. Such oxygen enrichment would produce Ni vacancies in the NiO lattice, and, if this is the case, the Ni-Ni mean coordination number should decrease. EXAFS is an experimental technique that can give both inter-atomic distances and coordination numbers of the first neighbour layers around an emitter atom. Consequently, this technique can help to confirm the previous hypothesis.

Figure 4.32 shows the absorption coefficient, μ, measured in fluorescence mode on coatings of series 100W-1h-RT grown both on Si and AAM. The range measured was 1 keV and the scan started several eV before the K absorption edge, located at 8.33 keV for Ni. After a high peak, called *white line*, which has a considerable height in the case of oxides, the oscillations are appreciable until they are completely extinguished. The oscillations are due to interference effects of the emitted photoelectrons with the first neighbours around the emitter atom, and decay exponentially due the dependence on several material properties such as disorder, energy to absorption edge, coordination number and space distance to scatter atom (see section 3.4.8). As it can be appreciated in figure 4.32 the higher the oxygen content, the more damped are the oscillations. This is directly related with the disorder around the emitter atom. The behaviour of the absorption signal is so similar in both substrates that we will centre our study on the coatings grown on the porous AAM substrates.

Here it must be remarked that this absorption coefficient is obtained from a large sample surface region (several mm^2) and due to the low thickness of the coatings the self absorption plays no important role in decreasing the outcoming fluorescence signal from the sample. The fluorescence signal reach the detectors (previously selected in the desired energy region) from the whole depth within the sample, so the information obtained from this technique is averaged in depth. Consequently, this technique is not sensitive to changes in the local structure of the thin films with the depth, but a systematic study within the whole series can provide useful information.

In order to study the EXAFS oscillations the independent variable is converted from eV to k, the reciprocal space, trough the relation $k = \sqrt{\frac{2m(E-E_0)}{\hbar^2}}$ and weighted to k^2 in order to emphasize the higher frequency region where the Ni atoms scattering predominates. The EXAFS signal is shown in figure 4.33, where the k-range goes from 2.3 to 10.3 $Å^{-1}$. Although the range measured was large enough to obtain k-values until 16 $Å^{-1}$ the signal was so noisy that the higher k region was not valid, and no oscillation could be clearly appreciated. At the right side of each curve the oxygen content in the plasma is shown.

The frequency of the oscillations is very similar for all samples, but, on the other hand, the amplitude clearly decreases when the oxygen content of the plasmas increases, especially at higher k-values. This damping occurs gradually along the whole series, increasing from 0% to 70%, with the highest amplitude for 0% O_2 and that with the lowest amplitude for 70% O_2. Such a decrease in the amplitude of the EXAFS oscillations can be caused by either a decrease of the coordination number or an increase of the structural disorder. In order to distinguish which effect is responsible for the amplitude damping, a precise analysis of the EXAFS data is required.

For this comparative study, the Fourier transform of the EXAFS signals was performed within the same range: $2.3 \leq k \leq 10.3$ $Å^{-1}$ using a Hanning window. Figure 4.34a shows the module of the Fourier transform (FT) of the EXAFS signal obtained for samples grown with 0%, 20%, 40% and 70% oxygen in the plasma. Phase corrections due to the central atom have been

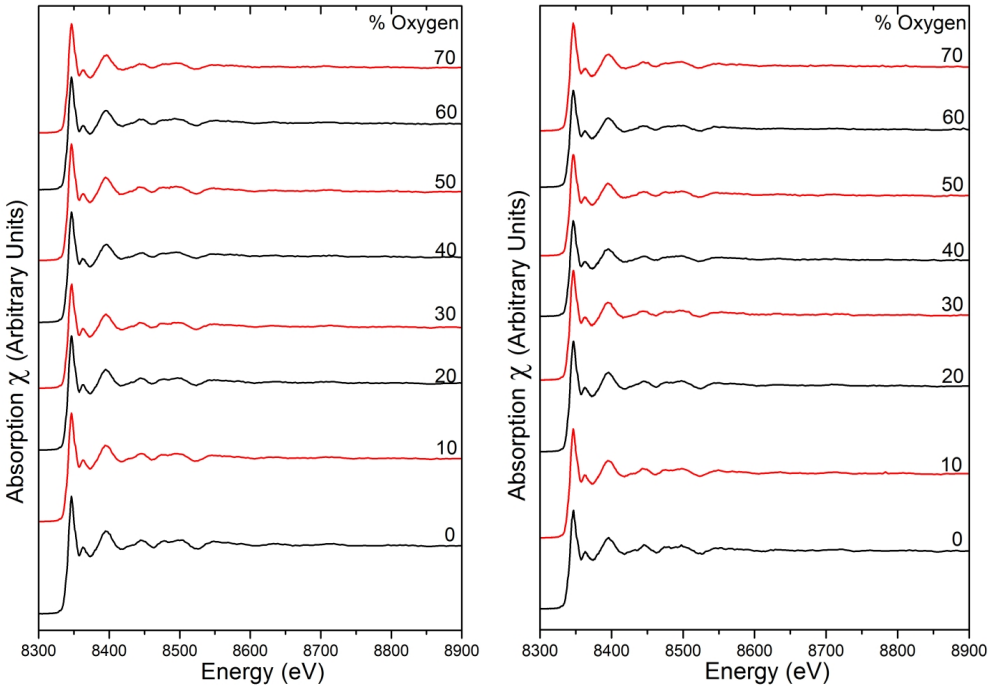

(a) AAM substrate (b) Si substrate

Figure 4.32: X-ray absorption spectra at the Ni K-edge of samples grown at 100W-1h-RT on Si and AAM substrates, respectively. The Ni K-edge is located at 8.33 keV, the absorption edge has an intense white line characteristic of oxides. The EXAFS oscillations spread over a large energetic region until they disappear. Samples grown with higher oxygen content have more damped oscillations than samples grown with pure Ar, indicating a higher disorder produced by the addition of O_2 to the sputtering gas.

included. This correction can be done without affecting the results because the EXAFS analysis does not take into account the close vicinity of r=0. The first peak, at 2.08 Å, corresponds to the Ni-O first-neighbour distance, and the second peak, located at 2.96 Å, to the Ni-Ni second-neighbour distance. These values are slightly larger than those of bulk NiO [76]. In the case of the 70% sample an expansion of about 1% in the interatomic distances is obtained from the fitting analysis, which confirms the lattice expansion observed by XRD.

The broad region above 3.5 Å corresponds to the contribution from multiple scattering events and from outer shells, made up of several Ni-Ni and Ni-O bonds, although the contribution of Ni-Ni bonds dominates [58]. Similarly to the amplitude of the EXAFS oscillations, the height of the peaks in the EXAFS FT curves is related to the structural disorder and the coordination number. In the cubic NiO lattice, each nickel atom is surrounded by a first-neighbour shell with 6 oxygen atoms, and by a second-neighbour shell with 12 nickel atoms. This explains the larger height of the Ni-Ni peak as compared to that of the Ni-O one observed in all curves shown in figure 4.34a. The intensity of the Ni-O peak clearly decreases down to a certain level upon oxygen addition to the plasma. On the other hand, the decrease of the Ni-Ni peak and that of the outer shells features is more gradual, with an intermediate level for the 20% sample, and a lower level for the 40% and 70% samples. Note that the Ni-Ni peak relative intensity of the 70% sample with respect to the 0% sample is much lower than that of the Ni-O peak for the same samples.

The intensity of the peak corresponding to the first neighbour, i.e., to Ni-O bonds, also shows a decrease for the 70% sample as compared to the 0% sample. Since no change in the coordination number is expected in this case, we associate this change to a larger disorder in this sample. Indeed, both effects, an increase of the disorder and a decrease of the second neighbour

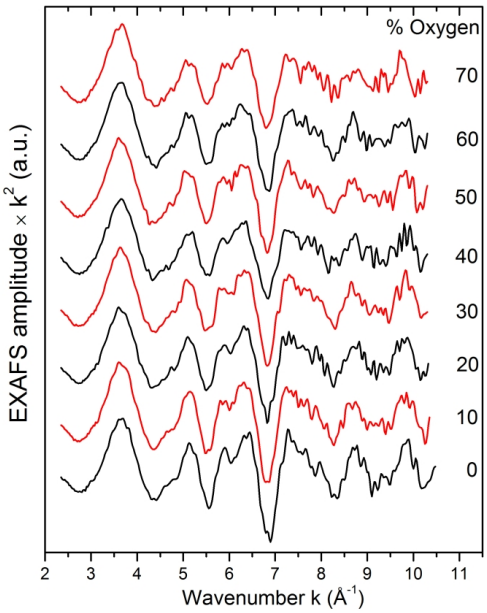

Figure 4.33: EXAFS signal, transformed from the μ absorption coefficient to the reciprocal space, for coatings grown at 100W-1h-RT on AAM substrates. The signal is multiplied by k^2 to emphasize higher frequencies. Higher O_2 content samples have lower amplitude due to the damping, related with the disorder level of internal structure.

coordination number, were needed to fit the EXAFS data. This large degree of disorder for samples grown with oxygen was already mentioned in the discussion of the XRD results, where an increase of the Gaussian contribution in the pseudo-Voigt curve was needed in order to correctly fit the diffraction data.

Figure 4.34b shows the radial distribution with detailed components for 0% and 70% oxygen samples: real part and its fitting are plotted in dark circles and green line, respectively. As it can be observed in this figure 4.34b, the intensity of both peaks for the 70% sample is lower than for the 0% sample. Such a decrease is related to the damping observed in the EXAFS signal when the oxygen content increases, and is thus related to a decrease of the coordination number and an increase of the disorder. Both real an imaginary parts are obtained because the Fourier transform is a complex function. The envelope of the two components is the absolute part and is determined mainly by the number of neighbours and the disorder of the lattice. The imaginary component, after a precise fitting, gives information about the absorber-scatterer distance [51].

NiO usually grows in a non-stoichiometric form as $Ni_{1-x}O$, *i.e.*, with excess oxygen in the lattice. This results in the presence of a variable amount of Ni vacancies. As the oxygen content of the plasma increases, it is expected that more oxygen incorporates to the lattice, generating a larger amount of Ni vacancies.

In figure 4.35 the Backscattered Fourier Transform (BFT) signal is superimposed over the EXAFS signal after the fittings for the 0% and 70% films. This BFT signal was obtained by performing again the FT in r-space in the range $0.8 \leq R \leq 3.2$ Å with a Hanning window. The mismatch between signals and fit is due to the reduced data selected through the windows in k- and r-space. The oscillations are composed of a mix of frequencies from each scattering path, where the closer and farther neighbours affect the lower and higher frequencies, respectively. Only when the EXAFS signal has enough quality the imaginary part of the FT and BFT operations can be used to discover unknown contributions. This is not the case because the data obtained in this experiment had a high noise level for k-vales larger than 11 Å^{-1}.

The range in the k-space is $2.3 \leq k \leq 10.3$ Å^{-1} and in r-space is $0.8 \leq R \leq 3.2$ Å. Using the Nyquist criterion, as explained in section 3.4.8, the available data range here is $\Delta k = 8$

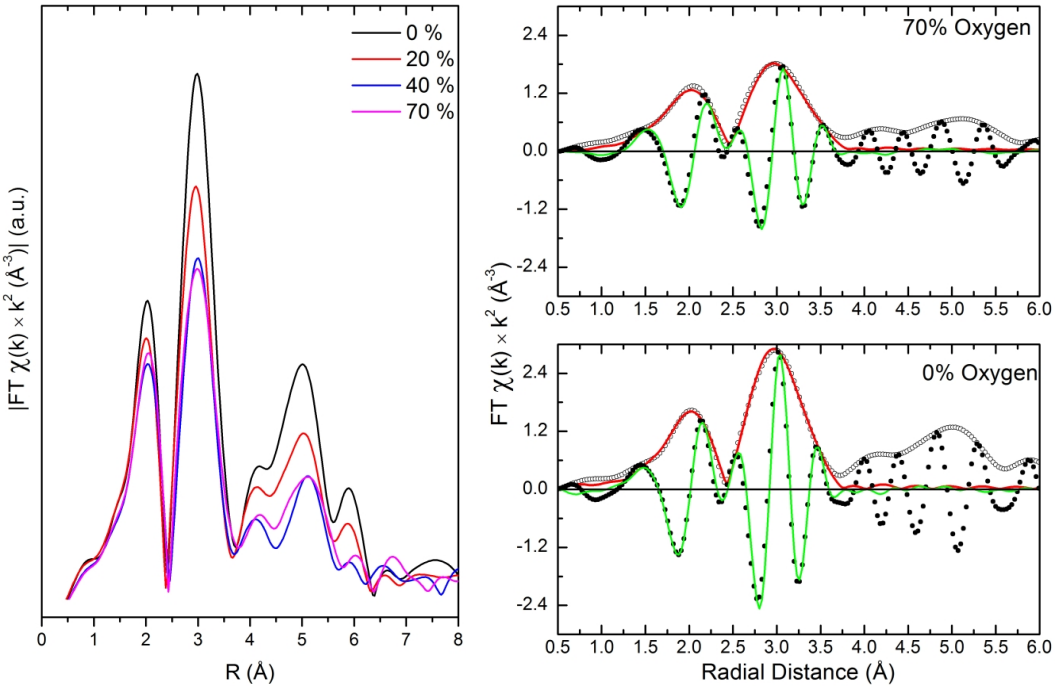

(a) Radial distribution (b) FT of EXAFS of the 0% and 70%, with real component

Figure 4.34: Fourier Transform of the EXAFS signal: (a) The radial distribution function determines the positions of the neighbours of the scatter atom (Ni), the first peak is located at 2.08 Å and the second at 2.96 Å, which correspond to Ni-O and Ni-Ni neighbours, respectively. Samples with different oxygen content are plotted where the evolution of the oxygen addition can be observed: the peak intensity decreases with the amount of O_2, though the second peak has a lower decrease, indicating the correlation between the disorder of the crystal and coordination number. Higher values were not treated in the analysis. (b) Radial distribution with detailed components for 0% and 70% oxygen samples: real part and its fitting are plotted in dark circles and green line, respectively. The experimental data is painted with hollow circles and the red line represents the module calculation. The intensity of both peaks for the 70% sample is lower than for the 0% sample.

and $\Delta R = 2.4$ therefore thirteen independent points can be used to define parameters to fit. We fit P=8 parameters (four per shell, and boundary conditions imposed correlate the energy displacements to the edge) and therefore the degrees of freedom are $\nu = 13 - P = 5$.

4.4.1. EXAFS quantification

The quantification of EXAFS requires a complex data treatment and rely greatly on the quality of acquired experimental data in order to obtain a successfully and reliable outcome. In our case the low thickness of the sample and the high disordered structure made the experimental absorption coefficient of medium quality.

Using the ATOMS software [60], a NiO cluster (fcc symmetry) of 6 Å size and 93 atoms was calculated. The backscattering amplitude, phase, and photoelectron mean free path factors simulated for this NiO cluster were obtained using the software FEFF5 [61] for a maximum of 4 legs (path segments between atoms). Least squares fitting of the extracted signals was performed using VIPER software [54]. Although FEFF5 calculates every possible scattering path, only the most relevant were included in the fitting (too many parameters would be impossible to fit). A disordered system like the present one does not allow a better precision, neither allows including more than the two first shells in the calculations due to the great sensitivity to disorder of the

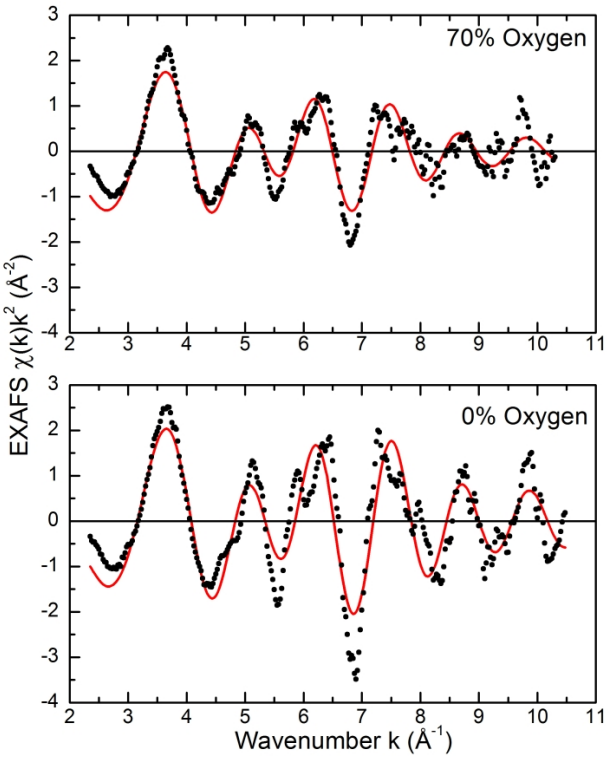

Figure 4.35: BFT (red line) over EXAFS signal (dots): the treated and double Fourier transformed EXAFS signal is plotted superimposed to its original value. The mismatches between the signals correspond to the reduced data selected through the windows in k- and r-space.

EXAFS technique. The fittings are performed both in the r-space and k-space until a compromise is obtained in the two spaces and the parameters met up the boundaries imposed. The fitting procedure was systematically performed for samples deposited on AAM and Si substrates, with no significant difference.

The results of the fitting are shown in table 4.5 and plotted in figure 4.36. The analysis of the bond lengths (R) reveals a lattice expansion of about 0.5% when going from 0% to 70% oxygen in the plasma, which is consistent with the lattice expansion found by XRD. The difference between both values is probably originated by relaxation of the atomic positions around the Ni vacancies, as it is proposed in references [108, 109] and firstly estimated by E. Gulbransen [110].

The degree of disorder (σ) can be quantified from the analysis of the EXAFS data through a parameter originally described for X-ray and neutron diffraction, the Debye-Waller factor, usually denoted as σ^2. This parameter represents the mean squared relative displacements and is a summation of the thermal disorder term and the crystal disorder [57], *i.e.*, it is indicative of increasing disorder/strain through increasing oxygen incorporation. Since all measurements were performed at room temperature, the thermal disorder affects equally all samples. Consequently, the changes observed in the Debye-Waller factor between the different samples can be assigned directly to structural disorder. Figure 4.36a shows the variation of the Debye-Waller factor, σ^2, for the second neighbour shell (Ni–Ni), as obtained from the EXAFS fit, with the oxygen content of the plasma. The fitting shows an increasing tendency in the σ^2 disorder term with the oxygen content, which confirms that the oxygen content in the plasma increases the disorder of the sample.

Finally, the coordination number (N), which indicates the number of neighbours in each shell surrounding the scatter atom, decreases with the oxygen content of the plasma for the second shell. In the case of the Ni-Ni bond, this parameter could be set to 12 for the sample grown with 0% O_2, but it gradually decreased with the oxygen content. Best fits (see table 4.5) indicate that

the Ni-Ni coordination number gradually decreases down to ~ 11 for the sample grown with 70% O_2. An estimation of the errors of the fitting gives $\pm$ 0.002 Å^2 and 10% for the s^2 factor and the coordination number, respectively [111].

% Oxygen	Coord. number		Neighbour Dist. (Å) $\pm$ 0.003		Debye-Waller (Å^2) $\pm$0.002	
	N_1	N_2	R_1	R_2	S_1	S_2
0	6	12	2.084	2.954	0.010	0.010
10	6	11.8	2.084	2.954	0.010	0.011
20	6	11.7	2.084	2.958	0.012	0.012
30	6	11.7	2.080	2.958	0.011	0.012
40	6	11.4	2.082	2.956	0.014	0.013
50	6	11.3	2.083	2.956	0.014	0.014
60	6	11	2.083	2.955	0.013	0.013
70	6	11	2.082	2.956	0.014	0.014

Table 4.5: EXAFS fitted parameters for coatings grown under 100W-1h-RT on AAM substrates: Coordination number, Neighbour distance and Debye-Waller factor (energy displacement to the edge is not shown). The fitting is performed using the first two shells for NiO [76], where the phase and amplitude were simulated by FEFF software on a 93 atoms cluster of 6 Å side. Error estimations are an standard upper bound. The oxygen addition reduces the coordination number of the second shell (N_2) from the stoichiometric value of 12 to 11 which suggests the presence of the Ni vacancies. The Debye-Waller factor σ increases due to the disorder generated by the oxygen. The neighbour distance increases for the second neighbour (R_2) suggesting a lattice expansion as calculated from XRD results.

Although the maximum uncertainty in the coordination number determination is of the order of 10%, these results point towards an increasing presence of Ni vacancies as the oxygen content of the plasma increases, in agreement with recent results reported by Anspoks *et al.* on nanosized NiO [112]. The presence of Ni vacancies, with the consequent oxygen enrichment, is expected to have some effect on the macroscopic properties of the deposited films, especially in their electrical properties [113, 15, 114, 115, 116].

Similar EXAFS results have been previously reported on different NiO nanostructured systems [95, 58]. Similar to what was obtained with the NiO sputtering targets composition (see figure 4.4) Ni defective NiO films have been reported as well [115]. In these works, a damping of the EXAFS signal and a consequent decrease of the FT peaks has also been observed, and explained in terms of lattice relaxation at the grain boundaries of nanocrystalline samples. Such relaxation produces an increase of the structural disorder, a decrease of the coordination number, and a slight expansion of the crystal lattice. In our case, the nanostructured morphology shown in figure 4.13, together with the expected oxygen enrichment induced by the presence of oxygen in the plasma during growth, lead to similar results.

4.5. Summary of chapter 4

In this chapter we have shown experimental results on the morphology and structure of different NiO coatings grown on both planar and nanoporous substrates. In the first case, Si wafers were used, and in the second case anodic alumina membranes, with hexagonally arranged pores of 45 nm diameter, and a distance between pores of 100 nm. NiO coatings were grown under different conditions. The magnetron power was varied between 100 W and 200 W, the substrate temperature between RT and 300ºC, and the oxygen content in the plasma between 0% and 100%. Through FESEM micrographs we have presented the set of different morphologies obtained for a wide range of sputtering conditions. From these conditions we have chosen those

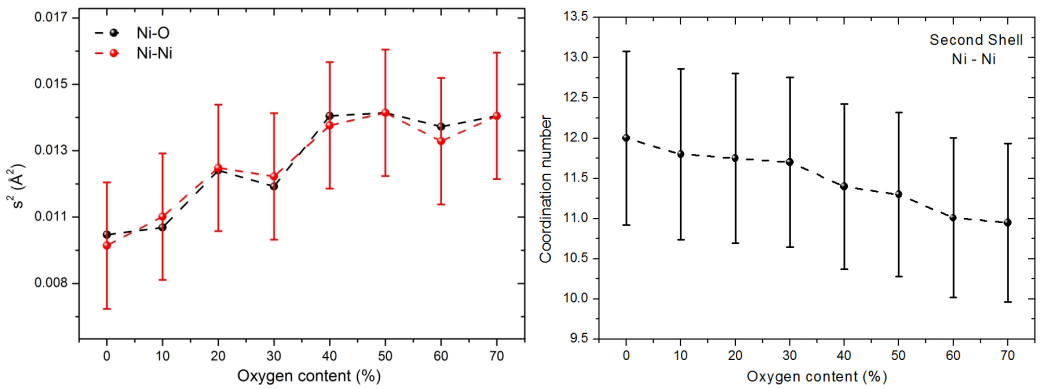

(a) σ^2 for the first and second shells

(b) N_2 in the second shell

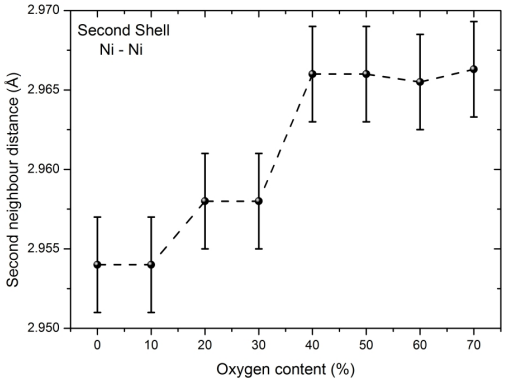

(c) R_2

Figure 4.36: Results of the EXAFS fits for coatings grown under 100W-1h-RT conditions on AAM substrates versus the oxygen content in the sputtering plasma. The disorder is increased and the atomic distances expanded, which agrees with XRD results. The number of Ni neighbours decreases, indicating the presence of nickel vacancies or oxygen excess.

which are more adequate to obtain porous coatings (for the case of NiO deposited on AAM substrates) and we have explored other conditions in order to understand the growth dynamics and the effects of certain sputtering conditions on the out-of-equilibrium synthesis method. The structure zone model predicted for sputtering has been confirmed for the substrate temperature and pressure used in this work. The growth dynamics model proposed can explain the evolution of the coatings: the growth has an initial stage of horizontal competition driven by surface diffusion. During this competition the grain size has lower values and after occluding the less favoured grains the coatings evolve towards a columnar structure. Until a given height the columns preserve the porosity of the AAM substrates, but from this limiting height the pores are totally closed. The oxygen addition decreases the size of the grains and makes them more amorphous and less faceted.

The crystal structure has been studied with XRD and GIXRD. All the coatings have polycrystalline structure and only the face centred cubic phase of NiO has been found. The preferred orientation changes with respect to the stoichiometric *Bunsenite* of NiO and certain growing conditions produced highly texturized films. Some XRD results confirm the morphology observations: the addition of O_2 reduces the crystallite size and increases the disorder in almost all crystallographic orientations. The signal-to-noise ratio is reduced with the oxygen content used in the plasma, indicating a decrease in crystal quality and an increase of the disorder. The lattice parameter has been calculated with the Pawley method. The addition of oxygen to the sputtering plasma expands the lattice up to 2%. When the diffraction profile is refined with more

than one fcc NiO phase the asymmetry of the peaks is resolved and a different lattice parameter is obtained. The possibility of a variation of the lattice parameter with the thickness confirms the competition growth model and is supported by GIXRD data, which show different peak positions when study the deeper layers with respect to the most superficial ones of the film.

The local order has been studied with EXAFS, which is very sensitive to the local environment. With this technique the relative disorder of the samples, the coordination number and first and second neighbours distance have been quantified for one set of samples. The oxygen addition increases the relative disorder with respect to the pure Ar growth and reduces the coordination number from 12 Nickel atoms in the second shell to 11 atoms. This supports the amorphization of the grain size observed with FESEM and the broadening of the XRD peaks, indicating an increase of the disorder caused by a reduction of the crystallites size and to the presence of Nickel vacancies. Finally the distance of the second neighbour (Ni) increases as well with the oxygen addition, confirming the lattice expansion observed by the XRD analysis.

Chapter 5

Experimental Results II: electrical and optical properties

"*Without experiment I am nothing.*"

Michael Faraday

This chapter will deal with some functional properties of NiO thin films grown with the parameters described in previous chapter. The electrical and optical properties are intimately related in solid state physics. Nickel Oxide has been a controversial semiconductor oxide in which single-particle band theories fail to explain its insulator properties. This chapter will present the main results of these two properties.

The presence of Ni vacancies, with the subsequent oxygen enrichment, is expected to have some effects on the macroscopic properties of the deposited films, especially in their electrical properties [114, 116, 115, 15]. The optical properties of the films are related to the electrical properties and consequently both will be treated simultaneously.

In our work the electrical resistivity has been studied for films grown on different substrates under the parameters mentioned in the previous chapter. However, the selected parameters are not the optimal for an outstanding electrical behaviour compared with other works on NiO. The cause is that the growing conditions were chosen in order to have nanostructured porous films and, therefore, some of the films have a high resistivity with different dependence on the oxygen content. The variations of the resistivity with the oxygen content in the plasma during growth, the amount of material deposited, the substrate temperature and the ageing time of the films will be studied.

The effect of the oxygen content in the plasma and its effects on the crystal lattice, grain size, disorder level and amount of Ni vacancies is expected as well to have influence on the optical parameters. Both the electrical and optical measurements were performed at room temperature.

5.1. Electrical measurements

The electrical conductivity of Nickel Oxide cannot be explained using single-particle band theory. N. Mott proposed in 1949 an explanation for its insulating behaviour based on Coulomb repulsion of the d-d localized states. Since then much debate and controversy has been created around this transition metal oxide. The transport properties of NiO are highly influenced by the impurity states and carriers introduced by defects. The electrical conduction has been proposed to be due to a small polaron hopping (within the narrow 3d band, strongly localized states) or large polaron (in the wide 2p-band) transport. At low temperatures the carriers are trapped by the impurities while at high temperatures they can be treated as free polarons. The hopping transport generates a local lattice distortion, called polaron (if the distortion affects only the

local vicinity of the vacancy it is named small polaron), with a temperature dependence on the mobility that reduces at high values. In turn, the band-like transport of high polarons has a mobility which increases with temperature [1]. The trapping of carriers by the impurities at low temperatures gives more importance to the temperature influence, which can activate the electrical transport to liberate the polarons. Thus the carrier density has as well a temperature dependence [1, 15, 117].

Despite a large list of experimental and theoretical works, a complete theory that describes the electrical transport mechanism in NiO has not yet been developed. NiO conductivity has been enhanced with different dopants such as the monovalent cations Li and Na, or Al [118, 119, 120]. Li doping greatly reduces the activation energy, which leads to a major influence of the carrier concentration as compared with the effects of mobility in the electrical transport [1]. In our work the excess oxygen takes the role of dopant concentration, through the presence of Ni vacancies.

On the other hand, non-doped NiO is a strong insulator. Reported values of the DC resistivity of single crystalline NiO at room temperatures are in the range $\rho \sim 10^{13}(\Omega \cdot cm)$ [15]. However, NiO grown under different chemical and physical methods, out of thermodynamic equilibrium or with a distorted crystal lattice full of point defects in the form of Ni vacancies and, above all, grown in an oxidizing environment gives a very different resistivity values. The literature shows values of the resistivity in the range from 10^{-2} to 90 $(k\Omega \cdot cm)$ [90, 5, 121, 122, 23, 114, 123]. Among these studies the resistivity varies within a certain range owing to different factors: thickness of the films, Ni vacancies, Oxygen content in the atmosphere during the films growth, annealing temperature, etc. All of them refer to the existence of Ni^{3+} vacancies to explain the conduction, however no agreement exists about the variation of the Ni vacancies with the oxygen partial pressure.

In our work we will study the influence of the growth conditions on the electrical resistivity of the NiO thin films. NiO has a Néel Temperature of 520 K [124] but in this work the resistivity will be studied in almost all cases at Room Temperature and, therefore, the films will always be in the anti-ferromagnetic phase.

In order to check the good performance of the ceramic deposit material, the NiO powder sintered sputtering targets were first measured by using a high sensitivity current source. With a four probe disposition [42] and using very low current values (of the order of nA) the Sheet Resistance, $R_{\square}$, of these materials was obtained at room temperature. The different targets finally used in this work and their resistance are presented in table 5.1. Targets with lower resistivity were not used in order to assure a stoichiometric starting material. The equipment used for these measurements actually gave the sheet resistance, which is shown in table 5.1. This sheet resistance can be easily converted into resistivity using the relation $\rho = R_{\square} \cdot t$, where t is the thickness of the film. However, this is a naive model that holds for metals, while a similar relation is quite complex when applied to semiconductors. In any case the thickness of the target was about 0.5 cm and, therefore, the sheet resistance can give an approximate idea of the high insulating behaviour of the stoichiometric departing material used in this work. Although the sintered NiO targets are polycrystalline ceramics and the reported values of high resistivity are single crystal measurements, these ceramic values will be our reference from now on. Most of the samples were grown using the AJA International target. However every complete set of samples (a set of deposition parameters with the variation of Oxygen content in the plasma) was grown with the same sputtering target in order to, at least, coherently observe differences between the samples in the same set.

The DC resistivity measurements of the NiO thin films was carried out at room temperature using the Van der Pauw four-probe method [41]. At the same deposition parameters chosen in chapter 4 the resistivity was measured just after taking out the samples from the high vacuum chamber, once the pressure recovered after deposition down to the base value and the samples were cooled down to RT. Figure 5.1 shows the resistivity of the NiO films on flat insulating glass substrates (with exception of the first set, were AAM substrate were used as well). The trend of

% Target	Resistance ($\Omega/\square$)
AJA Int.	1.3×10^{10}
ICV-CSIC	1.1×10^{9}
GoodFellow	9.4×10^{9}

Table 5.1: Sheet Resistance of NiO sputtering targets (powder sintered) obtained by the four-point probe technique.

the resistivity is clearly decreasing with the oxygen addition, in some cases this decrease reaches four orders of magnitude.

Figure 5.1a shows as well the resistivity of NiO films grown on AAM nanoporous substrates at 100W-1h-RT. In both cases there is a clear decreasing trend with the oxygen content of the plasma. Resistivity values of samples grown on AAM substrates are higher than those of samples grown on flat substrates by approximately two orders of magnitude. This difference must be related to the presence of pores in the first case, which hinder the in-plane electronic movement, increasing the resistivity. According to Reference [41] the reliability of Van der Pauw method holds provided that the contacts are small and located at the periphery of the film sample and the film is uniform in thickness and free of holes. This last requirement was not accomplished in the case of AAM substrates and therefore an increasing factor is expected when comparing the resistivity on porous and planar substrates. In any case, for both substrates the effect of increasing the oxygen content is to decrease the electrical resistivity. By comparing figure 5.1a with figures 4.24a and 4.24b, one can observe a clear correlation between the measured resistivity and the lattice parameter. The higher the oxygen content of the plasma, the larger the lattice parameter, and the lower the electrical resistivity.

Even sample grown with 0% oxygen, with a lattice parameter slightly larger than stoichiometric NiO, shows a reduced resistivity value [15]. The observed changes in resistivity are correlated to the concentration of Ni vacancies, i.e., to the coordination number observed by EXAFS (see section 4.4): the lower the second shell coordination number, the lower the resistivity. Interestingly, the EXAFS analysis shows a similar behaviour for samples grown with 40% and 70% oxygen in the plasma, which agrees with the saturation-like trend observed in the lattice parameter variation and in the electrical resistivity measurements. For samples grown under other conditions, such as 100 W and 200 W of applied power at RT and 200ºC, the trend with the oxygen in the sputtering plasma is maintained: the oxygen addition lowers the films resistivity. The evolution of samples grown at 100W-1h-RT represents the maximum in the variation of the resistivity of four orders of magnitude. Samples grown at 200W-1h-RT as shown in figure 5.1b have a decrease of three orders of magnitude between pure Ar and pure O_2 growths. When the temperature is raised to 200ºC the resistivity decreases by a factor of 100 as seen in figure 5.1c. Three orders of magnitude is the decrease when growing the films under a double increase of the parameters: 200W-1h-200ºC shown in figure 5.1d. Finally the samples grown under the extreme parameters: 200W-2h-300ºC show a behaviour with different trend. For this set of films the resistivity decreased only by a factor of 10 between the extremes of plasma composition (from pure argon to pure oxygen atmosphere) but the intermediate content of 60% shows the lowest value of the resistivity, with a change of two orders of magnitude with respect the pure Ar growth. However, the main tendency is preserved, which fits coherently with the rest of the work and the literature. This trend of resistivity decrease with oxygen addition has already been observed in the literature [5, 116, 114, 92]. Similar studies performed decades ago, [125, 126] and references therein [127], with more emphasis on the chemical diffusion observed as well an increase of the resistivity with the external oxygen pressure and with high temperatures (above 600ºC).

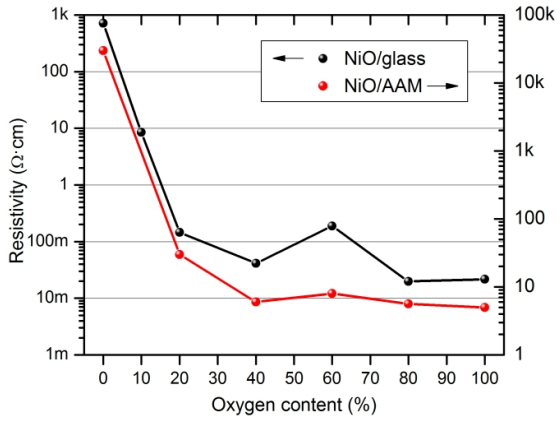

(a) 100W-1h-RT over AAM and glass substrates

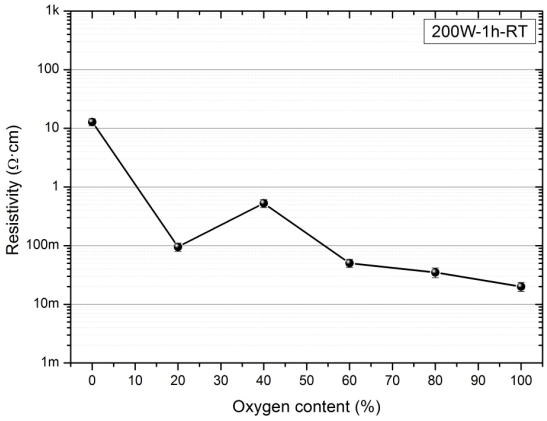

(b) 200W-1h-RT

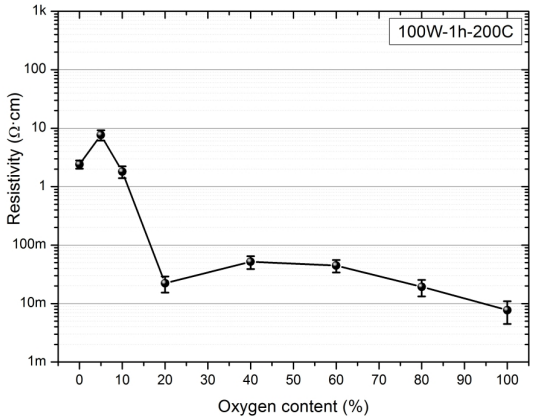

(c) 100W-1h-200℃

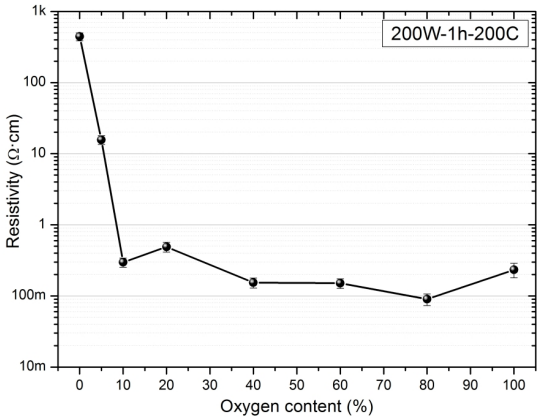

(d) 200W-1h-200℃

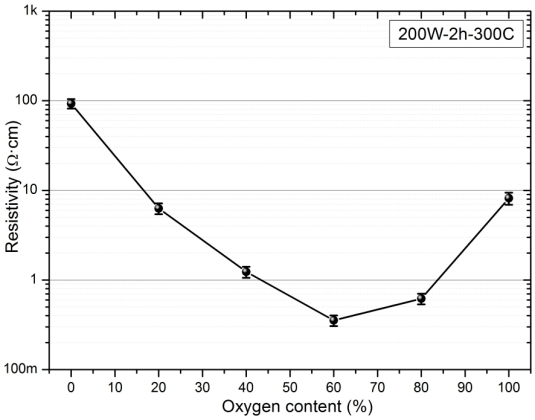

(e) 200W-2h-300℃

Figure 5.1: Evolution of the electrical resistivity of NiO films grown under different parameters with the oxygen content in the sputtering plasma. The general trend is an important decrease in the resistivity with the addition of a small amount of O_2, reaching a plateau for higher oxygen contents. Only high temperature (300℃) changes this trend.

From data shown in figure 5.1 it could be inferred that the thickness of the samples plays an important role in the resistivity, enhancing the conductivity by allowing the formation of more conductive paths. In order to have en estimation of this possible effect the data were presented in the form showed in figure 5.2a. It can be seen that the majority of points concentrate in the blue coloured region for lower thickness values (below 200 nm), which coincide with lower

resistivity values (below 1 $\Omega \cdot cm$). In the orange coloured region the resistivity values are above 1 $\Omega \cdot cm$) with thickness larger than 200 nm. The correlation between both parameters, thickness and resistivity, is not perfect, but there is a general trend of higher resistivity for higher film thickness. Here it must be remarked that the thickness has an inverse relation with the oxygen partial pressure, as shown in section 4.2.3: due to the lower efficiency of the sputtering process with the oxygen atoms the amount of material deposited is lower and the films thinner.

When representing the electrical resistivity in terms of the substrate temperature it can be concluded that room temperature and 200ºC values present no appreciable differences between them. However, when the sample holder was heated up to 300ºC the resistivity range was reduced as can be observed in figure 5.2b. This effect of the substrate temperature can be understood in terms of a higher crystalline lattice of the films and therefore decreasing their conductivity. Growths at room temperature were performed with no heating of the sample holder but, as was described in chapter 3, the sputtering plasma can heat up the sample holder with the substrates up to 50ºC as was measured at the end of the growth (see section 3.1.1). The applied magnetron power and the heat transfer of the plasma can therefore shift all data shown in figure 5.2b but because it is a linear displacement of the axis the conclusions are not affected. Unfortunately no samples were grown with other parameters in order to check the actual effect of this parameter and reduce the data dispersion.

In order to have comparative values of other oxides resistivity some examples are given here. While metals have resistivity values within the range $\rho \sim 10^{-6} - 10^{-4}(\Omega \cdot cm)$, semiconductors resistivity spreads into a huge range of values depending on their stoichiometry, doping, temperature and ambient pressure. The resistivity of Germanium lies in $5 \times 10^{-4} - 5 \times 10^{1}(\Omega \cdot cm)$ and Cadmium Sulphide in $10^{-8} - 10^{12}(\Omega \cdot cm)$ [128]. From Chromium to Copper their binary oxides are all insulators whereas band theory predicted they would be conductors. ZnO films grown by sol-gel method have a resistivity in the range of $10^{3}(\Omega \cdot cm)$ [129]. CoO is, as Nickel Oxide, a high insulating oxide with resistivity close to $10^{5}(\Omega \cdot cm)$ at room temperature [124]. V_2O_3 at RT has a metallic like resistivity of $10^{-3}(\Omega \cdot cm)$ while at temperatures below 150 K it experiments a transition into insulating (the so called MIT: Metal to Insulator Transition) where $\rho \sim 10^{4}(\Omega \cdot cm)$. For compounds such as Cadmium Telluride doped with Zinc, CdZnTe, the high resistivity ($10^{10} - 10^{11}(\Omega \cdot cm)$) is required for γ-ray spectrometry applications [130].

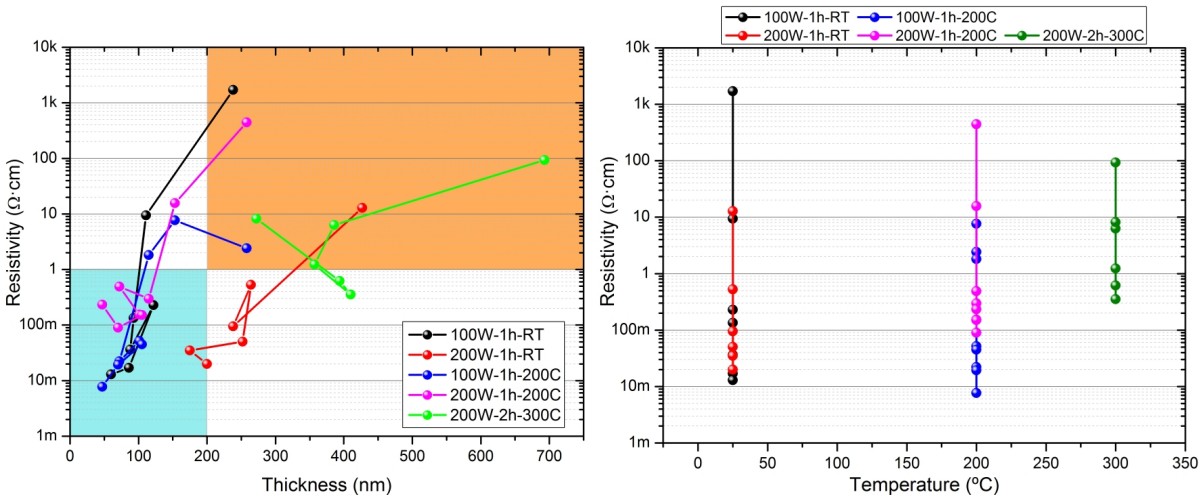

(a) ρ evolution with thickness

(b) ρ values versus substrate temperature

Figure 5.2: Resistivity evolution with thickness (a) and with substrate temperature (b). As seen in (a), low thickness coatings have higher resistivity values.

5.1.1. Role of vacancies in the conductivity

NiO is quite usually reported as a p-type semiconductor [5, 131, 1]. This electrical behaviour is based on the conduction by holes. The observed oxygen enrichment in the NiO lattice, would create the necessary holes to produce p-type conduction. In figure 5.3 Nickel Oxide lattice schematics are shown. Figure 5.3a shows a stoichiometric rock salt type structure where the dashed line square represents the crystal charge neutrality at equilibrium. The hollow circles represent the oxygen ions and the smaller blue circles the nickel ions. Note that the ionic radii of oxygen is almost double than that of nickel, as was mentioned in section 4.3.4 and hence the difference in size in these figures. It must be remarked that there is no space in the NiO lattice to allow interstitial oxygen atoms due to their large ionic radii [131]. When a Nickel atom is not present in its lattice site a vacancy is created, which is a point defect in the solid (it is not a Schottky defect, in which both anions and cations are missing in equal number from the lattice). This Ni vacancy means that two elementary charges are vanished from the lattice but in order to maintain the charge neutrality two other Nickel ions are forced to have higher charge, these are the Ni^{3+} ions, which act as acceptors. An acceptor is defined as an impurity atom that provides less electrons than the atom it replaces. This is shown in figure 5.3b. Another way to interpret this oxygen excess or, more precisely, a deficiency of Ni in terms of conductivity, is that the Ni^{3+} ions are able to move from one site to another acting as p-type carriers. Actually these Ni^{3+} ions are not moving themselves but are the electrons which move from one Ni^{2+} site to another Ni^{3+} site, which has higher potential energy. Therefore the Ni^{3+} sites act as impurities levels above the valence band (Ni 3d states bonded with O 2p states) so that electrons at these higher levels produce holes in the band. This behaviour results in positive holes that move through the lattice sites: a p-type conductivity. In figure 5.3c the positive carriers, or holes, are shown close to Ni vacancies. A hole moves through the lattice if it is energetically favourable, i. e.: thermally activaded or through a sufficiently high vacancy concentration which takes the NiO lattice out of the stoichiometry, favouring the p-type conductivity. In such case the hole produces a local deformation of the ionic arrangement of the lattice (as indicated in figure 5.3c by means of displaced oxygen ions): the hole polarizes locally the lattice, which screens its field reducing the electrostatic energy. This hole, together with the induced lattice polarization, is called a *polaron* and its characterized by its higher mobility than other point defects (Frenkel or Schottky), which originates complex models of the conductivity in ionic crystals [37]. Polaron conductivity together with hole hopping is the base of the charge-transfer conductivity models in transition metals [1].

A simple description of the p-conductivity is expressed as:

$$Ni^{3+} \longrightarrow Ni^{2+} + p \tag{5.1}$$

where p states for hole carrier, having as a general expression of nickel and oxygen atoms the reaction:

$$2\,Ni^{2+} + \tfrac{1}{2}\,O_2 \longrightarrow O^{2-} + 2\,Ni^{3+} + V_{Ni} \tag{5.2}$$

where V_{Ni} is a vacancy at the cation nickel site. The relationship between the defects concentration and oxygen environment has been expressed by means of the equilibrium constant, which defines the point at which reversible reactions occur following the mass-action law. Although this equilibrium is reached for NiO at very high temperatures (at least 1300°C), it is instructive to find out the dependence of conductivity with the oxygen pressure. By means of the equilibrium constant the solid state composition and the influence of the oxygen pressure are related, which are important factors in the determination of the conductivity by means of bulk diffusion:

$$K_{eq} = \frac{[Ni^{3+}]^2[V_{Ni}]}{P_{O_2}^{1/2}} \tag{5.3}$$

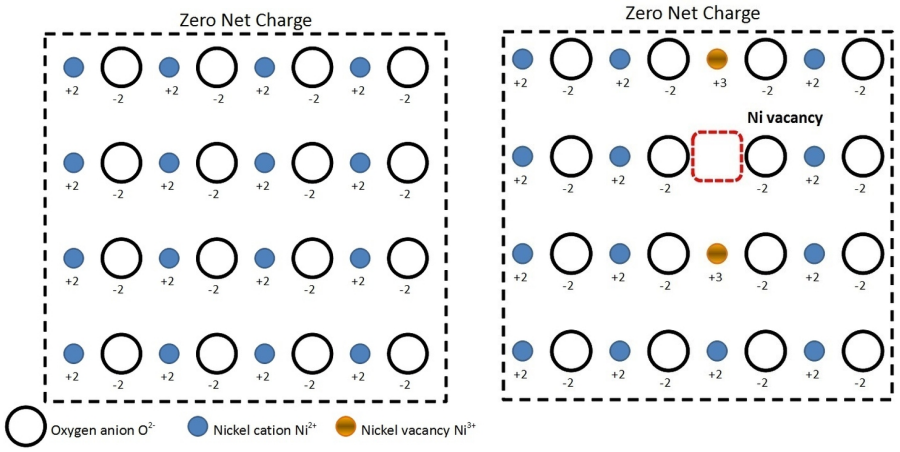

(a) Stoichiometric NiO lattice (b) NiO lattice with Ni vacancy

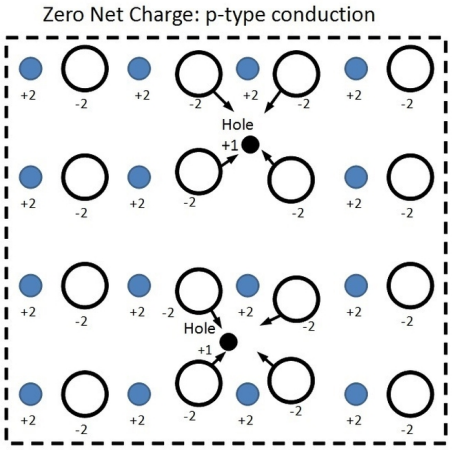

(c) Schematic of NiO lattice with hole conduction

Figure 5.3: Schematic views of NiO lattices: the stoichiometry is broken due to Ni vacancies, which produce Ni^{3+} ions in order to maintain lattice charge neutrality. Adapted from [132].

Considering small variations from stoichiometry the activities of Ni^{2+} and O^{2-} are considered equal to one: no variation occur for these concentrations, where the number of nickel and oxygen atoms remain constant (we consider in this treatment only small variations of V_{Ni} and Ni^{3+}). Each vacancy produces two Ni^{3+} ions. Consequently, $[V_{Ni}]=2[Ni^{3+}]$, and it follows that:

$$[Ni^{3+}] = \left(\frac{K_{eq}}{2}\right)^{1/3} P_{O_2}^{1/6} \tag{5.4}$$

Therefore the conductivity, which depends on the concentration of Ni vacancies, that is, the number of holes, should vary with the one sixth power of oxygen pressure [125, 131]. Subsequently the equilibrium constant depends on the enthalpy and entropy of formation of the reaction 5.2.

For low Ni vacancy concentration the relation with the oxygen pressure is $P_{O_2}^{1/6}$ while for high concentration is of the form $P_{O_2}^{1/4}$ [133]. In [127] a complete list of works are cited which show that this relation is followed with variations, owing to the conductivity dependency on carrier concentration as well as hopping mobility. Unfortunately the temperature at which these equilibrium reactions occur are far above our experimental work. In any case, the role of the oxygen partial pressure on the holes concentration, and hence on the conductivity, is clear.

The oxygen enrichment would also produce a distortion of the NiO lattice, which would

result in the lattice expansion observed in previous chapter. The EXAFS results confirm the presence of Ni vacancies when oxygen is added to the sputtering plasma as shown in section 4.4. Although the range of oxygen pressure in this work is short: pressure is 1.5×10^{-2} mbar when the plasma is pure in oxygen and 7.5×10^{-4} mbar when the partial oxygen pressure is 5% in content, the effect of oxygen on the electrical properties of the films is evident. This variation of the conductivity is more relevant for higher pressures but it must be noted that in our work the resistivity measurements were all performed at RT and ambient pressure (10^3 mbar) without variation of these parameters. In the next chapter we will study by means of X-Ray Absorption (XAS) measurements the presence of vacancies in the films related to the oxygen addition in the plasma.

Another way of creating Ni^{3+} ions, and, consequently, vacancies, is by doping NiO with monovalent ions. Historically NiO has been doped with Lithium atoms in order to increase its conductivity [124, 134, 118]. As explained in [134] the decrease in the resistivity and activation energy with the increase of Li atoms reduces the attracting potential around the Li^+ ions enhancing the conductivity. The importance of the doping in the conduction mechanism by means of Li or by Ni vacancies supports the idea that the electric transport is due to the activation of the carriers. When the carrier concentration is high enough (above 1.5% [134, 1]) the activation energies are lowered, enhancing the electrical conduction.

Another material properties such as Hall effect, Magnetoresistance and Mobility of the samples have been measured. However, the dispersion of the data was too high, owing to the high resistivity of the samples. The mobility could be estimated in the plateau current zone, but the data dispersion was high, showing values within the range $\mu \sim 0.01 - 0.25(cm^2/V \cdot s)$, similar results can be found at [135, 15]. There were, however, no correlation between these Mobility values and the oxygen content in the plasma, result which has been previously observed [5]. Values of the Hall coefficient and magnetoresistance consisted on a data dispersion without any trend due to the highly insulating behaviour of the samples.

5.1.2. Ageing effect

The electrical resistivity measurements reported up to now were performed just the very first day the samples were taken out from the high vacuum chamber to avoid any contamination from the environment and minimize as much as possible the ageing effects. These ageing effects were observed after measuring some samples several days after deposition, and noticing different resistivity values than those of the first day. Consequently, we decided to study these ageing effects in detail. In order to preserve samples in the same conditions, they were maintained at room temperature in foodsaver vacuum sealed bags at a pressure of 0.8 bar. The study of the time evolution of the resistivity was carried out by measuring the samples at different times, with a time span that reached in some cases the three months.

In general, it was observed that, after several days, the resistivity increased from its initial value. After approximately one month the resistivity increased by a factor which ranges from 2 to 25, depending on the growing conditions. This increment of the resistivity was observed to be non-reversible. This effect can be explained taking into account the out-of-equilibrium nature of the deposition technique used, which creates unstable vacancies that evolve with time. Residual stress also have some effect with time through a crystal relaxation process, but this can be discarded because we performed XRD in samples after annealing at 150ºC during one and four hours and observed no decrease of the averaged microstrain when refinement methods were performed.

A microstructural defect recovery (a process in which the stoichiometry is slowly recovered) through bulk diffusion together with oxygen desorption seems to be more plausible. This hypothesis agrees with the results that will be presented in next chapter, in which annealing samples in vacuum and oxygen atmosphere have different behaviour. According to these results, the amount of Ni vacancies decreases upon heating under vacuum, whereas it does not change

upon heating in the presence of oxygen. It must be noted that the amount of vacancies is related to the electrical conduction [136]. However the reason for this phenomenon has not yet been profoundly discussed and the references about it in the literature are scarce [135, 113, 137].

Figure 5.4 shows the electrical resistivity with time for a complete set of samples grown at 200W-1h-RT with different oxygen contents. The measurements were performed at RT from the first day after deposition, covering almost 100 days in some cases.

The valid region for the resistivity measurements corresponds to the plateau region. Above a certain current value, which depends on the sample resistivity, the power source used for these measurements cannot give enough power, and the resistivity measured is incorrect. Measurements over a wide current range guarantees a correct value, which corresponds to the value at the plateau. This plateau has a width of approximately four orders of magnitude of the current range for most of the measurements, with the exception of the sample grown with pure Argon plasma: 0% oxygen in figure 5.4a. This is due to the higher resistivity of this sample. The ageing effect clearly increases the initial resistivity value by a factor of 2.5 in the case of intermediate oxygen content (from 10% to 80%) and a factor of 10 for the extreme values (0%, 5% and 100%).

The evaluation of the ageing effect of the films was performed on every sample as shown in figure 5.5. The resistivity has been measured along several days, in some cases reaching up to three months. Each data point in the graph is the result of the average of the values obtained at the plateau. The resistivity of the films increases in all cases with time and this ageing progression seems to follow a saturation effect. The ageing net factor at the end of the measurements ranges from 2 to 25 for films grown at 100 W , as shown in figure 5.5a. Some of the films grown in pure argon plasma or low oxygen concentration (0% and 5%) had very high resistance, and they were out of the measurement range of the equipment, so they do not appear in the graph. NiO films grown at 200W-1h-200ºC have a maximum increase of 10 times the initial value and finally samples grown at the highest temperature, 300ºC have the lowest ageing factor: its maximum value is only 3. This shows that the higher the substrate temperature at deposition, the lower the ageing effect.

If the ageing effects are caused by a relaxation of the crystal lattice or a desorption of oxygen, it has sense that samples grown at 300ºC have the lowest evolution because the structure is already more free of defects. This same effect of a smaller variation of the ageing effect due to a higher substrate temperature during deposit has already been reported by W-L. Jang *et al.* [138].

The proposed model of microstructural defect recovery with time, originated by oxygen diffusion and desorption through the surface, resembles the evolution of metallic oxidation with time, though in this case the oxygen diffuses inwards, instead of outwards. The thickness of the oxide scale formed at the surface of metals increases at a decreasing rate, since oxygen diffusion is hindered by the oxide scale itself. Stable scales give rise to a so called parabolic behaviour (in fact, the dependence with time is as $t^{1/2}$). In some extreme cases of very stable oxide scales, the behaviour can be cubic, and in the less stable ones, it can approach linear behaviour. Following this analogy, we propose a model for the evolution of the resistivity described empirically by a power law relationship:

$$\rho = \rho_0 + b(t-1)^c \tag{5.5}$$

where ρ_0 is the resistivity of the fresh sample measured in the first day, b is a constant, the time t is measured in days therefore the resistivity measured on the very first day (t=1) is $\rho = \rho_0$ and c is a parameter which determines the ageing effects on the film. We want this model not only to describe the experimental results of the resistivity evolution but also as an analogy with the concepts of metallic oxidation mentioned above. In [139] and references therein reported data of oxides under thermal treatment relate the thickness of the oxide layer L with time, following a parabolic ($L^2 \propto t$) or even a cubic ($L^3 \propto t$) law. The evolution of the oxide layer with time can be accelerated under thermal treatment. In our study the samples were preserved at room

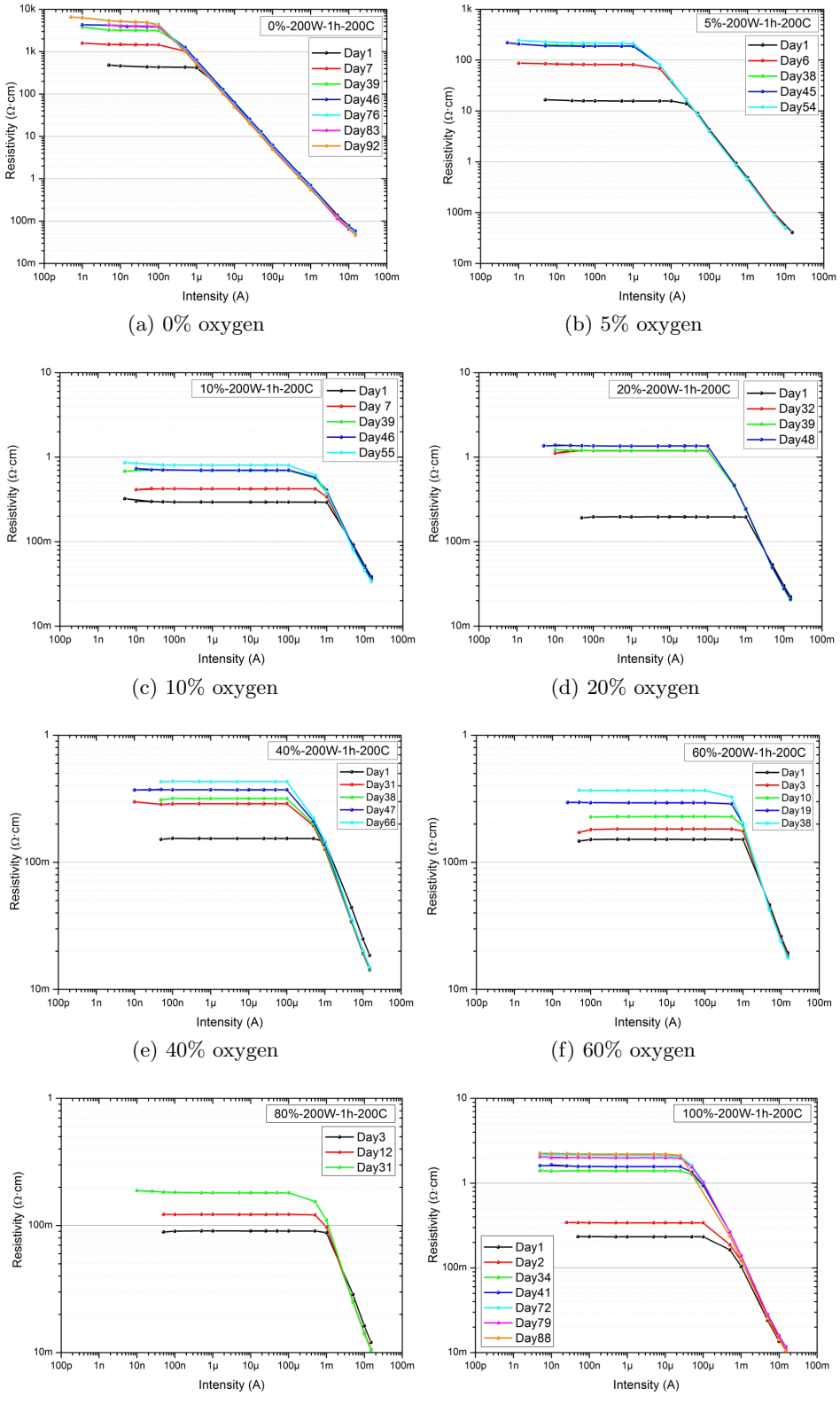

(a) 0% oxygen

(b) 5% oxygen

(c) 10% oxygen

(d) 20% oxygen

(e) 40% oxygen

(f) 60% oxygen

(g) 80% oxygen

(h) 100% oxygen

Figure 5.4: Electrical resistivity evolution of NiO films grown at 200W-1h-200℃. Each graph represents a different oxygen concentration in the plasma.

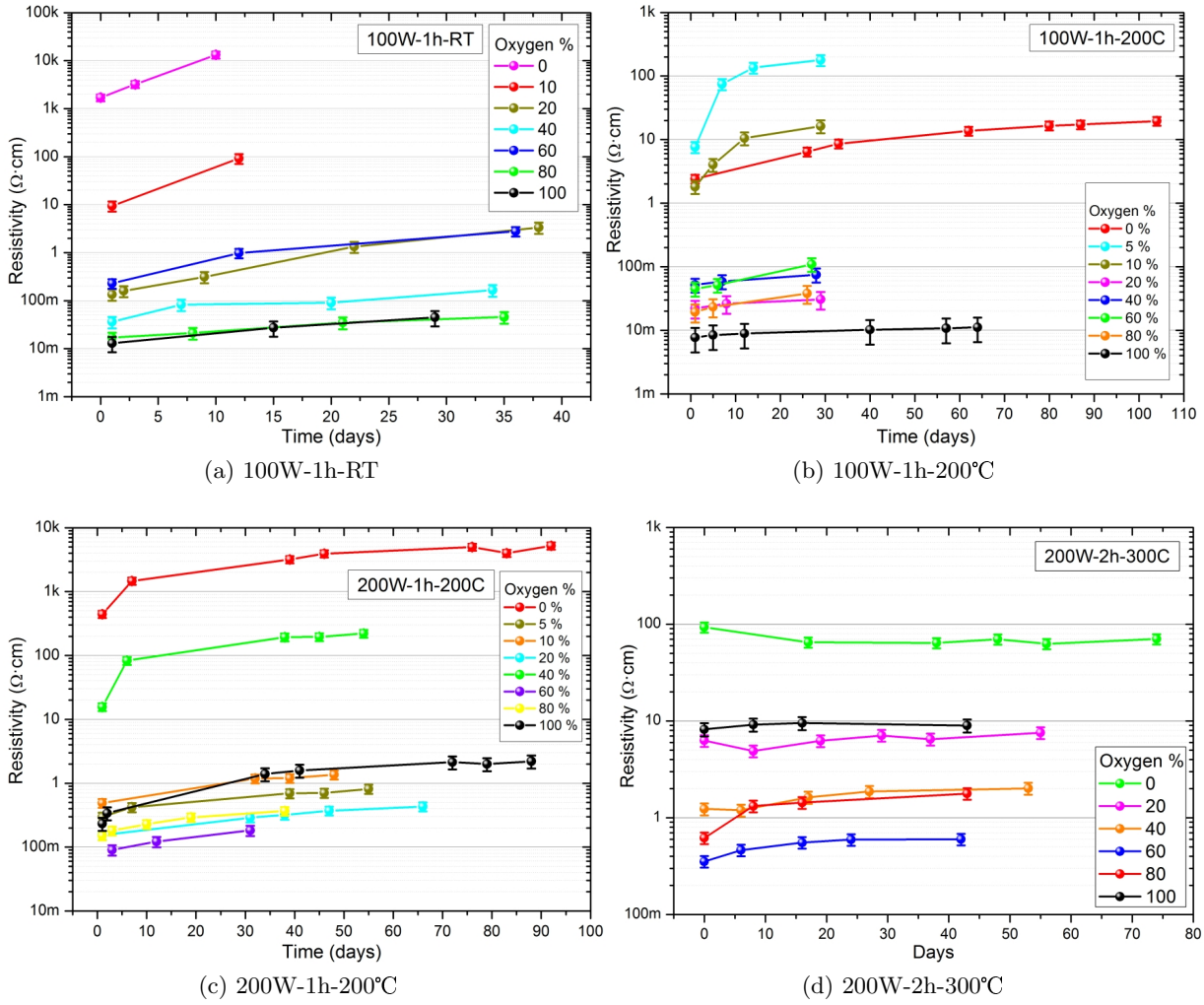

(a) 100W-1h-RT

(b) 100W-1h-200℃

(c) 200W-1h-200℃

(d) 200W-2h-300℃

Figure 5.5: Ageing effect of the electrical resistivity of NiO films grown under different parameters on planar glass substrates.

temperature in sealed bags at rough vacuum, which avoided degradation upon contact with the air.

The main result is the exponent in equation 5.5 which determines the parabolic (for $c \leq 0.5$) or the linear tendency (for $c \to 1$). In most of the samples, the exponent takes values below 1. Figure 5.6a shows an example of the fit for sample 80%-100W-1h-RT using the proposed model of equation 5.5. In this case, the power exponent parameter is $c = 0.8 \pm 0.1$ with coefficient of determination $R^2 = 0.96$. When the statistical information is enough the fitting of this model gives values for the exponent c in the range $[0.5, 1]$, as expected for a saturation effect.

In figure 5.6b the values of the exponent c for samples grown at 200W-1h-200℃ with different oxygen content in the plasma is shown. Although the error bars are large, a general trend of increasing c with the oxygen in the plasma is observed. Lower values for the exponent c in equation 5.5 give slow variations of the resistivity with time while higher values of c stand for rapid increase of the resistivity. The nonstoichiometric surface layer which interacts with the environment recovers the equilibrium when oxygen atoms are diffused out of the crystal, it is expected that thicker layers with more oxygen excess will increase faster their resistivity with time, reaching the saturation (or equilibrium) after more days.

The proposed power law model holds provided that the resistivity is directly affected by the layer forming on top of the samples. If the interaction of the surface of the NiO thin film with the air environment enhances the oxygen desorption as has been proposed [135] therefore the oxide

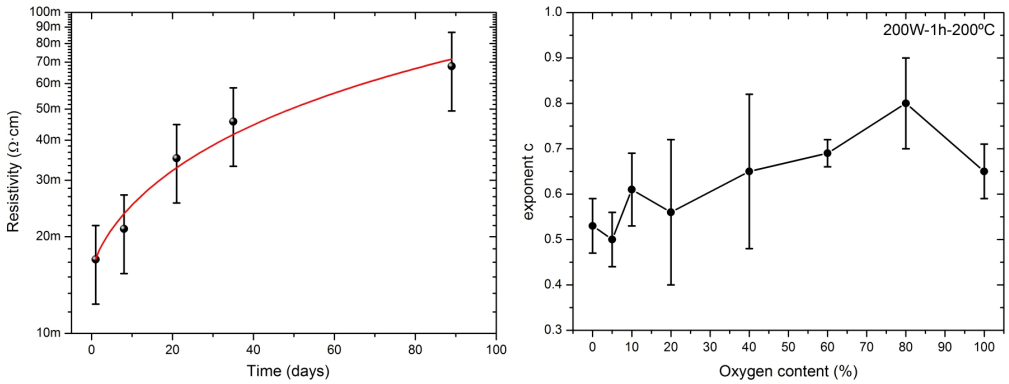

(a) Ageing effect model (b) c exponent for a set of samples

Figure 5.6: Fittings of the ageing model for the resistivity. left) Power law fit of the resistivity values of the ageing effect for sample 80%-100W-1h-RT. The power exponent parameter is $c = 0.8 \pm 0.1$ right) Values for the exponent c of equation 5.5 for samples grown at 200W-1h-200ºC, the oxygen addition increases the value of c.

layer, which has oxygen excess, will evolve to a more stoichiometric layer. As this stoichiometric layer increases in thickness with time the ionic diffusion of oxygen outwards becomes less effective, so the resistivity increases at a slower rate. Since this ageing effect is due to oxygen desorption and a disordered lattice, then samples grown with the highest substrate temperature will show the lowest ageing effect, as it is indeed the case. This also suggests that the defects in the films decrease slowly after deposition.

As a diffusive process, the temperature should play an important role in the ageing effect. In order to check the effect of temperature a sample was annealed in a furnace in air. It is expected that the annealing will accelerate the ageing effect and increase the resistivity until its saturation value or even further.

Figure 5.7 shows an experiment in which the electric resistivity was measured after annealing. The sample belongs to the most studied set of growth parameters: 100W-1h-RT, with a 80% oxygen in the plasma, an already aged sample after 90 days which was afterwards annealed. After the ageing process the sample was annealed in a furnace at 140ºC for 19 hours. The result is observed in the red curve of figure 5.7. This first annealing changed the resistivity by a factor of 1500, increasing from 0.069 $(\Omega \cdot cm)$ to 106 $(\Omega \cdot cm)$ and the plateau, which is related to the conductivity, reduced from five to two orders of magnitude in current. When the sample was annealed again for another 19 hours at 140ºC as well, the resistivity increased to 684 $(\Omega \cdot cm)$, that is a factor of 6 from the previous value. The plateau in this latter case was slightly reduced in comparison to the previous value.

It can be concluded that annealing is much more efficient than the natural ageing process (observed in figure 5.5) by accelerating the increase of the resistivity. This annealing process is irreversible when applied and reduces the conductivity of the film.

5.2. Optical measurements

With a wide band gap close to 4.0 eV [1] Nickel Oxide presents a non-absorption region in the visible spectrum. Historically stoichiometric NiO has been observed to be of green colour whereas tends to be darker and even black when it has an excess of oxygen. In our work the thin films deposited on the glass substrates were observed to be dark brown and even black when the thickness was large enough and therefore optically denser in appearance. This fact has also been reported in the literature [140, 5]. The visible light region, with photon energy $\sim 1.7 - 3.1$ eV, is of the utmost importance in transparent conducting coatings applications [5]

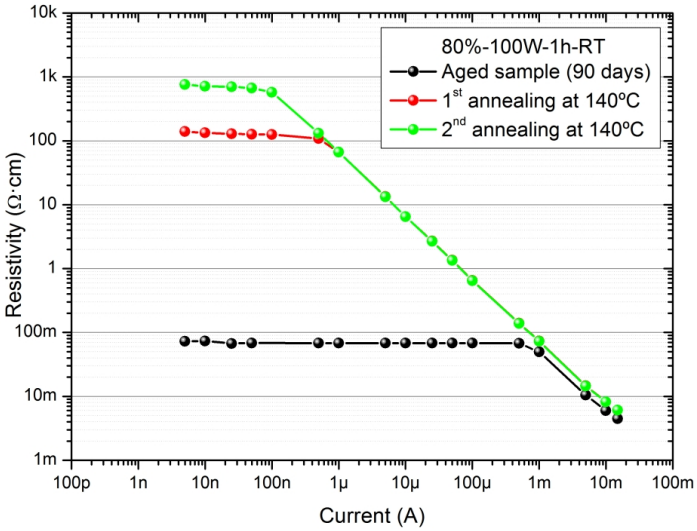

Figure 5.7: Resistivity evolution of a sample aged for 90 days and after two annealing processes at 140ºC for 19 hours. The resistivity increases considerably after heating treatment.

and in electrochromic devices [141]. The green colour of NiO is due to the absorption band in the red (1.75 eV) and violet (2.75 and 2.95 eV) being transparent for green [140]. The oxygen excess in the lattice increases the absorbance in the green range, darkening the final colour, as we observed in our films.

The optical properties of the NiO thin films were measured by IR-Vis-UV Spectrophotometry in a wavelength range from 300 to 900 nm. The absorptance was measured and through a simple transformation the absorption coefficient could be obtained.

5.2.1. Glass substrates

Films were deposited simultaneously on AAM, Si wafer, glass microscope slides and glass cover slips in order to study the film properties with different characterization techniques. Commercial glass cover slips were D263M Coverglass from *Menzel-Gläser* which have a uniform transmittance in the visible region, a refractive index of $n = 1.52(5)$, according to the manufacturer, and presents no absorption in the visible region. Their chemical composition is 72% SiO_2, 14% Na_2O, 6% CaO, 4% MgO and other oxides in lower quantities.

The air influence in the beam path was not taken into account for the measurements, considering its transmittance 100% with no absorption and its real refractive index $n_{air} = 1.0$.

In order to check the performance of the Spectrophotometer and the quality of the glass substrates a first measurement of their transmittance and absorption was performed and used consequently as a baseline to eliminate the substrate influence in the absorption. The results of the absorbance and transmittance are shown in figure 5.8. Both measurements are complementary to each other and behave correctly within the Visible range: only a low percentage of beam light is reduced by the glass substrate and uniformly. The effect of the NiO absorption can therefore be easily detected when deposited on these substrates.

5.2.2. Optical measurements

In figure 5.9 the absorbance of the thin films measured at RT is shown. The substrate absorbance is plotted in dashed grey line for comparison. In the case of the 100W-1h-RT series, sample grown with pure oxygen has the highest absorbance. In general, films with higher thickness (those grown with 200W of applied power), present the higher absorbance. The intensity of optical absorption structures in the visible range is quite low, as expected from NiO [140, 1], but

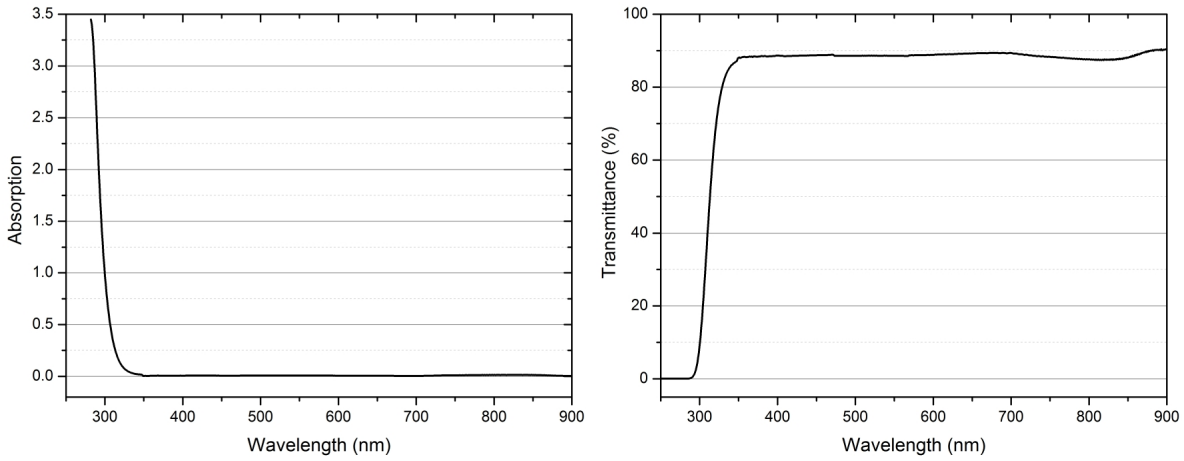

(a) Absorbance (b) Transmittance

Figure 5.8: Absorbance and Transmittance of the glass substrate used in the optical measurements. In the visible region the glass substrates from *Menzel-Gläser* have uniform transmittance.

nanostructured NiO with high defect concentration can give rise to variations with respect the well known single-crystal previous results. Optical absorption in this low-energy range corresponds to $3d^8 \longrightarrow 3d^{8*}$ intraband transitions (the NiO octahedral crystal field splitting is about 1.5 eV). These transitions occur between 3d localized states with no transport of charge where the crystal field and multiplet splittings play an important role, especially in non-stoichiometric NiO. Using these experimental data the optical band gap would be estimated.

5.2.3. Band Gap

The energy band gap of a semiconductor is defined as the energy separation between the lowest state of the conduction band and the highest state of the valence band. The complex shape of these bands depends on the cohesive energy and distances of the atoms in the lattice, the doping, number of defects of the crystal structure and the temperature, which will change the carriers concentration following a Fermi-Dirac distribution and the density and energy of phonons in the lattice. Estimations of the band gap in NiO as obtained from photoemission and X-ray absorption data give values around 4 eV. In this section we will obtain band gap values from the optical spectroscopy data.

If the energetic separation of these bands corresponds to the energy of a photon (usually from IR to UV) then the electrons in the valence band can promote to the conduction band and participate in the electrical conduction. The optical band gap is the threshold above which photons are absorbed by the material. The difference between electrical and optical band gap occurs only in those materials in which it is necessary to create an exciton (an electron-hole pair, electrostatically attracted) and separate it to participate in the electrical transport. The optical band gap is lower in energy than the electrical band gap. However, for Nickel Oxide and many other semiconductors there is almost no difference between the optical and electrical band gap.

The absorption process is the most useful tool to study the band gap of a material, although this method is not free from controversial interpretations. Absorption can be studied in terms of the absorption coefficient, which measures the decrease in light intensity when crossing a distance x through the medium:

$$\alpha = \frac{1}{L(h\nu)} \frac{d(L(h\nu))}{dx} = A \sum P_{ij} n_i n_j \tag{5.6}$$

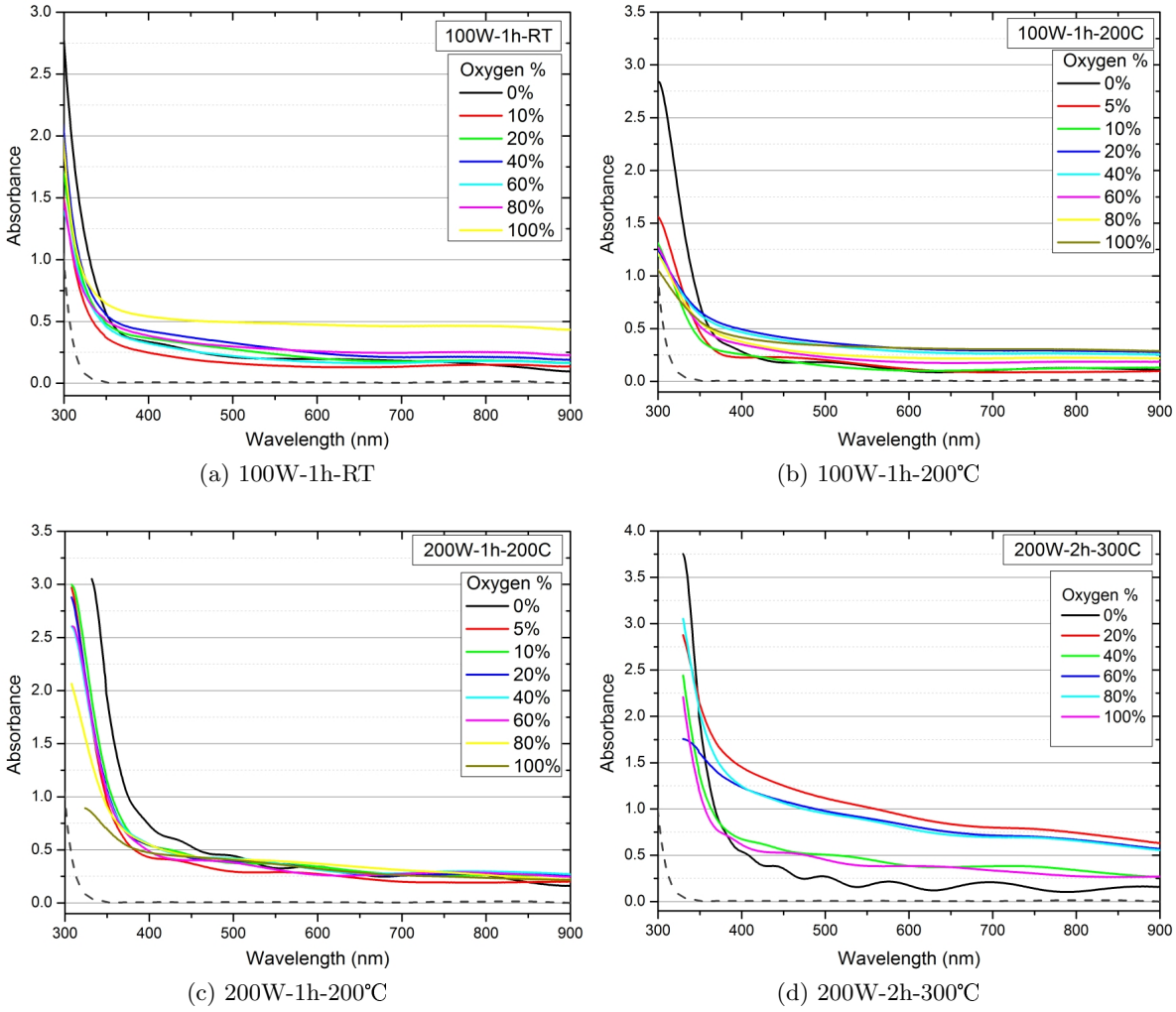

(a) 100W-1h-RT (b) 100W-1h-200℃

(c) 200W-1h-200℃ (d) 200W-2h-300℃

Figure 5.9: Spectral absorbance of NiO films grown over planar glass substrates under different growing conditions as indicated. Substrate transmittance is plotted in dashed grey line.

Where P_{ij} is the transition probability from an initial occupied state i to an empty final state j, n_i is the electron density at initial states and n_j is the density of empty final states [142]. The absorption coefficient decreases fast once the energy drops below the band gap energy.

A method widely used to obtain the band gap of a semiconductor film was developed by J. Tauc *et al.* [143] in 1966. This method is based on several assumptions not always easy to accomplish by different systems, namely the fact that it was developed for amorphous semiconductors in which the electron transition is momentum conservative at high absorption values. The Tauc relation is defined as:

$$(h\nu\alpha)^n = A(h\nu - E_{gap}) \tag{5.7}$$

where h is the Plank constant, ν is the photon frequency, α is the absorption coefficient, A is a constant related to the band tail at higher energies and E_{gap} is the gap energy. The value of n depends on the nature of the transition: $n = 2$ in a direct allowed transition, $n = 1/2$ in a indirect allowed transition [142]. An allowed direct transition occurs between energy valleys of the valence and conduction band in which the momentum is conserved: the transition probability P_{ij} does not depend on the photon energy $h\nu$. An allowed transition is caused by a charge transfer from the ligands (p orbitals of the oxygen) to the central ion (nickel atom in the centre

of an octahedron).

For a forbidden direct transition $n = 2/3$ occurs when the selection rules do not allow a direct transition where the momentum is varied $k' = 0$ but in turn they allow a direct transition where $k' \neq 0$. An indirect transition is a two-step process in which a change in the momentum and in energy occurs. The variation of the momentum is caused by the emission or absorption of a phonon of the lattice. In an indirect transition all the occupied states in the valence band can connect to all the empty states in the conduction band provided that interaction with a phonon occurs. However, the selection rules determine that allowed transition are stronger in intensity than forbidden transitions.

In an absorption process the electron mainly conserves its momentum because the photon momentum, $p_\gamma = \frac{h}{\lambda}$, is much smaller than the crystal or electron momentum, $p_e = \frac{h}{a}$ owing to the difference between the lattice parameter $a \sim 5\mathring{A}$ and the wavelength $\lambda \sim 10^3$ Å [142]. This allows to approximate the problem to the case of amorphous semiconductors: when plotting $(h\nu\alpha)^n$ versus the photon energy $h\nu$, a linear fit in the high energy absorption region can be extrapolated to the neighbourhood of the optical absorption edge. According to the equation 5.7 when the extrapolated line cross the abscissa axis (photon energy) it results $0 = (h\nu - E_{gap})$, and the gap energy is estimated.

The band gap of NiO films has been measured by spectrophotometric methods by many authors, giving values within the range of 3.0 and 4.2 eV, centred at 3.7 eV [123, 121, 122, 78, 91, 92, 144, 145, 146]. All these referenced values were obtained using the Tauc plot to extrapolate the optical band gap. The majority of authors claim to have a direct transition to obtain the energy band gap but generally give no reason for this choice. However, some other authors prefer to use indirect transitions. In our work it was difficult to decide between indirect and direct because in many curves the data could be extrapolated linearly with almost no difference in the R^2 coefficient of the least squares linear fit. According to the experimental results previously shown and the influence of the oxygen content in the plasma and other deposition parameters it is expected to observe a variation of the energy gap, even if this variation is slight. Taking into account the variety of references and the not yet established optical transition theory for p-type NiO we will consider these transitions to be indirect allowed type for our NiO films. Furthermore we expect a variation of the optical properties with the oxygen addition due to the variation in the carrier concentration and this is only obtained through indirect transitions. The visual aspect of films brown-coloured indicates the absorption of blue light, which is in accordance with a lower band gap as obtained from the estimations.

Theoretical approaches of band structure calculations are ambiguous about the transition type although the band gap value is estimated to be between 3.1 eV to 5 eV for transitions within 2p, 3d and the forbidden 3d-4s bands [147, 148, 149].

The Tauc plot of the substrate was calculated in order to distinguish correctly the influence of the glass on the experimental data. According to the manufacturer there is no absorption in the visible region therefore the energy gap of the glass substrate should be above 3.2 eV, i.e.: above the ultraviolet region. Figure 5.10 shows the Tauc plot for the glass substrate, with the linear fit extrapolated to the axis, where it crosses at an energy of $E_{gap} = 4.0 \pm 0.4$ eV, far above the visible region and therefore do not interfere with the measurements of the band gap of the NiO thin films.

Similarly to the approximation carried out for the glass substrate in figure 5.10, the absorption data for NiO films were treated in order to obtain the corresponding Tauc plot. The absorption coefficient multiplied by the photon energy is powered to the n value, that corresponds to an indirect transition, *i.e.*, $n = 1/2$. The results are shown in figure 5.11 for samples of the series 200W-1h-200℃, where the linear extrapolation is depicted only for the sample with the 5% oxygen content. The rest of the linear fits were calculated for all the other samples, obtaining an estimation of the band gap. In the indirect transition for this set of samples the least squares for every linear fit was always $R^2 > 0.996$.

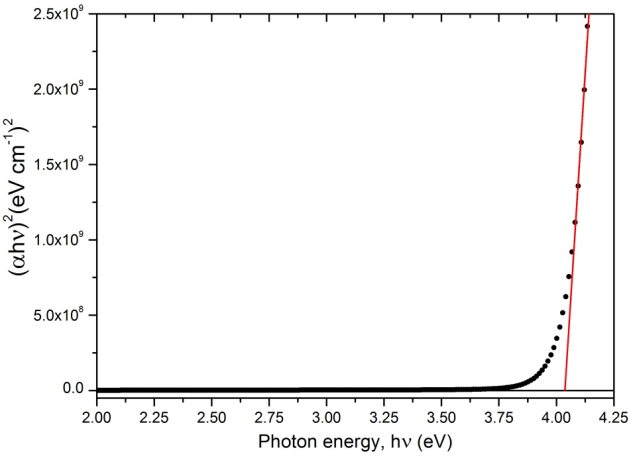

Figure 5.10: Tauc plot of the glass substrate, the linear fit is extrapolated to the energy axis, where it crosses in the proximity of the band gap material.

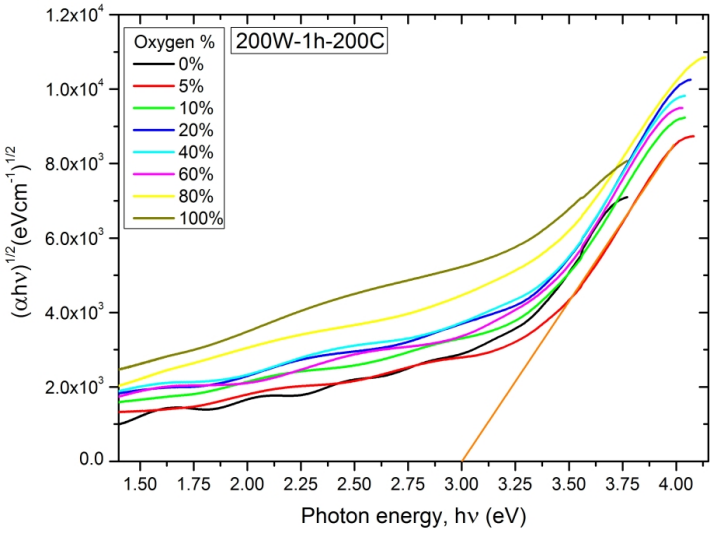

Figure 5.11: Tauc plot of the films deposited at 200W-1h-200℃. Following equation 5.7 the absorption data have been transformed. As an example the linear fit of the 5% oxygen content at high photon energies is extrapolated to the energy axis, the intersect point is the band gap material estimation.

Band gap values were obtained in this way for all samples, and the results are shown in figure 5.12. Transmittance data and absorbance data reported the same band gap values, as expected. In general, a decreasing trend of the band gap with the oxygen content of the plasma can be observed in all cases, except for samples grown at the highest temperature, 300℃. The missing points are due to the impossibility of perform a good linear fit within the high energy range, giving rise to values extremely far from the expected trend.

The reduction of the band gap initiates from the standard value for the optical band gap reported for stoichiometric NiO around 3 eV and then continues progressively until a quite lower value. This final value was coherent with the visual aspect of the brown coloured films. In contrast with other parameters obtained such as grain size or thickness the gradual variation resembles that of the Ni vacancies obtained for EXAFS results for coordination number and will also be supported by XANES results of following chapter. These results suggest that the optical transitions within the visible range are related to the amount of vacancies.

Similar oxides have band gaps close to the one of Nickel Oxide: ZnO in single crystal form

has values close to 3.37 eV [129], CoO which depends greatly on the doping concentration has a band gap of 3.2 eV, TiO_2 has a band gap of 3.2 eV [150], on the other hand semiconductor like CdTe doped with Zn presents values of 1.6 eV [130] and GaN of 3.4 eV [142].

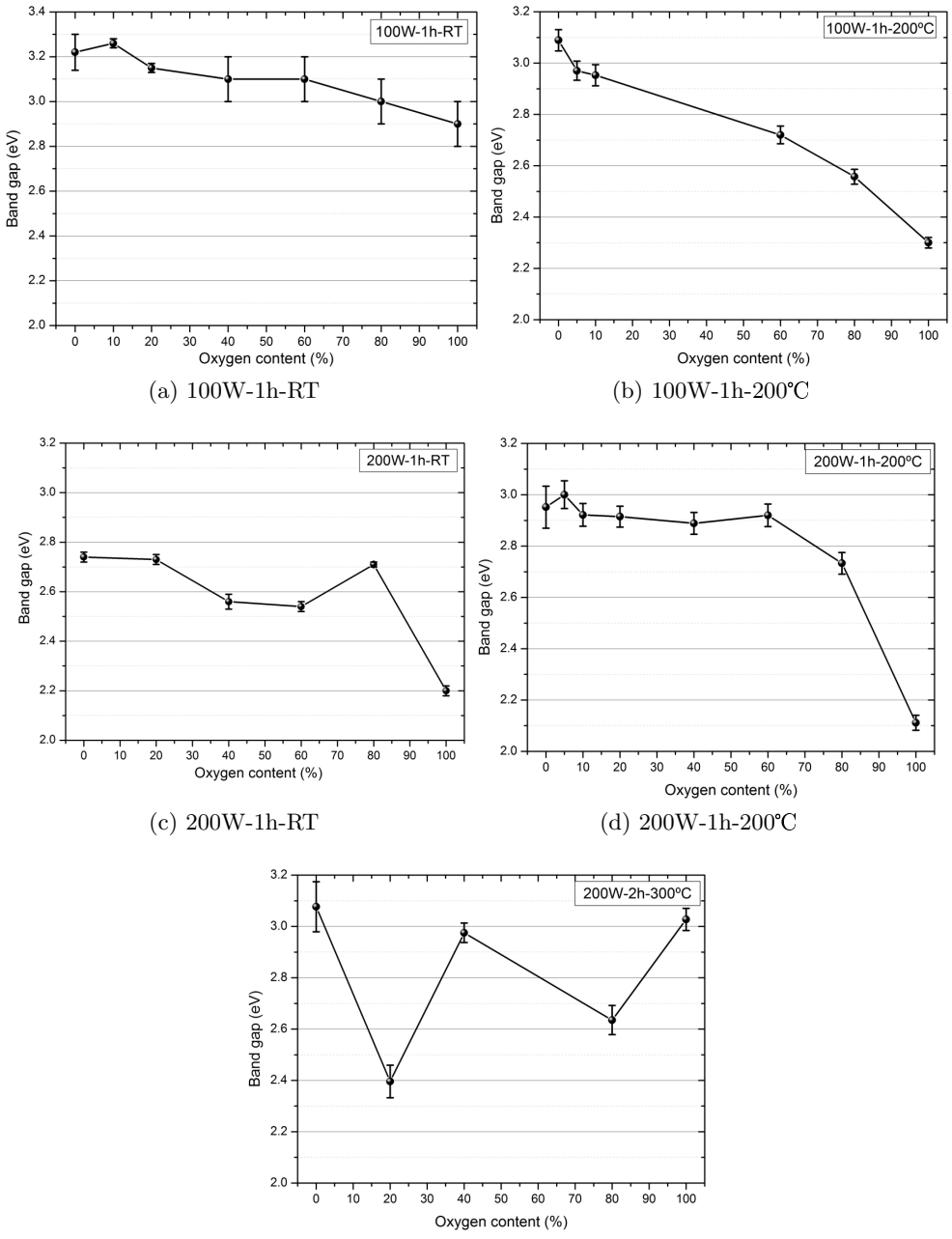

(a) 100W-1h-RT

(b) 100W-1h-200℃

(c) 200W-1h-RT

(d) 200W-1h-200℃

(e) 200W-2h-300℃

Figure 5.12: Energy band gap evolution with the oxygen content in the plasma of the different sets of samples. The band gap values were obtained used the Tauc method considering an indirect transition.

5.2.4. Refractive index and Extinction coefficient

The refractive index is characteristic of semiconductors and metals owing to its absorption component κ, defining this parameter with real and imaginary part as $\tilde{n} = n + i\kappa$, where n is known as the refractive index and κ the absorption or extinction coefficient. The refractive index of the medium is related to the complex relative dielectric constant by: $\epsilon = \epsilon_1 + i\epsilon_2 = (n + i\kappa)^2$.

The resolution of the models to obtain n and k is a complicated task due to the fact that coupled functions arise which are dependent on the film thickness, absorption and reflectance and the incident wavelength.

A set of films grown at 100W-1h-RT was measured with other equipment (with wavelength in the range 300 to 1500 nm) and fitted using the Wemple-diDomenico and Forouhi-Bloomer models for dispersive relations [151]. The results obtained are shown in figure 5.13. The oxygen content in the plasma produces two different regions of values for the refractive index, in which lower oxygen content thin films have values close to 2 whereas higher oxygen content films have refractive index values close to 2.2 as seen in figure 5.13a. The extinction coefficient has a general similar trend although not as correlated with the oxygen addition, as shown in figure 5.13b. The fact that the extinction coefficient increases with the oxygen addition supports the visual aspect of the films, which are darker when more oxygen is added to the plasma even though the thickness is lower. The refractive index and extinction coefficient are decreasing functions with the wavelength, $n(\lambda) \geq 1$ and $\kappa(\lambda) \geq 0$ and $n(\lambda)$ is a convex function. These behaviour and values are similar to those reported in the literature [151, 127, 152].

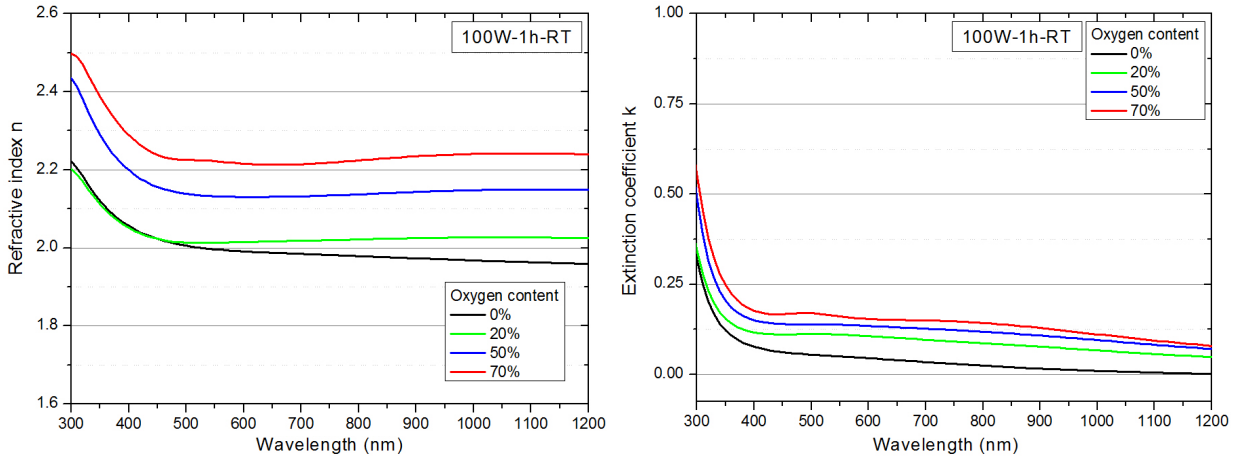

(a) $n(\lambda)$ (b) $\kappa(\lambda)$

Figure 5.13: Refractive index $n(\lambda)$ and extinction coefficient $\kappa(\lambda)$ for thin films grown at 100W-1h-RT. The films grown with pure oxygen have the lowest n and κ values while higher oxygen content generally increases the value of both parameters.

5.3. Summary of chapter 5

In this chapter the optical and electrical properties of NiO coatings deposited by magnetron sputtering under different conditions, as well and their analysis has been shown. The data obtained for the electrical resistivity and energy band gap allowed to correlate the influence of the growth parameters on the final properties of the NiO thin films.

The DC electrical resistivity shows a clear decreasing trend with the oxygen addition to the plasma due to the creation of Ni vacancies. This oxygen addition can reduce the resistivity down to a factor 1000 under certain conditions. The evolution of the NiO thin films p-type conductivity with time shows an ageing effect which can be described by a power law: $\rho \sim t^c$ where t is the time and c is an exponent below the unity, giving rise to a saturation effect. According to this model, non-stoichiometric NiO films recover the chemical equilibrium and reduce their conductivity. This behaviour is similar to the formation of an oxide layer during the oxidation of a metal. Films grown at higher substrate temperatures show lower variation of the resistivity. Under thermal treatment the ageing effects are greatly enhanced.

Optical absorbance measurements have been performed. The band gap has been approximated by the Tauc method giving rise to a gradual decrease of the energy band gap with the oxygen addition at low substrate temperatures. The starting value of the energy band gap is in accordance to that of NiO values found in the literature (around 3.2 eV) and this is gradually reduced with the oxygen addition, as expected from the visual aspect of the films (brown-coloured). Finally a study of the refractive index and extinction coefficient shows an increase of the refractive index with the oxygen addition and low absorption coefficient.

The electrical results suggest a clear effect of the excess oxygen in the transport properties of the NiO films as well as an out-of-equilibrium behaviour which evolves with time. The increase of disorder observed by XRD and EXAFS is coherent with the electrical conductivity, which is enhanced by the oxygen excess within the crystal lattice. The optical absorption shows variations in the band gap of the films with increasing oxygen which suggest the presence of Ni vacancies, supporting the EXAFS results.

Chapter 6

Experimental Results III: electronic structure

"Por primera vez experimenté la magnífica sensación de encontrar una teoría que estaba de acuerdo con las mediciones, una de las experiencias más agradables que he conocido."

Max Born

The electronic structure of transition metal oxides has been thoroughly studied since the foundations of solid state physics. Additionally, the electronic properties of materials have a direct effect on their macroscopic properties. The aim of this chapter is to study the variations of the electronic structure of NiO films under different deposition conditions, and its relation with the macroscopic properties studied in the previous chapter. the electronic structure has been studied by means of X-rays absorption and photoemission spectroscopies, techniques which are sensitive mainly to the surface (except the absorption in fluorescence mode and in transmission mode). This fact, far from being a disadvantage can provide useful information about the surface dynamics of the coatings, for further potential applications where the effective surface plays an important role.

6.1. XANES results

The study of unoccupied states by means of X-ray absorption near edge Spectroscopy (XANES or NEXAFS) is complemented with the information on the occupied states obtained with XPS. Both spectroscopic techniques are based on the excitation of an occupied state by a photon. At a certain energy the excited electron escapes from its initial state and ends in an unoccupied final state. The difference between both techniques used in this work rely on the type of final state. In the case of X-ray Absorption, i.e., XANES, the final states are bound unoccupied states, while in the photoelectron spectroscopy, or XPS, the final states are free vacuum states, whose number is virtually infinite. X-ray absorption spectroscopy is a suitable technique to use to study the electronic structure in the case of Nickel Oxide, because it is very sensitive to the chemical environment and gives information on the covalent character of bondings and on the ground state and symmetry of a specific ion. This method was already applied for studying the electronic structure of Li-doped NiO [153], [136], and that of the nickel perovskites $LaNiO_3$ [154] and $PrNiO_3$ [155].

As explained in section 3.4.8 XANES spectra were collected in the soft X-rays range, at BESSY.

6.1.1. Substrates

XANES spectra from the substrates were obtained to check their quality and to exclude any influence from the substrates on the NiO spectra obtained subsequently. Before start the experiment, the substrates and NiO bulk reference were measured at both beamlines.

The substrates measured were a Si (1 0 0) wafer and a nanoporous Anodic Alumina Membrane (AAM). Figure 6.1 shows the XANES spectra of both substrates as expected, and despite the Si wafer was cleaned as indicated in section 4.1.1 the surface consists of a native oxide layer a few nanometers thick, as observed in the upper curve of figure 6.1. This spectrum, obtained at the oxygen K-edge, corresponds to transitions from 1s core states to empty 2p states, hybridized with Si 2p states, and is typical of SiO_2.

The bottom curve of figure 6.1 represents the XANES spectrum at the O K-edge of the AAM substrate. The absorption peak at 535 eV presents a double band corresponding to the hybridized O 2p states with the Al 3sp. This double structure is assigned to transitions to σ^* and π^* bands [156].

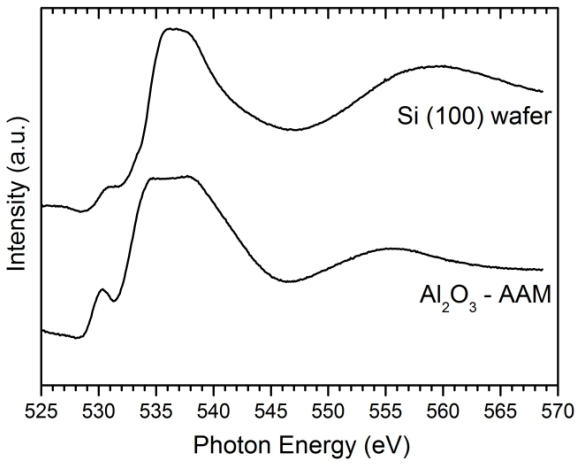

Figure 6.1: XANES spectra at the oxygen K-edge of the substrates used: native oxide layer on the Si wafer and Al_2O_3 in the AAM.

Influence of the beamline optics

The incident signal I_0 provided by the storage ring is itself dependent on variations of the beam, mainly of intensity. The X-ray beam generated at the bending magnet or at the undulator is lately reflected on the different optical elements of the beamline, including the plane grating monochromator, and is focused on the sample, more than 36 m away from the source.

The optical elements of the beamline can absorb a small amount of the incoming X-rays. The transmission function of the beamline can, thus, be influenced by the chemical composition of the optical elements, and, especially, by the surface contamination deposited on top of them. This is particularly important for studies on carbon or oxygen containing samples, since oxygen and carbon are the most typical atoms that contaminate the optical elements surfaces.

In order to estimate the influence of the optical elements and determine the transmission function of the beamline in the region of interest, a cleaned gold foil reference was measured in the same range as the oxygen region (525-575 eV). The gold film was previously cleaned during one hour by an Argon sputtering. The Ar ions were accelerated at 1.5 kV at a pressure of 3×10^{-5} mbar. Gold has no absorption structures at the oxygen K-edge region nor at the nickel L-edge region (the Au L_3 edge is located at 11.9 keV) and behaves monotonically with photon energy. Therefore any peak observed in the Au spectrum within this region can be assigned to contamination of the optical elements of the beamline. If this is the case, the experimental spectra obtained for NiO samples will have to be corrected for this transmission function.

Figure 6.2 shows at the bottom panel a XANES spectrum at the O-K edge of a NiO thin film grown with pure Ar plasma. The middle panel represents the experimental signal from the gold reference sample, which is a measure of the transmission function of the beamline, as explained above. Both spectra are represented at equivalent scales. A small structure can be observed in the spectrum of the gold reference, with broad absorption peaks at 530 eV and 538 eV. These absorption lines, as mentioned above, are due to contamination of the optical elements. However, the relative intensity of these features is rather small as compared with the signal-to-noise ratio observed for the NiO sample. The upper curve is the normalized signal resulting from dividing the spectrum of the NiO sample by the transmission function obtained from the spectrum of the gold foil. Except for an increase in the noise, due to the noisy signal from the gold reference, there is no appreciable variation in the normalized spectrum with respect to the direct spectrum due to the optical elements of the beamline. Therefore, along this work the experimental spectra have not been normalized to the transmission function of the beamline, although the fluctuations in I_0 due to changes in the ring current have been taken into account. A bigger influence of the transmission function would have been observed for the case of very thin samples (thickness lower than 30 Å) due to the small contribution to the absorption spectrum from the film in comparison to the already distorted beam signal. In this work the thickness of every sample measured was in every case larger than 50 nm and, therefore, we are far from the influence of the absorption signal coming from the optical elements. Although it is not expected to have Ni atoms as surface components of the optical elements this possibility was checked as well during the experiment by measuring the Ni L-edge signal on the Au reference sample. We observed no variation with respect to the monotonic behaviour from gold within the L-edge range studied (not shown).

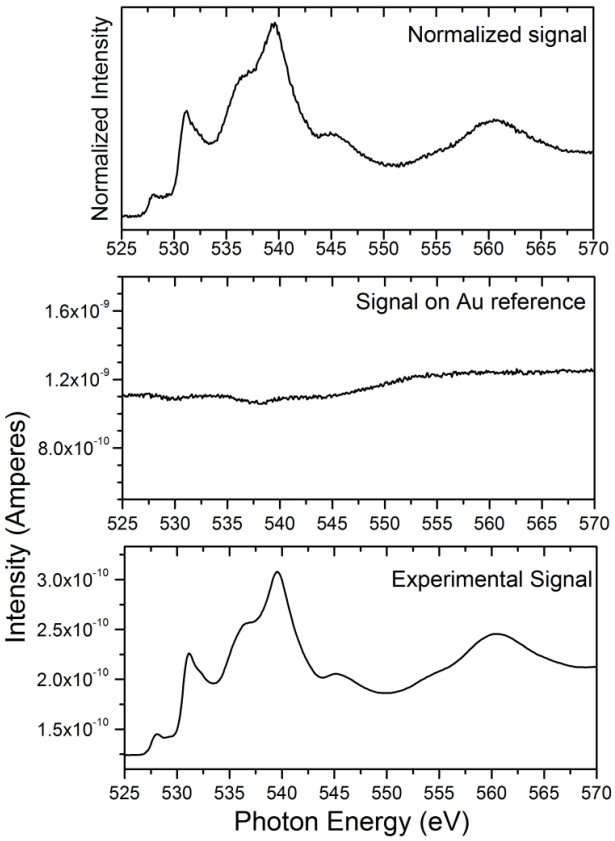

Figure 6.2: XANES spectra at the O-K edge obtained for a NiO thin film grown with pure Ar plasma (down) and for a Au reference sample (middle). The upper curve corresponds to the normalized signal, obtained by dividing the bottom spectrum by the middle spectrum: the possible effect of the optical contamination are negligible.

6.1.2. Crystal field, Ligand field and Multiplet effects

We present here a basic introduction of the different aspects of the complex approaches used to study the electronic structure of an atomic cluster and how they can be extrapolated to a bulk solid. A deep study of these effects can be read in several handbooks [52, 157, 158, 159].

The chemical environment surrounding a transition metal ion affects the energy position of the d levels via differences in electronegativity, hybridization and spacial distribution. As a consequence, in transition metal oxides (with the $3d^n$ band partially filled) the atomic distribution around the metal ion determine the symmetry of the energy levels. Ni $3d^8$ is a paradigmatic case of how this spherical distribution of d-orbitals modify their position to locate themselves in the octahedron of the six oxygen ions (positioned at the vertices of the octahedron). This spatial and energetic rearrangement of the orbitals due to the atomic positions of the neighbour atoms is called crystal field. The overlapping between the d-orbitals of the metal ion and the p-orbitals of the ligand (oxygen) creates new energy states by splitting the atomic states. This splitting is due to the crystal field when reducing the spherical symmetry of the 3d orbitals to an octahedral symmetry, named O_h. The simplest NiO cluster is composed by a Ni atom surrounded by six O atoms located at the vertices of an octahedron. This electrostatic basic model helps to understand the orbital splitting: the atomic Ni orbitals pointing towards the charges (along the lines that connect the Ni and O atoms) are the apical (d_{z^2}) and basal ($d_{x^2-y^2}$) orbitals. These orbitals have higher energy than the other group of threefold orbitals which point toward the space between the point charges: d_{xy}, d_{xz} and d_{yz}, which in the case of the NiO are fully occupied. In the scheme of figure 6.3b) the polar diagrams for these orbital orientations can be seen.

The energy difference between these two groups of orbital energy levels, named Δ in figure 6.3a), depends on the strength of the electric field created between the point charges of the electrostatic model, namely on the distance and magnitude of the charges. As indicated in the crystal field scheme (6.3), the crystal field splitting raises 3/5 of the energy and 2/5 is lowered.

For transition metal oxides the energy splitting values are $\Delta \sim 1-3$ eV, falling in the visible electromagnetic region. For the early transition metal oxides this energy splitting is larger and decreases linearly with n, the filling of the d^n band, being about 1 eV for late transition metal oxides such as NiO and ZnO. In the cluster model calculations the parameter of the crystal field splitting is also defined as $10Dq$ instead of Δ.

As shown in figure 6.3a) a further splitting can occur. When the point charges along the z-axis are removed or the octahedral distorted along this axis, the energy of the e_g orbitals increases for $d_{x^2-y^2}$ while the energy of orbital d_{z^2} decreases. This happens as well to the t_{2g} levels, in which the orbital component d_{xy} increases in energy because it has no z-dependence while orbitals d_{xz} and d_{zy} lower their energy. This last splitting is due to the distortion that changes the octahedral symmetry O_h to a tetragonal D_{4h} symmetry [160]. The four energy levels of D_{4h} symmetry are labelled b_{1g}, b_{2g}, a_{1g} and e_g, decreasing in energy. This distortion will be shown in XANES and XPS spectra.

When the interaction between the ligand charges and metal atom is strong enough then they can no more be treated as point charges. Therefore the crystal field must be improved by means of the *Ligand Field* approximation. This approach rely on the molecular orbitals (MO) treatment, which takes into account the overlap between the d^n orbitals of the metal and the orbitals of the ligand atom, L, (oxygen in our case) forming the electronic shell instead of using only pure d orbitals. The overlapping (80% of metal d and 20% of ligand orbitals) gives rise to the 3d band observed in the XANES spectrum. For our case of metallic nickel atoms, the orbital filling is Ni:[Ar]$4s^2 3d^8$, thus $n = 8$ (the filling number of the transition metal). The ligand (O) atoms have the following orbital filling: O:[He]$2s^2 2p^4$.

The ligand molecular orbitals are divided into σ (bonding) and π (antibonding) depending on whether they are cylindrically symmetrical with respect to the ligand-metal bond or not, respectively. The σ-bond is symmetrical while the π-bond is not. Therefore, the energy of the

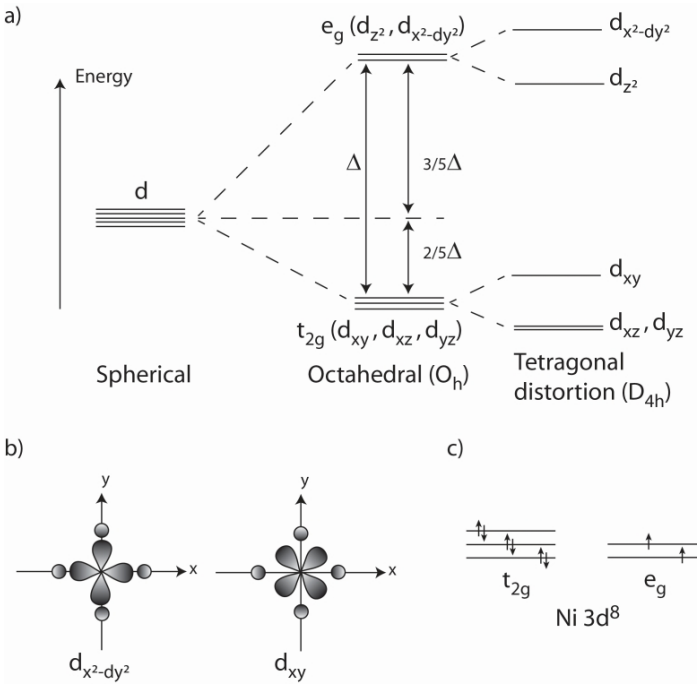

Figure 6.3: Crystal field scheme: a) Splitting due to Octahedral symmetry from spherical 3d to t_{2g} and e_g states: two energy levels appear. b) Polar diagrams for atomic orbitals: orbitals like $d_{x^2-y^2}$ point toward the ligand charges while orbitals d_{xy} point toward the separation between the charges, lowering its energy. c) Spin-up configuration in the split states: t_{2g} is filled while e_g has two holes.

σ-bond is higher than the π-bond. The σ-bonds are as well classified into a_{1g}, e_g and t_{1u} orbitals within the octahedral O_h symmetry [157]. In an octahedral system the metal e_g orbitals, which point directly to the oxygen ligands, form strong σ-bonds with the oxygen p_z orbitals. Among the e_g states, the d_{z^2} levels form σ-bonds with apical oxygen p_z orbitals while levels $d_{x^2-y^2}$ form σ-bonds with basal p_x and p_y orbitals. On other hand the metal t_{2g} orbitals form π-bonds with the oxygen p_x and p_y orbitals. This bonding and antibonding fact is useful to study systems with linearly polarized radiation, due to the polarization-dependence of these bonds [157]. In O_h symmetry, there are a_{1g}, t_{1u}, t_{1g}, t_{2u} and t_{2g} states, where a_1 has angular momentum L=0 (s-like orbital), t_1 has angular momentum L=1 (p-like orbital) and t_2 and e have both angular momentum L=2 (d-like orbital), from all these states only t_{2g} and e_g molecular orbitals take part in the hybridization between the transition metal (Ni) and ligand (O) atomic states.

The electron spin arrangement in the orbitals of octahedral symmetry is shown in the scheme of figure 6.3c), where the spin-up configuration is represented. This configuration has the lowest energy, being the high-spin ground state $^3A_2$ though different final states of higher energy include holes in the t_{2g} sub-band and a different spin configuration, raising the energy. The configuration interaction method takes into account the spin configuration for the possible final states with one or more holes.

The so-called multiplet effects are a group of interactions found in the set of initial and final states. Within the single-particle density of states the Hamiltonian which describes the set of initial states (the ground state $3d^N$) is dominated by the Coulombian interaction between the 3d-3d states. The final states, composed by a set of empty states ($2s^2 3d^{N+1}$), have two terms related to the core-hole (2p is the case of the L-edge): the spin-orbit coupling of the 2p hole (which generates the splitting into $2p_{3/2}$ and $2p_{1/2}$) and the 2p-3d Coulomb and exchange interaction. Therefore the Hamiltonian which describes this atomic multiplet has these three terms. Anyhow, the atomic multiplets have no visible effects on the 3d metals K-edge while they have an important role in the interpretation of the L-edge [161]. Further models to simulate the

bulk solid add another term due to the crystal cubic symmetry [162]. Here we will not cover any study of these different approaches, which are beyond the scope of this experimental work, but more information can be found in the comprehensive book of F. De Groot [52].

6.1.3. O K-edge and Ni L-edge features

In this subsection the main structures of the oxygen K-edge and nickel L-edge X-ray absorption spectra will be explained. The origin of some structures depends greatly on the distribution of the orbitals, its hybridization strength and the presence of ions in the bulk crystal lattice.

Oxygen K-edge structures

The XANES spectra at the oxygen K-edge measured for our NiO bulk reference and a nanostructured NiO thin film are shown in figure 6.4. The main structures are labelled according to the molecular orbital diagram of a Nickel Oxide molecule [163]. XANES can provide an approximation to the density of unoccupied states within a solid. In the case of the oxygen K-edge this technique explores the density of states (DOS) p-projected and the shape of the spectrum is proportional to n, the number of d^n electrons, the spin configuration and the crystal structure. The structures observed are only those allowed by the dipolar selection rules for electronic transitions, where the orbital quantum number l must change in one unit: $\Delta l = \pm 1$.

However, some of the final states observed in XANES are due to covalent hybridization of the Ni 3d and O 2p states, where transitions from the O 1s can occur, relaxing the selection rule. If there were no p-d hybridization the intensities of the structures in the XANES spectrum (the 3d band at 532 eV in figure 6.4) would be zero for both curves due to the forbidden $s \rightarrow d$ transition. The degree of interaction between the metal nd and O 2p orbitals is named hybridization strength.

The peak at 532 eV is assigned to the Ni 3d crystal field splitted e_g states, which are unoccupied in the 3d shell. In our nanostructured NiO films, this peak has a double structure, marked with dashed vertical lines, due to an additional splitting caused by surface effects whereas in the bulk reference the 3d contribution is sharper and does not present such a splitting, being formed by just one peak, see figure 6.4. This surface splitting of the e_g states in the nanostructured film has two contributions: one from the octahedral clusters NiO_6, which contribute to the main peak at 531.8 eV and a second one from the incomplete octahedral cluster NiO_5, at 532.8 eV, where the apical oxygen is missing. An incomplete octahedron cluster distorts the crystal field splitting breaking the double degeneration and raising the energy by around 1 eV of the orbitals in plane of the octahedron's square ($e_g : d_{x^2-y^2}$) with respect to the vertical orbitals pointing to the apical oxygen ($e_g : d_{z^2}$) [164, 165], as shown in the energy levels diagram of figure 6.3a). In the nanostructured NiO, the upper curve of figure 6.4, the pre-peak before the oxygen absorption edge is assigned to Ni vacancies, where O 2p states are mixed with $Ni^{3+}3d$ states [153].

The structures above 535 eV are usually assigned to hybridization between Ni 4s and Ni 4p states with oxygen 2p states: the molecular diagram of NiO [163] assigns the hybridization between Ni 4s and O 2p states as σ-bonding a_{1g} at 537 and 540 eV, and that between Ni 4p and O 2p states as σ-bonding and π-antibonding states at t_{1u}. Actually, further possible final states at energies above 540 eV are normally not assigned within the molecular orbital diagram terminology but in the multiple-scattering approximation, which is said to arise from long- and medium-range contributions due to several single-scattering processes between the oxygen (absorber atom) and the nickel (neighbour atoms). At 561 eV the structure is associated to a single-scattering process between the absorber atom and the second oxygen shell (second neighbour) [166, 167]. Similar structures have been previously reported in the literature, obtained both with XANES and Electron-Energy Loss Spectroscopy (EELS) techniques [166, 167, 168, 169]. This is an example of how the XANES and EXAFS techniques connect as the energy shifts far above the absorption edge until a point where it is difficult to distinguish the border of application of the different approaches. However, only a complex treatment of the experimental XANES data such as that

carried out for the EXAFS data presented in section 4.4 could show a variation of the disorder, lattice parameter and coordination number. Such a treatment was not performed in the XANES data due to the additional complexity of the oxygen region.

As can be seen in figure 6.4, the spectrum of the nanostructured sample has broader structures. This broadening can be explained in terms of the crystal grain size. The width of a XAS peak depends inversely on the lifetime of the excited state. Following Heisenberg uncertainty in energy, a decrease in this lifetime leads to an increase in the energy uncertainty and, consequently, to a broadening of the spectral features. Such a decrease in the lifetime occurs when the crystal grain size decreases in the nanoscale. Consequently, the smaller the grain size, the broader the structures in the XAS spectra. Also the disorder of the crystal lattice and the experimental broadening in determining the energy (bandwidth of the experiment) have an effect on the peaks width. But above all we can remark the fact that the width of a peak is inversely proportional to the lifetime of a state [52], and, therefore, for equal experimental conditions, the smaller crystallite size the larger the peak width. This will be repeatedly observed throughout this chapter when the growing conditions are varied for different coatings and when an annealing is performed.

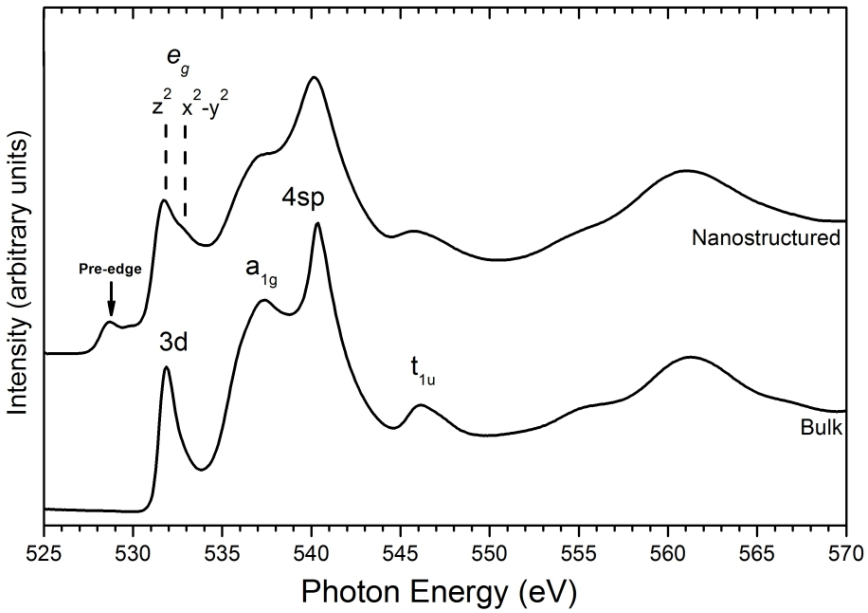

Figure 6.4: XANES signal obtained at the oxygen K-edge in nanostructured and bulk NiO. The structures assigned are: before the edge the pre-peak related to the $Ni^{3+}3d$ states, the Ni 3d peak with the double structure due to surface effects and the multiple-scattering effects or higher final hybridized states between Ni 4s and Ni 4p with O 2p.

Nickel L-edge

Using soft X-rays the Ni L edge region was studied as well. The peak positions and relative intensities of the L edge structures in a metal are related to their oxidation state. This is due to the variation of the resonance energies for the transitions $2p \rightarrow 3d$ with the average electrostatic energies of the metal, which can shift with the valence electrons [49]. In our work these L edge structures do not vary, showing that the Ni oxidation state is the same under different deposition parameters.

In figure 6.5 an example of this region measured for the NiO bulk reference is shown. The Ni L-edge double structure corresponds to the 2p splitting due to the spin-orbit interaction into $2p_{3/2}$ and $2p_{1/2}$, as labelled in the figure. According to the single-particle scheme the relative

intensities of these two peaks should be 2:1 due to its electron filling (four electrons in the $2p_{3/2}$ and two in the $2p_{1/2}$). However, this relation is not observed experimentally due to more complex effects (strong spin-spin coupling, multiplet effects, etc.) in any of the 3d transition metal oxides. The energetic separation between these structures should be 3/2 of the spin-orbit coupling. More details about this intensity relations, its different trends and possible explanations can be found in [49] and references therein.

Each of these spin-orbit structures have their own substructure labelled A, B and A', B' in figure 6.5. These further subdivisions are due to the octahedral crystal field splitting, affected by the ligand-field interaction [49, 162]. The dipole selection rule ($\Delta l = \pm 1$) allows transitions from 2p electrons into empty states 3d or 4d. In transition metal oxides for lower occupancy in the d^n orbitals occur both transitions $2p \rightarrow t_{2g}$ and $2p \rightarrow e_g$ but in our system, due to the completely filled t_{2g} orbitals in the $3d^8$ configuration, only the channel $2p \rightarrow e_g$ is open.

The fact that this last subdivision depends on the exchange interactions makes the L edge structures sensitive to the local symmetry of the initial state, as will be shown. The low intense and wide structure labelled as C is assigned to be a transition $2p \rightarrow 4s$ to the continuum ligand states [3, 164].

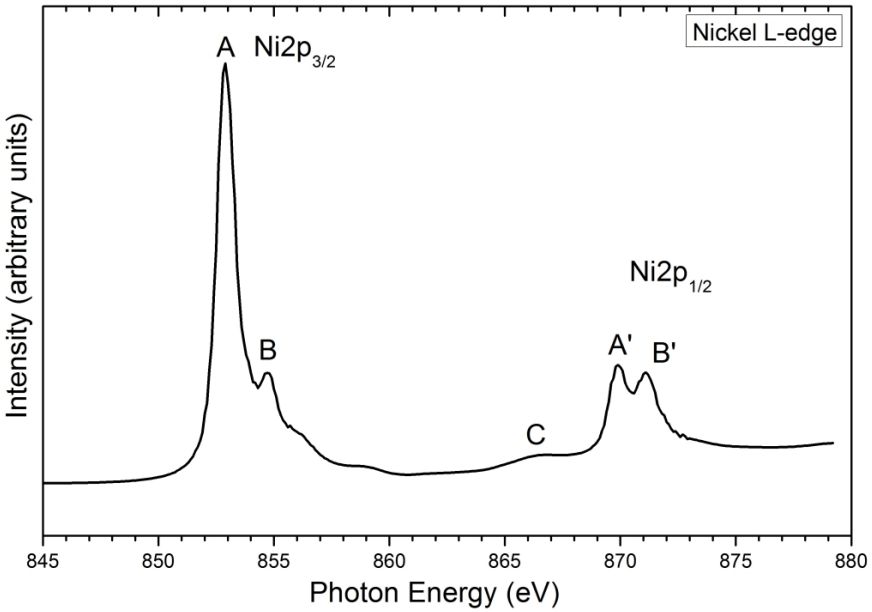

Figure 6.5: Experimental XANES signal obtained at the nickel L-edge for the NiO bulk reference. The two main structures correspond to the 2p doublet split by the spin-orbit interaction in $2p_{3/2}$ and $2p_{1/2}$. Within each peak a further split occurs due to ligand-field interaction, creating the substructures A,B and A',B'. C peak is due to allowed dipolar transitions to 4s states, which have a much lower probability to occur.

6.1.4. XANES results

In this section, XANES results obtained on NiO films grown under different conditions will be shown, with special attention to the oxygen content of the plasma. Figure 6.6 shows XANES spectra at the O K-edge of thin films grown at 200W-1h-RT on nanoporous AAM (figure 6.6a) and Si (100) (figure 6.6b) substrates.

Figure 6.6a shows from bottom to top the absorption spectra of the NiO thin films grown on AAM substrates with increasing oxygen content in the sputtering plasma, being the bottom curve the NiO bulk reference (non-nanostructured) for comparison. The spectrum for the sample with no oxygen content (0%) is in very good agreement with the spectrum for bulk NiO shown in the curve at the bottom as well as with other results taken from the literature [153, 170, 171, 164].

The absence of O_2 during the sputtering deposition could lead to a decrease in the oxygen content of the films, and hence to partially reduced NiO. This would be evidenced by the presence of metallic Ni in the films. However, no traces of metallic Ni were observed either in the XAS spectra or in XPS (which will be shown in section 6.2), as reported in our own work [172].

The structures observed in an oxygen K-edge spectrum, as shown in figure 6.6a, are classified in two groups regarding its origin:

The first group, close to the absorption edge, is composed by those structures due to the hybridization of the empty O 2p states covalently mixed with the Ni^{2+} 3d states, at around 532 eV. The small component, at 532.8 eV, is attributed to the splitting of Ni 3d orbitals, due to surface effects [165]. This splitting generates the t_{2g} and e_g peaks, marked in figure 6.6a with dashed vertical lines. The e_g orbitals contain only two electrons of its four possible and is therefore half-filled so that they can be seen with XANES, which explores the accessible empty finals states.

The second group, above 535 eV are empty O 2p states covalently mixed with Ni 4sp states. These states are less influenced by the variation of the film deposition parameters.

On the other hand, when samples are grown in the presence of O_2 there is a change in the Ni 3d region of the spectra. The surface related contribution, at about 533 eV, becomes more prominent, and a new feature appears, at around 529 eV. This new peak is attributed to O 2p states mixed with Ni^{3+} 3d states [153]. Quadrupolar transition has about 1% of probability of the permitted dipole transition to occur therefore its influence in the final spectra can be neglected. If the symmetry of the O_h is distorted the pre-peak is highly enhanced. In this work the addition of oxygen to the sputtering plasma creates Ni vacancies, as seen by EXAFS, and increases greatly the effective surface, as seen by SEM and XRD results.

The relative intensity of these features indicates that the oxygen content during growth causes two effects: (i) an increase in the surface-to-bulk ratio in the samples, and (ii) an increasing presence of Ni vacancies. The first effect is attributed to the diminution of crystalline size when the oxygen content in the plasma increases, a fact already presented in section 4.3.1. On the other hand, the increase of the pre-edge feature in the O 1s XAS spectra, attributed to Ni^{3+} states induced by the presence of Ni vacancies, can explain the increase of the electrical conductivity of the NiO films with the oxygen content in the plasma during growth. This pre-edge related to Ni vacancies in the crystal structure has been recently found in NiO with ferromagnetic dislocations by EELS analysis [173].

As observed in figure 6.6 there is almost no difference between samples grown on Si and AAM substrates. This can be explained by the fact that the decrease of the crystallite size with the oxygen content, as shown in chapter 4, implies an increase of the interfaces between crystallites within the grains. This enhanced surface is due to the NiO crystal size, which is smaller than the porous structure of the AAM substrates, so the properties of the films are independent of the substrate used.

Figure 6.7 shows the same spectra already shown in figure 6.6a, but superimposed and normalized to the NiO bulk reference sample, which makes it easier to appreciate the changes upon oxygen addition. The magenta coloured curve represents the bulk NiO reference and the black curve is the pure Argon grown film, considerably different from the other samples with higher oxygen content in the plasma.

XANES L-edge spectra for samples grown at 200W-1h-RT are shown in figure 6.8. Again the bottom curves represent the 2p doublet of the NiO bulk reference while the curves from bottom up have an increasing oxygen percentage in the sputtering plasma. The 2p doublet represents the $2p^6 3d^8 \rightarrow 2p^5 3d^9$ transitions, which are separated by spin-orbit interactions into the Ni $2p_{3/2}$ and Ni $2p_{1/2}$ components, and further split by multiplet effects in two main features, AB and A'B', respectively, as mentioned in subsection 6.1.3.

Again, the result for the sample with no oxygen content (0%) is similar to a typical NiO spectrum [3]. The spectra do not change much when samples are grown in the presence of O_2.

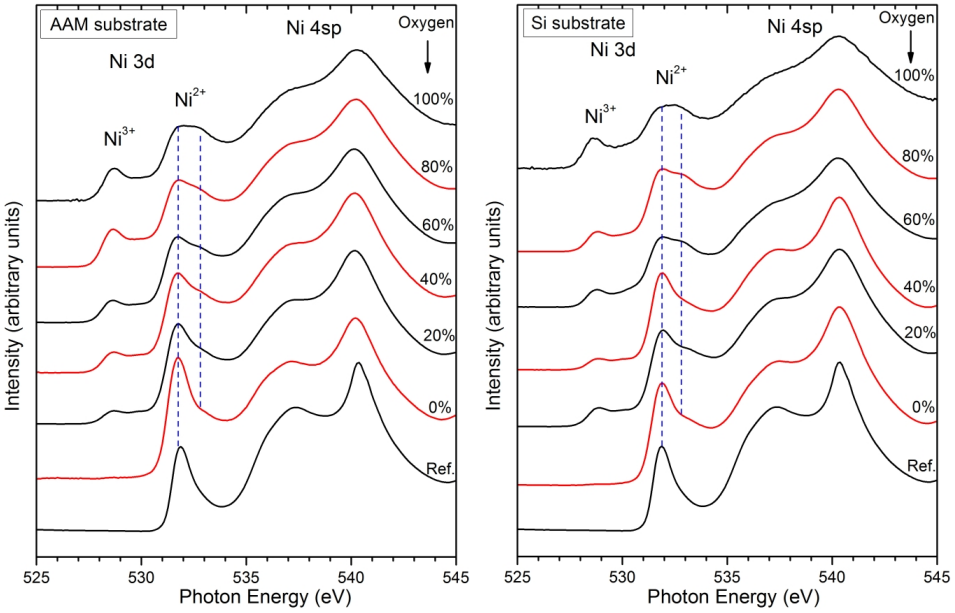

(a) AAM substrate (b) Si substrate

Figure 6.6: XANES spectra of the evolution of the O K-edge of NiO films grown at 200W-1h-RT on AAM and Si substrates. The bottom curve represents the NiO bulk reference. The pre-edge at about 528 eV due to Ni^{3+} ions is present when oxygen is added to the sputtering plasma and increases its intensity with this addition. The splitting of the 3d band due to surface effects increases as well with the oxygen content and peaks broaden for higher energies (Ni 4sp states). These structures behave similarly on both substrates.

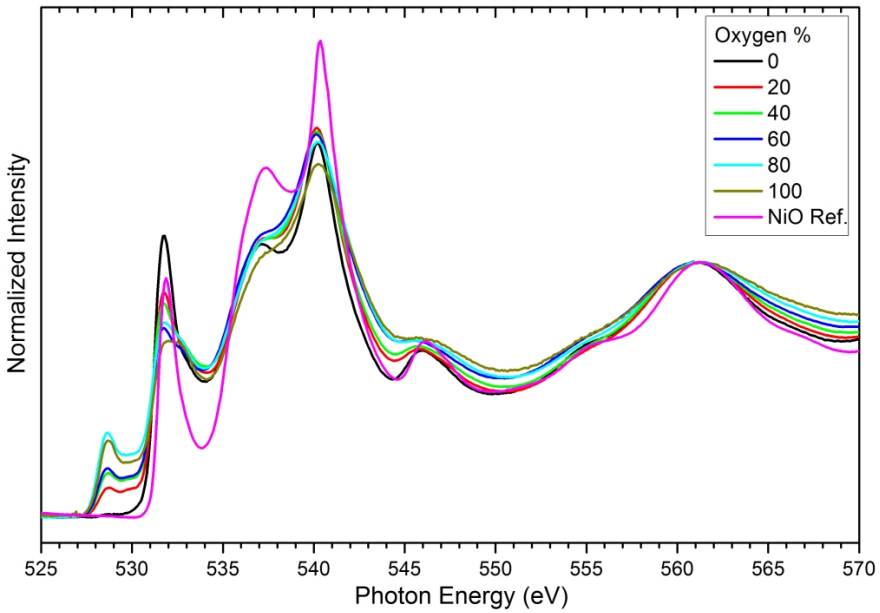

Figure 6.7: Normalized XANES oxygen K-edge spectra of samples 200W-1h-RT (on AAM substrate): the variation of the different structures with the oxygen addition is clearly observed. These data are the same as in figure 6.6a but in this case are superimposed in order to observe the evolution of the structures: the increasing pre-edge with oxygen addition, the surface splitting and the consequent broadening of the peaks due to a more hybridized system and smaller grain size.

The only difference is that the intensities of peaks B and B' become slightly larger as the O_2 content increases. At first, this seems to contradict the results for the O 1s XAS where we had great variations on the spectra but, as we will show in the next subsection, smaller effects on this absorption edge are expected.

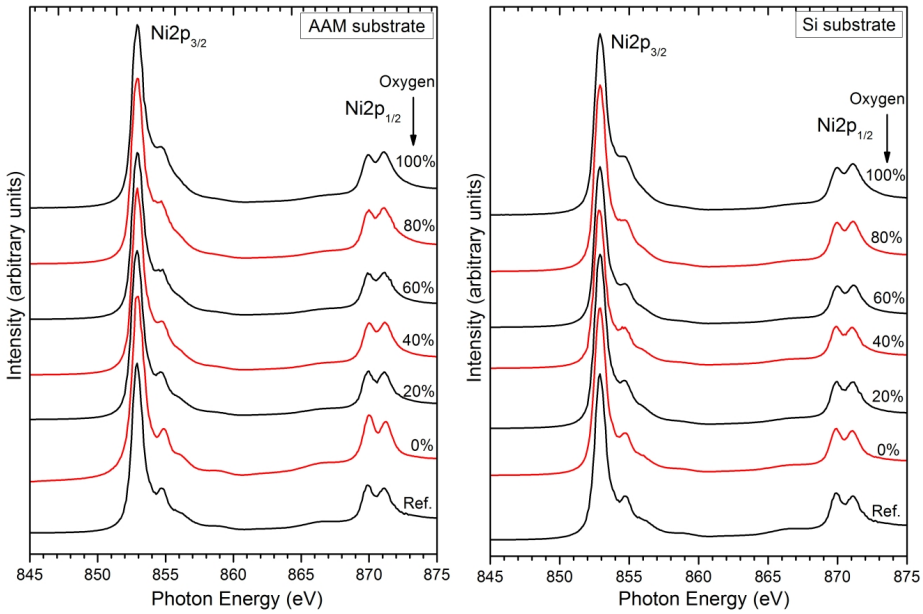

(a) AAM substrate (b) Si substrate

Figure 6.8: XANES spectra of the evolution of the nickel L-edge of NiO films grown at 200W-1h-RT on AAM and Si substrates. Similar structures as in figure 6.5 are observed: the main spin-orbit splitting and the further substructures (into A,B and A,B') due to ligand field interaction. Almost no tendency is observed apart from a slight increase of the A and A' with respect to their minor companion (B and B').

6.1.5. Cluster model calculations

Theoretical calculations are able to describe the XANES spectra to certain degree of accuracy. In condensed matter systems and in particular in the transition metal oxides the cluster model and the multiple-scattering calculations are two of the most used methods. Cluster model calculations are useful with both ordered and disordered systems. However, some structures (the double a_{1g} and the t_{1u} in figure 6.4) of the oxygen K-edge are not well reproduced by the multiple-scattering. This is due to the strong 3d-2p hybridized ground-state wave function of NiO, which is no longer a simple $3d^8$ but instead:

$$\Psi_0 = \alpha \left|3d^8\right\rangle + \beta \left|3d^9\underline{\mathrm{L}}\right\rangle, (\alpha^2 + \beta^2 = 1) \tag{6.1}$$

where $\underline{\mathrm{L}}$ denotes a hole in the ligand (oxygen) valence band. This relation is an approach of the regular octahedron NiO_6 cluster [4].

As observed in the previous section the experimental results obtained on the NiO thin films show variations with the addition of oxygen to the sputtering plasma: an e_g surface splitting occurs due to an increase of the surface-to-volume ratio; a pre-peak appears due to the presence of Ni vacancies, which create Ni^{3+} states, and slight variations of the Ni 4sp final states are detected. In order to quantify the effect of each different contribution, cluster model calculations were performed to account for the pre-peak and the surface splitting effect.

We used the standard configuration interaction method to elaborate the cluster calculations. This method consists in the resolution of the Schrödinger equation for a many electron system, the

atomic cluster of NiO. Two clusters have been used in the simulations: a regular octahedral NiO_6 for NiO in a bulk environment, and a pyramidal NiO_5 truncated octahedron which simulates NiO at the surface. Even for such a small cluster the calculations are complex and require time and CPU resources, therefore the calculations must be truncated at a certain point under several assumptions (more details for a similar system can be found in the work of R. Mossanek *et al.* [174]). The Hamiltonian which describes the cluster model is separated into two terms: an intra-cluster term which describes the Ni 3d-O 2p charge fluctuations of the octahedrons (regular and truncated) and the inter-cluster term of the Hamiltonian, which describes the metallic phase charge fluctuation. The Hamiltonian is solved by diagonalization and the ground state, the state without electron and with an added electron, are expanded as combinations of charge transfer configurations: d^n, $d^{n+1}\underline{\mathrm{L}}$, $d^{n+2}\underline{\mathrm{L}}^2$, etc.

Oxygen K-edge calculations

The ground state is expanded further than in relation 6.1 taking into account different configurations of possible hole states: $3d^8, 3d^9\underline{\mathrm{L}}, 3d^{10}\underline{\mathrm{L}}^2$, $3d^{11}\underline{\mathrm{L}}^3$. The addition state wavefunction is expanded in the $3d^9, 3d^{10}\underline{\mathrm{L}}, 3d^{11}\underline{\mathrm{L}}^2$. The weight in the spectra is calculated by the sudden approximation [175].

The parameters used in the calculations are the charge transfer energy Δ, the d-d Mott Hubbard repulsion U, and the p-d transfer integral $pd\sigma$. Each state configuration is subsequently split by multiplet effects, expressed in terms of the Racah parameters (B, C) and the crystal field splitting $10Dq$ or Δ, previously introduced. The Racah parameters are a linear combination of normalized Slater-Condon parameters, F_k, which represent the radial integrals used in the calculations of the direct Coulomb repulsion and Coulomb exchange interaction, within the charge transfer multiplet theory [52].

The values presented in table 6.1 were used in these calculations already published [175] as well as in previously investigations related to Nickel Oxide [176, 177, 154]. The different ground

Parameter	Ni^{2+}	Ni^{3+}
Δ	4.0	1.0
U	7.5	7.0
$pd\sigma$	1.5	1.8
B	0.13	0.16
C	0.58	0.60
$10Dq$	1.0	1.2

Table 6.1: Cluster model parameters for O K-edge (values in eV)

state configurations for Ni^{2+} and Ni^{3+} were calculated individually. There are two contributions: one of the bulk with octahedral symmetry for the NiO_6 cluster, where the interaction between p-d electrons in the e_g band is given by $T_\sigma = \sqrt{3}pd\sigma$, and the second one with pyramidal symmetry from the surface with a truncated octahedron NiO_5, where the interaction between the p-d electrons is in this case split into $T_{basal}=T_\sigma$ and $T_{apical}=0.6\,T_\sigma$ due to the absence of an apical oxygen.

In table 6.2 the two ground states decomposition is presented. The Ni^{3+} calculation is in negative charge transfer regime due to the larger $3d^9\underline{\mathrm{L}}$ contributions and the $3d^7$ configurations is in a low spin state ($t^3_{2g\uparrow}t^3_{2g\downarrow}e^1_{g\uparrow}$). Figure 6.9 presents the oxygen 1s XANES spectra calculated for octahedral Ni^{2+}, pyramidal Ni^{2+} and Ni^{3+} ions. The relative intensities of these discrete final states were preserved but the absolute energy scale was shifted to best agreement with the experimental O K-edge XANES spectra. The experimental data have to be taken into account to be broader than the model calculations. This intrinsic broadening arise from lifetime

Ground State	$3d^8$	$3d^9\underline{L}$	$3d^{10}\underline{L}^2$	$3d^{11}\underline{L}^3$
Ni^{2+}	79%	20%	1%	-
Ni^{3+}	34%	58%	7%	1%

Table 6.2: Ground state occupancy for O K-edge

effects, vibrations and hybridization. Therefore the calculations were convoluted with a 0.3 eV Lorentzian and a 0.5 eV Gaussian function, to simulate lifetime and experimental broadening effects, respectively.

The Ni^{2+} calculations show final states mainly related to the $3d^9$ configuration. In octahedral symmetry, there is only one structure, at 531.8 eV, related to the addition of an electron to the e_g sub-band. In pyramidal symmetry, the e_g degeneracy is split into two contributions, at 532.4 and 533.0 eV, due to the addition of an electron into the apical (z^2) or basal ($x^2 - y^2$) sub-bands. The Ni^{3+} calculations are similar to those in previous reports [154] and show final states mainly related to the $3d^8$ configuration. The structures appear at lower energies than in the Ni^{2+} case, at around 528.6, 529.5 and 530.3 eV, and are attributed to the addition of different majority or minority spin e_g electrons, because of the low spin state of Ni^{3+} ions.

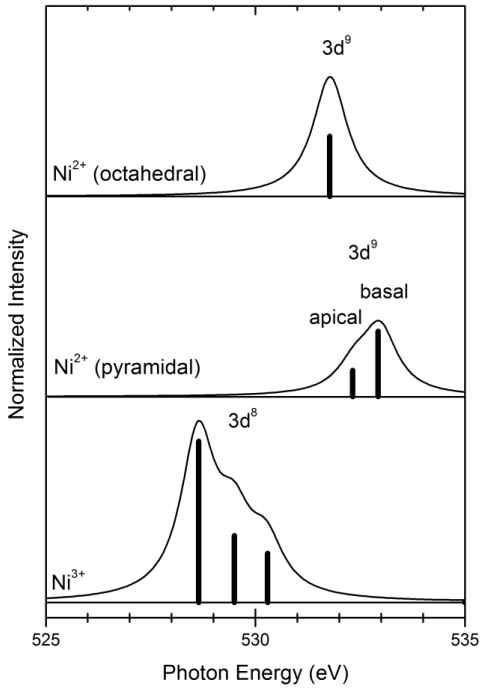

Figure 6.9: Calculated O K-edge XANES contributions for octahedral Ni^{2+}, pyramidal Ni^{2+} and Ni^{3+} ions.

Figure 6.10a shows calculated O 1s XANES spectra for samples with different oxygen concentrations grown at 200W-1h-RT and the weights of the different contributions. The labels at the right indicate the amount of oxygen in the sputtering plasma. The calculated contributions are shown in figure 6.10b: the total spectra are the sum of the calculated octahedral Ni^{2+}, pyramidal Ni^{2+}, and Ni^{3+} contributions, which were weighted in order to give the best agreement with the experimental results. These spectra have been obtained after being convoluted with Lorentzian and Gaussian functions as mentioned above.

The spectrum for the sample with no oxygen content (see figure 6.10a) is formed only from Ni^{2+} contributions, 60% in octahedral (bulk) and 40% in pyramidal (surface) symmetries. In contrast, the spectrum of the sample grown with 100% O_2 content is formed from 14% of Ni^{3+}

and 86% of Ni^{2+} contributions, which are split into 30% octahedral (bulk) and 56% pyramidal (surface) ones. The fact that according to the cluster calculations the pure oxygen growth has an amount of 14% of Ni^{3+} ions is in agreement with the already estimated values from the EXAFS results, which show a reduction of 10% in the coordination number for the case of 70% oxygen growth (although those EXAFS calculations were performed on measurements of 100W-1h-RT thin films).

Again, the results indicate that the relative intensity of these features seems to be directly influenced by the O_2 content during growth. Not only is the intensity of each contribution linearly proportional to the oxygen content during growth (see figure 6.10b), but also both Ni^{3+} and pyramidal Ni^{2+} parts have the same rate of increase, in detriment to the octahedral Ni^{2+} contribution.

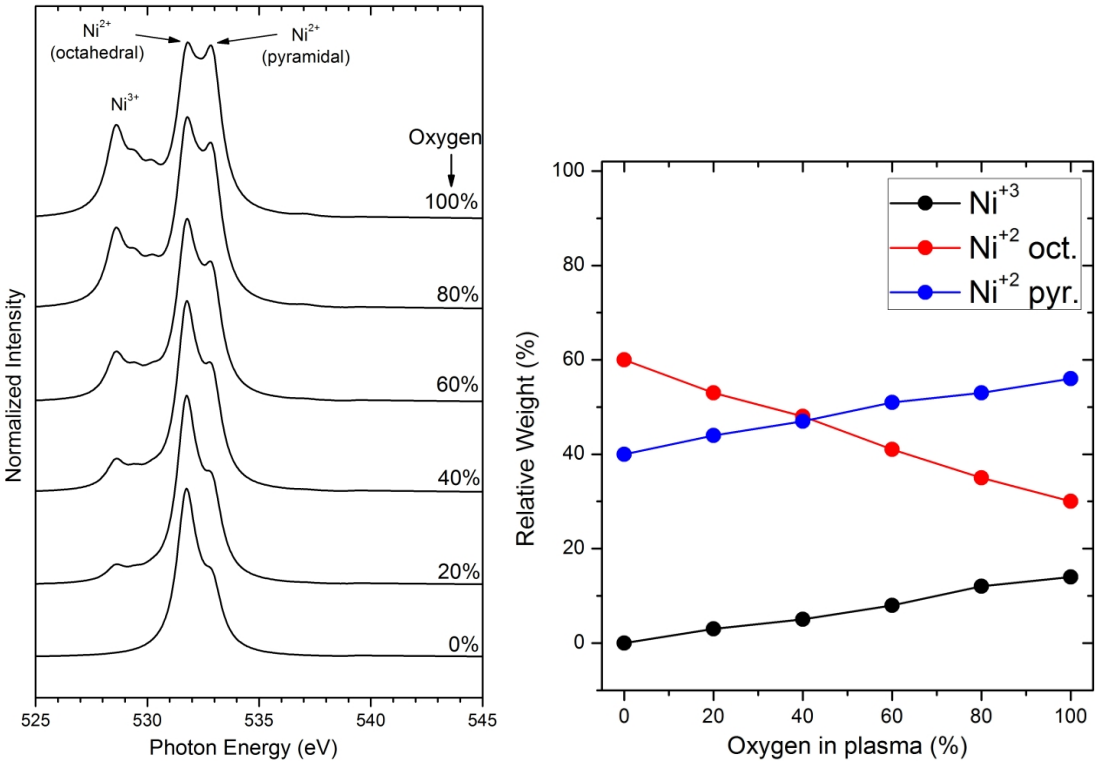

(a) XANES spectra calculated for O 1s edge

(b) Weights contributions to XANES spectra

Figure 6.10: XANES spectra at the O 1s edge calculated for different oxygen contents with weighted contributions of octahedral Ni^{2+}, pyramidal Ni^{3+} and Ni^{3+} ions.

Nickel L-edge calculations

In order to interpret the Ni 2p XAS results, we also performed calculations using the CTM4XAS code [178]. This code includes charge transfer configurations and also full atomic multiplet effects, which are crucial for describing transition metal $L_{2,3}$ edges. The charge transfer and crystal field parameters are the same as those presented in table 6.1, and the Coulomb and exchange interactions were scaled down to 80% of their atomic values.

Figure 6.11a shows the Ni 2p X-ray absorption spectra calculated in the case of octahedral Ni^{2+}, pyramidal Ni^{2+}, and Ni^{3+} ions. As in the O 1s XAS spectra, the discrete final states were again convoluted with a Lorentzian and a Gaussian function. The Ni^{2+} calculations show final states mainly related to $2p^6 3d^8 \rightarrow 2p^5 3d^9$ transitions, since the ground state is mostly formed from the $3d^8$ configuration (about 80%, according to table 6.2). In both symmetries, these transitions are split into the AB and A'B' structures. This splitting is somewhat greater in the octahedral symmetry, whereas the intensity of the B' peak is larger in the pyramidal case.

On the other hand, the Ni^{3+} spectrum is not mostly related to $2p^6 3d^7 \rightarrow 2p^5 3d^8$ transitions, but to $2p^6 3d^8 \underline{L} \rightarrow 2p^5 3d^9 \underline{L}$ excitations, because the ground state is mainly due to the $3d^8 L$ configuration (about 60%, according to table 6.2). As a result, the calculation is much more similar to a Ni^{2+} spectrum than to a typical high spin Ni^{3+} one [162]. Then, the spectrum is formed by a small pre-edge structure, and two main features, in each Ni $2p_{3/2}$ or Ni $2p_{1/2}$ region, which end up lying in about the same energy positions as the AB and A'B' structures.

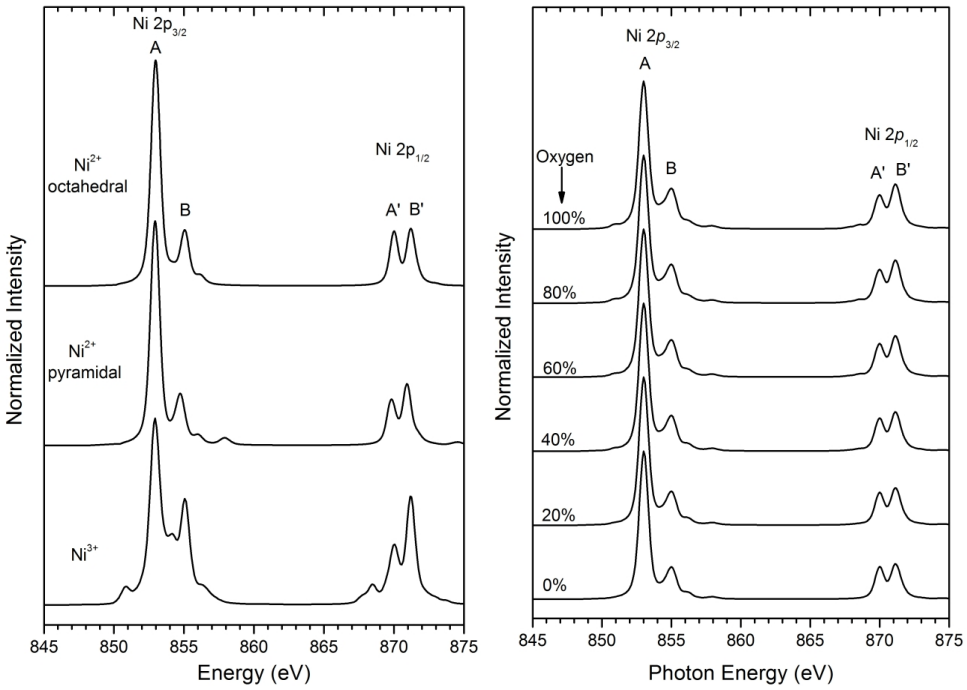

(a) Cluster calculations (b) Spectra calculated for different oxygen contents

Figure 6.11: Clusters calculations for Ni L-edge XANES contributions of octahedral Ni^{2+}, pyramidal Ni^{2+} and Ni^{3+} ions (a) and convoluted spectra for different oxygen concentrations in the sputtering plasma (b).

Figure 6.11b presents the calculated Ni 2p X-ray absorption spectra of samples with different oxygen concentrations in the plasma (labelled at the left of each curve). These calculations were performed for the NiO thin films grown at 200W-1h-RT, whose experimental data have been presented in previous section. The total spectra are the sums of the calculated octahedral Ni^{2+}, pyramidal Ni^{2+}, and Ni^{3+} contributions (see figure 6.11a), whose weights are the same as those obtained for the O 1s XAS calculations, shown in figure 6.10b.

The results confirm that, in this case, the spectra do not vary much as a function of oxygen content during growth. The only difference in the experimental spectra is a small increase in the relative intensities of peaks B and B', which is reproduced by our calculations. Therefore, the apparent lack of influence of oxygen content in the Ni 2p edge can be attributed to the similarities in the Ni^{2+} and Ni^{3+} contributions, in contrast to what we found in the O 1s edge. Note that the small pre-edge feature in the Ni^{3+} spectrum does not contribute much to the simulation because the relative concentration of Ni^{3+} ions in the films was estimated to be at most 13%, according to figure 6.10b.

6.1.6. More XANES results: parameters influence

After the discussion of XANES results and calculations corresponding at the set of films grown at 200W-1h-RT, we will discuss now the rest of the results obtained for NiO coatings grown under other sputtering conditions. As in previous chapters the results of the NiO thin films

grown under different parameters, magnetron power (100 W to 300 W), deposition time (from 1 hour to 2 hours) and substrate temperature (from RT to 300ºC) will be shown. These parameters, already presented in chapter 4, are the optimal parameters which accomplish for a nanoporous array in the form of thin film (a nanostructure in which two features are in the nanoscale: the thickness and the pores). From the rest of the XANES experimental data obtained, only films grown on AAM will be taken into account due to the similar behaviour of the Si planar and the AAM substrates.

Similar results as those presented for films with 200W-1h-RT conditions have been obtained for films grown at 100W-1h-RT (see figure 6.12). The oxygen K-edge shown in figure 6.12a presents the same trend with the oxygen addition to the sputtering plasma. This trend shows an increase of the surface-to-volume ratio. As it was explained in chapter 4 when oxygen is added to the plasma the crystallite size is reduced and the effective surface is enhanced. This increase of the effective surface splits the 3d e_g band in the XANES spectra into the sub-bands originated from regular and truncated octahedral symmetries, $e_g : z^2$ and $e_g : x^2 - y^2$, respectively. As observed previously with films grown at 200W-1h-RT, the pre-edge located at 528.6 eV, totally absent in pure Ar growths, increases with the addition of oxygen in the plasma, resembling the increment of the Ni vacancies to which it is related. In figure 6.12b the XANES Ni L-edge spectra are presented. As explained in the previous section there is no major variation with the increase of oxygen. Similarly to previous data, the minor influence of the oxygen in the XANES 2p spectrum is due to the similar contribution of the Ni^{2+} and Ni^{3+}, as confirmed by the calculations.

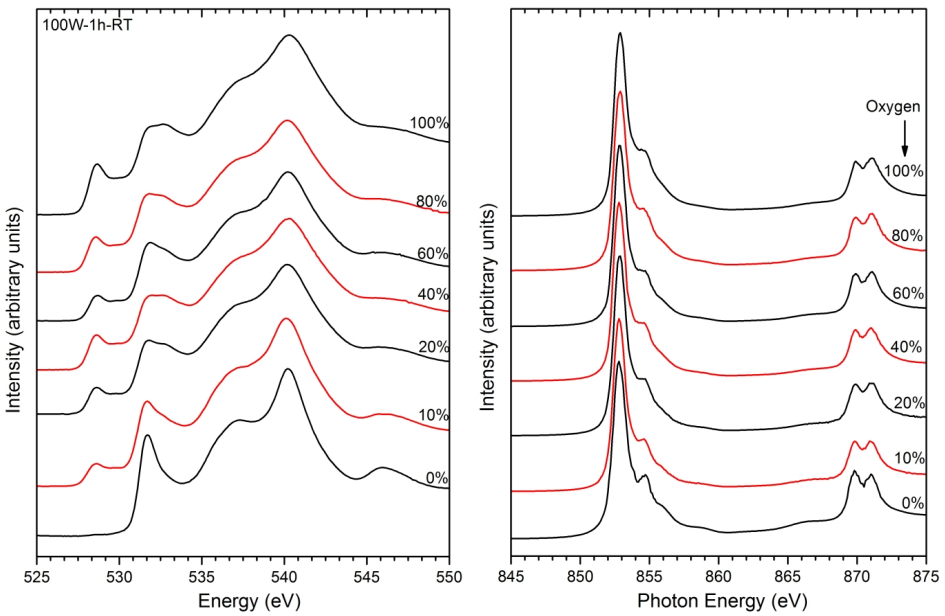

(a) Oxygen K-edge (b) Nickel L-edge

Figure 6.12: XANES obtained for O K and Ni L edges of NiO thin films grown on AAM substrate under 100W-1h-RT conditions.

We now present the results for the NiO thin films grown at 200ºC substrate temperature, during one hour and both 100 W and 200 W of magnetron power. Figures 6.13 and 6.14 show XANES spectra for both oxygen and nickel regions for NiO thin films grown at the mentioned growing conditions. In both sets of samples the trend is similar: the pre-edge due to the Ni^{3+} vacancies is observed (see figures 6.13a and 6.14a) although lower in intensity in comparison with results for films grown at 100 W of magnetron power. Also the splitting of the e_g states due to surface effects is not as pronounced as in the series grown at room temperature. When the substrate temperature is increased to 200ºC the structures in the XAS spectrum that originate

from the nanostructured nature of the film appear somewhat reduced: this temperature increase gives extra energy to the system and allows for a diffusion driven ordering of the crystalline structures, which reduces the effective surface. This is known as healing effect, and has a direct impact on the carrier concentration (recovering the stoichiometry and balancing the Ni^{3+} impurities) and surface effects. In XANES this is observed as a recovery of the more stoichiometric spectrum of bulk NiO.

For samples grown with 100 W of magnetron power, there is still a slight effect of the splitting of the 3d band, as shown in figure 6.13a. However, its intensity in the spectra for samples grown at 200 W of magnetron power is much lower (see figure 6.14a). Additionally, films grown at 200 W of magnetron power need a larger amount of oxygen in the sputtering plasma in order to observe the effect of the nickel vacancies in the XANES spectra whereas in previous results the incorporation of a 20% of oxygen was enough to observe such effect. This can be due to the higher substrate temperature, which, as mentioned above, has a healing effect in the crystal structure, reducing the disorder and therefore decreasing the number of vacancies. This decrease is related to the electrical results shown in section 5.1, where the resistivity of the films grown at 200ºC substrate temperature is larger, owing to the lower concentration of Ni vacancies.

Regarding the Ni L-edge, the effects of the substrate temperature are quite difficult to estimate due to the similar contributions of the different initial configurations. As already explained in previous section, the oxygen addition does not have a big effect on the lineshape of the XAS Ni L-edge spectra. This is also confirmed for samples grown at 200ºC of substrate temperature, where no big differences between sample grown with pure Argon and that grown with pure oxygen is observed (see figures 6.13b and 6.14b). If the effect of the substrate temperature is to decrease the number of Ni^{3+} vacancies, no big differences between XAS spectra at the Ni L-edge are expected due to the fact that the contributions of the Ni^{3+} and Ni^{2+} configurations are similar to each other. The substrate temperature is a parameter that decreases the effect of the oxygen content in the plasma on the final XANES spectra and subsequently on the electronic structure.

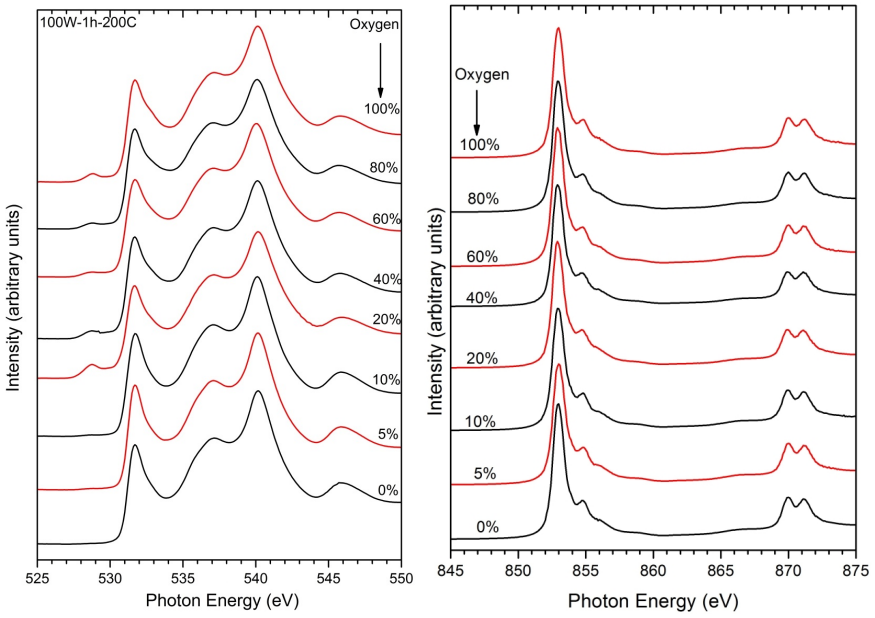

(a) Oxygen K-edge (b) Nickel L-edge

Figure 6.13: XANES spectra at both the O K and Ni L edges for NiO thin films grown at 100W-1h-200ºC with different oxygen contents in the sputtering plasma.

Finally we present the results for NiO thin films grown at 300ºC substrate temperature. In figure 6.15 XANES spectra at both the O K and Ni L-edges for samples grown at 200W-2h-300ºC

are shown. XANES spectra at the oxygen K-edge region show almost no presence of the Ni_3^+ pre-peak for any oxygen concentrations in the sputtering plasma (see figure 6.15a). Not only the pre-peak is almost missing, also the splitting at the 3d band is not observed. These two facts clearly indicate that both the surface effects and the presence of Ni vacancies are not present under these deposition conditions. The effect of the substrate temperature, seems, thus, to be determinant: by healing the crystal structure, at least near the surface and therefore showing no variation in the XANES spectra due to its short depth probe.

As expected, the Ni L-edge region for these samples show no variation with the oxygen content in the plasma, (see figure 6.15b). It can be remarked now, after observation of all the XANES Ni L-edge results, the slight difference between samples grown at room temperature and at higher temperatures. For RT the Ni L-edge shows a small variation of the B' structures with oxygen, especially appreciated at the $2p_{1/2}$ states in figures 6.8a and 6.12b, and its origin has been explained in subsection 6.1.5. On the contrary, films grown at higher substrate temperature (see figure 6.15b) show no variations for this structure.

As shown up to now, the effect of the substrate temperature seems to have a major role in the XANES spectra. To make this more clear, we show in figure 6.16 XANES spectra at the O K-edge of samples grown at the same magnetron power (200 W), for the two extreme oxygen contents (0% and 100%), and for the three different temperatures used in this work: RT for the curves at the bottom, 200℃ for the curves in the middle and 300℃ for the curves at the top. The intensities have been normalized in order to compare between each other. The effect of the temperature is now easily observed: as the substrate temperature increases, the main features of the XANES spectra converge to those of the NiO bulk reference, represented in dashed line at the top of the figure. For higher temperatures the pre-edge almost disappears. The 3d splitting due to surface effects is also greatly affected by the increase of temperature: at 200℃ it is barely observed, more clearly for the sample grown with pure oxygen. Nevertheless, remanent surface effects are present even at 300℃, as evidenced by the differences observed between the thin films and the bulk NiO spectra in the top graphs. Even at this temperature, the nanostructured morphology of the films with respect to bulk NiO preserves some amount of surface effects. The rest of the peaks above 535 eV, related to higher energy final states due to the hybridization between higher orbitals of the metal ion and ligand atom, are more defined and narrower with the increase of temperature, suggesting a lower hybridization and higher lifetime of these states, being this spectrum closer to the bulk reference spectrum.

In-depth measurements: Fluorescence Yield

When estimating the probing depth for different XAS modes of measurement it can be established that the probing depth of XAS in TEY measurement mode is larger than in XPS for any material [179]. In our study the probing depth for the XAS results is between the estimated 40 nm by M. Abbate *et al.* [179] and 100 nm (which is the minimum thickness observed in the thinnest measured sample, see figure 4.14). However, as explained in chapter 3 the fluorescence yield is a mode of measurement in X-ray Absorption Spectroscopy. In this work we performed total fluorescence yield (TFY) because the photodiode detector used measures the fluorescence emission in the whole energy range. The incident X-rays excite the atoms in the solid until they are completely absorbed. This is determined by the attenuation length, which is related to the absorption of these atoms. The fluorescence emission comes out from the atoms in the solid (if the self absorption allows this radiation to escape) from a length that corresponds to the probing depth of the technique. For XAS, the probing depth of TFY is longer than in TEY due to the short IMFP of the electrons compared with the attenuation length of photons within the solid. This fact will be used to a better understanding of the electronic structure of the growth films.

The absorption of NiO for the energy range corresponding to soft X-rays can be simulated using the mass attenuation coefficients and the cross sections from the X-ray database from the Berkeley Lab's [40]. Figure 6.17 shows the calculated attenuation length for stoichiometric NiO

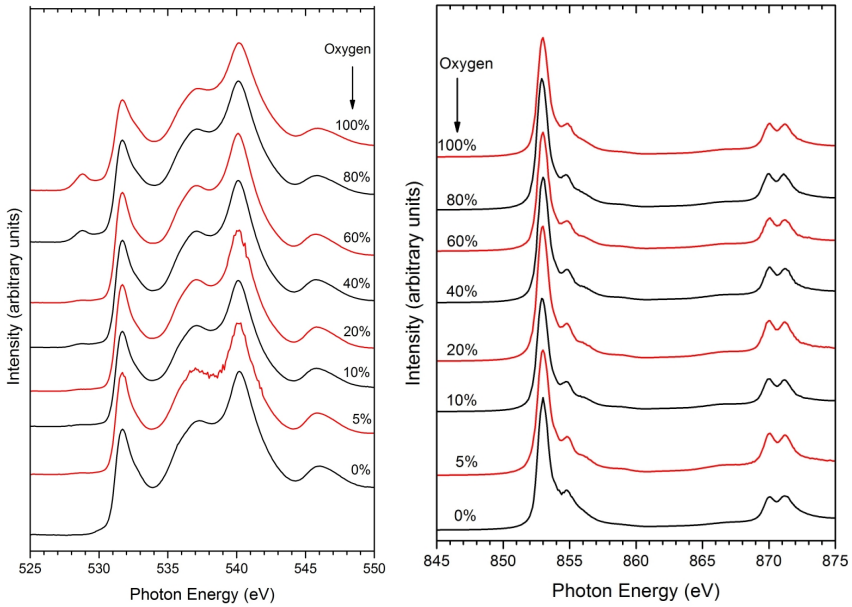

(a) Oxygen K-edge (b) Nickel L-edge

Figure 6.14: XANES spectra at both the O K and Ni L edges for NiO thin films grown at 200W-1h-200℃ with different oxygen contents in the sputtering plasma.

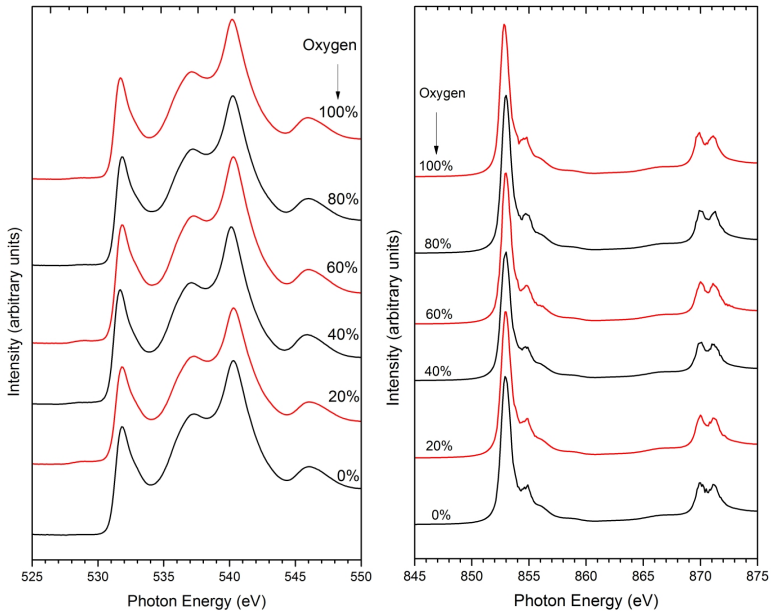

(a) Oxygen K-edge (b) Nickel L-edge

Figure 6.15: XANES spectra evolution with oxygen in plasma obtained at the O K and Ni L edges of NiO thin films grown on AAM substrate at 200W-2h-300℃ conditions.

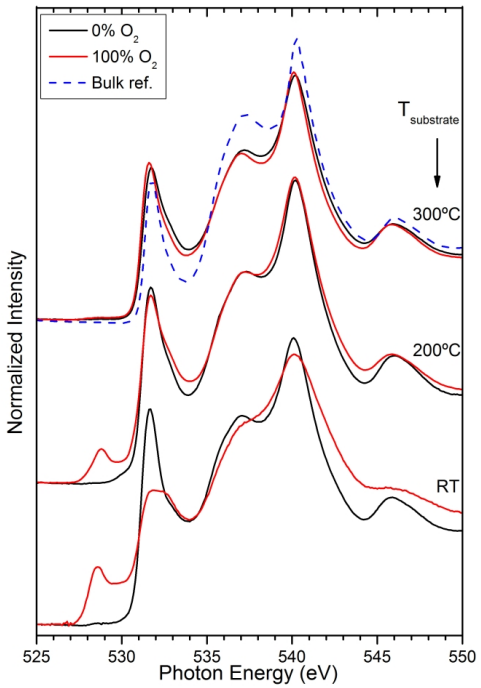

Figure 6.16: XANES spectra for films grown on AAM at 200 W of magnetron power during one hour. The bottom curve is grown at RT, the middle one at 200°C and the top curve at 300°C. Black lines represent the pure Argon growth and red lines the pure oxygen growths, with the dashed blue curve represents the reference of bulk NiO. The structures of the XANES spectra related to nanostructured NiO (pre-edge and 3d splitting) converge to the NiO bulk reference as the temperature increases.

($\rho = 6.67 gr/cm^3$) as a function of the photon energy of the incident X-rays. At 535 eV and 850 eV the curve presents maxima related to the oxygen K and nickel L edges, respectively (this graph has not enough resolution to split the Ni L-edge into two contributions). At the edges, the incident radiation resonates with the transition cross sections producing higher absorption and therefore the attenuation length increases. Therefore, according to the estimation of figure 6.17, the maximum attenuation length at the oxygen K-edge region is 340 nm and at the nickel L-edge is 520 nm. The attenuation length is defined as the path length that reduces the intensity a factor $1/e \simeq 0.37$, therefore after one unit of attenuation length (535 nm for the oxygen K-edge) the remaining intensity is only 37% of the original and after two units of attenuation length ($2 \times 340 = 680$ nm) only 13% of the initial intensity remains, and so forth.

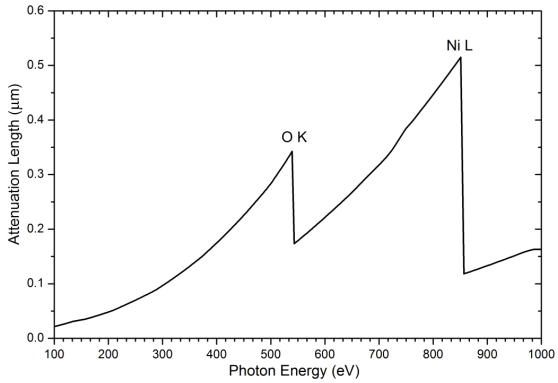

Figure 6.17: Calculated attenuation length for stoichiometric NiO.

However, in our study the thickest NiO thin film is about 500 nm thick (see figure 4.14) and, therefore, self absorption does not play a major role in the FTY measurements. Nevertheless, a residual effect can be present, so we can observe a diminution of the TFY signal with respect the TEY signal. When comparing the TEY and TFY modes of measure in XAS one must take into account that the information given by TEY comes from the outermost atomic layers of the solid whereas TFY reports information of the solid bulk until the intensity is attenuated by self absorption effects.

Until now the TEY XANES has provided information from the surface region. Now, we will show XANES results obtained in TFY mode, which is more sensitive to the bulk than TEY. In figure 6.18 a comparison of XANES spectra obtained with both detection modes on NiO films for 100W-1h-RT conditions is shown. The evolution with the oxygen content in the sputtering plasma clearly shows the effects discussed above: the pre-peak corresponding to the Ni^{3+} vacancies increases in intensity, the surface effects splitting is also observed as well as the broadening of the structures at higher energies.

The pre-edge related to the Ni^{3+} vacancies loses no intensity when measured in TFY mode. This fact indicates that the contribution of the Ni^{3+} ions is not limited to the surface region, but it spreads within the solid. Also the 3d splitting due to surface states at 532 eV is present in the TFY measurements. Indeed, both effects seem more pronounced in the bulk sensitive measurements. Although these coatings are thin (see 4.14) there is some self-sorption effect that reduce somewhat the intensity of the main peaks in the TFY curve (red line).

For the case of the nickel L-edge region little variation is observed between the TEY and TFY modes (see figure 6.18b) due to the reasons explained in the section 6.1.5: the contributions from the different states are similar to each other therefore it is not straightforward to distinguish whether the spectrum contributions come up from the surface or from the bulk states.

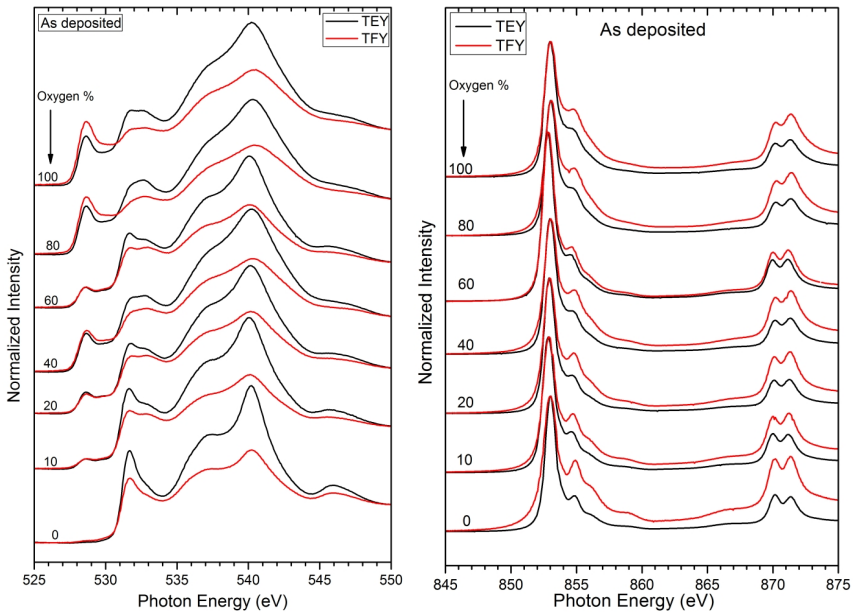

(a) O K-edge as deposited (b) Ni L-edge as deposited

Figure 6.18: XANES evolution with the oxygen content in the sputtering plasma of the O K-edge and Ni L-edge regions measured both in electron yield (TEY) and in fluorescence yield (TFY) for films grown under 100W-1h-RT conditions. The black and red lines represent the TEY and TFY measurement modes, respectively.

6.1.7. Thermal Treatment

As shown in a previous subsection, the effect of the temperature during the sputtering growth clearly affects the properties of the NiO films, both by increasing the crystalline order and by decreasing the amount of Ni vacancies. In this section, we will show the effects of the temperature after the thin films have been grown. Two types of thermal treatments were carried out: one in an open furnace (*ex situ*), in an air environment, carried out in our laboratory, and another one inside a vacuum chamber (*in situ*) at beamline *UE52-PGM* at BESSY and in a pure oxygen environment in order to see the effect of the atmosphere on the nickel vacancies within the crystal structure. For this study only the series grown at 100W-1h-RT on Si substrates has been used.

Annealing in air (*ex-situ*)

The *ex-situ* annealing experiments were performed in a conventional furnace in air. Samples were heated up to 150℃ for two treatment times: one hour and four hours. The aim of this experiment was to estimate the effect of temperature on the electronic structure and the influence of the environment. Performing this annealing in air is a way to accelerate the ageing process, already presented in chapter 5. A dynamic process occurs usually faster when some amount of thermal energy is provided.

We show in figure 6.19 XANES spectra (TEY mode) of NiO films grown at 100W-1h-RT as deposited (black line) and after annealing during one hour at 150℃ (red line). As it can be seen, the intensity of the pre-peak corresponding to Ni^{3+} ions decreases after annealing. Even at these low temperatures (150℃) the crystal structure reorders and the vacancy concentration is somewhat reduced. On the other hand the effects of the annealing on the splitting of the 3d e_g sub-band is less evident, suggesting that the two main effects produced by the nanostructuration of the NiO coating do not behave in the same way upon annealing, at least at this low temperature.

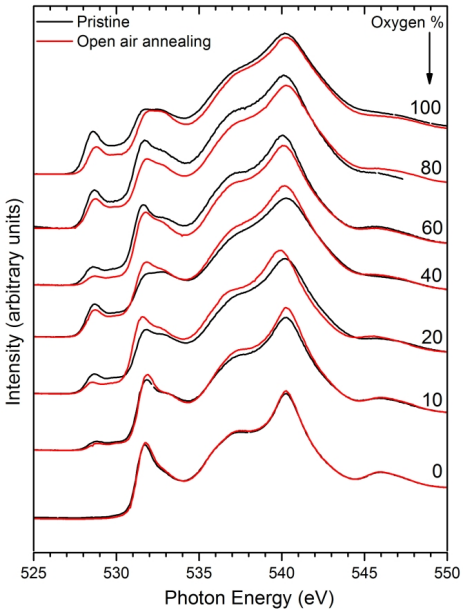

Figure 6.19: XANES spectra (TEY mode) of films grown at 100W-1h-RT conditions. Pristine (black line) and after annealing during 1 hour at 150℃ (red line).

In figure 6.20 XANES spectra at the oxygen K-edge taken in both TEY and TFY modes of samples grown at 100W-1h-RT conditions after one hour (figure 6.20a) and four hours annealing (figure 6.20b), are shown. As explained above, the difference between both detection modes is the probing depth, being TFY mode more bulk sensitive. For both annealing times, one and four hours at 150℃, clear differences are observed in both detection modes. Despite the

self-absorption effects, which lowers the intensity of the features of the TFY spectra, the pre-peak at 529 eV is clearly more intense in the TFY spectra in all cases. This pre-edge peak is related to the presence of Ni^{3+} ions. The fact that it is less intense for the TEY spectra suggests that the amount of Ni^{3+} ions is lower near the surface. On the other hand, the 3d e_g splitting at 532.5 eV seems to be less intense for the TEY spectra, which suggests that surface effects start to become less intense at the outermost region of the samples. In both cases, the annealing seems to cause an increase of the order of the system and, although 150℃ is still a low temperature, a reduction of the effective surface and of the amount of vacancies seems to occur. When comparing the two annealing processes, the 3d e_g splitting is lower for annealing during four hours while annealing for only one hour still shows a high intensity of this surface splitting. The comparison between the TEY and TFY results suggests that the effects of the annealing on the structure of the samples are more evident at the surface region than in the bulk.

This interpretation is consistent with the ageing model proposed to explain the trend observed in the resistivity of the samples. The almost parabolic behaviour was explained as a healing process that occurs by diffusion of oxygen ions through the surface.

On the other hand, XANES spectra at the Ni L-edge region do not experiment almost variation after annealing at 150℃ in air. This is expected, similarly to what occurs with other growing conditions, and is in agreement with the proposed theoretical calculations.

After these results it can be concluded that the temperature has a direct effect on the electronic structure of the NiO films as the slight variations observed in figures 6.19 and 6.20 indicate. However, this mild annealing at only 150℃ is not enough to greatly modify the electronic structure: still the pre-peak in the oxygen K-edge spectra and the splitting of the 3d band are observed. Fluorescence data provide a key hint: this process of evolution to a less nanostructured electronic structure (according to the features depicted in figure 6.4) seems to be happening at the surface. On the top of the thin film (TEY mode is more surface sensitive) the exchange of oxygen ions with the atmosphere occurs. This process can be understood in terms of an oxygen diffusion from inside the bulk out of the material.

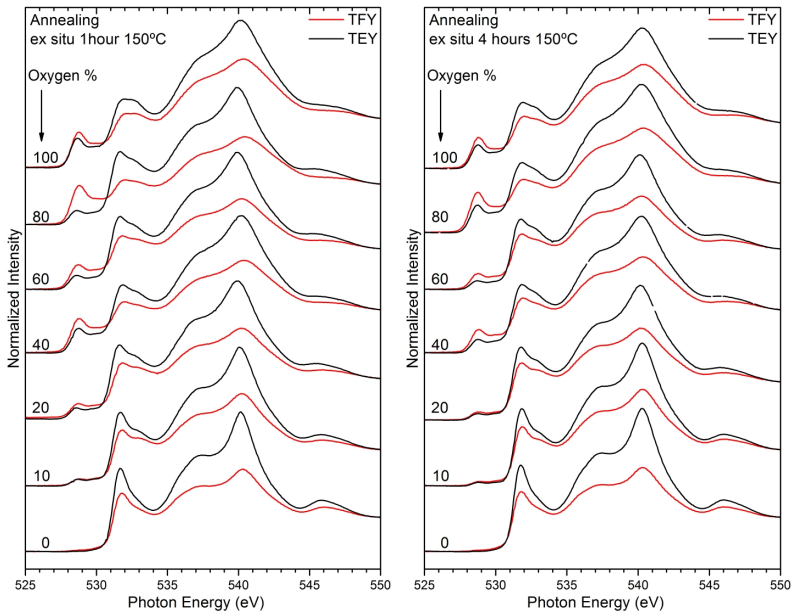

(a) 1 hour of annealing (b) 4 hours of annealing

Figure 6.20: XANES oxygen K-edge spectra evolution for annealed *ex situ* at 150℃ during 1 and 4 hours for samples grown at 100W-1h-RT. The TFY spectra show that the pre-edge assigned to Ni^{3+} ions is present deeper in the bulk with higher intensity.

In situ annealing under vacuum

In order to further study the effects of the annealing on the properties of the NiO films, a different experiment was carried out. In this case, freshly grown samples were heated in high vacuum and subsequently measured *in situ* by XANES at the oxygen K-edge during the heating ramp time. These experiments were carried out at the beamline *UE52-PGM* at BESSY. The sample holder of the UHV system was equipped with a heater located under the sample to reach high temperatures (higher than the 150℃ used in the *ex situ* experiments) at UHV (below $5 \cdot 10^{-9}$ mbar).

The effect of the annealing in vacuum can be observed even for the NiO coatings, grown with a pure Argon, as shown in figure 6.21a. In black colour the XANES spectrum of the film as deposited, before thermal treatment is shown, whereas the red curve corresponds to the spectrum after *in situ* annealing at 350℃ in UHV. Though weak, the effect of the annealing is evident: the structures of the oxygen absorption edge are narrower, the main structure assigned to the 1s edge increases its intensity and the 3d e_g shoulder assigned to surface effects almost disappears after heating up the sample. Also the structures at higher energy, corresponding to Ni 4sp hybridized states become narrower. Therefore it is evident that annealing at intermediate temperatures (between 150℃ and 450℃) has clear effects on the electronic structure of the NiO thin films, as revealed by the XANES spectra. These effects are even stronger for NiO films grown with pure oxygen plasma, as shown in figure 6.21b. The black curve corresponds to the as-grown NiO film and the red curve to the same sample after annealing at 450℃ in UHV. As it is evident, the XANES spectrum undergoes a dramatic change after this thermal treatment: The pre-edge due to Ni^{3+} ions as well as the shoulder due to the 3d e_g sub-band splitting completely vanish. Final states located at higher energies, above 535 eV, increase their intensity and get narrower, resembling a more ordered crystal structure and larger crystallite size, where the lifetime of the excited states is longer. It should be remarked here that both red curves, corresponding to different samples after the annealing process, are very similar to each other. This fact suggest a convergence to a Nickel Oxide structure with similar stoichiometry and long range order.

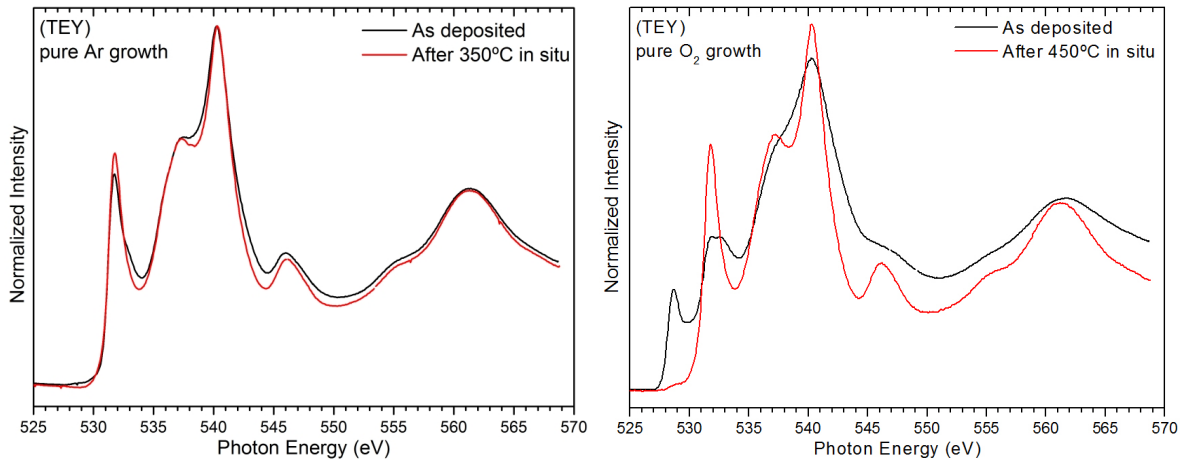

(a) Pure Ar growths

(b) Pure O_2 growths

Figure 6.21: XANES spectra at the oxygen K-edge region of samples grown with pure Ar and (a) pure O_2 (b) as deposited (black line) and after *in situ* annealing *in situ* (red line). The pre-peak related to Ni^{3+} ions in sample grown with pure oxygen vanishes completely after the treatment. Also the shoulder at higher energy in the 3d e_g sub-band splitting considerably decreases its intensity after annealing and the different peaks at higher energies get narrower.

Figure 6.22 shows the pre-edge region at the oxygen absorption K-edge of samples of the 100W-1h-RT series grown with different oxygen content in the plasma, and the effect of annealing

in situ under UHV conditions. The XANES spectra were acquired simultaneously to the sample heating. This experiment was carried out only in TEY mode because the photo-diode used to measure in TFY mode was sensible to the infra-red radiation coming from the sample during the annealing and the range scale was overflowed. The XANES spectrum corresponding to the sample grown in pure Argon (%0) is not shown due to the absence of pre-peak for this sample. In all cases the temperature increase reduced the intensity of the pre-edge peak until it almost disappeared. Each graph inside figure 6.22 has at the upper-right corner the oxygen content in the sputtering plasma. As it can be observed, the higher the oxygen content in the plasma the higher the annealing temperature needed for the pre-edge peak to disappear.

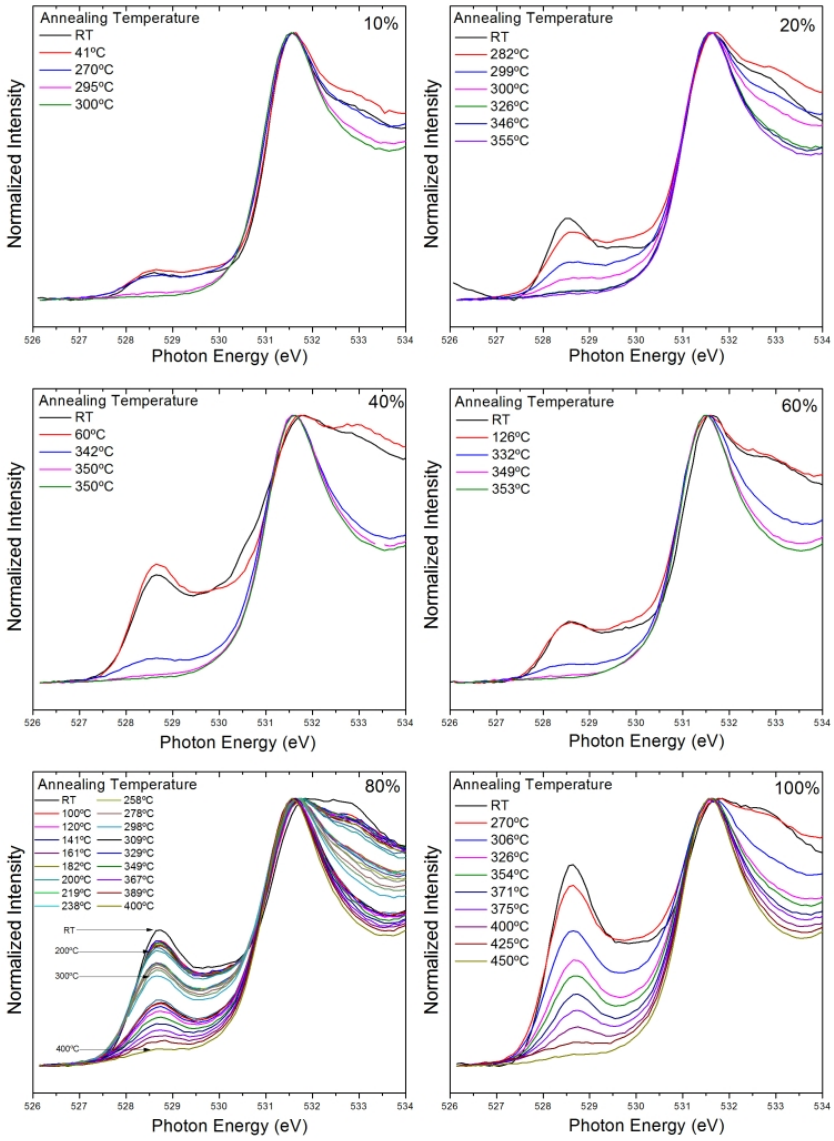

Figure 6.22: XANES Pre-peak and oxygen K-edge evolution with annealing temperature *in situ* for samples grown at 100W-1h-RT with different oxygen concentrations. The annealing temperature reduces the pre-peak in the XANES spectra. This pre-edge is related to the Ni^{3+} vacancies within the crystal structure.

This increase of the limit temperature with the oxygen content can be more clearly seen in figure 6.23 where the temperature at which the pre-edge peak disappears is shown as a function of the oxygen content in the sputtering plasma. The limit temperatures go from about 300ºC for the case of only 10% oxygen to 450ºC for the sample grown with pure oxygen. As explained in section 4.4 the lattice disorder created by the addition of oxygen to the sputtering plasma

increases the amount of Ni vacancies within the crystal. The pre-edge structure observed in the XANES oxygen K-edge spectra is directly associated with this increase of Ni_3^+ ions. The annealing of the thin films has a healing effect that brings the system into a more ordered state in which the number of point defects decreases [37]. Consequently, the more thermal energy is transferred to the system by annealing, the higher the decrease of Ni vacancies, reducing the intensity of the pre-edge peak in the XANES spectra. The criterion used to define this threshold temperature was the that the intensity of the pre-edge (located 1.5 eV before the O K-edge) was negligible when measured in electron yield mode, according to the spectra shown in figure 6.22.

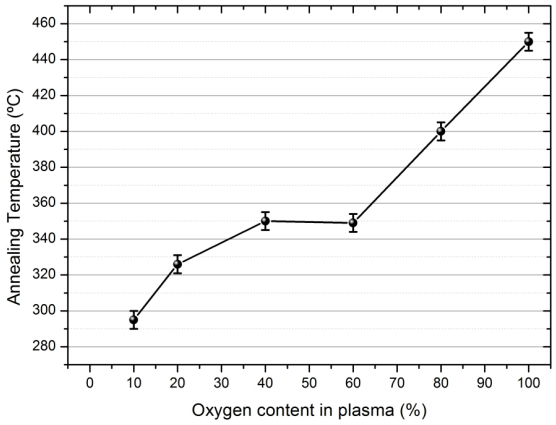

Figure 6.23: Annealing temperature (*in situ*) at which the pre-edge of the oxygen K-edge disappears: the more oxygen content during the sputtering growth the higher the critic temperature.

All previous measurements on *in situ* annealed samples were performed in TEY mode. However, it is interesting to compare with the results obtained in TFY mode. This was not possible to accomplish in real-time due to overload of the photodiode during annealing, but we could carry out XANES measurements after the annealing was finished. In figure 6.24 we show the pre-peak region at the oxygen K-edge after annealing. The regions for each oxygen content are shown measured in both electron and fluorescence yield. In all cases the limit temperature has been reached, so the pre-peak is no longer observed in the electron yield mode (black line). However, in the spectra obtained in fluorescence yield mode, the pre-peak is still visible (red line), although with a reduced intensity as compared to the initial intensity. The changes induced by the annealing are related to a healing effect that tries to bring the NiO to the right stoichiometry. This process is driven by diffusion. The excess oxygen in the lattice escapes from the samples after crossing the surface. Consequently, there seems to be a depletion zone near the surface where the amount of defects is lower. This is indicated by the absence of the pre-peak after annealing in TEY. However, the pre-peak is still visible in TFY because below this surface region the system has not yet recovered the equilibrium situation. Much higher temperature and larger times would be required to reduce the pre-peak in the bulk. When the thin film loses its oxygen excess and recovers the stoichiometry its behaviour remembers that of the NiO reference in terms of XANES signal. As this process of oxygen diffusion continues, the layer of stoichiometric Nickel Oxide on top of the thin film increases in thickness and therefore acts as a protective coating which hinders further oxygen diffusion. In this sense the expected behaviour is approximately parabolic, as it was observed for the ageing effect in the resistivity measurements, shown in previous chapter. When the films are annealed the resistivity increases (the stoichiometric NiO layer does not allow the charge carriers to move easily through the lattice) as shown previously in figure 5.7.

When the thin film loses its oxygen excess and recovers the stoichiometry its behaviour remembers that of the NiO reference in terms of XANES signal (see figure 6.4). As this process of oxygen diffusion continues, the layer of stoichiometric Nickel Oxide on top of the thin film

increases in thickness and therefore acts as a protective coating which do not allow the oxygen to diffuse out of the bulk. In this sense this behaviour is parabolic, as is the resistivity ageing effect shown in previous chapter. When the films are annealed the resistivity increases (the stoichiometric NiO layer do not allow the charge carriers to move easily through the lattice) as shown previously in figure 5.7.

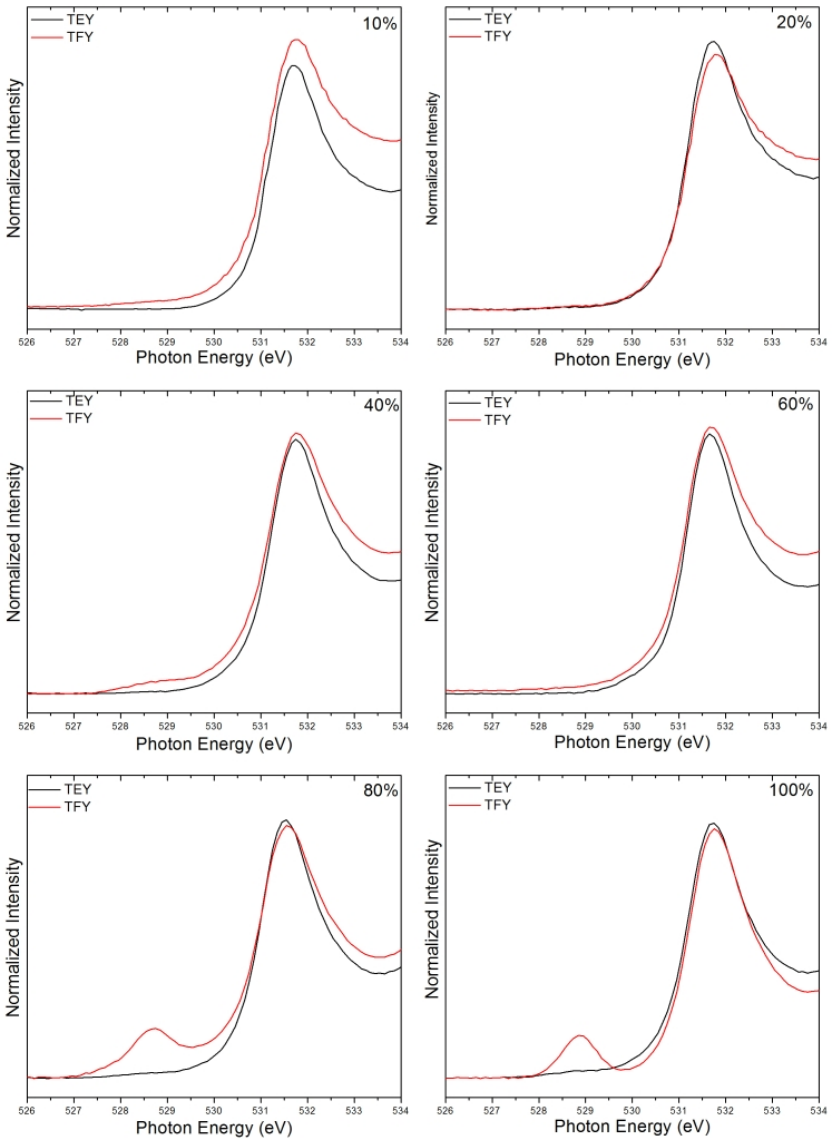

Figure 6.24: XANES Pre-peak and oxygen K-edge spectra after annealing *in situ* for samples grown at 100W-1h-RT with different oxygen concentrations. After annealing at the maximum temperature the pre-peak vanishes when measured as seen in TEY mode but in some cases is still present when measured in TFY mode, more bulk sensitive. This pre-edge is related to the Ni^{3+} vacancies within the crystal structure.

Some of the annealed samples were also measured by X-ray Diffraction at grazing incidence and compared with the measurements before annealing. In figure 6.25 we show diffraction patterns of some samples grown at 100W-1h-RT conditions as deposited (black line) and after the annealing in vacuum (red line), the oxygen content is labelled on the right of each curve. The intensity scale is maintained for all curves, in order to compare the relative intensities at each oxygen concentration. These diffractograms were acquired with a Co source. As can be seen in the diffraction pattern, after annealing in vacuum the polycrystalline nature of the coatings

is maintained and even enhanced. The peaks corresponding to Nickel Oxide maintain their position and become narrower after the annealing, as expected from a recrystallization process. The deposited samples did not have a preferred orientation but after the annealing the coatings evolve to the preferred orientation (2 2 0) and (1 1 1). The Pawley fittings preformed on these samples give values for the lattice parameter between 4.161 Å and 4.198 Å showing no trend with the oxygen addition.

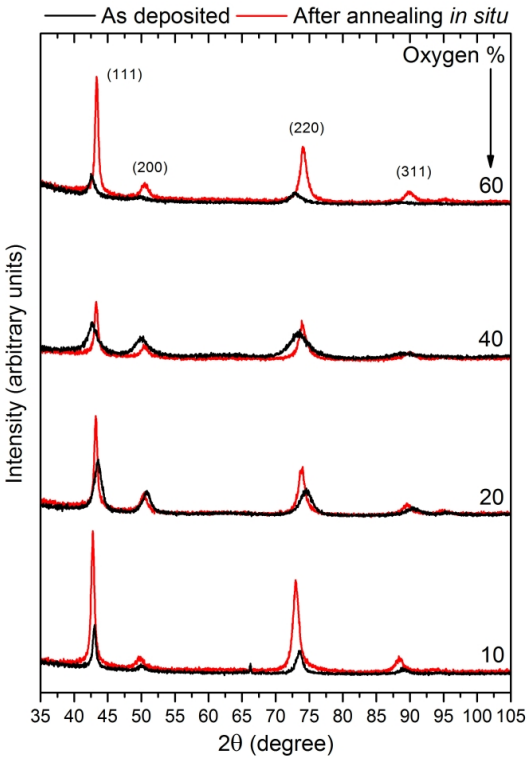

Figure 6.25: XRD pattern of samples grown at 100W-1h-RT as deposited (black line) and after annealing in situ (red line). Measured with Co source. The annealing process increases the crystalline quality of the films by healing effect. The initial polycrystalline film maintains the NiO phase while orientations (1 1 1) and (2 0 0) are dominant in the diffractogram.

In situ annealing in an oxygen environment

The experimental set-up used for the XANES measurements included the possibility of measuring in a gas environment thanks to a nozzle directed towards the sample, through which the desired gas can be directed to the sample without breaking the high vacuum conditions needed to carry out the experiment. With this nozzle the local pressure on the sample was about 2×10^{-2} mbar whereas in the whole chamber the pressure was much lower, about 2×10^{-6} mbar. We decided to study the effect of oxygen during the annealing.

This study was only performed on sample 80%-100W-1h-RT, which has already been thoroughly studied with other techniques so that its behaviour is well known.

The aim of annealing at high temperature in an oxygen environment is to reproduce similar pressure conditions to those used during growth and monitor the changes by measuring *in situ* the oxygen K-edge.

The annealing was performed in oxygen atmosphere with increasing temperature during one hour for each step, from room temperature to 300°C in three steps of 100°C, summing up to three hours of annealing, as shown in figure 6.26. The evolution with this annealing from the as deposited nanostructured NiO XANES spectrum, shown in the bottom curve, to the more

stoichiometric-like NiO (top curve, after 300ºC) is clearly observed. The pre-edge disappears after the thermal treatment as well as the surface splitting of the 3d band and the peaks corresponding to higher energy final states become narrower. Under annealing the system converges to a more stoichiometric Nickel Oxide. Although this behaviour is similar to what was obtained when annealing in vacuum, there is a key difference: the needed temperature to obtain the XANES spectrum similar to that of the reference is reduced from 400ºC to 300ºC. Therefore the presence of oxygen in the environment of the sample seems to accelerate this process by reducing the critic temperature, in comparison to what was observed for 80% oxygen content in plasma growth in figure 6.23.

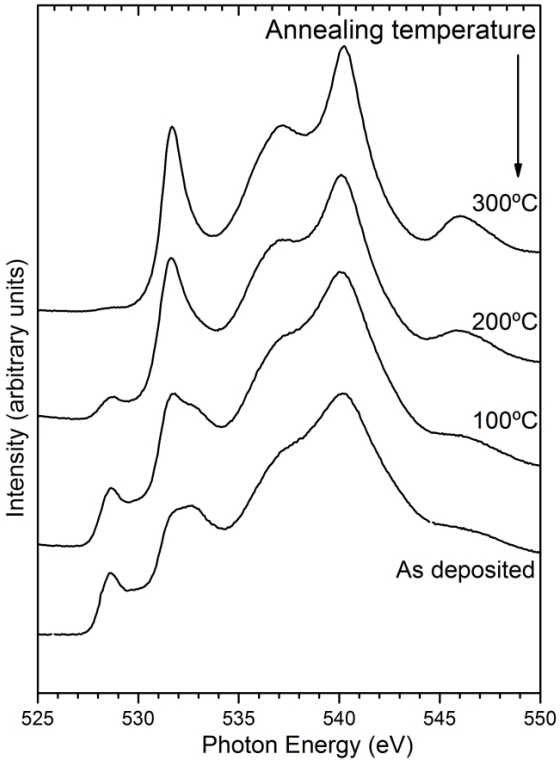

Figure 6.26: Evolution of XANES spectra at the O K-edge of sample 80%-100W-1h-RT after annealing (*in situ*) in oxygen atmosphere. The annealing was kept for one hour at each temperature step (3 hours of cumulative annealing of increasing temperature). After the thermal process the nanostructured NiO XANES spectrum converges to that of a NiO reference where the pre-peak is not present, the 3d splitting is vanished and the higher energy final states gets narrower.

In an oxygen environment a last experiment was carried out: for the well known sample of 80% oxygen content in the plasma an annealing at low temperature, 150ºC, during one and four hours was performed. This simple experiment was intended to compare the annealing at low oxygen pressures with the *ex situ* annealing in air. The *in situ* annealing in oxygen was performed at high clean conditions, in order to achieve similar clean conditions the high vacuum chamber was driven to a very low pressure and then to a pure oxygen atmosphere of about 2×10^{-2} mbar. In such manner the effect of the oxygen in the environment could be isolated. In figure 6.27 we show the XANES spectra of samples annealed in air (*ex situ*) and those of samples annealed *in situ*, both in electron and fluorescence measurement modes, represented in black and red lines, respectively for both thermal treatments of one and four hours. As can be observed there is no variation between heatings at open air furnace and in the vacuum chamber. Due to the fact that TFY mode is more sensitive to the bulk, the intensities of the pre-edge are higher in every case, because in the bulk the amount of Ni^{3+} vacancies is greater than in the sample surface (as observed before in previous subsection). This last experiment proves that the

annealing in presence of oxygen, is equivalent to the annealing in an external furnace in air.

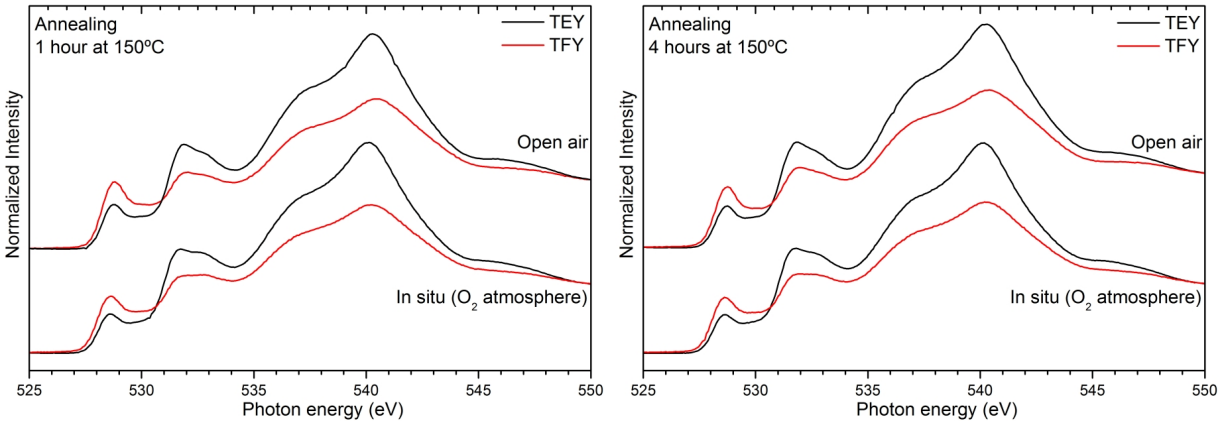

(a) 1 hour of annealing

(b) 4 hours of annealing

Figure 6.27: XANES spectra (both in TEY and TFY modes) at the oxygen K-edge spectra for samples annealed *ex situ* at 150ºCduring 1 and 4 hours for sample grown at 80%-100W-1h-RT. There is no difference between the open air, *ex situ*, and the oxygen environment in the vacuum chamber, *in situ*, annealing.

6.2. XPS results

The structures arising from XPS, for the case of Nickel Oxide, are well known and object to much debate in the last decades, specially the Ni 2p doublet, in which we will centre our study. By means of X-ray photoelectron spectroscopy we will be able to study the surface electronic structure of the nanostructured NiO thin films.

Nickel Oxide coatings have been measured in our XPS experimental set-up, described in section 3.4.7. Samples grown on both AAM and Si substrates were measured. Because of charging effect problems (already explained in section 3.4.7) every sample has been charge-corrected with respect to the carbon 1s peak, located at 284.5 eV. This charging shift affects mainly to the more insulating samples (those grown with pure argon plasma, named 0%). The AAM is supported by an Al foil and the Si wafers have a relatively low resistivity, $\rho = (7.0 - 17.0)$ Ω·cm, therefore allowing a good connection to ground.

6.2.1. NiO XPS interpretation

Before analysing the XPS structures of each sample (Ni 2p doublet and O 1s, with C 1s for calibration reference) a complete scan was measured in order to identify the composition of the surface sample, see figure 6.28. This wide scan (named *Survey*) is performed with less point density and higher pass energy, 50 eV (lower energy resolution).

XPS is a very surface sensitive characterization technique so the substrate is never detected in the survey: the Al_2O_3 of the AAM or even the Al of the support and the Si of the wafers substrate never appear in the Survey, and if they do it means that the NiO thin film is not being correctly measured or it is incorrectly located on the sample-holder. The Survey shown in figure 6.28 has all the main structures identified and labelled for a NiO thin film: the Ni 2p doublet, located at higher energy between 860 and 900 eV, will be the most studied region together with the O 1s peak at 531 eV and C 1s, due to contamination, at 285 eV (useful to correct the charge shift of the spectrum). The valence band is also detected near the Fermi energy, in the range of 15 to 0 eV. From nickel atoms also other minor structures arise: Ni 2s, 3s and 3p, but the useful information is obtained from the most intense 2p doublet. The Auger lines fortunately do not

fall in the regions of interest: these structures are labelled KLL for oxygen and LMM and KLL for nickel in figure 6.28, following the Siegbahn notation.

In this example survey of figure 6.28 a small peak, not labelled, at 685 eV appears in some samples and is identified as F 1s, according to Briggs database [46]. No Argon lines are observed at 320 eV (Ar 2s) and at 240 (Ar 2p doublet), as both should appear, or none. This survey belongs to a very clean surface sample: the intensity of the C 1s is very small.

The vacuum chamber used for the synthesis (that equipped with the RF magnetron sputtering system) is different to the UHV chamber where the XPS measurements were carried out. This means that during the process of taking out a sample from the vacuum chamber to open air and again putting it into vacuum, the surface sample can be easily contaminated. Special care was taken during this work to measure the samples right after taking them out from the vacuum deposition chamber, obtaining therefore low intensity of the carbon peaks, like in spectrum shown in figure 6.28.

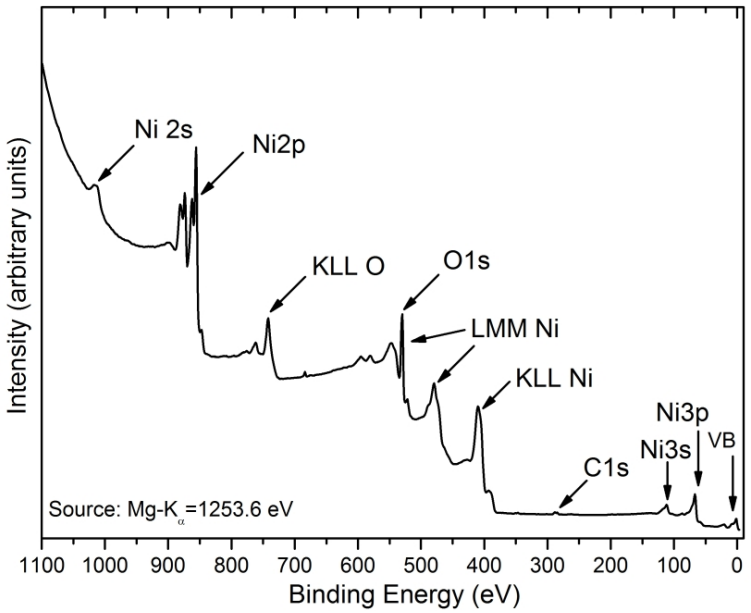

Figure 6.28: XPS Survey scan of the Nickel Oxide thin film obtained with Mg source. The main structures labelled are: the Ni 2p doublet and others levels (2s, 3s, 3p), O 1s and C 1s, the Valence Band (VB) near the Fermi energy and the corresponding Auger lines. The survey helps to locate the main structures and identify the atomic composition on the surface sample.

Due to the short probing depth of the XPS technique, about 3 nm for NiO, measuring the substrates do not provide extra information about the Nickel Oxide electronic structure: there is no big influence of the surface substrate electronic structure to our NiO thin films. This is due to the thickness we are working with: the thinnest of our NiO coatings is above 50 nm, found for the 100W-1h-RT growing conditions (see figure 4.14). For such a thickness any influence of the electronic structure of the substrate which can be detected by the XPS (minor defects, covalency, atomic composition) has no major impact on the electronic structure surface of the Nickel Oxide thin film. However, the surface orientation or contamination can have influence in the growth dynamics (see section 4.2) but the XPS is not sensitive to that structural parameters but to the electronic structure: the occupied states below the Fermi energy.

For these reasons measuring the substrates with XPS is useful to diagnose how clean is a surface and to check its chemical composition and oxidation state. However, for the aim of this research work: the electronic structure of the NiO thin films under certain variations of the growing parameters, the analysis by XPS of a substrate which has been properly cleaned and characterized by other techniques, provides no further information and, more important, has no

great influence on the final results. Works of our own research group which concern the early stages of growth of evaporated materials on different substrates need a profound study with XPS of the substrates, whose electronic structure has a big influence on the properties of the deposited material [156, 180, 176, 181].

Ni 2p doublet

NiO is a charge transfer oxide whose electronic structure gives rise to a complex Ni 2p spectrum with multiple peaks. The Ni 2p photoemission spectrum of Nickel Oxide has attained much debate in the last decades due to its intrinsic complexity which could not be explained using the single-electron band theories [70]. Its interpretation has been discussed for many years and much effort has been made to explain the different contributions arising from this photoemission structure [182, 165, 183]. The interpretation of the Ni $2p_{3/2}$ spectrum is summarized in figure 6.29, where cluster model calculations are included, the different contributions to the photoemission structure can be easily observed, and will be explained here:

NiO ground state is composed by a mixture of at least three relevant configurations: the main line (here named *Volume* or *Bulk* peak) painted in green in figure 6.29, $\underline{c}3d^9\underline{L}$; the charge-transfer broad satellite, which corresponds to transitions $\underline{c}3d^8$ and $\underline{c}3d^{10}\underline{L}^2$ represented with cyan line in figure 6.29; and the last contribution, a shoulder separated 1.5 eV from the Bulk peak. Initially the shoulder of the main peak was assigned to Ni^{3+} ions by some authors, and later proposed as a consequence of non-local screening effects [182]. Finally, this shoulder results to be composed by non-local and surface components [183], represented with pink and blue lines in figure 6.29. Our research group has contributed to clarify some aspects of this Surface shoulder within the last years with the support of cluster model calculations [165, 183, 184, 177, 176, 172]. The Surface component arises from the Ni ions in pyramidal symmetry at the surface while the Bulk component comes from octahedrally coordinated NiO_6 complete clusters. Together with the non-local screening effects the surface contribution has completed the theoretical interpretations needed for an almost perfect fit between simulation and experimental data. The contribution $\underline{c}3d^8$ is due to the asymmetry of the final state centred at 862 eV. These contributions arise from the multiple ground state described in equation 6.1 plus a higher-order term, having:

$$\Psi_0 = \alpha \left|3d^8\right\rangle + \beta \left|3d^9\underline{L}\right\rangle + \gamma \left|\underline{c}3d^{10}\underline{L}^2\right\rangle, (\alpha^2 + \beta^2 + \gamma^2 = 1) \tag{6.2}$$

The fact that the peak $2p_{3/2}$ is composed by a surface and a bulk contribution will be considered the key of this section: with XPS technique we will measure and quantify the relative intensity of the surface component with respect to the bulk component for the deposited NiO thin films. It is expected to observe a variation in this relation with the addition of oxygen to the sputtering plasma, the amount of deposited material and the substrate temperature.

The region studied by XPS for each NiO deposited sample is the Ni 2p doublet. In figure 6.30 two curves are shown: the experimental Ni $2p_{3/2}$ photoemission spectrum of a NiO single-crystal with (1 0 0) orientation (bottom curve) and that of a NiO thin film grown on AAM substrate (upper curve), measured with the Mg X-ray source. The single-crystal reference has been previously measured and interpreted by our research group [180, 176].

As can be observed in figure 6.30 the structures $2p_{1/2}$ and $2p_{3/2}$ originated by the spin-orbit coupling are separated by 18.5 eV. Due to its non-monochromatic emission spectrum the Mg X-ray source generates satellite structures for each measured peak with intensity and distance indicated in table 3.3. The peaks that form the doublet are labelled as described previously in figure 6.29, composed by final states, that arise from the different ground state configurations of the NiO thin film, as previously explained ($\underline{c}3d^{10}\underline{L}^2$, $\underline{c}3d^8$). As it can be clearly seen, the surface component is much lower for the single crystal sample, where the surface-to-volume ratio is lower than in the nanostructured NiO thin film.

In the following we will centre our attention only on the main structure of this doublet: the

$2p_{3/2}$ peaks.

Metallic Ni is not observed in the XPS spectra of the NiO thin films. Metallic Ni appears at a binding energy of 852.7 eV, almost 2 eV away from the Ni^{2+} in NiO. On the other hand, Ni^{3+}, if present, is very difficult to observe in the XPS spectra. Due to their low cross section and overlapping with other states of NiO. Additionally, there are very few works reporting the existence of Ni^{3+} by XPS, but they are not conclusive enough [185, 186, 187].

O 1s

The oxygen 1s region measured by XPS can provide additional information to that obtained on Ni 2p states. According to the literature the peak position for O 1s states in NiO lies within the range: 529.5-533.3 eV [188, 189]. In our case, the oxygen 1s spectra present two peaks for all the samples measured. It must be remarked that samples were in contact with the atmosphere during a short time when transferring them between the deposition chamber and the analysis chamber. The origin of the second peak can be due to several factors:

- In a contaminated surface oxygen-related compounds like H_2O and OH^- would appear in the photoemission spectrum at higher binding energy [189, 190, 191].
- Adsorbed oxygen would contribute as well to the photoemission spectrum, however this last possibility can be cleared up after performing an annealing *in vacuum* of the surface in order to re-evaporate the adatoms, as shown in reference [188].
- The formation of layers or islands of oxyhydroxides such as β- and γ-NiOOH lead to different new peaks at higher and lower BE [192].

6.2.2. XPS results

In this section we will show the XPS results for the Ni 2p and O 1s regions measured for our NiO thin films. The spectra were collected with pass energy (CAE) of 20 eV in order to have a good equilibrium between count rate and resolution. For the case of the Ni 2p, the relation between the main, surface and non-local contributions will be shown. Under certain growing conditions the surface-to-volume ratio can be greatly enhanced [172]. Together with the Ni2p region the oxygen region was measured as well. Every sample showed the main peak located around 530 eV and another peak at 532 eV.

The oxygen 1s region is subject of more uncertainty due to the high reactivity of this element with the environment, as explained before. Although charge transfer corrections have been performed, the position of O 1s has a wide range of values according to the literature. The separation between the two peaks for any oxygen content and for both substrates is about 1.9 eV, being the most intense peak position at 529.5 eV. As happened to the Ni 2p spectra the O 1s results show similar tendency on both substrates.

Quantification

The spectra were analysed with the program *newfit*, developed by Christian Schüßler-Langeheine to quantify photoemission data [193]. This software employs the CERN numerical minimization program *Minuit* to solve the algorithms, which uses different strategies to perform a least squares fittings of the experimental data [194]. *Newfit* program performs a double convolution of Gaussian and Lorentz curves to fit the photoemission peaks of a XPS spectrum. A *Shirley* background is included in the calculations. This background is proportional to the integrated intensity between the Fermi energy and the point evaluated [46].

We estimate an error in each fitting between 5% and 10% as an upper bound, although the mathematical error given by the program *newfit* corresponds to the statistical error of the fit, being quite complicated to give a correct value for the uncertainty in the fittings.

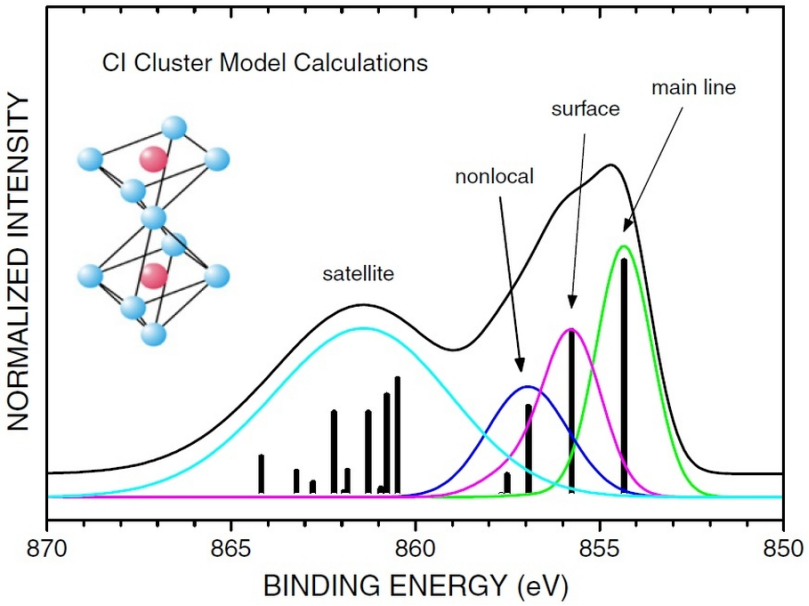

Figure 6.29: Cluster model calculations of the Ni 2p XPS spectrum (figure from [177]). Calculations were done using an octahedral NiO_6 cluster with a pyramidal NiO_5 cluster on top simulating the surface states.

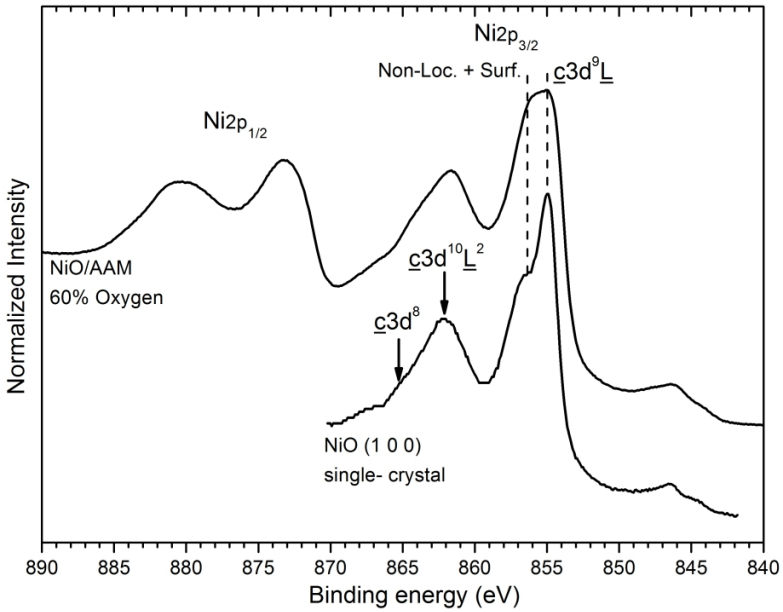

Figure 6.30: XPS Ni 2p spectrum of nanostructured NiO deposited on AAM for a 60% oxygen content in plasma (up) and Ni $2p_{3/2}$ of a single-crystal NiO sample (down). The dashed lines indicate the surface and bulk components that vary between single-crystal and nanostructured deposited NiO coating. The doublet structure is labelled ($2p_{1/2}$) and ($2p_{3/2}$). At lower binding energy the satellites structure are located at approximately 8.3 eV from each peak due to the Mg X-ray source.

According to the contributions that form the Ni 2p spectrum, as explained previously, three peaks were included to simulate to the main structure: Volume, Surface and Non-Local Screening contributions. The final states that form the structure between 860 eV and 865 eV (see figure 6.30) were simulated for fit consistency by means of wider peaks. The spurious satellites coming from the X-ray anode used to measure the sample (Mg or Al) were as well included in the fitting. Every photoemission peak was characterised according to three parameters: position, FWHM and intensity. The Non-Local peak intensity is proportional to the Volume peak with a fixed ratio [182]. Every parameter is related to the main line (Volume contribution). The relative intensity of the Surface and Bulk contributions to the main peak provides structural information about the effective surface of a coating. Coatings grown under conditions that enhance nanostructured samples present a higher relative intensity of the Surface peak in comparison to the Volume peak.

The oxygen region was as well fitted in order to extract some conclusions. The quantification of the two peaks that form the O 1s region has been carried out with two peaks, one located at around 530 eV, named *main peak*, and another located at higher binding energy, around 532 eV, named *adsorbed peak*.

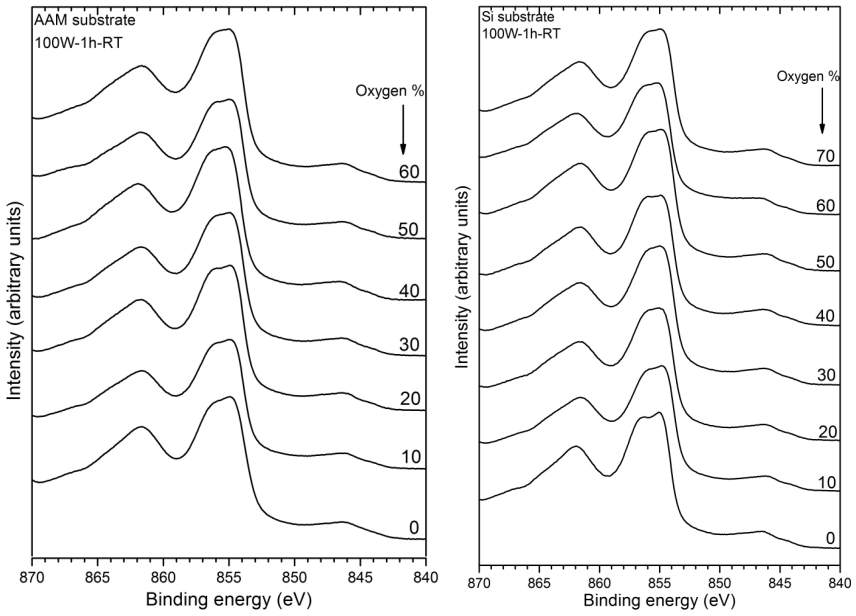

(a) AAM substrate (b) Si substrate

Figure 6.31: XPS spectra of the evolution of the Ni 2p of NiO films grown at 100W-1h-RT on AAM and Si substrates. The bulk and surface contributions at 854.5 eV and 856 eV, respectively, form the Ni $2p_{3/2}$ main structure. These structures behave similarly on both substrates.

Samples grown at RT

We start presenting XPS results for films grown at 100W-1h-RT. Ni 2p spectra for both Si and AAM substrates are shown in figure 6.31. The evolution of the structures with the oxygen content in the plasma is not as clear as observed with other techniques like EXAFS or XANES. Here the variation is smaller and there is a big step between the sample grown with pure Ar and the rest of coatings grown with some oxygen content. There is not a big difference between the spectra of coatings grown on Si wafer and on AAM substrates.

As mentioned above, the least squares fittings were performed on both substrates. An example of the deconvoluted spectra is shown in figure 6.32a. The different contributions, explained in the description of figure 6.30, are included in the fit: the Volume and Surface contributions are

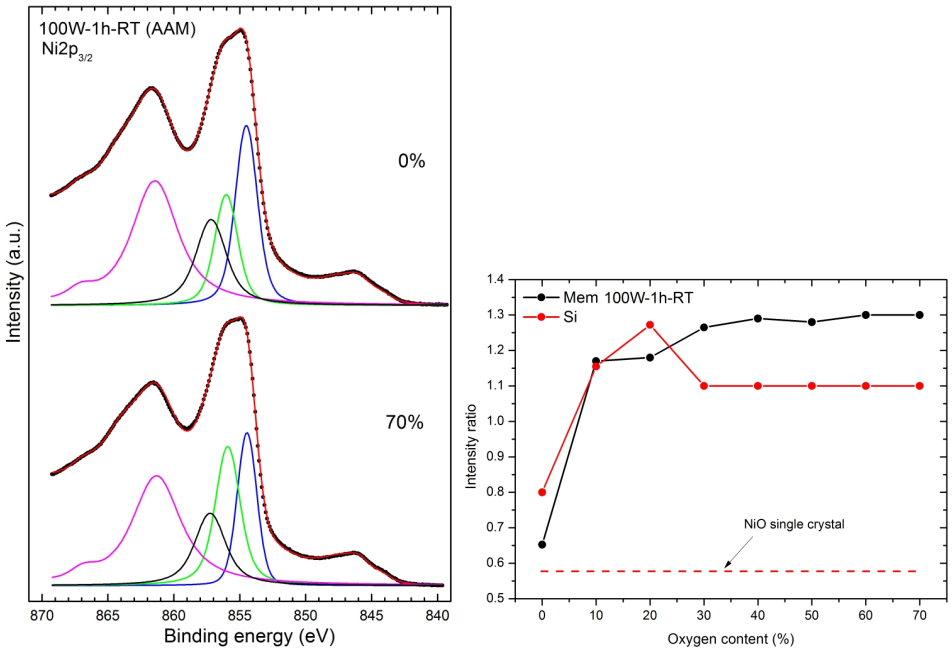

(a) Fittings of Ni 2p 100W-1h-RT 0% and 70%

(b) Surface-to-Volume ratio

Figure 6.32: (left) XPS deconvoluted spectra of the Ni $2p_{3/2}$ level for films grown at 100W-1h-RT on AAM at 0% and 70% oxygen plasma composition. The main contributions are: blue line for the main peak, green line for surface peak, black line for the non-local screening effects. The pink line represents other final-states, plus a background (not shown) and the red line is the result of the fitting. The surface component increases when oxygen is added to the plasma. (right) Surface to Volume ratio summarized for the fittings performed on AAM and Si substrates at 100W-1h-RT conditions.

painted in blue and pink lines, respectively. The green line represents the Non-Local peak. The ratio between the intensity of the main component and that of the non-local component was imposed to be the same for all samples. On the other hand, the intensity of the surface component was allowed to vary and its relative intensity gives information on the surface-to-volume ratio of the sample. Indeed, as it can be clearly observed in figure 6.32a, the surface component for sample grown with 70% oxygen in the plasma is relatively more intense than for the sample grown with pure Ar. As it has been shown in section 4.3.1, the grain size of the NiO films decreases upon oxygen addition to the plasma, which is consistent with a higher surface-to-volume ratio for samples grown with oxygen.

In figure 6.32b the fitting results of the surface-to-volume peak intensity ratios for this set of samples on both substrates as a function of the oxygen content of the plasma are shown. The ratio between the surface peak and the main bulk peak of the XPS Ni $2p_{3/2}$ spectra can give information on the relative signal coming from the surface, which should be correlated with the crystallite size. The value obtained for the 0% sample is ≈ 0.65, slightly larger than the value of 0.54 expected for single crystal NiO [176], indicated with an horizontal dashed red line (figure 6.32b). By adding 10% oxygen to the plasma, a sudden increase in this ratio is observed, to a value close to 1.2, which indicates a larger contribution of the surface. For higher oxygen content, the surface-to-volume ratio remains approximately constant. No relevant differences in the trend are observed between both substrates. This behaviour correlates very well with the reduction in crystal size shown in figure 4.19, in which a sudden drop in the crystallite size was observed when going from 0% to 10%, and afterwards it remained almost constant. This result provides an excellent example of the correlation between electronic and structural properties in this material. It also confirms that the intensity variations of the 1.5 eV shoulder in the Ni $2p_{3/2}$ XPS spectra

of NiO can be associated with surface effects.

The O 1s spectra on the same set of samples are shown in figure 6.33. As it can be observed in the figure, there is almost no variation of the position of the peak located at higher binding energies (around 531.5 eV) both at the Si wafer and AAM substrates. The slight variation of the relative intensity will be shown below together with the quantification.

Figure 6.34 shows an example of the fitting of the oxygen region where the two deconvoluted peaks are shown. These fitted spectra correspond to NiO thin films grown on AAM substrate under 0% and 70% oxygen in the sputtering plasma. The main peak, painted in blue, is located at 529.5 eV, whereas a second peak, the adsorbed peak, painted in green line, locates around 2 eV higher binding. The Shirley background is not shown. In figure 6.34b the intensity ratio (adsorbed-to-main peak) for coatings grown on both substrates (Si and AAM) is shown. As it can be seen, the oxygen addition to the plasma changes the ratio between both peaks increasing the adsorbed peak, which suggests that it can be associated with the surface effects. However, this increase is more gradual than the surface-to-volume variation observed for the Ni 2p contributions, which can be explained by the influence from surface contamination.

Effects of substrate temperature

As seen in previous sections, the substrate temperature has important effects on the properties of the films. In this subsection we show the XPS results obtained on samples grown at a substrate temperature of 200℃ for two magnetron power values: 100 W and 200 W.

The deconvoluted photoemission spectra of pure argon and pure oxygen growths for samples grown at 100W-1h-200℃ and 200W-1h-200℃ are shown in figure 6.35. As for films grown at 100W-1h-RT: the Surface peak increases its intensity and width with the addition of Oxygen to the sputtering plasma. However, this increase in intensity is lower than for samples grown at 100W-1h-RT shown in figure 6.32a. This fact is actually an expected behaviour taking into account the slight variation of the 3d sub-band observed in the XANES spectra (see section 6.1.4) which suggests that the temperature is a more important factor than the oxygen addition for these coatings. In figure 6.36 the evolution of the Surface-to-Volume ratio with the oxygen content is shown for both series grown at 200℃. It can be seen that the variation of the Surface component of the Ni $2p_{3/2}$ with the oxygen addition is very slight for both set of samples, in a range between 0.7 and 0.9, as compared with the range between 0.7 and 1.3 observed for the series grown at RT (see figure 6.32b). This slow variation is in accordance with XANES results (where the 3d sub-band splitting is barely appreciable). The higher substrate temperature produces samples with larger crystallite size, as seen in chapter 4 by SEM and XRD, and, hence, the surface effects are lower.

Concerning the oxygen region, also a small evolution with the oxygen addition to the plasma is observed. After performing fittings in all O 1s XPS spectra for both set of samples grown at 100W-1h-200℃ and 200W-1h-200℃, the summary of the intensity ratios is shown in figure 6.37. A similar trend to that obtained for the Ni 2p peak is observed, showing that the addition of oxygen to the sputtering plasma is not the relevant parameter when the substrate temperature is increased, as seen in the slope of the curves.

When the coatings are grown under the most extreme conditions of this work, 200W-2h-300℃, confirms the trend shown for samples grown at 200℃. This is shown in figure 6.38.

As seen in previous subsection, an increase in the substrate temperature produces a very slow variation of the surface-to-volume ratio with respect to room temperature. In figure 6.38a the results of the fittings of the Surface-to-Volume ratios for coatings grown at 200W-2h-300℃ for both substrates are summarized. At this high substrate temperature no clear evolution of the surface contribution with the oxygen addition to the plasma is observed. Similarly to what was observed in the XANES results, the effective surface at this temperature is very low even when the growth is performed at pure oxygen atmosphere. However, we must remark here that the fittings had more uncertainty than for others coatings, meaning a higher error at each

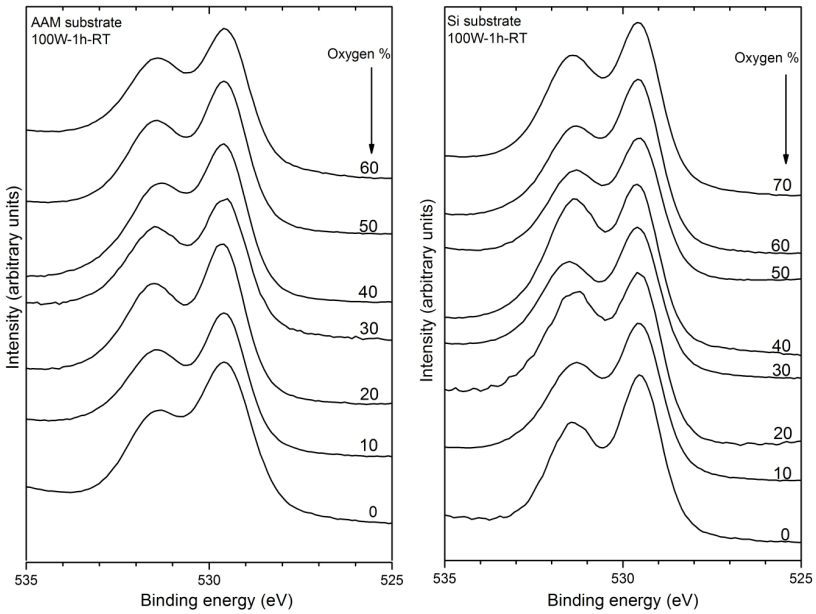

(a) AAM substrate (b) Si substrate

Figure 6.33: XPS spectra of the evolution of the O 1s of NiO films grown at 100W-1h-RT on AAM and Si substrates. There are two positions for O 1s, separated by 1.7 eV. The peak located at 529.5 eV corresponds to the main line of O 1s and the satellite at about 531.2 eV, of lower intensity, could have a relation with the growing parameters.

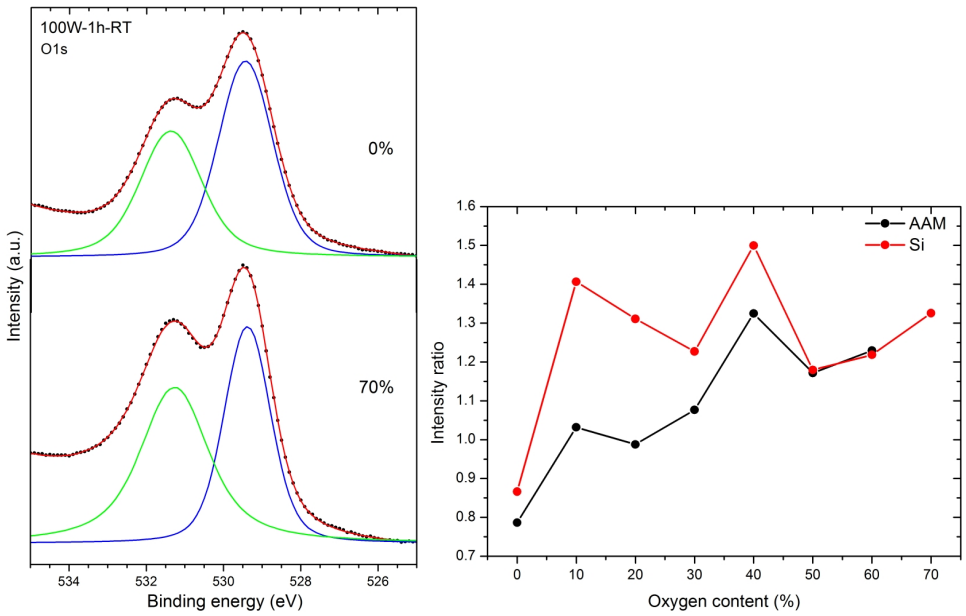

(a) Fittings of O 1s 100W-1h-RT 0% and 70% (b) Intensities ratio

Figure 6.34: (left) Results of the XPS fit deconvolution of the XPS spectra at the oxygen region for NiO thin films grown on AAM substrate under 0% and 70% oxygen in the sputtering plasma at 100W-1h-RT conditions. The peak at higher BE (around 2 eV) increases slightly its intensity in the 70% sample with respect to the pure Ar growth. (right) Intensity ratio between both peaks with the oxygen content of the plasma. Summarized for coatings on both substrates.

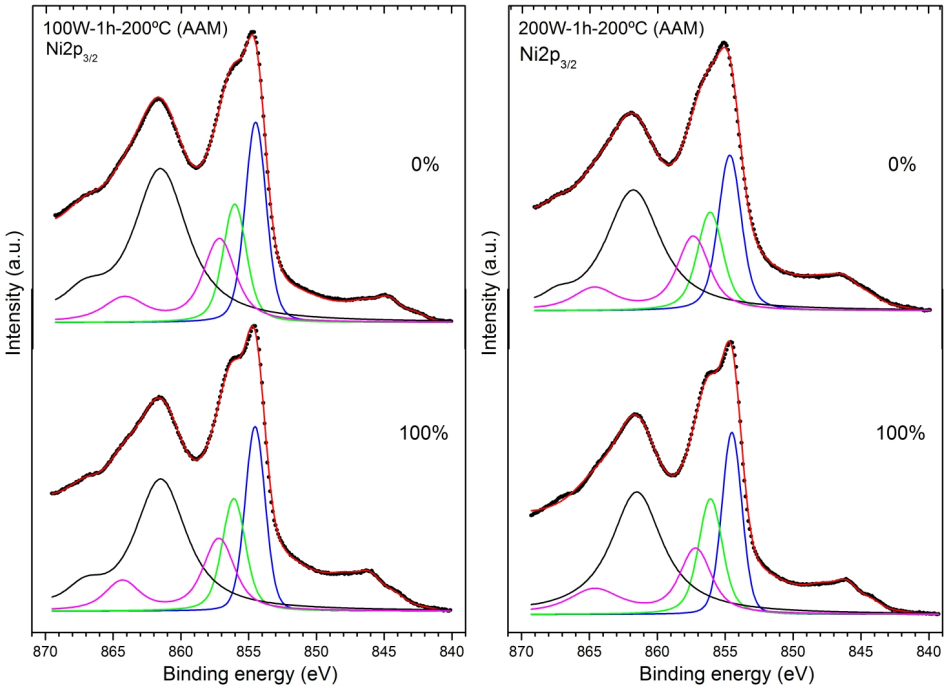

(a) 100W-1h-200ºC (b) 200W-1h-200ºC

Figure 6.35: XPS deconvoluted spectra for films grown on AAM substrate with pure argon and pure oxygen plasma. Blue and green lines represent the volume and surface components, respectively. In samples grown with pure argon a lower contribution of the Surface peak can be observed, although not as clearly as for coatings grown at 100W-1h-RT.

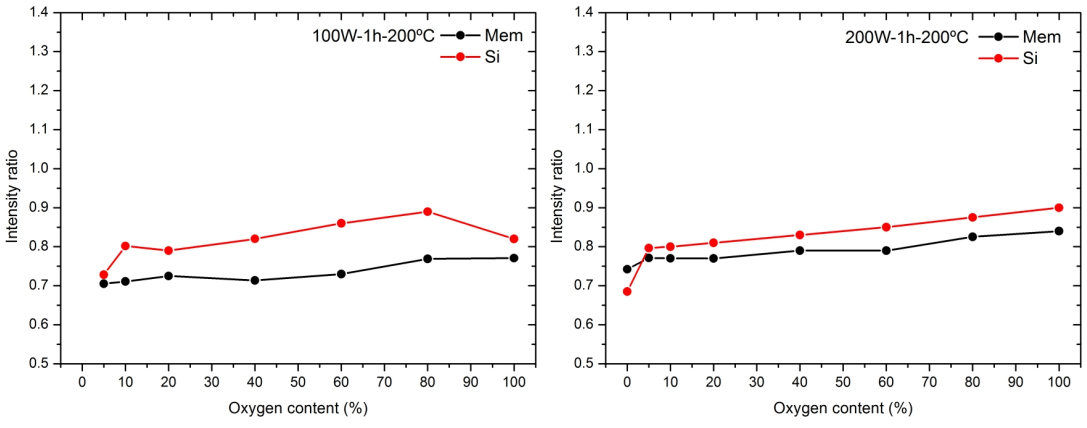

(a) 100W-1h-200ºC (b) 200W-1h-200ºC

Figure 6.36: Evolution of the Surface-to-Volume ratio with the oxygen content of the plasma for coatings grown at 200ºC. The variation of the Surface component of the Ni $2p_{3/2}$ with the oxygen addition is very slight for both set of samples due to the influence of the substrate temperature.

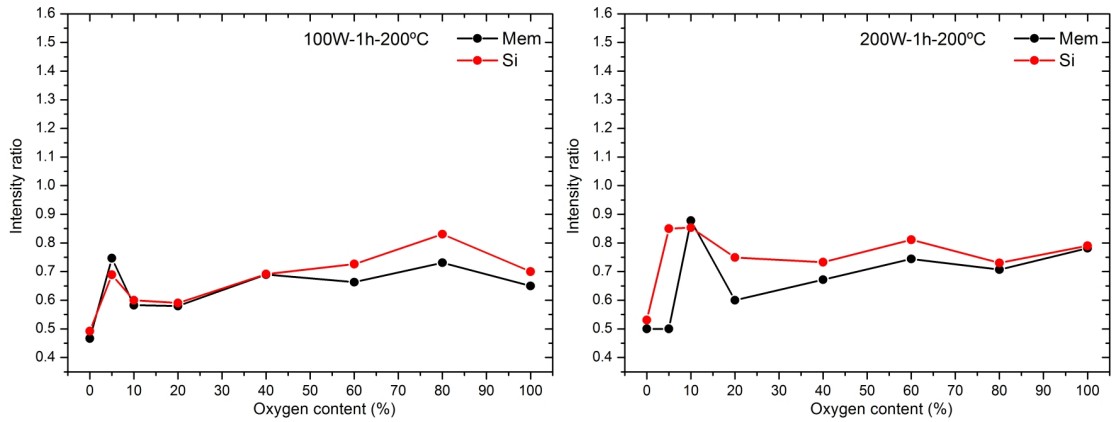

(a) 100W-1h-200℃ (b) 200W-1h-200℃

Figure 6.37: Intensity ratio of the O1s XPS peaks with the oxygen content in the plasma for samples grown at 200℃. There is almost no variation between substrates and between magnetron power, indicating the strong influence of the substrate temperature.

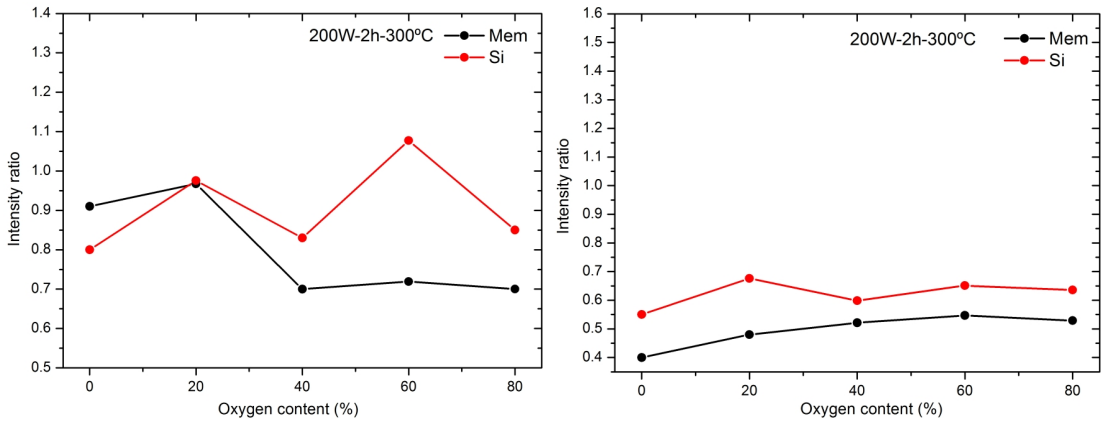

(a) Surface-to-Volume ratio (b) Oxygen relative intensities

Figure 6.38: Results of XPS fittings for samples grown at 200W-2h-300℃ on both substrates: (left) Surface to volume intensity ratios for coatings on both substrates (Si and AAM) for films grown at 200W-2h-300℃. There is almost no variation between substrates and between magnetron power, indicating the strong influence of the substrate temperature.
(right) Intensity ratio between the O 1s peaks for films grown at 200W-2h-300℃. Again, there is almost no variation between substrates and the slope of the intensity ratio with the oxygen content in the plasma is very low, indicating the strong influence of the substrate temperature. The y-axis scale is kept equal for all the O 1s fitting parameters in order to an easy comparative between results.

point. Films grown on Si substrate seem to behave coherently with the others results previously presented.

The intensity ratios obtained after fitting all oxygen regions for these sputtering conditions are shown in figure 6.38b. A slight tendency of the intensity ratio with the oxygen content in the plasma is observed, though it is difficult to assign the effect of the oxygen in plasma and the substrate temperature.

To summarize the XPS results, figure 6.39 shows: the Surface-to-Volume ratio for the Ni $2p_{3/2}$ structure and the Adsorbed-to-main ratio for the O 1s peaks of all series. The ratios shown correspond to the average of the fittings performed on XPS spectra of NiO films on both AAM and Si substrates. The data shown are classified into three regions, corresponding to the three different substrate temperatures, which, as has been shown, have a relevant effect on the surface-to-volume ratio and the oxygen peaks ratio as well.

The separation between the oxygen peaks lies within the range of 1.8 and 2.1 eV, though there is no relation between the oxygen content in the plasma or any growing parameter with this peak separation. There is a good correlation between the surface-to-volume ratio of the Ni 2p spectra and the intensity ratio of the two peaks observed in the O 1s spectra, which suggests that there is a correlation of the high energy peak in the O 1s spectra and the surface effects observed by XPS and XANES.

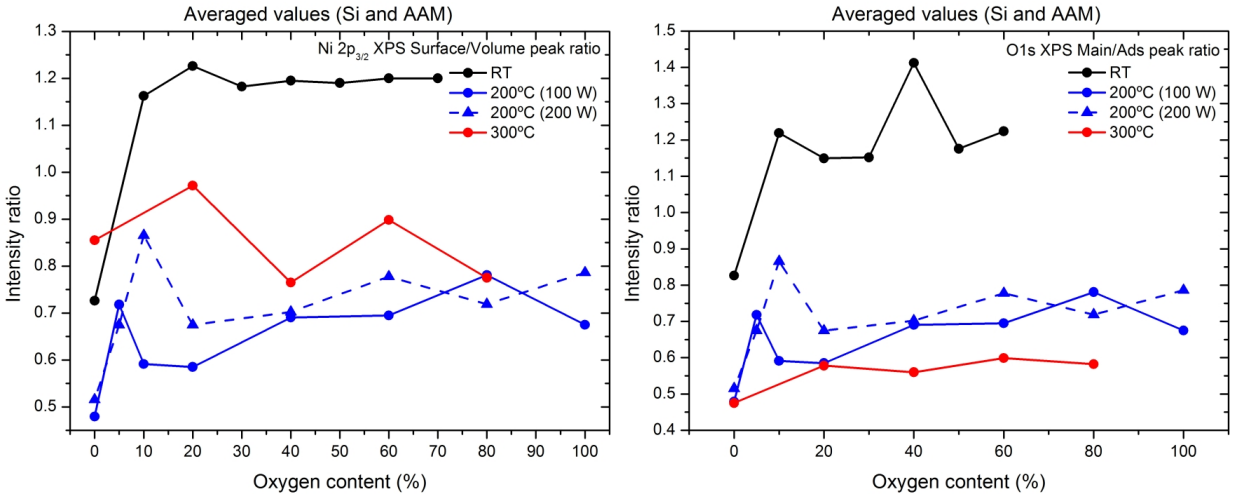

(a) Surface-to-Volume peaks intensity ratios for Ni 2p

(b) Intensity peaks ratios of O 1s

Figure 6.39: Summary of the main fitting parameters averaged from fittings performed on AAM and Si substrates. Similar results were obtained on Si substrates. (up) Surface-to-Volume peaks intensity ratios for Ni $2p_{3/2}$ region. The higher variation with the oxygen addition to the plasma occurs for samples grown at RT while the substrate temperature reduces this dependence. (bottom) Intensity ratios of the satellite and adsorbed peak for the O 1s region. The intensity ratio have a slight dependence with the oxygen content in the plasma but the substrate temperature reduces this trend.

6.3. Summary of chapter 6

The electronic structure and chemical state of the NiO thin films has been related to the crystal structure by means of XANES and XPS analysis.

The O 1s XAS spectra show a splitting of the peak assigned to Ni e_g states, caused by an enhancement of the surface effects due to the reduction of the crystal size. The lack of apical oxygen in the octahedra generates a distortion that breaks the O_h symmetry and splits the 3d

e_g sub-band. The oxygen absorption edge measured by XANES also shows a pre-edge peak associated with the presence of Ni vacancies, which produces Ni^{3+} ions and subsequently hole conductivity.

The Ni 2p XAS spectra do not change much for different growth conditions. The distinct changes in each spectrum, both at the O 1s and at the Ni 2p edges, have been successfully reproduced by cluster model calculations for growing conditions 200W-1h-RT, which showed that the Ni^{3+} and Ni^{2+} surface contributions increase linearly with the oxygen content in the plasma. Thus, the changes in this parameter (oxygen content in the sputtering plasma) during growth affect the electronic structure of these NiO films, which, in turn, can be associated with the changes in their structural and transport properties.

The amount of deposited material, given by the magnetron power and the deposition time, seems not to be determining in the trend in the absorption K-edge structures (splitting of the 3d sub-band and pre-edge). In contrast, the substrate temperature greatly affects these nanostructures by recovering the bulk reference NiO absorption spectrum. Therefore the less nanostructured the thin film the more similar the XANES spectra to the NiO bulk reference, as expected.

Through fluorescence yield measurements we have been able to determine that the variations of the oxygen spectrum are a surface phenomenon. After performing annealing experiments at open air and *in vacuum* it has been observed that: the variations of the oxygen absorption edge occur first on the surface. The fact that this effect occurs at the surface rather than in the bulk is coherent with the model proposed to explain the ageing effect in the resistivity results, by which a nearly stoichiometric oxide layer "protects" the NiO bulk hindering the oxygen diffusion outwards and therefore reducing the electrical conduction.

Similarly, the Ni absorption spectrum almost does not change with any of the growing parameters, as expected due to the similitude between the different initial atomic configurations which determine the final states. The annealing experiments confirm this fact by the lack of variations of the Ni L-edge.

Ni $2p_{3/2}$ XPS spectra of samples grown with oxygen show a larger intensity of the peak assigned to surface atoms that can be associated with the grain refinement observed by XRD and EXAFS. Fittings of the Ni 2p spectra confirm a direct relation of the oxygen addition to the sputtering plasma with an increase of the surface peak intensity, however this factor is attenuated when growth conditions are far from the more nanostructured thin films, where the effective surface is much less. This fact is in absolute accordance with the XANES results where the 3d sub-band splitting is much lower for those films.

Oxygen 1s photoemission spectra show two peaks whose relative intensities have a slight variation with the substrate temperature where three distinct slopes can be established, related with three different temperatures (RT, 200℃ and 300℃).

Therefore the oxygen addition plays a key role in both the electronic and crystal structure of the NiO thin films when the growing conditions favour the nanostructured properties of the coatings. This correlation between the average crystal size and the surface contribution of the Ni 2p photoemission peak together with the splitting of the 3d band observed with XANES allow us to determine the high effect of the oxygen addition to the sputtering plasma in creating nanostructured coatings at low substrate temperatures.

Chapter 7

Summary and conclusions

> "*Men moet anderen niet meedeelen ideeën die nog niet uitgewerkt, plannen die nog niet volvoerd, proeven die nog niet genomen zijn.*"
>
> Pieter Zeeman

The main objective of this research work is to study the properties of nanostructured Nickel Oxide thin films grown by off-axis RF reactive magnetron sputtering. A comprehensive study of the films grown on planar and porous substrates under different sputtering conditions from a NiO target has been done using several characterization techniques. The strategy to achieve the aim of this work has followed this scheme:

- Several growth parameters were varied in order to study how they affect the morphology and structure: magnetron power, deposition time and substrate temperature, together with variations of the oxygen content in the plasma.
- The morphology and structure were studied by means of SEM, profilometry, GIXRD and EXAFS in order to determine the dynamics of growth, the long range order and local order.
- The electro-optical properties were studied by resistivity and optical absorption measurements.
- Finally, the electronic structure of the films was studied by XPS and XANES.

According to this strategy, sample deposition and characterization iterations were performed in order to finally obtain the more suitable sets of parameters that generate porous films of high effective surface with our experimental set-up. Firstly we show a study of the sputtering NiO targets, which were analysed until a correct stoichiometry and quality was provided by the suppliers. This fact is not commonly mentioned in the literature but due to the importance of a good quality starting material, a considerable amount of time was dedicated to test and check them before deposit samples with reproducibility.

We have explored several combinations of the growth conditions by varying the magnetron power (from 100 to 200 W), the deposition time (from 1 to 2 hours), the substrate temperature (from room temperature to 300ºC) and the Ar/O_2 plasma composition (increasing the amount of Oxygen from 0% to 100%). Surprisingly the sputtered NiO keeps the porosity of the Alumina template. In order to explain this fact, in chapter 4 we propose and discuss a growth model on porous substrates based on the FESEM results, which shows a **columnar growth that maintains the porosity** of the AAM substrates and results in NiO hexagonally ordered nanoporous structures. A competition of initial grains occurs favouring growth on certain preferred

orientations until one is prominent and the growth develops in columns, which occurs mainly in the vertical axis. Columnar NiO grown on top of the AAM interpore area reaches about 200 nm until pores are closed. How the deposition parameters affect this growth dynamics is discussed and upper bound limits for the sputtering conditions are shown. Independently of the porosity of the deposited coatings, the **addition of oxygen to the plasma reduces the grain size** as well as decreases the amount of deposited material. Further analysis using diffraction techniques provides structural information on the influence of the deposition parameters, especially the oxygen addition.

Grazing incidence XRD shows **crystallographic textures that depend on the O_2 content of the plasma**, being the (2 0 0) direction the preferential one at lower oxygen content, and the (1 1 1) direction that at higher oxygen content for certain deposition conditions. Approximative Scherrer calculations performed on the **broadening of the diffraction peaks** suggest that the grain size is reduced as oxygen is incorporated to the sputtering gas by a factor of 4, supporting the FESEM observations. The lower intensity of the diffraction peaks for the samples grown with oxygen suggests partial lattice disorder. Apart from the qualitative study of the GIXRD with tube and synchrotron X-ray sources, an analysis of the diffraction curves reveals a **lattice expansion of about 2%** associated with the oxygen addition. Grazing incidence XRD shows that the diffraction peaks move to lower 2θ positions in the bulk whereas more surface sensitive diffraction measurements shows the opposite behaviour. This indicates that more than one average lattice parameter coexist within a sample, having a gradient with thickness. This fact is a strong proof of the great influence that certain deposition conditions have on the films structure, where we must remark the oxygen addition and the substrate temperature. A further investigation should be performed in order to fully understand the grain size evolution and growth dynamics, which is more complex owing to the out-of-equilibrium nature of the magnetron sputtering process.

Complementary analysis shown in the last section of chapter 4, add local structure information by means of EXAFS, showing a decrease of the Ni-Ni coordination number when the oxygen content of the plasma increases, which can only be explained by an **increasing presence of Ni–vacancies in the NiO lattice**. The EXAFS analysis confirms an increase of the disorder with the O_2 in plasma, as quantified by the Debye–Waller factor, as well as an increase of the second neighbour distance, i.e., a lattice expansion; supporting the XRD results. However, due to the high disorder of the samples it was not possible to perform a very accurate study of the amount of Ni vacancies as well as an estimation of the expansion lattice, but these facts provide a hint on how the structural variations are correlated with the electrical behaviour of the samples, as is discussed in next chapter.

The electrical and optical results of the grown films are shown in chapter 5. The **electrical resistivity of the NiO films decreases with the oxygen content** in the plasma up to four orders of magnitude, which is consistent with p-type conductivity originated by an oxygen enrichment in the NiO lattice. As suggested by the EXAFS results, **Ni vacancies generate Ni^{3+} ions**, responsible for the conduction mechanism by holes. This result is observed for all deposition conditions and has a direct relation with the oxygen influence, which generates disorder and subsequently Ni vacancies. Non-stoichiometric Nickel Oxide is known to be p-type conductor and in this work we show this result together with comprehensive structural and optical information obtained with other techniques.

In turn, substrate temperature has a major impact on the electrical behaviour, reducing the effect of the oxygen addition. An ageing effect was also observed for films exposed to air, which increase their resistivity with time. A model based on an analogy with the oxide layer that grows on top of metals was used to explain this result. In our case the diffusion of oxygen through the surface will imply a more stoichiometric layer on the top which interacts with the environment. Such model of ageing stablishes an increase of the resistivity which evolves like $\rho \sim t^c$, being t

the time exposed to air and c close to 0.5, resembling a parabolic behaviour.

The **optical absorption confirms a reduction of the energy band gap**, highly correlated with the oxygen addition to the plasma and substrate temperature. The reduced gap and increased conductivity are results that support the influence of the Ni vacancies on these macroscopic properties and give rise to solid interpretations of the electronic structure studied in chapter 6.

The electronic structure of the grown NiO thin films has been measured by X-ray absorption (XANES) and photoemission (XPS), as shows chapter 6. X-ray absorption (in electron yield mode) measured at the oxygen K-edge of nanostructured NiO has several structures very different from the stoichiometric single-crystal NiO. A **pre-edge peak is assigned to Ni^{3+} ions**, a **shoulder appears in the 3d Ni sub-band due to e_g states splitting**, caused by an enhancement of the surface effects due to the reduction of the grain size and higher energy final states appear as broad structures, suggesting a widening mechanism related to the nanostructured NiO. In turn, the Ni 2p XAS spectra do not change much for different growth conditions. The distinct changes in each spectrum, both at the O 1s and at the Ni 2p edges, have been successfully reproduced by **cluster model calculations**, which **showed that the Ni^{3+} and Ni^{2+} surface contributions increase linearly with the oxygen content** in the plasma up to 14% and 56%, respectively. On the contrary, the bulk contribution with complete (not broken) octahedral NiO_6 clusters decreases linearly with the oxygen addition supporting once more an increase of the effective surface and the disorder of the crystal structure.

Upon thermal treatment the surface contributions to the XANES spectra are greatly decreased recovering the well-known stoichiometric NiO spectrum, i.e., the pre-edge and 3d splitting gradually disappear and the higher energy final states peaks get narrowed. This annealing of the sample has a consequence in an increase of the resistivity, as was observed in chapter 5. Based on these results, fluorescence yield was performed showing absorption structures from a nanostructured instead of stoichiometric NiO. The higher probe depth of fluorescence yield indicates that inside the bulk the disordered and Ni-deficient structures still remains whereas on the surface the thermal treatment turned it into a stoichiometric layer. This fact supports the electrical resistivity ageing model presented, which is based on a forming surface layer.

Further complementary information about the electronic core level states and the influence of the oxygen added to the plasma was observed by photoemission experiments. As a model accepted recently, the XPS Ni $2p_{3/2}$ spectrum shows a shoulder peak assigned to surface states. This contribution can be associated with the broken octahedra NiO_5 located at the grain surface, and is enhanced for samples grown with oxygen due to the grain refinement. The behaviour of the surface peak intensity in the presence or absence of oxygen content in the plasma correlates very well with that observed on the average grain size obtained by XRD at low substrate temperatures. As observed previously with XANES, an important factor is the substrate temperature: when heating during growth the surface peak in the Ni $2p_{3/2}$ spectrum decreases, suggesting lower surface-to-volume ratio and lowering the effect of the oxygen addition to the plasma.

The major contribution of this work is to show how the growth conditions affect the properties of nanostructured NiO thin films and the properties that arise from these variations. Changes in the oxygen content of the sputtering plasma during growth affect the electronic structure of these NiO films, which, in turn, can be associated with changes in their morphological, structural, transport and optical properties.

Chapter 8

Resumen y conclusiones

El principal objetivo de este trabajo de investigación es estudiar las propiedades de láminas delgadas nanoestructuradas de óxido de níquel crecidas por pulverización catódica reactiva por magnetrón de radiofrecuencia con una disposición no centrada del magnetrón. Se ha realizado un exhaustivo estudio de las láminas delgadas crecidas sobre substratos planos y porosos bajo diferentes condiciones de pulverización con un blanco de NiO utilizando varias técnicas de caracterización. La estrategia para conseguir el objetivo de este trabajo ha seguido el siguiente esquema:

- Eplorar diferentes parámetros de crecimiento con el fin de estudiar cómo afectan a la morfología y estructura: potencia del magnetrón, tiempo de deposición y temperatura de substrato, junto con variaciones en el contenido de oxígeno en el plasma.
- Estudiar la morfología y estructura mediante SEM, perfilometría, GIXRD y EXAFS para determinar la dinámica de crecimiento, el orden en rango local y global.
- Estudiar las propiedades electro-ópticas mediante medidas de resistividad y absorción óptica.
- Finalmente, estudiar la estructura electrónica de las láminas mediante XPS y XANES.

Según esta estrategia, se realizaron iteraciones de crecimiento de muestras y su análisis con el fin de obtener un conjunto de parámetros adecuado con nuestro montaje experimental que genere láminas porosas de gran superficie efectiva. En primer lugar mostramos un estudio de pulverización de los blancos de NiO, que fueron analizados hasta que los proveedores proporcionaron una correcta estequiometría y calidad. Este hecho no es comúnmente mencionado en la literatura, pero debido a la importancia de partir de un material de buena calidad, se dedicó una considerable cantidad de tiempo a testear y comprobar los blancos antes de depositar muestras con reproducibilidad.

Hemos explorado varias combinaciones de condiciones de crecimiento variando la potencia del magnetrón (entre 100 y 200 W), el tiempo de crecimiento (de una a dos horas), la temperatura del substrato (desde temperatura ambiente hasta 300℃) y la composición Ar/O_2 del plasma (aumentando la cantidad de oxígeno de 0% a 100%). Sorprendentemente el NiO pulverizado mantiene la porosidad del patrón de Alúmina. A fin de explicar este hecho, en el capítulo 4 proponemos y discutimos un modelo de crecimiento sobre substratos porosos basado en los resultados de FESEM, que muestran un **crecimiento columnar que mantiene la porosidad** del substrato de AAM y resulta en estructuras nano-porosas de NiO ordenadas hexagonalmente. La competición inicial de los granos ocurre favoreciendo el crecimiento en ciertas orientaciones preferenciales hasta que una de ellas prevalece y el crecimiento se desarrolla en columnas, lo que ocurre principalmente en el eje vertical. El NiO crecido columnarmente sobre el área entre poros de la AAM alcanza cerca de 200 nm hasta que cierra el poro debido al ensanchamiento de estas columnas. Se ha discutido cómo afectan los parámetros de pulverización a esta dinámica

de crecimiento y se han establecido límites superiores para las condiciones de pulverización. Independientemente de la porosidad de los recubrimientos depositados, **la adicción de oxígeno al plasma reduce el tamaño de grano** así como disminuye el material depositado. Un análisis más detallado, llevado a cabo a continuación, usando técnicas de difracción proporciona información estructural de la influencia de los parámetros de deposición, especialmente la adicción de oxígeno, como se muestra en el capítulo 4.

Los resultados de difracción de rayos-X en incidencia rasante muestran **texturas cristalográficas que dependen del contenido de O_2 en el plasma**, siendo la (2 0 0) la dirección preferencial para bajo contenido de oxígeno, y la dirección (1 1 1) para alto contenido de oxígeno bajo ciertas condiciones de crecimiento. Cálculos aproximativos de Scherrer realizados en el ensanchamiento de los picos de difracción sugieren que el tamaño de grano se reduce en un factor cuatro con la incorporación de oxígeno al gas de pulverización, apoyando las observaciones de FESEM. La menor intensidad de los picos de difracción para muestras crecidas con oxígeno sugiere un desorden parcial de la red. Aparte de un estudio cualitativo mediante GIXRD con fuentes de rayos-X de tubo y sincrotrón, un análisis de las curvas de difracción revela una **expansión de la red de cerca de un 2%** asociada a la adicción de oxígeno. La XRD en incidencia rasante muestra que los picos de difracción se mueven a posiciones 2θ menores en el volumen mientras que medidas de difracción más sensibles a la superficie muestran un comportamiento opuesto. Esto indica que más de un parámetro de red coexiste dentro de la muestra, exhibiendo un gradiente con el espesor. Este hecho es una prueba sólida de la gran influencia que ciertas condiciones de deposición tienen en la estructura de la lámina, donde debemos remarcar la adicción de oxígen y la temperatura del substrato. Una investigación más detallada debe realizarse a fin de entender completamente la evolución del tamaño de grano y la dinámica de crecimiento, que es más compleja debido a la naturaleza fuera del equilibrio del proceso de pulverización por magnetrón.

Un análisis complementario en la última sección del capítulo 4 añade información estructural mediante EXAFS, mostrando un descenso del número de coordinación Ni–Ni cuando el contenido de oxígeno en el plasma aumenta, lo que sólo puede ser explicado por el **aumento de la presencia de vacantes de Ni en la red del NiO**. El análisis de EXAFS confirma un aumento del desorden con el O_2 en el plasma, cuantificado por el factor de Debye–Waller, así como un aumento de la distancia del segundo vecino, i.e., una expansión de la red; apoyando los resultados de XRD. Sin embargo, debido al alto desorden de las muestras no fue posible realizar un estudio muy preciso de la cantidad de vacantes de Ni así como una estimación de la expansión de la red, pero estos factores proporcionan un indicio sobre cómo las variaciones estructurales están correlacionadas con el desarrollo eléctrico de las muestras, como se discute en el siguiente capítulo.

Los resultados eléctricos y ópticos de las láminas crecidas se muestran en el capítulo 5. **La resistividad eléctrica de las láminas delgadas de NiO decrece con el contenido de oxígeno** en el plasma hasta cuatro órdenes de magnitud, lo que es consistente con la conductividad tipo-p originada por un enriquecimiento de oxígeno en la red del NiO. Como sugieren los resultados de EXAFS, **las vacantes de Ni generan iones Ni^{3+}**, responsables del mecanismo de conducción por huecos. Este resultado se observa para todas las condiciones de crecimiento y tiene una relación directa con la influencia del oxígeno, que genera desorden y, consecuentemente, vacantes de Ni. El óxido de níquel no estequiométrico es conocido por ser conductor tipo-p y en este trabajo mostramos este resultado junto con una información exhaustiva estructural y óptica obtenida con otras técnicas.

A su vez, la temperatura del substrato tiene un gran impacto en el comportamiento eléctrico, reduciendo el efecto de la adicción de oxígeno. Un efecto de envejecimiento ha sido también observado en láminas expuestas al aire, cuya resistividad aumenta con el tiempo. Para explicar este resultado se ha usado un modelo basado en una analogía con la capa de óxido que crece sobre los metales. En nuestro caso la difusión del oxígeno a través de la superficie implicará una capa más estequiométrica sobre la superficie que interacciona con el entorno. Un modelo así para

el envejecimiento establece un aumento de la resistividad que evoluciona como $\rho \sim t^c$, siendo t el tiempo de exposición al aire y c menor que 1, similar a un comportamiento parabólico.

La absorción óptica confirma una redución de la energía de la banda prohibida, altamente correlacionada con la adicción de oxígeno al plasma y la temperatura del substrato. La banda prohibida reducida y la conductividad aumentada son resultados que apoyan la influencia de las vacantes de Ni en estas propiedades macroscópicas y dan lugar a sólidas interpretaciones sobre la estructura electrónica estudiada en el capítulo 6.

La estructura electrónica de las láminas delgadas de NiO crecidas ha sido medida por absorción de rayos-X (XANES) y fotoemisión (XPS), como se muestra en capítulo 6. La absorción de rayos-X medida (en modo de medida de emisión de electrones, TEY) en el borde K del oxígeno del NiO nanoestructurado muestra varias estructuras muy diferentes del monocristal estequiométrico de NiO. Un **pre-pico asignado a iones Ni^{3+}**, un **hombro que aparece en la sub-banda del Ni 3d debido a la división de los estados** e_g, causada por un aumento de los efectos de superficie debido a la reducción del tamaño de grano; y unas estructuras anchas correspondientes a estados finales de mayor energía, que sugieren un mecanismo de ensanchamiento relacionado con el NiO nanoestructurado. A su vez, los espectros de XAS del Ni 2p no cambian mucho para diferentes condiciones de crecimiento. Los distintos cambios en cada espectro, tanto en los bordes del O 1s como en del Ni 2p, han sido exitosamente reproducidos por **cálculos de clusters**, que **muestran que la contribución superficial de Ni^{3+} y Ni^{2+} aumenta linealmente con el contenido de oxígeno** en el plasma hasta un 14% y un 56%, respectivamente. Por el contrario, la contribución de volumen por clusters octahédricos completos (NiO_6, sin truncar) decrece linealmente con la adicción de oxígeno, apoyando una vez más el aumento de la superficie efectiva y el desorden de la estructura cristalina.

Bajo tratamiento térmico las contribuciones superficiales a los espectros de XANES disminuyen considerablemente recuperando el conocido espectro del NiO estequiométrico, i.e., el pre-pico y la división de la banda 3d desaparecen gradualmente y los estados finales de mayor energía se estrechan. Este calentamiento de la muestra tiene como consecuencia un aumento de la resistividad, como fue observado en el capítulo anterior. Basado en estos resultados se han realizadas medidas de emisión de fotones (TFY) mostrando estructuras de absorción propias de un NiO nanoestructurado en lugar de un NiO estequiométrico. La mayor profundidad de análisis de las medidas TFY indican que dentro del volumen las estructuras desordenadas y deficientes en Ni aún permanecen mientras que en la superficie el tratamiento térmico las convierte en una capa estequiométrica. Este hecho apoya el modelo presentado para el envejecimiento de la resistividad eléctrica, que se basa en la formación de una capa superficial.

Información complementaria sobre los estados electrónicos profundos (core levels) y la influencia del oxígeno añadido al plasma ha sido observada mediante experimentos de fotoemisión. Según un modelo aceptado recientemente, el espectro XPS del Ni $2p_{3/2}$ muestra un pico asignado a estados de superficie. Esta contribución de octahedros truncados (NiO_5) localizados en la superficie del grano aumenta para muestras crecidas con oxígeno debido al refinamiento del grano. El comportamiento de la intensidad del pico de superficie en presencia o ausencia de oxígeno en el plasma correlaciona muy bien con lo observado en el promedio del grano obtenido por XRD a bajas temperaturas. Como se observa previamente con XANES, un factor importante es la temperatura del substrato: calentando durante el crecimiento el pico de superficie en el espectro de Ni $2p_{3/2}$ decrece, sugiriendo una menor relación superficie–volumen y contrarrestando el efecto de la adicción de oxígeno al plasma.

La mayor contribución de este trabajo es mostrar cómo las condiciones de crecimiento afectan las propiedades de las láminas delgadas de NiO nanoestructurado así como las propiedades que surgen de estas variaciones. Cambios en el contenido de oxígeno del plasma de pulverización durante el crecimiento afectan a la estructura electrónica de estas láminas de NiO que, a su vez,

pueden estar asociados con cambios en sus propiedades morfológicas, estructurales, ópticas y de transporte.

Appendix I

The FESEM micrographs shown in chapter 4 were taken in three different instruments at three different institutions: SIdI-UAM, CENIM-CSIC and ICV-CSIC, although we have selected some figures among all obtained to present in this work.

The following table shows the parameters at which these images were obtained, in order to provide enough information about the acquiring procedure: the acceleration voltage of the electron beam used as probe, the spot diameter of the collimated beam, the magnification used in the micrography, the working distance of the lenses, the measurement mode (**TLD**: Trough Lens Detector and **SEI**: Secondary Electron Image), the Institution where the Electron Microscope belongs and the intrument model used.

Figure	Acc. voltage	Spot diam.(μm)	Magnification	Working Dist. (mm)	Mode	Institution	Instrument
3.6a	10.0 kV	3	50000x	6.1	TLD	SIdI	Philips XL30 S-FEG
4.2a	20.0 kV	3	100000x	6.1	TLD	SIdI	Philips XL30 S-FEG
4.2b	20.0 kV	3	100000x	6.1	TLD	SIdI	Philips XL30 S-FEG
4.6a	7.0 kV		50000x	3.9	SEI	CENIM-CSIC	JEOL JSM 6500F
4.6b	10.0 kV	3	150000x	6.2	TLD	SIdI	Philips XL30 S-FEG
4.6c	7.0 kV		40000x	3.9	SEI	CENIM-CSIC	JEOL JSM 6500F
4.6d	20.0 kV	3	100000x	5.6	TLD	SIdI	Philips XL30 S-FEG
4.11	20.0 kV	3	100000x	5.5	TLD	SIdI	Philips XL30 S-FEG
4.10a	20.0 kV	3	100000x	6.1	TLD	SIdI	Philips XL30 S-FEG
4.10b	15.0 kV	3	90000x	6.1	TLD	SIdI	Philips XL30 S-FEG
4.10c	10.0 kV	3	100000x	6	TLD	SIdI	Philips XL30 S-FEG
4.10d	15.0 kV	3	200000x	6.4	TLD	SIdI	Philips XL30 S-FEG
4.13a	10.0 kV	3	200000x	6.2	TLD	SIdI	Philips XL30 S-FEG
4.13b	10.0 kV	3	200000x	5.6	TLD	SIdI	Philips XL30 S-FEG
4.13c	10.0 kV	3	200000x	5.3	TLD	SIdI	Philips XL30 S-FEG
4.13d	10.0 kV	3	200000x	5.7	TLD	SIdI	Philips XL30 S-FEG
4.13e	10.0 kV	3	200000x	5.9	TLD	SIdI	Philips XL30 S-FEG
4.13f	10.0 kV	3	200000x	6.1	TLD	SIdI	Philips XL30 S-FEG
4.12a	20.0 kV	3	200000x	6	SEI	SIdI	Philips XL30 S-FEG
4.12b	20.0 kV	3	200000x	6	SEI	SIdI	Philips XL30 S-FEG
4.12c	7.0 kV		100000x	4	SEI	CENIM-CSIC	JEOL JSM 6500F
4.12d	20.0 kV	3	200000x	6.2	TLD	SIdI	Philips XL30 S-FEG
4.20a	20.0 kV	3	200000x	5.4	SEI	SIdI	Philips XL30 S-FEG
4.20b	20.0 kV	3	200000x	5.7	SEI	SIdI	Philips XL30 S-FEG
4.20c	10.0 kV	3	200000x	5.6	TLD	SIdI	Philips XL30 S-FEG
4.20d	10.0 kV	3	200000x	6.1	TLD	SIdI	Philips XL30 S-FEG
4.20e	10.0 kV	3	200000x	5.6	TLD	SIdI	Philips XL30 S-FEG
4.20f	10.0 kV	3	200000x	6.1	TLD	SIdI	Philips XL30 S-FEG
4.23a	20.0 kV	3	100000x	4.9	TLD	SIdI	Philips XL30 S-FEG
4.23b	20.0 kV	3	100000x	5.1	TLD	SIdI	Philips XL30 S-FEG

Appendix II

List of Publications related to this work

During this research work we have published several contributions related to NiO nanostructured in international peer reviewed journals:

- **Effects of grain refinement and disorder on the electronic properties of nanocrystalline NiO.** G. Domínguez-Cañizares, A. Gutiérrez, J. Chaboy, D. Díaz-Fernández, G. R. Castro, L. Soriano. *Journal of Materials Science (2014) 49:2773-2780*

- **Effects of Ni vacancies and crystallite size on the O 1s and Ni 2p X-ray absorption spectra of nanocrystalline NiO.** R. J. O. Mossanek, G. Domínguez-Cañizares, A. Gutiérrez, M. Abbate, D. Díaz-Fernández, and L. Soriano. *Journal of Physics: Condensed Matter 25 (2013) 495506 (7pp)*

- **Hexagonally-arranged-nanoporous and continuous NiO films with varying electrical conductivity.** A. Gutiérrez and G. Domínguez-Cañizares, J.A. Jiménez, I. Preda, D. Díaz-Fernández, F. Jiménez-Villacorta, G.R. Castro, J. Chaboy and L. Soriano. *Applied Surface Science, Vol. 276 pp. 832-837 (2013)*

Conferences

- **Effect of grain size and disorder on conductive NiO thin films.** G. Domínguez-Cañizares, A. Gutiérrez, D. Díaz-Fernández1, J. Chaboy, G.R. Castro, J.A. Jiménez, M. Abbate, R.J.O. Mossanek and L. Soriano. *XVI Young researchers meeting, Instituto Nicolás Cabrera (INC), La Cristalera* 19^{th} *December 2013*

- **Hole conductivity in NiO thin films.** G. Domínguez-Cañizares, A. Gutiérrez, D. Díaz-Fernández, M. Abbate, R.J.O. Mossanek and L. Soriano. 3^{rd} *Workshop early stage researchers in nanoscience, IMDEA Nanoscience Madrid (2013)*

- **Effects of Microstructure and disorder on the electronic states of nanostructured NiO.** G. Domínguez-Cañizares, A. Gutiérrez, J.A. Jiménez, J. Chaboy and L. Soriano. 7^{th} *International Conference on Surfaces, Coatings and Nano-Structured Materials. Prague (2012)* **Winner of the Young Scientist Lecture Competition**

- **Local structure characterization of nanoporous NiO membranes.** Domínguez-Cañizares, G. Jiménez-Villacorta F., Castro G.R., Gutiérrez A., Soriano, L. *Users Meeting of SpLine - BM25, CRG Beamline at the ESRF, ICMM-CSIC Madrid (2012)*

- **Growth and characterization of NiO hexagonally arranged nanoporous membranes.** A. Gutiérrez, G. Domínguez, I. Preda, D. Díaz, L. Soriano. 14^{th} *International Conference on Solid Films and Surfaces. Dublin (2008)*

Posters

- **Analysis of empty states in p-type conducting nanostructured NiO thin films with tailored physical properties.** Domínguez-Cañizares G., Gutiérrez A., Krause S., Ovsyannikov R., Abbate M., Díaz-Fernández D., Soriano L. *ImagineNano2013 (NanoSpain conference), Bilbao (2013)*
- **Effects of microstructure on the electronic states of nanostructured NiO.** G. Domínguez-Cañizares, A. Gutiérrez, J.A. Jiménez, J. Chaboy, G.R. Castro, D. Díaz-Fernández, L. Soriano. *Fourth Joint BER II and BESSY II User Meeting. Berlin (2012)*
- **Growth and characterization of nanostructured nickel oxide with tailored physical properties.** G. Domínguez-Cañizares, L. Soriano, A. Gutiérrez. *Instituto Nicolás Cabrera Summer School, UAM. Madrid (2011)*
- **Coercivity, morphology and anionic defects in Fe/NiO layers on nanoporous Al_2O_3 membranes.**, M. Iglesias, G. Domínguez-Cañizares, E. Navarro, E. Paz, D. Díaz Fernández, A. Gutiérrez, L. Soriano, M. Alonso, F. Soria, F. Cebollada, J. M. González and F.J. Palomares. *ImagineNano2011 (NanoSpain conference), Bilbao (2011)*

List of other publications

Besides the works directly related to this manuscript in previous section another collaborations were done:

- **The growth of cobalt oxides on HOPG and SiO_2 surfaces: a comparative study.** D. Díaz-Fernández, J. Méndez, O. Bomatí-Miguel, F. Yubero, R.J.O. Mossanek, M. Abbate, G. Domínguez-Cañizares, A. Gutiérrez, S. Tougaard and L. Soriano. *Surface Science Vol. 624, 145153 (2014)*
- **Study of the early stages of growth of Co oxides on oxide substrates.** D. Díaz-Fernández, J. Méndez, F. Yubero, G. Domínguez-Cañizares, A. Gutierrez, L. Soriano. *Surface and Interface Analysis, ECASIA special issue paper (2014)*
- **X-ray absorption study of the local structure at the NiO/Oxide interfaces.**, Preda I., Soriano L., Díaz-Fernández D., Domínguez-Cañizares G., Gutiérrez A., Castro G.R., Chaboy J. *Journal of Synchrotron Radiation Vol. 20, Part 4. (2013)*
- **Surface Functionalization of Nanostructured Porous Silicon by APTS: Toward the Fabrication of Electrical Biosensors of Bacterium Escherichia coli.**, G. Recio-Sánchez, G. Domínguez-Cañizares, M. Manso, I. Preda, V. Torres-Costa, A. Gutiérrez, L. Soriano and R.J. Martín-Palma. *Current Nanoscience Vol.7 pp. 178-182 (2011)*
- **Study of ammonium fluoride passivation time on CdZnTe bulk crystal wafers.** Bensalah, H., Crocco, J., Carcélen, V., Plaza, J. L., Zheng, Q., Marchini, L., Zanichelli, M., Domínguez, G., Soriano, L., Diéguez, E. *Crystal Research and Technology Vol. 46 No. 7 pp. 659-663 (2011)*
- **Generador electrostático de Van de Graaff de 250.000 Voltios.** (Conference in Spanish), D. Gallach, G. Domínguez-Cañizares. *XI Semana de la Ciencia. Comunidad de Madrid (2011)*

Agradecimientos

El trabajo de una tesis doctoral en ciencia experimental supone la culminación de una etapa en la vida de un investigador. Muchas personas han contribuido de alguna u otra manera a este trabajo, y aquí lo agradezco humildemente:

Al grupo GRIN: A mi director Alejandro Gutiérrez Delgado, por su paciencia, sabiduría, apoyo, confianza y todo su trabajo, tanto o más que el mío. Ha sido un placer aprender a tu lado. A Leonardo Soriano de Arpe, quien me ofreció trabajar y aprender con él embarcándome en esta aventura. A Iulian Preda, de quien tanto aprendí y espero seguir aprendiendo. A Óscar Bomatí, siempre laborioso. A Pablo Pernas, por tener una sonrisa preparada.

A los colaboradores e investigadores sin los que esta tesis no habría tenido diferentes visiones, enfoques y dimensiones necesarias: José Antonio Jiménez del CENIM-CSIC, con quien tanta difracción he aprendido; Miguel Ángel Rodríguez del ICV-CSIC, por su inestimable ayuda con el SEM y los targets de NiO; a Miguel Abbate y Rodrigo Mossanek de la Universidade Federal do Paraná, por sus hermosos cálculos que tanto han apoyado este trabajo; a Germán Castro y Juan Rubio, por enseñarme los detalles de SpLine en el ESRF y por su ayuda en cada beamtime; a Félix Jiménez y Jesús Chaboy, por enseñarme EXAFS con tanto rigor; a Juan Trigo por su ayuda con las medidas y cálculos ópticos; a Carlos Sánchez por su sabidura y tiempo. Al personal del SIDI de policristal, Noemí y Mario, y microscopía: Isidoro, Enrique y Esperanza. A million thanks to Dr. Stefan Krause, for his invaluable help in BESSY. Thanks to Maximilian Bauer and Dr. Ruslan Ovsyannikov for their assistance during the beamtimes in BESSY.

A los profesores con los que tuve el gran placer de enseñar Física y aprender a su vez mucho de ellos: Carlos Palacio, Basilio García, Aurelio Climent, Manuel Hernández y Eduardo Elizalde.

Al resto del equipo de Spline, allá en las montañas, imperturbables a los tiempos de recortes: Eduardo Salas, Álvaro Muñoz y Ana Gutiérrez.

A tantos profesores y compañeros del Departamento de Física Aplicada que han aguantado mis corbatas y pajaritas y de quienes necesité ayuda más de una o tres veces: José Antonio, Félix, Luis y Tomás, sabios; a Beatriz Luna, que puede con todo; Carmen Morant, José Luis Castaño, David Martín, Antonio Arranz, Pilar Prieto, Alejandro Braña, Rafael Pérez y Miguel Manso.

A mis incansables compañeros del *Bocata Seminar*, de mini-golf, de las charlas divulgativas, de tantas aventuras... Por su apoyo estos años: Darío Gallach, binomio con mucha energía de ligadura; Arancha Gómez, Esther Punzón, Dr. Jacobo Hernández, Dr. Gonzalo Recio, Dra. Noelia Benito, Eduard Garía, Luis Antonio González y Valentín Nistor. Y por encima de todos, Daniel Díaz, hermano de laboratorio y de Tesis.

Esta tesis no habría existido ni se habría podido terminar sin mi padre, que me hizo científico, ni sin mi madre, que nunca se rindió.

Bibliography

[1] Fujimori A. Siratori K. Tsuda N., Nasu K. *Electronic conduction in oxides.* Springer, 2000.

[2] Bärbel Fromme. *d-d Excitations in Transition-Metal Oxides.* Springer, 2001.

[3] G. van der Laan, J. Zaanen, G. A. Sawatzky, R. Karnatak, and J.M. Esteva. Comparison of X-ray absorption with X-ray photoemission of nickel dihalides and NiO. *Phys. Rev. B*, 33:4253–4263, 1986.

[4] Atsushi Fujimori and Fujio Minami. Valence-band photoemission and optical absorption in nickel compounds. *Phys. Rev. B*, 30:957–971, 1984.

[5] H. Sato, T. Minami, S. Takata, and T. Yamada. Transparent conducting p-type NiO thin films prepared by magnetron sputtering. *Thin Solid Films*, 236(1-2):27 – 31, 1993.

[6] P.J Kelly and R.D Arnell. Magnetron sputtering: a review of recent developments and applications. *Vacuum*, 56(3):159 – 172, 2000.

[7] André Anders. Metal plasmas for the fabrication of nanostructures. *Journal of Physics D: Applied Physics*, 40(8):2272, 2007.

[8] Donald M. Mattox. *Handbook of physical vapor deposition (PVD) processing.* Noyes Publications, 1998.

[9] M. Ohring. *Material Science of Thin Films.* Academic Press, second edition, 2001.

[10] T. L. Cox, V. G. L. Desmukh, D. A. O. Hope, A. J. Hydes, N. St. J. Braithwaite, and N. M. P. Benjamin. The use of Langmuir probes and optical emission spectrocopy to measure electron energy distribution functions in RF-generated argon plasmas. *Journal of Physics D: Applied Physics*, 20:820–831, 1987.

[11] Makoto Kitabatake Kiyotaka Wasa and Hideaki Adachi. *Thin Films Materials Technology: Sputtering of Compound Materials.* William Andrew - Springer, 2004.

[12] Wolfgang Eckstein (Eds.) Rainer Behrisch. *Sputtering by Particle Bombardment: Experiments and Computer Calculations from Threshold to MeV Energies.* Springer, 2007.

[13] S. Pratontep, S.J. Carroll, Xirouchaki M. Streun, and R. E. Palmer. Size-selected cluster beam source based on radio frequency magnetron plasma sputtering and gas condensation. *Review of scientific instruments*, 76:045103–1–9, 2005.

[14] A. Anders. Fundamentals of pulsed plasmas for materials processing. *Surface and Coatings Technology*, 183:301–311, 2004.

[15] Feinleib J. Adler D. Electrical and optical properties of narrow-band materials. *Phys. Rev. B*, 2:3112–3134, 1970.

[16] B.A. Movchan and A.V. Demichishin. Study of the structure and properties of thick vacuum condensates of nickel, titanium, tungsten, aluminium oxide and zirconium dioxide. *Phys. Met. Metallogr.*, 28(4):83–90, 1969.

[17] A. van der Drift. Evolutionary selection, a principle governing growth orientation in vapour-deposited layers. *Philips Research Reports*, 22:267–288, 1967.

[18] C.R.M. Grovenor, H.T.G. Hentzell, and D.A. Smith. The development of grain structure during growth of metallic films. *Acta Metallurgica*, 32(5):773 – 781, 1984.

[19] R. Messier. Toward quantification of thin film morphology. *Journal of Vacuum Science Technology A*, 4(3):490–495, 1986.

[20] J. M. Thijssen, H. J. F. Knops, and A. J. Dammers. Dynamic scaling in polycrystalline growth. *Phys. Rev. B*, 45:8650–8656, 1992.

[21] John A. Thornton. The microstructure of sputter-deposited coatings. *Journal of Vacuum Science Technology A*, 4(6):3059 –3065, 1986.

[22] A. Mazor, D. J. Srolovitz, P. S. Hagan, and B. G. Bukiet. Columnar growth in thin films. *Phys. Rev. Lett.*, 60:424–427, 1988.

[23] Nandy S., Goswami S., and Chattopadhyay K.K. Ultra smooth surfaces NiO thin films on flexible plastic (PET) substrate at room temperature by RF magnetron sputtering and effect of oxygen partial pressure on their properties. *Applied Surface Science*, 256:3142–3147, 2010.

[24] T.Y. Kuo, S.C. Chen, W.C. Peng, Y.C.Lin, and H.C.Lin. Influences of process parameters on the texture and microstructure of nio films. *Thin Solid Films*, 519:4940–4943, 2011.

[25] Rossnagel S.M., Yang I., and Cuomo J.J. Compositional changes during magnetron sputtering of alloys. *Thin Solid Films*, 199:59–69, 1991.

[26] R. Álvarez, J M García-Martín, M. Macías-Montero, L. González-García, J. C. González, V. Rico, J. Perlich, J. Cotrino, A. R. González-Elipe, and A. Palmero. Growth regimes of porous gold thin films deposited by magnetron sputtering at oblique incidence: from compact to columnar microstructures. *Nanotechnology*, 24(4):045604, 2013.

[27] JEOL USA. A guide to scanning microscope observation, 2013.

[28] JEOL USA. Scanning electron microscope A to Z, 2009.

[29] M.D. Abramoff, P.J. Magelhaes, and S.J. Ram. Image processing with ImageJ. *Biophotonics Int.*, 11(7):36–42, 2004.

[30] Alejandro Gutiérrez, José Ángel Martín-Gago, and Salvador Ferrer. La luz sincrotrón: una herramienta extraordinaria para la ciencia. *Apuntes de Ciencia y Tecnología*, 12:37–46, 2004.

[31] G. Margaritondo. Synchrotron light and free-electron lasers. *Rivista del nuovo cimento*, 18(1):1–24, 1995.

[32] Albert C. Thompson and Douglas Vaughan. X-ray data booklet. Lawrence Berkeley National Laboratory, 2009.

[33] Philip Willmott. *An Introduction to Synchrotron Radiation.* John Wiley & Sons, 2011.

[34] Ernst-Eckard Koch, editor. *Handbook of Synchrotron Radiation*, volume Volume 1a. Nord Holland Publihsing Company, 1983.

[35] Vitalij K. Pecharsky and Peter Y. Zavalij. *Fundamentals of Powder Diffraction and Structural Characterization of Materials*. Springer, second edition, 2009.

[36] B. D. Cullity. *Elements of X-ray Diffraction*. Addison-Wesley, 1978.

[37] N. Ascroft and I. Mermin. *Solid State Physics*. Thomson Learning, 1976.

[38] H. M. Rietveld. A profile refinement method for nuclear and magnetic structures. *J. Appl. Cryst.*, 2:65–71, 1969.

[39] G. S. Pawley. Unit-cell refinement from powder diffraction scans. *J. Appl. Cryst.*, 14:357–361, 1981.

[40] Centre for X-ray Optics database. Berkeley Laboratories.

[41] L. J. van der Pauw. A method of measuring specific resisitivity and hall effect of discs of arbitrary shape. *Philips Research Reports*, 13(1):1–9, 1958.

[42] Simon M. Sze. *Physics of semiconductor devices*. John Wiley & Sons, 1981.

[43] Kotaro Kato, Terukazu Ono, and Yoshihito Amemiya. A physical mechanism of current-induced resistance decrease in heavily doped polysilicon resistors. *IEEE Transactions on Electron Devices*, ED-29(8):1156–1161, 1982.

[44] K. Siegbahn and K. Edvarson. β-ray spectroscopy in the precision range of $1 : 10^5$. *Nuclear Physics*, 1:137–159, 1956.

[45] S. Tanuma, C. J. Powell, and D. R. Penn. Calculations of electron inelastic mean free paths. *Surf. Interf. Anal.*, 21:165, 1993.

[46] Seah M.P. Briggs D. *Practical Surface Analysis. Volume 1: Auger and X-ray Photoelectron Spectrocopy*. John Wiley & Sons, second edition, 1994.

[47] H. Kuhlenbeck, G. Odörfer, R. Jaeger, G. Illing, M. Menges, Th. Mull, H.-J. Freund, M. Pöhlchen, V. Staemmler, S. Witzel, C. Scharfschwerdt, K. Wennemann, T. Liedtke, and M. Neumann. Molecular adsorption on oxide surfaces: Electronic structure and orientation of NO on NiO(100)/Ni(100) and on NiO(100) as determined from electron spectroscopies and *ab initio* cluster calculations. *Phys. Rev. B*, 43:1969–1986, 1991.

[48] S. Tougaard. Quantitative analysis of the inelastic background in surface electron spectroscopy. *Surface and Interface Analysis*, 11:453, 1988.

[49] Jingguang G. Chen. NEXAFS investigations of transition metal oxides, nitrides, carbides, sulfides and others interstitial compounds. *Surface Science Reports*, 30:1–152, 1997.

[50] Grant Bunker. *Introduction to XAFS*. Cambridge University Press, 2010.

[51] Boon K. Teo. *EXAFS: Basic Principles and Data Analysis*. Springer-Verlag, 1986.

[52] Frank de Groot and Akio Kotani. *Core level spectroscopy of solids*. CRC Press. Taylor & Francis Group, 2008.

[53] J. H. Hubbell and S. M. Seltzer. Tables of X-ray mass attenuation coefficients and mass energy-absorption coefficients, 1996.

[54] K.V. Klementiev. Extraction of the fine structure from x-ray absorption spectra. *Journal of Physics D: Applied Physics*, 34:209–217, 2001.

[55] B. Ravel and M. Newville. ATHENA, ARTEMIS, HEPHAESTUS: data analysis for x-ray absorption spectroscopy using IFEFFIT. *Journal of Synchrotron Radiation*, 12:537–541, 2005.

[56] Olsen K. Dragoset R.A. Chang J. Kishore A.R. Kotochigova S.A. Chantler, C.T. and D.S. Zucker. X-ray form factor, attenuation and scattering tables (version 2.1), 2005.

[57] ML Theye, Gheorghiu A, and Launois H. Investigation of disorder effects in amorphous GaAs and GaP by EXAFS. *J. Phys. C: Solid State Phys.*, 13:6569–6584, 1980.

[58] J. Purans A. Kuzmin and A. Rodionov. X-ray absorption spectrocopy study of the Ni K edge in magnetron-sputtered nickel oxide thin films. *Journal of Physics: Condensed Matter*, 9:6979–6993, 1997.

[59] P. H. Citrin, P. Eisenberger, and B. M. Kincaid. Transferibility of phase shifts in extendend X-ray absorption fine structure. *Phys. Rev. Lett.*, 36(22):1346–1349, 1976.

[60] B. Ravel. ATOMS: crystallography for the X-ray Absorption spectroscopist. *Journal of Synchrotron Radiation*, 8:314–316, 2001.

[61] J.J. Rehr, J. Mustre de Leon, S.I. Zabinsky, , and R.C. Albers. Multiple scattering calculations of X-ray Absorption spectra. *J. Am. Chem. Soc.*, 113:5135, 1991.

[62] Edward A. Stern. Number of relevant independent points in x-ray-absorption fine-structure spectra. *Phys. Rev. B*, 48:9825–9827, 1993.

[63] B.L. Mojet D.C. Koningsberger and, G.E. van Dorssen, and D.E. Ramaker. XAFS spectroscopy; fundamental principles and data analysis. *Topics in Catalysis*, 10:143–155, 2000.

[64] Franciscus Wilhemus Henricus Kampers. *EXAFS in Catalysis. Intrumentation and Applications.* PhD thesis, Technische Universiteit Eindhoven, 1988.

[65] W. Gudat and C. Kunz. Close similarity between photoelectric yield and photoabsorption spectra in the soft-X-ray range. *Phys. Rev. Lett.*, 29:169–172, 1972.

[66] G. Michael Bancroft Masoud Kasrai, Zhanfeng Yin and Kim H. Tan. X-ray fluorescence measurements of x-ray absorption near edge structure at the Si, P, and S L edges. *Journal of Vacuum Science Technology A*, 11:2694–2699, 1993.

[67] Dimitrios Vlachos, Alan J. Craven, and David W. McComb. Specimen charging in X-ray absorption spectroscopy: correction of total electron yield data from stabilized zirconia in the energy range 250-915 ev. *Journal of Synchrotron Radiation*, 12(2):224–233, 2005.

[68] D. J. W. Mous, A. Gottdang, R. G. Haitsma, G. García López, F. Agulló-López, and D. O. Boerma. Performance and Applications of the first HVE 5MV Tandetron^{TM} at the University of Madrid. *AIP Conf. Proc.*, 680:999, 2003.

[69] M. Mayer. SIMNRA, a simulation program for the analysis of NRA, RBS and ERDA. *American Institute of Physics Conference Proceedings*, 475:541, 1999.

[70] Hideki Masuda and Kenji Fukuda. Ordered metal nanohole arrays made by a two-step replication of honeycomb structures of anodic alumina. *Science*, 268(5216):1466–1468, 1995.

[71] K.Y. Ng, Y. Lin, and A.H.W. Ngan. Deformation of anodic aluminum oxide nano-honeycombs during nanoindentation. *Acta Materialia*, 57(9):2710 – 2720, 2009.

[72] ICDD No.: 64700-International Center of Diffraction Data.

[73] Gao-Rong Han Xin Wang. Fabrication and characterization of anodic aluminum oxide template. *Microelectronics Engineering*, 66:166–170, 2003.

[74] K.S. Choudhari, P. Sudheendra, and N.K. Udayashankar. Fabrication and high-temperature structural characterization study of porous anodic alumina membranes. *Journal of Porous Materials*, 19:1053–1062, 2012.

[75] K Surana, H Lepage, J M Lebrun, B Doisneau, D Bellet, L Vandroux, G Le Carval, M Baudrit, P Thony, and P Mur. Film-thickness-dependent conduction in ordered Si quantum dot arrays. *Nanotechnology*, 23(10):105401, 2012.

[76] Powder Diffraction File PDF 00-047-1049. International Center of Diffraction Data. ICDD.

[77] Yao-Sheng Yang Hao-Long Chen. Effect of crystallographic orientations on electrical properties of sputter-deposited nickel oxide thin films. *Thin Solid Films*, 516(516):5590–5596, 2008.

[78] Zhengjun Zhang, Ye Zhao, and Minmin Zhu. NiO films consisting of vertically aligned cone-shaped nio rods. *App. Phys. Lett.*, 88(3):033101, 2006.

[79] HW Ryu, GP Choi, GJ Hong, and JS Park. Growth and surface morphology of textured NiO thin films deposited by off–axis RF magnetron sputtering. *Japanese Journal of Applied Physics*, 43(8A):5524–5525, 2004.

[80] H. Torii E. Fujii, A. Tomozawa and R. Takayama. Preferred orientations of NiO films prepared by plasma-enhanced metalormetal chemical vapor deposition. *Japanese Journal of Applied Physics*, 35(3A):L 328 – L 330, 1996.

[81] Jang Ho Park, Hoang Ba Cuong, Sang Hun Jeong, and Byung Teak Lee. Growth and characterization of group-ii-alloyed ZnAlO UV-range transparent conductive films prepared by RF magnetron sputtering. *Vacuum*, 97(0):15 – 19, 2013.

[82] E.M. Feldmeier, A. Fuchs, J. Schaffner, H.J. Schimper, A. Klein, and W. Jaegermann. Comparison between the structural, morphological and optical properties of CdS layers prepared by close space sublimation and {RF} magnetron sputtering for CdTe solar cells. *Thin Solid Films*, 519(21):7596 – 7599, 2011.

[83] H. Jung, Kulijc R., Stroscio M.l A., and Dutta M. Confinement in PbSe wires grown by rf magnetron sputtering. *App. Phys. Lett.*, 96:153106–1–3, 2010.

[84] J. A. Thornton. High rate thick film growth. *Annu. Rev. Mater. Sci.*, 7(1):239–260, 1977.

[85] C. V. Thompson. Structure evolution during processing of polycrystalline films. *Annu. Rev. Mater. Sci.*, 30:159–190, 2000.

[86] P. B. Barna I. Petrov and, L. Hultman, and J. E. Greene. Microstructural evolution during film growth. *Journal of Vacuum Science Technology A*, 21:117–128, 2003.

[87] P.B Barna and M. Adamik. Fundamental structure forming phenomena of polycrystalline films and the structure zone models. *Thin Solid Films*, 317(1-2):27–33, 1998.

[88] John A. Thornton. Influence of apparatus geometry and deposition conditions on the structure and topography of thick sputtered coatings. *Journal of Vacuum Science Technology*, 11(4):666–670, 1974.

[89] Julien Bachmann, Andriy Zolotaryov, Ole Albrecht, Silvana Goetze, Andreas Berger, Dietrich Hesse, Dmitri Novikov, and Kornelius Nielsch. Stoichiometry of nickel oxide films prepared by ALD. *Chemical Vapor Deposition*, 17(7-9):177–180, 2011.

[90] Yang-Ming Lu Hao-Long Chen and Weng-Sing Hwang. Effect of film thickness on structural and electrical properties of sputter-deposited Nickel Oxide films. *Materials Transactions*, 46(4):872–879, 2005.

[91] A. Karpinski, A. Ferrec, M. Richard-Plouet, L. Cattin, M. A. Djouadi, L. Brohan, and P. Y. Jouan. Deposition of Nickel Oxide by direct current reactive sputtering effect of oxygen partial pressure. *Thin Solid Films*, 520(9):3609–3613, 2012.

[92] Nandy S., Saha B., Mitra M.K., and Chattopadhyay K.K. Effect of oxygen partial pressure on the electrical and optical properties of highly (2 0 0) oriented p-type $Ni_{1-x}O$ films by DC sputtering. *J. Mater. Sci.*, 42:5766–5772, 2007.

[93] J. I. Langford and A. J. C. Wilson. Seherrer after sixty years: A survey and some new results in the determination of crystallite size. *J. Appl. Cryst.*, 11:102–113, 1978.

[94] H.W. Ryu, G.P. Choi, W.S. Lee, and J.S. Park. Preferred orientations of nio thin films prepared by rf magnetron sputtering. *Journal of Materials Science*, 39(13):4375–4377, 2004.

[95] T. Y. Kuo S. C. Chen and T. H. Sun. Microstructures, electrical and optical properties of non-stoichiometric p-type nickel oxide films by radio frequency reactive sputtering. *Surface and Coatings Technology*, 205:S236–S240, 2010.

[96] Diffrac Suite TopAs (BRUKER).

[97] T. Miki K. Yoshimura and S. Tanemura. Nicke oxide electrchromic thin films prepared by reactuve DC magnetron sputtering. *Japanese Journal of Applied Physics*, 34(5A):2240–2446, 1995.

[98] JCPDS-no.:44-1159. International Center of Diffraction Data. ICDD.

[99] I. Hotovy, J. Huran, and L. Spiess. Characterization of sputtered NiO films using XRD and AFM. *Journal of Materials Science*, 39(7):2609–2612, 2004.

[100] M. T. Hutchings and E. J. Samuelsen. Measurement of spin-wave dispersion in NiO by inelastic neutron scattering and its relation to magnetic properties. *Phys. Rev. B*, 6:3447–3461, 1972.

[101] W. L. Roth. Magnetic structures of MnO, FeO, CoO, and NiO. *Physical Review*, 110:1333–1341, 1958.

[102] N. Mironova-Ulmane, A. Kuzmin, J. Grabis, I. Sildos, V.I. Voronin, I.F. Berger, and V.A. Kazantsev. Structural and magnetic properties of Nickel Oxide nanopowders. *Solid State Phenomena*, 168-169:341–344, 2011.

[103] P. W. Tasker. The stability of ionic crystals surfaces. *J. Phys. C: Solid State Phys.*, 12:4977–4984, 1979.

[104] A. Barbier, C. Mocuta, H. Hulenbeck nad K. F. Peters, B. Richter, and G. Renaud. Atomic structure of the polar NiO(111)-p(2x2) surface. *Phys. Rev. Lett.*, 84(13):2897–2900, 2000.

[105] Jmol: an open-source Java viewer for chemical structures in 3D.

[106] R. D. Shannon. Revised effective ionic radii and systematic studies of interatomic distances in halides and chalcogenides. *Acta Crystallographica Section A*, 32(5):751–767, 1976.

[107] P. M. Oliver, G. W. Watson, and S.C. Parker. Molecular-dynamics simulations of nickel oxide surfaces. *Phys. Rev. B*, 52(7):5323–5330, 1995.

[108] A. Anspoks, A. Kalinko, R. Kalendarev, and A. Kuzmin. Atomic structure relaxation in nanocrystalline NiO studied by EXAFS spectroscopy: Role of nickel vacancies. *Phys. Rev. B*, 86:174114, 2012.

[109] Anspoks A., Kalinko A., Kalendarev R., and Kuzmin A. Atomic structure relaxation in nanocrystalline NiO studied by EXAFS spectroscopy: Role of nickel vacancies. *Phys. Rev. B*, 86:174114, 2012.

[110] Andrew K. F. Gulbransen E.A. The kinetics of oxidation of high purity nickel. *J. Electrochem. Soc.*, 101(3):128–140, 1954.

[111] A. Corrias, G. Mountjoy, G. Piccaluga, and S. Solinas. An X-ray Absorption study of the Ni K edge in NiO-SiO2 nanocomposite materials prepared by the sol-gel method. *Journal of Physical Chemistry B*, 103(46):10081–10086, 1999.

[112] A. Anspoks and A. Kuzmin. Interpretation of the Ni K-edge EXAFS in nanocrystalline nickel oxide using molecular dynamics simulations. *Journal of Non-Crystalline Solids*, 357(14):2604 – 2610, 2011.

[113] Wei-Luen Jang, Yang-Ming Lu, Weng-Sing Hwang, Tung-Li Hsiung, and H. Paul Wang. Point defects in sputtered NiO films. *App. Phys. Lett.*, 94:062103–1–062103–2, 2009.

[114] O. Kohmoto, H. Nakagawa, F. Ono, and A. Chayahara. Ni-defective value and resistivity of sputtered NiO films. *Journal of Magnetism and Magnetic Materials*, 226230:1627 – 1628, 2001. Proceedings of the International Conference on Magnetism (ICM 2000).

[115] Dong Soo Kim and Hee Chul Lee. Nickel vacancy behavior in the electrical conductance of nonstoichiometric nickel oxide film. *J. Appl. Phys.*, 112:034504, 2012.

[116] Yong Hun Kwon, SungHyun Chun, Jae-Hee Han, and HyungKoun Cho. Correlation between electrical properties and point defects in NiO thin films. *Metals and Materials International*, 18(6):1003–1007, 2012.

[117] W. E. Spear and D. S. Tannhauser. Hole transport in pure nio crystals. *Phys. Rev. B*, 7:831–833, 1973.

[118] J. van Elp, H. Eskes, P. Kuiper, and G. A. Sawatzky. Electronic structure of li-doped NiO. *Phys. Rev. B*, 45:1612–1622, 1992.

[119] Ghosh C.K. Chattopadhyay K.K. Nandy S., Maiti U.N. Enhanced p-type conductivity and band gap narrowing in heavily Al doped NiO thin films deposited by RF magnetron sputtering. *Journal of Physics: Consended Matter*, 21:115804, 2009.

[120] Murayama N. Shin Woosuck. High performance p-type thermoelectric oxide based NiO. *Materials Letters*, 45(6):302–306, 2000.

[121] Xin Wang, Ye Li, GuoZheng Wang, Rong Xiang, DeLong Jiang, ShenCheng Fu, Kui Wu, XiaoYu Yang, QingDuo DuanMu, JingQuan Tian, and LiChen Fu. Characterization of NiO thin film grown by two-step processes. *Physica B: Condensed Matter*, 404(811):1058 – 1060, 2009.

[122] Reddy A.M. and Reddy P. S. Reddy A.S., Lee Kee-Sun. Effect of oxygen partial pressure on the structural, optical and electrical properties of sputtered NiO films. *Ceramics International*, 37:2837–2843, 2011.

[123] P.S. Patil and L.D. Kadam. Preparation and characterization of spray pyrolized Nickel Oxide (NiO) thin films. *Applied surface Science*, 199:211–221, 2002.

[124] H.J. van Daal and A. J. Bosman. Hall effect in CoO, NiO and $\alpha - Fe_2O_3$. *Physical Review*, 158:736–747, 1967.

[125] S P Mitoff. Electrical conductivity and thermodynamic equilibrium in Nickel Oxide. *Journal of Chemical Physics*, 35:882–889, 1961.

[126] J.B. Eror N.G., Wagner Jr. Electrical conductivity of single crystalline Nickel Oxide. *Phys. Stat. Sol.*, 35:641651, 1969.

[127] Schulz M. Madelung O., Rössler U., editor. *NiO SpringerMaterials - The Landolt-Börnstein Database*, volume 41D. Springer.

[128] K.V. Shàlimova. *Física de los Semiconductores*. Editorial MIR, 1975.

[129] Addonizio Maria Luisa Daliento Santolo Fanelli Esther Pernice Pasquale Tari Orlando, AronneAntonio. Solgel synthesis of ZnO transparent and conductive films: A critical approach. *Solar Energy Materials & Solar Cells*, 105:179–186, 2012.

[130] Bensalah H., Crocco J., Carcélen V., Plaza J. L., Zheng Q., Marchini L., Zanichelli M., Domínguez G., Soriano L., and Diéguez E. Study of ammonium fluoride passivation time on CdZnTe bulk crystal wafers. *Crystal Research and Technology*, 46(7):659–663, 2011.

[131] Walter J. Moore. *Seven solid states an introduction to the chemistry and physics of solids*. W. A. Benjamin Inc., 1967.

[132] Stefano Passerini and Bruno Scrosati. Chracterization of nonstochiometric Nickel Oxide thin-film electrodes. *J. Electrochem. Soc.*, 141(4):889–895, 1994.

[133] Per Kofstad and Truls Norby. *Defects and transport in crystalline solids*. University of Oslo, 2207.

[134] S. Koide. Electrical properties of $Li_xNi_{(1-x)}O$ single crystals. *Journal of the Physical Society of Japan*, 20:123–132, 1965.

[135] Hao-Long Chen, Yang-Ming Lu, and Weng-Sing Hwang. Characterization of sputtered NiO thin films. *Surface and Coatings Technology*, 198(13):138 – 142, 2005.

[136] J. van Elp, B.G. Searle, G.A. Sawatzky, and M. Sacchi. Ligand hole induced symmetry mixing of d^8 states in $Li_xNi_{1-x}O$, as observed in Ni 2p x-ray absorption spectroscopy. *Solid State Communications*, 80(1):67 – 71, 1991.

[137] Jang Wei-Luen, Lu Yang-Ming, and Hwang Weng-Sing. Effect of different atmospheres on the electrical stabilization of NiO films. *Vacuum*, 83:596–598, 2009.

[138] Jang Wei-Luen, Lu Yang-Ming, Hwang Weng-Sing, Hsiung Tung-Li, and Wang Paul H. Effect on the substrate temperature on the electrically conductive stability of sputtered NiO films. *Surface and Coatings Technology*, 202:5444–5447, 2008.

[139] Verheijkee M.L. Meijering J.L. Oxidation kinetics in the case of ageing oxide films. *Acta Metallurgica*, 7:331–338, 1959.

[140] R. Newman and R. M. Chrenko. Optical properties of Nickel Oxide. *Physical Review*, 114(6):1507–1513, 1959.

[141] Granqvist C. G. Estrada W., Andersson A. M. Electrochromic Nickel Oxide based coatings made by reactive dc magnetron sputtering: Preparation and optical properties. *J. Appl. Phys.*, 64:3678, 1988.

[142] Jacques I. Pankove. *Optical processes in semiconductors*. Dover, 1975.

[143] Vancu A. Tauc J., Grigorovici R. Optical properties and electronic structure of amorphous germanium. *Phys. Stat. Sol.*, 15:627–637, 1966.

[144] John Kennedy L. Manikandan A., Judith Vijaya J. Comparative investigacion of NiO nano- and microstructures for structural, optical and magnetic properties. *Physica E*, 49:117–123, 2013.

[145] Kamal H. Abdel-Hady A. Mahmoud S.A., Akl A.A. Opto-structural, electrical, and electrochromic properties of crystalline nickel oxide thin films prepared by spray pyrolysis. *Physica B*, 311:366–375, 2002.

[146] Hagfeldt A. Boschloo G. Spectroelectrochemistry of nanostructured NiO. *J. Phys. Chem. B*, 105:3039–3044, 2001.

[147] E. Engel and R. N. Schmid. Insulating ground states of transition-metal monoxides from exact exchange. *Phys. Rev. Lett.*, 103:036404, 2009.

[148] Seitsonen A. Brouder Ch. Shukle A Gougoussis C., Calandra M. and Mauri F. Intrinsic charge transfer gap in NiO from Ni K-edge X-ray Absorption Spectroscopy. *Phys. Rev. B*, 79:045118, 2009.

[149] J Hugel and C Carabatos. Band structure and optical properties of NiO. I. Band structure calculations. *Journal of Physics C: Solid State Physics*, 16(35):6713, 1983.

[150] Wan-Jian Yin, Shiyou Chen, Ji-Hui Yang, Xin-Gao Gong, Yanfa Yan, and Su-Huai Wei. Effective band gap narrowing of anatase TiO_2 by strain along a soft crystal direction. *App. Phys. Lett.*, 96:221901, 2010.

[151] Poelman D. and Frederic Smet P. Methods for the determination of the optical constants of thin films from single transmission measurements: a critical review. *Journal of Physics D: Applied Physics*, 36:1850–1857, 2003.

[152] Kamal H. Abdel-Hady K. Mahmoud S.A., Akl A.A. Opto-structural, electrical and electrochromic properties of crystalline nickel oxide thin films prepared by spray pyrolysis. *Physica B*, 311:366–375, 2002.

[153] P. Kuiper, G. Kruizinga, J. Ghijsen, G. A. Sawatzky, and H. Verweij. Character of holes in $Li_xNi_{1-x}O$ and their magnetic behavior. *Phys. Rev. Lett.*, 62:221–224, 1989.

[154] M. Abbate, G. Zampieri, F. Prado, A. Caneiro, J. M. Gonzalez-Calbet, and M. Vallet-Regi. Electronic structure and metal-insulator transition in $LaNiO_{3-\delta}$. *Phys. Rev. B*, 65:155101, 2002.

[155] T. Mizokawa, A. Fujimori, T. Arima, Y. Tokura, N. M ōri, and J. Akimitsu. Electronic structure of $PrNiO_3$ studied by photoemission and x-ray-absorption spectroscopy: band gap and orbital ordering. *Phys. Rev. B*, 52:13865–13873, 1995.

[156] M Sánchez-Agudo, L. Soriano, C. Quirós, J. Avila, and J.M. Sanz. Electronic interaction at the $TiO_2 - Al_2O_3$ interface as observed by X-ray Absorption Spectroscopy. *Surface Science*, 482485, Part 1(0):470 – 475, 2001.

[157] J. Michael Hollas. *Modern Spectroscopy.* John Wiley and Sons, fourth edition, 2004.

[158] F. Albert Cotton. *Chemical applications of group theory.* John Wiley & Sons., 1989.

[159] Victor M. S. Gil. *Orbitals in Chemistry: A Modern Guide for Students.* Cambridge University Press, 200.

[160] S.E. Barnes S. Ishihara W. Koshibae S. Maekawa, T. Tohyama and G. Khaliullin. *Physics of Transition Metal Oxides.* Springer, 2004.

[161] Frank De Groot. Multiplet effects in X-ray spectroscopy. *Coordination Chemistry Reviews*, 249:31–63, 2005.

[162] F. M. F. de Groot, J. C. Fuggle, B. T. Thole, and G. A. Sawatzky. 2p X-ray Absorption of 3d transition-metal compounds: An atomic multiplet description including the crystal field. *Phys. Rev. B*, 42:5459–5468, 1990.

[163] Helena A.E Hagelin-Weaver, Jason F Weaver, Gar B Hoflund, and Ghaleb N Salaita. Electron energy loss spectroscopic investigation of Ni metal and NiO before and after surface reduction by Ar^+ bombardment. *Journal of Electron Spectroscopy and Related Phenomena*, 134(23):139 – 171, 2004.

[164] L. Soriano, M. Abbate, J. Vogel, J.C. Fuggle, A. Fernández, A.R. González-Elipe, M. Sacchi, and J.M. Sanz. The electronic structure of mesoscopic NiO particles. *Chemical Physics Letters*, 208(56):460 – 464, 1993.

[165] L. Soriano, A. Gutiérrez, I. Preda, S. Palacín, J. M. Sanz, M. Abbate, J. F. Trigo, A. Vollmer, and P. R. Bressler. Splitting of Ni3d states at the surface of NiO nanostructures. *Phys. Rev. B*, 74:193402, 2006.

[166] Dongliang Chen, Jun Zhong, Xiang Wu, Ziyu Wu, Nina Mironova-Ulmane, Alexei Kuzmin, and Augosto Marcelli. Oxygen K-edge XANES investigation of $Ni_cMg_{1-c}o$ solid solutions. *Spectrochimica Acta Part A: Molecular and Biomolecular Spectroscopy*, 70(2):458 – 461, 2008.

[167] Z. Y. Wu, C. M. Liu, L. Guo, R. Hu, M. I. Abbas, T. D. Hu, , and H. B. Xu. Structural characterization of nickel oxide nanowires by X-ray Absorption Near-Edge Structure Spectroscopy. *J. Phys. Chem. B*, 109:2512–2515, 2005.

[168] H. Kurata, E. Lefèvre, C. Colliex, and R. Brydson. Electron-energy-loss near-edge structures in the oxygen K-edge spectra of transition-metal oxides. *Phys. Rev. B*, 47:13763–13768, 1993.

[169] I. Davoli, A. Marcelli, A. Bianconi, M. Tomellini, and M. Fanfoni. Multielectron configurations in the x-ray-absorption near-edge structure of NiO at the oxygen K threshold. *Phys. Rev. B*, 33:2979–2982, 1986.

[170] Nakai Shun-ichi, Mitsuishi Tsutomu, Sugawara Hidenao, Maezawa Hideki, Matsukawa Tokuo, Mitani Shichiro, Yamasaki Kazuo, and Fujikawa Takashi. Oxygen K X-ray absorption near-edge structure of alkaline-earth-metal and 3d-transition-metal oxides. *Phys. Rev. B*, 36:9241–9246, 1987.

[171] F. M. F. de Groot, M. Grioni, J. C. Fuggle, J. Ghijsen, G. A. Sawatzky, and H. Petersen. Oxygen 1s X-ray absorption edges of transition-metal oxides. *Phys. Rev. B*, 40:5715–5723, 1989.

[172] G. Domínguez-Cañizares, A. Gutiérrez, J. Chaboy, D. Díaz-Fernández, G. R. Castro, and L. Soriano. Effects of grain refinement and disorder on the electronic properties of nanocrystalline NiO. *Journal of Materials Science*, 49(7):2773–2780, 2013.

[173] Issei Sugiyama, Naoya Shibata, Zhongchang Wang, Shunsuke Kobayashi, Takahisa Yamamoto, and Yuichi Ikuhara. Ferromagnetic dislocations in antiferromagnetic NiO. *Nature Nanotechnology*, 8:266–270, 2013.

[174] R J O Mossanek, M Abbate, T Yoshida, A Fujimori, Y Yoshida, N Shirakawa, H Eisaki, S Kohno, P T Fonseca, and F C Vicentin. Electronic structure of the band-filling-controlled $CaVO_3$ and $LaVO_3$ compounds. *Journal of Physics: Condensed Matter*, 22(9):095601, 2010.

[175] R. J. O. Mossanek, G. Domínguez-Cañizares, A. Gutiérrez, M. Abbate, D. Díaz-Fernández, and L. Soriano. Effects of Ni vacancies and crystallite size on the O 1s and Ni 2p x-ray absorption spectra of nanocrystalline NiO. *Journal of Physics: Condensed Matter*, 25(49):495506, 2013.

[176] I. Preda, R.J.O. Mossanek, M. Abbate, L. Alvarez, J. Méndez, A. Gutiérrez, and L. Soriano. Surface contributions to the XPS spectra of nanostructured NiO deposited on HOPG. *Surface Science*, 606(1718):1426 – 1430, 2012.

[177] R.J.O. Mossanek, I. Preda, M. Abbate, J. Rubio-Zuazo, G.R. Castro, A. Vollmer, A. Gutiérrez, and L. Soriano. Investigation of surface and non-local screening effects in the Ni 2p core level photoemission spectra of NiO. *Chemical Physics Letters*, 501(46):437 – 441, 2011.

[178] Eli Stavitski and Frank M.F. de Groot. The CTM4XAS program for EELS and XAS spectral shape analysis of transition metal L edges. *Micron*, 41(7):687 – 694, 2010.

[179] M. Abbate, J. B. Goedkoop, F. M. F. de Groot, M. Grioni, J. C. Fuggle, S. Hofmann, H. Petersen, and M. Sacchi. Probing depth of soft X-ray absorption spectroscopy measured in total-electron-yield mode. *Surface and Interface Analysis*, 18(1):65–69, 1992.

[180] I. Preda, A. Gutiérrez, M. Abbate, F. Yubero, J. Méndez, L. Alvarez, and L. Soriano. Interface effects in the Ni2p x-ray photoelectron spectra of NiO thin films grown on oxide substrates. *Phys. Rev. B*, 77:075411, 2008.

[181] D. Díaz-Fernández, J. Méndez, F. Yubero, G. Domínguez-Cañizares, A. Gutiérrez, and L. Soriano. Study of the early stages of growth of Co oxides on oxide substrates. *Surf. Interf. Anal.*, ECASIA special issue paper, 2014.

[182] M. A. van Veenendaal and G. A. Sawatzky. Nonlocal screening effects in 2p x-ray photoemission spectroscopy core-level line shapes of transition metal compounds. *Phys. Rev. Lett.*, 70:2459–2462, 1993.

[183] L. Soriano, I. Preda, A. Gutiérrez, S. Palacín, M. Abbate, and A. Vollmer. Surface effects in the Ni 2p x-ray photoemission spectra of NiO. *Phys. Rev. B*, 75:233417, 2007.

[184] S. Palacín, A. Gutiérrez, I. Preda, M. Hernández-Vélez, R. Sanz, J.A. Jiménez, and L. Soriano. Core-level electronic properties of nanostructured NiO coatings. *Applied Surface Science*, 254(1):278 – 280, 2007. Proceedings of the 13th International Conference on Solid Films and Surfaces ICSFS 13.

[185] Andrew P. Grosvenor, Mark C. Biesinger, Roger St.C. Smart, and N. Stewart McIntyre. New interpretations of XPS spectra of nickel metal and oxides. *Surface Science*, 600(9):1771 – 1779, 2006.

[186] Liang Qiao and Xiaofang Bi. Direct observation of Ni^{3+} and Ni^{2+} in correlated $LaNiO_{3-\delta}$ films. *Europhysics Letters*, 93(5):57002, 2011.

[187] Dong Soo Kim and Hee Chul Lee. Nickel vacancy behavior in the electrical conductance of nonstoichiometric nickel oxide film. *Journal of Applied Physics*, 112(3):034504, 2012.

[188] J.M. Sanz and G.T. Tyuliev. An XPS study of thin NiO films deposited on MgO(100). *Surface Science*, 367(2):196 – 202, 1996.

[189] D. Alders, F. C. Voogt, T. Hibma, and G. A. Sawatzky. Nonlocal screening effects in 2p x-ray photoemission spectroscopy of NiO (100). *Phys. Rev. B*, 54:7716–7719, 1996.

[190] St. Uhlenbrock, C. Scharfschwerdt, M. Neumann, G. Illing, and H.-J. Freund. The influence of defects on the Ni 2p and O 1s XPS of NiO. *Journal of Physics: Condensed Matter*, 4(40):7973, 1992.

[191] Jeffrey M. McKay and Victor E. Henrich. Surface electronic structure of NiO: Defect states, O_2 and H_2O interactions. *Phys. Rev. B*, 32:6764–6772, 1985.

[192] Andrea G. Marrani, Vittoria Novelli, Stephen Sheehan, Denis P. Dowling, and Danilo Dini. Probing the redox states at the surface of electroactive nanoporous NiO thin films. *ACS Applied Materials & Interfaces*, 6(1):143–152, 2014.

[193] C. Schuessler-Langeheine. Newfit Software for Photoemission Analysis, 1999.

[194] F. James and M. Roos. Minuit - a system for function minimization and analysis of the parameter errors and correlations. *Computer Physics Communications*, 10(6):343 – 367, 1975.

Notes